Cavity Optomechanics with Silica Toroidal Microresonators down to Low Phonon Occupancy

Rémi Rivière

München 2011

Cavity Optomechanics with Silica Toroidal Microresonators down to Low Phonon Occupancy

Rémi Rivière

Dissertation
an der Fakultät für Physik
der Ludwig–Maximilians–Universität
München

vorgelegt von
Rémi Rivière
aus Toulouse, Frankreich

München, den 29. August 2011

Erstgutachter: Prof. Dr. T. W. Hänsch

Zweitgutachter: Prof. Dr. J. P. Kotthaus

Tag der mündlichen Prüfung: 30. September 2011

A mes parents, Christine et Jean et à ma soeur, Laura.

Contents

List of Figures

List of Publications

[1] A. Schliesser, R. Rivière, G. Anetsberger, O. Arcizet, and T. J. Kippenberg
"Resolved-Sideband Cooling of a Micromechanical Oscillator"
Nature Physics **4**, 415 (2008).

[2] G. Anetsberger, R. Rivière, A. Schliesser, O. Arcizet, and T. J. Kippenberg
"Ultralow-Dissipation Optomechanical Resonators on a Chip"
Nature Photonics **2**, 627 (2008).

[3] A. Schliesser, G. Anetsberger, R. Rivière, O. Arcizet, and T. J. Kippenberg
"High-Sensitivity Monitoring of Micromechanical Vibration using Optical Whispering Gallery Mode Resonators"
New Journal of Physics **10**, 095015 (2008).

[4] O. Arcizet*, R. Rivière*, A. Schliesser, G. Anetsberger, and T. J. Kippenberg
"Cryogenic Properties of Optomechanical Silica Microcavities"
Physical Review A **80**, 021803 (2009).

[5] A. Schliesser*, O. Arcizet*, R. Rivière*, G. Anetsberger, and T. J. Kippenberg
"Resolved-Sideband Cooling and Position Measurement of a Micromechanical Oscillator Close to the Heisenberg Uncertainty Limit"
Nature Physics **5**, 509 (2009).

[6] G. Anetsberger, O. Arcizet, Q. P. Unterreithmeier, R. Rivière, A. Schliesser, E. M. Weig, J. P. Kotthaus, and T. J. Kippenberg
"Near-Field Cavity Optomechanics with Nanomechanical Oscillators"
Nature Physics **5**, 909 (2009).

[7] S. Weis*, R. Rivière*, S. Deléglise*, E. Gavartin, O. Arcizet, A. Schliesser, and T. J. Kippenberg
"Optomechanically Induced Transparency"
Science **330**, 1520 (2010).

---

*Equal contributions

[8] R. Rivière*, S. Deléglise*, S. Weis*, E. Gavartin, O. Arcizet, A. Schliesser, and T. J. Kippenberg
"Optomechanical Sideband Cooling of a Micromechanical Oscillator Close to the Quantum Ground State"
Physical Review A **83**, 063835 (2011).

---

*Equal contributions

List of Conference Talks

[1] Walther-Meissner-Institut Seminar, Garching, Germany, (Nov. 2008), **Invited talk**
"Cavity Optomechanics at Low Temperatures"
R. Rivière, G. Anetsberger, J. Dobrindt, J. Hofer, A. Schliesser, O. Arcizet, and T. J. Kippenberg

[2] MINOS Workshop, IQOQI, Vienna, Austria, (Dec. 2008)
"Cavity Optomechanics at Low Temperatures"
R. Rivière, G. Anetsberger, J. Dobrindt, J. Hofer, A. Schliesser, O. Arcizet, and T. J. Kippenberg

[3] CLEO/IQEC, Baltimore, US,A (June 2009)
"Cryogenic Properties of Optomechanical Silica Microcavities"
O. Arcizet*, R. Rivière*, A. Schliesser, G. Anetsberger, and T. J. Kippenberg

[4] CLEO/IQEC, Baltimore, USA, (June 2009), **Invited talk**
"Resolved-Sideband Laser Cooling and Measurement of a Micromechanical Oscillator Close to the Quantum Limit"
A. Schliesser*, O. Arcizet*, R. Rivière*, G. Anetsberger, and T. J. Kippenberg

[5] CLEO/EQEC, Munich, Germany, (June 2009)
"Cryogenic Properties of Optomechanical Silica Microcavities"
O. Arcizet*, R. Rivière*, A. Schliesser, G. Anetsberger, and T. J. Kippenberg

[6] IEEE Group IV Photonics 2009, San Francisco, USA, (Sept. 2009), **Invited talk**
"Cavity Optomechanics: Cooling of Mechanical Oscillators Using Backaction"
R. Rivière, G. Anetsberger, O. Arcizet, J. Dobrindt, E. Gavartin, A. Schliesser, S. Weis, X. Zhou, and T. J. Kippenberg

[7] CLEO/IQEC, San Jose, USA, (May 2010)
"Optical Response of Silica Microcavities in Gaseous and Superfluid ^{4}He"
R. Rivière, O. Arcizet, A. Schliesser, X. Zhou, and T. J. Kippenberg

---

*Equal contributions

[8] Joint Workshop MPQ - University of Freiburg, Garching, Germany, (Oct. 2010), **Invited talk**
"Optomechanically Induced Transparency and Laser Cooling of a Mechanical Oscillator to Low Phonon Numbers"
<u>R. Rivière</u>, S. Weis, S. Deléglise, E. Garvartin, O. Arcizet, A. Schliesser, and T. J. Kippenberg

[9] NIM Area D Meeting, Munich, Germany, (Oct. 2010), **Invited talk**
"Optomechanically Induced Transparency and Laser Cooling of a Mechanical Oscillator to Low Phonon Numbers"
<u>R. Rivière</u>, S. Weis, S. Deléglise, E. Garvartin, O. Arcizet, A. Schliesser, and T. J. Kippenberg

[10] IBM Watson Research Center, Yorktown Heights, USA, (Nov. 2010), **Invited talk**
"Cavity Optomechanics"
<u>R. Rivière</u>

[11] 2nd International Workshop on Fundamentals of Light-Matter Interaction, Porto de Galinhas, Brazil, (Feb. 2011), **Invited talk**
"Cavity Optomechanics"
<u>R. Rivière</u>, S. Weis, S. Deléglise, E. Garvartin, O. Arcizet, A. Schliesser, and T. J. Kippenberg

[12] DPG Tagung, Dresden, Germany, (March 2011)
"Optomechanical Cooling Close to the Ground State"
<u>R. Rivière</u>, S. Weis, S. Deléglise, E. Garvartin, O. Arcizet, A. Schliesser, and T. J. Kippenberg

[14] Phononics 2011, Santa Fe, USA, (June 2011), **Invited talk**
"Cooling of a Micromechanical Oscillator into the Quantum Regime"
<u>R. Rivière</u>, S. Weis, S. Deléglise, E. Garvartin, O. Arcizet, A. Schliesser, and T. J. Kippenberg

[15] Silicon Photonics Summer School, Saint Andrews University, UK, (July 2011), **Invited lecture**
"Cavity Optomechanics"
<u>R. Rivière</u>, S. Weis, S. Deléglise, E. Garvartin, O. Arcizet, A. Schliesser, and T. J. Kippenberg

Zusammenfassung

Im Rahmen dieser Arbeit beschreibe ich die Kühlung von makroskopischen, harmonisch oszillierenden Massen in der Größenordnung von 10 ng in die Nähe des quantenmechanischen Grundzustandes. Um die Kühlung durchzuführen, nutzen wir die Licht-Materie Wechselwirkung aus, die die mechanischen Freiheitsgrade über den Strahlungsdruck des Lichts im Resonator an eine Resonatormode koppelt. Die verzögerte Antwort des kohärenten optischen Feldes auf mechanische Vibrationen führt zu einem viskosen Strahlungsdruck und damit zu einer Kraft die eine Kühlung der Bewegung bewirkt. Die theoretischen Grundlagen dieser Kühlung mittels dynamischer Rückwirkung werden in Kapitel 1 erläutert.

In Kapitel 2 wird das verwendete experimentelle System vorgestellt: Der Quarzglas Mikrotoroid Resonator. Der Vorteil dieses Resonators ist, dass in ihm optische Flüstergalleriemoden hoher Finesse (nahe 10^6) mit einer radial schwingenden mechanischen Mode im Radiofrequenzbereich (mehrere 10 MHz) koppeln können.

Kapitel 3 zeigt eine detaillierte Beschreibung der experimentellen Erfolge die Kühlung des Systems zu verstärken und damit die durchschnittliche Besetzungszahl von Phononen, Quanten mechanischer Energie, weiter zu reduzieren. Des Weiteren werden verschiedene Quellen mechanischer Verluste untersucht und durch Optimierung der mechanischen Struktur, wodurch die Kopplung der mechanischen Mode an die warme Umgebung reduziert wird, verringert. Mit Hilfe der hierfür neu entwickelten, über Speichen befestigten Mikrotoroid-Resonatoren wird die Dämpfung des Systems durch Kopplung an andere Moden reduziert und auf intrinsische Materialeigenschaften von Quarzglas minimiert. Um die Temperatur der Umgebung selbst zu reduzieren, wird das Experiment zunächst in einem ^{4}He Kryostaten gekühlt. Dies ermöglicht die Beobachtung neuartiger dispersiver optischer Eigenschaften von Quarzglas und eine Untersuchung der Thermalisierung der Probe bei tiefen Temperaturen. Zur weiteren Kühlung wird der Aufbau schließlich in einen ^{3}He Kryostaten mit einer Betriebstemperatur von 850 mK implementiert. Die Kühlung wird unter Verwendung eines Homodyninterferometers zur Messung von Vibrationen mit quantenlimitierter Empfindlichkeit beschrieben. Voraussetzung für eine Kühlung in den Grundzustand ist, dass sich das System im Aufgelösten-Seitenband-Regime befindet. Wir erreichen eine mittlere Phononenbesetzungszahl von 9 ± 1 und die Tatsache, dass ausschließlich einfache technische Schwierigkeiten ein weiteres Kühlen einschränken zeigt, dass der entwickelte experimentelle Aufbau optimiert ist, um Signaturen von Quanteneffekten eines makroskopischen mechanischen Oszillators, gekühlt durch dynamische Rückwirkung, aufzuzeigen. Abschließend wird der Effekt der Licht-Materie Wechselwirkung auf die op-

tischen Eigenschaften des Resonators gemessen und analysiert. Damit wird die erstmalige Beobachtung von optomechanisch induzierter Transparenz beschrieben. Dies zeigt anhand experimenteller Messungen die Interaktion zwischen Licht und mechanischen Schwingungen.

Abstract

In this thesis, I report on the cooling of a macroscopic harmonic mechanical oscillator of mass on the order of $10\,\mathrm{ng}$ close to its quantum ground state. To perform the refrigeration, we exploit the optomechanical interaction that couples the mechanical degree of freedom to an optical cavity mode via the light's radiation pressure. The delayed response of the intracavity field upon mechanical vibration leads to a viscous intracavity radiation pressure force responsible for the *dynamical backaction cooling*, as is theoretically introduced in chapter 1.

In chapter 2, we review the experimental system accommodating this process: the silica microtoroidal cavity. It advantageously hosts a significant optomechanical coupling between the supported high-finesse (close to 10^6) optical whispering-gallery modes and the mechanical radial breathing mode oscillating at radio frequencies (tens of MHz).

In chapter 3, we detail the experimental efforts performed to improve the effect of the cooling on the system and thus to reach a lower average number of mechanical energy quanta, or phonons. The various sources of mechanical dissipations are studied. Their magnitude is diminished by optimizing the mechanical structure, therefore reducing the coupling of the mechanical mode to its warm thermal environment. In the newly developed spoke-anchored toroidal microcavities, engineering the intermode coupling minimizes the system's damping down to the limit imposed by the properties of the vitreous silica material. To reduce the temperature of the environment itself, the experiment is pre-cooled first in a prototype ^{4}He cryostat. This enables the observation of novel dispersive optical properties of fused silica and the study of the sample's thermalization at cryogenic temperatures. To further increase the pre-cooling, the setup is finally implemented in a colder ^{3}He cryostat operated at $850\,\mathrm{mK}$. Using the balanced homodyne interferometer constructed to detect the mechanical vibration with quantum-limited sensitivity, we report on the cooling performed in the resolved-sideband configuration that is fundamentally required to reach the ground state. A mean phonon occupancy of 9 ± 1 is achieved. The fact that only simple technical problems limit further cooling proves that the developed experimental system is finally optimized for revealing quantum signatures of a macroscopic mechanical oscillator cooled by dynamical backaction. Finally, the effect of the optomechanical interaction on the optical properties of the cavity is measured and analyzed, leading to the first observation of optomechanically induced transparency. This constitutes an experimental manifestation of the mutual character of interaction between light and mechanical motion.

Chapter 1

Theory of cavity optomechanics

1.1 Introduction

The optical interferometric measurement is today's most sensitive technique to detect small displacements. Gravitational wave detectors take advantage of this principle to measure tiny space-time fluctuations resulting from gravitational waves passing through. Despite an achieved sensitivity in relative space dilatation below 10^{-21}, this phenomenon, predicted almost a century ago by Einstein, has not yet been directly experimentally verified. The scientific investigations undertaken to further improve the detection performance revealed that the probing light affects the suspended mirrors of the interferometer via the *backaction*, mediated by the light's radiation pressure. In these detectors, the quantum aspect of this phenomenon – the *quantum backaction* – puts a strong limit on the sensitivity [1, 2]. Nevertheless, as predicted already four decades ago by Braginsky in his pioneering work [3, 4], the radiation pressure force can also be used to amplify a mechanical vibration, or intriguingly, to cool it down by adding extra optical damping, both within a process referred to as *dynamical backaction*.

The radiation pressure force carried by the light was in fact formally known to the scientific community beforehand, since Maxwell's theory of electromagnetism. Its existence had even been conjectured earlier, in the 17th century, by Kepler after he observed that a comet's tail always points opposite to the sun. The first experimental evidence of radiation pressure effects on a mechanical mass was independently demonstrated later by Lebedew [5] and by Nichols and Hull [6] in 1901 by observing that a mirror-covered fan could start rotating under the sole action of light. It is nonetheless within the context of "laser cooling" of atoms that the radiation pressure of light has first been put into practice to refrigerate a mechanical vibration. In the 1970ies, it has been demonstrated theoretically as well as experimentally that radiation pressure cooling can lead to the observation of the freeze-out of the mechanical motion of neutral atoms [7, 8] and harmonically trapped ions [9, 10]. As with gravitational wave detectors, the quantum character of the process leads to a fundamental limit on the lowest attainable temperature. The strength of this quantum backaction can however be arbitrarily reduced for trapped ions when operating in the

"resolved-sideband limit" where the mechanical vibration frequency exceeds the linewidth of the atomic transition, therefore enabling reaching the ions' motional ground state.

Recently, the advances of microfabrication have made it conceivable to envisage the experimental extension of this phenomenon to much larger scales [11]. By combining a macroscopic mechanical oscillator with an optical resonator, it is possible to use the *optomechanical* coupling to cool down the oscillatory movement of the mass. In the resolved-sideband regime (where the resonator's optical linewidth exceeds the oscillator's mechanical resonance frequency) [12, 13, 14], the macroscopic object can be cooled down to its motional ground state. This emerging field of *cavity optomechanics* opens then new interesting physical possibilities by enabling the preparation of the mechanical oscillator in a low entropy state while simultaneously harnessing the mutual coupling to measure the vibration.

The perspectives opened by this implementation are immense and numerous particularities of quantum mechanics previously observed at a microscopic scale are now within reach for mechanical systems closer to our everyday-life environment. This has recently sparked off various theoretical analyses demonstrating that the optomechanical system can host peculiar non-classical phenomena such as quantum state superposition of macroscopic mirrors [15], quantum entanglement of an optical cavity mode and a mechanical mode [16, 17] or quantum squeezing of a mechanical mode [18].

In this chapter, we pave the theoretical ground of the optomechanical coupling and the resulting dynamical backaction cooling [19, 20, 21].

Section 1.2 describes the cooling process in the generic optomechanical system made of a Fabry-Perot cavity for which the back mirror is mounted on a mechanical oscillator. The quantum Hamiltonian of the system is described and the resulting equations of motion of the mechanical and optical modes are used to characterize the static and dynamical backaction of the light acting on the mechanical system. The latter is responsible for the change of the dynamics of the oscillator by modifying the apparent mechanical oscillation frequency – the optical spring effect – and by modifying the effective damping of the mechanical oscillator, which leads to the amplification or the cooling of the mechanical mode. The quantum character of the optical field is discussed and it is demonstrated that the concomitant residual phonon occupancy reaches values much lower than one in the optimum configuration of the resolved sidebands. Finally, the regime of dynamical amplification is reviewed and the analogy with the "sideband cooling" of trapped ions is presented, bridging the gap between the two fields.

In section 1.3, the detection of the mechanical motion enabled by the optomechanical coupling is discussed from a quantum perspective. The notion of measurement quantum imprecision and backaction is introduced, and the optimal set of parameters allowing to reach the standard quantum limit of optical measurements is presented.

1.2   Theoretical framework of cooling

The theoretical framework of cavity optomechanics is built from the very generic scheme depicted in Fig. 1.1. This scheme applies to any experimental system consisting of an electromagnetic resonator for which one of the boundaries is can move to a significant extent. Any mechanical displacement will then change the electromagnetic pathlength and thus affect the electromagnetic resonance frequency.
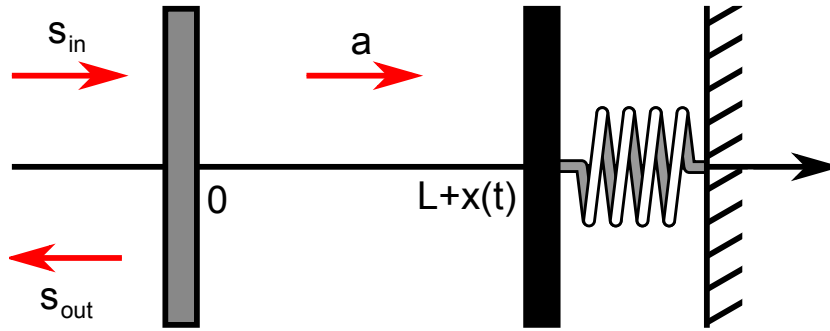
Figure 1.1: *Schematic optomechanical system in the illustrative case of an optical Fabry-Perot cavity consisting of one fixed coupling mirror and one movable back mirror. s_in, s_out and a represent the incoming pumping field, the outgoing field and the intracavity field, respectively.*

In the illustrative picture of Fig. 1.1, the optical resonator is pumped by an external field s_in through the input mirror, located at fixed position at the origin, leading to an intracavity field build up. The electromagnetic mode is described here as an optical mode for convenience, but the formalism applies at lower electromagnetic frequencies as well, for instance in the context of superconducting microwave electromechanical devices. For simplicity of the theoretical framework Following the simple formalism introduced by Haus [22], the intracavity amplitude is defined here to normalize its modulus square $|a|^2$ to the intracavity photon number The intracavity energy is then simply given by $\hbar\omega_\text{l}|a|^2$, where $\hbar$ is the reduced Planck constant and ω_l the wave angular frequency. In this picture, the back mirror of the resonator is a reflecting mirror of mass m_eff attached to a spring with spring constant k_m, constituting a one-dimensional mechanical oscillator. The coordinate of the back mirror is $x(t) + L$, where L is the coordinate in the absence of oscillations. For a small displacement $x(t)$ compared to L, the resonance angular frequency of the optical resonator can be developed to first order in displacement into

$$\omega \approx \omega_\text{c} + Gx(t), \tag{1.1}$$

where ω_c is the resonance angular frequency for the optical resonator of length L in the absence of any oscillations and G is the optomechanical coupling constant defined by

$$G = -\frac{\omega_\text{c}}{L}. \tag{1.2}$$

The condition of small oscillatory amplitudes ensures that the mechanical oscillator remains harmonic.

1.2.1   Hamiltonian of the optomechanical system

When the previously described classical physical quantities are replaced by their quantum operators, the quantum Hamiltonian of the optomechanical reads [23]

$$\hat{H} = \hat{H}_{\mathrm{m}} + \hat{H}_{\mathrm{em}} + \hat{H}_{\mathrm{int}}, \tag{1.3}$$

with

$$\hat{H}_{\mathrm{m}} = \frac{1}{2m_{\mathrm{eff}}} \left(m_{\mathrm{eff}}^2 \Omega_{\mathrm{m}}^2 \hat{x}^2 + \hat{p}^2 \right), \tag{1.4}$$

$$\hat{H}_{\mathrm{em}} = \hbar\omega_{\mathrm{c}} \left(\hat{a}^\dagger \hat{a} + \frac{1}{2} \right) + i\hbar\sqrt{\kappa_{\mathrm{ex}}} \left(\hat{s}_{\mathrm{in}} \hat{a}^\dagger e^{-i\omega_{\mathrm{l}}t} - \hat{s}_{\mathrm{in}}^\dagger \hat{a} e^{+i\omega_{\mathrm{l}}t} \right), \tag{1.5}$$

$$\hat{H}_{\mathrm{int}} = \hbar G \hat{x} \hat{a}^\dagger \hat{a}, \tag{1.6}$$

where $\Omega_{\mathrm{m}} = \sqrt{\frac{k_{\mathrm{m}}}{m_{\mathrm{eff}}}}$ is the mechanical resonance angular frequency.

- $\hat{H}_{\mathrm{m}}$ is the Hamiltonian operator of the mechanical oscillator with $\hat{x}$ and $\hat{p}$ being the coordinate and momentum quantum operators.

- $\hat{H}_{\mathrm{em}}$ is the Hamiltonian operator of the electromagnetic resonator with $\hat{a}^\dagger$ and $\hat{a}$ denoting the creation and annihilation operators of the intracavity field, respectively. The last term in the expression of $\hat{H}_{\mathrm{em}}$ accounts for the laser drive of the intracavity optical mode by the external field $\hat{s}_{\mathrm{in}}$ of angular frequency ω_{l} through the input mirror of *external* decay rate κ_{ex}.

- $\hat{H}_{\mathrm{int}}$ is the Hamiltonian of the mutual interaction responsible for the physical phenomena observed in cavity optomechanics. The optomechanical coupling can be thus understood by taking successively the two complementary point of views of the mechanical resonator and the optical field. For the latter, a small displacement of the mirror is responsible for a change in the resonance frequency, as can be seen by deriving in the Heisenberg picture the equation of motion for the amplitude of the intracavity field:

$$\frac{d\hat{a}}{dt} = \frac{i}{\hbar}[\hat{H}_{\mathrm{em}} + \hat{H}_{\mathrm{int}}, \hat{a}] = -i(\omega_{\mathrm{c}} + G\hat{x})\hat{a}. \tag{1.7}$$

If we now take the point of view of the mirror, the coupling is responsible for a force, that is defined as the rate of variation of the momentum due to the optical field

$$\hat{F}_{\mathrm{rp}} = \frac{d\hat{p}}{dt} = \frac{i}{\hbar}[\hat{H}_{\mathrm{int}}, \hat{p}] = -\hbar G \hat{a}^\dagger \hat{a} = -2\hbar k \frac{c}{2L} \hat{n}_{\mathrm{p}}, \tag{1.8}$$

with c being the speed of light in vacuum and $\hat{n}_{\mathrm{p}} = \hat{a}^\dagger \hat{a}$ the intracavity photon number. The last expression of equation (1.8) describes the intuitive picture that the radiation pressure force acting on the movable mirror comes from the momentum transfer $-2\hbar k$ of the $\hat{n}_{\mathrm{p}}$ intracavity photons per round-trip of duration $\tau_{\mathrm{rt}} = 2L/c$.

Since historically the electromagnetic field was actually used to measure the evolution of the mechanical oscillator, its influence on the mechanical oscillator mediated here by the radiation pressure has been named *backaction*.

The presented model can be conveniently expressed using only dimensionless creation and annihilation operators for the optical and mechanical variables. For the mechanical oscillator, the phonon is introduced as the quantum of mechanical energy

$$\hat{H}_{\rm m} = \hbar\Omega_{\rm m}\left(\hat{b}^{\dagger}\hat{b} + 1/2\right),\tag{1.9}$$

with the phonon number operator being $\hat{n} = \hat{b}^{\dagger}\hat{b}$, using the mechanical creation and annihilation operators $\hat{b}^{\dagger}$ and $\hat{b}$, respectively. The interaction Hamiltonian is then expressed as

$$\hat{H}_{\rm int} = g_0\hat{a}^{\dagger}\hat{a}(\hat{b}^{\dagger} + \hat{b}),\tag{1.10}$$

where g_0 is the vacuum optomechanical coupling rate [24]. This constant determines the mutual interaction energy of the coupled degrees of freedom and describes alone all the dynamics of the optomechanical interaction at any scale. It is expressed by

$$g_0 = G \times x_{\rm zpf},\tag{1.11}$$

where

$$x_{\rm zpf} = \sqrt{\hbar/(2m_{\rm eff}\Omega_{\rm m})}\tag{1.12}$$

is the zero-point fluctuation of the mechanical oscillator.

1.2.2   Equations of motion

From the Hamiltonian (1.3), the Heisenberg-Langevin approach [25] is used to derive the equations of motion of the quantum operators of interest $\hat{p}$ and $\hat{a}$, given by

$$\frac{d}{dt}\hat{x}(t) = \hat{p}(t)/m_{\rm eff},\tag{1.13}$$

$$\frac{d}{dt}\hat{p}(t) = -m_{\rm eff}\Omega_{\rm m}^2\hat{x}(t) - \Gamma_{\rm m}\frac{d}{dt}\hat{p}(t) - \hbar G\hat{a}^{\dagger}(t)\hat{a}(t) + m_{\rm eff}\sqrt{\Gamma_{\rm m}}\hat{\xi}_{\rm th}(t),\tag{1.14}$$

$$\frac{d}{dt}\hat{a}(t) = i\Delta\hat{a}(t) - \frac{\kappa}{2}\hat{a}(t) - iG\hat{x}(t)\hat{a}(t) + \sqrt{\kappa_{\rm ex}}\hat{s}_{\rm in}(t) + \sqrt{\kappa_0}\hat{s}_{\rm vac}(t).\tag{1.15}$$

For simplicity, the previous frame is transformed to a frame rotating at the angular frequency $\omega_{\rm l}$ of the driving electromagnetic field, thus introducing the detuning $\Delta = \omega_{\rm l} - \omega_{\rm c}$. In addition to the conservative dynamics of the system, the irreversible coupling to the environment through the optical (κ) and mechanical losses ($\Gamma_{\rm m}$) are introduced using the Heisenberg-Langevin approach. The electromagnetic decay rate κ is then

$$\kappa = \kappa_0 + \kappa_{\rm ex}\tag{1.16}$$

where κ_0 accounts for the intracavity losses. As in Ref. [22] and without a loss of generality, we take $\kappa_{\rm ex}$ as real. $\hat{\xi}_{\rm th}$ is the Brownian noise operator acting on the mechanical oscillator

and $\hat{s}_{\text{vac}}$ is the vacuum field noise operator of the intracavity field. Both terms are direct manifestations of the fluctuation-dissipation theorem [25].

To separate the static and dynamical contributions from the coupled equations (1.14) and (1.15) each time dependent operator is linearized around its mean value: $\hat{a}(t) = \bar{a} + \delta\hat{a}(t)$, $\hat{s}_{\text{in}}(t) = \bar{s}_{\text{in}} + \delta\hat{s}_{\text{in}}(t)$ and $\hat{x}(t) = \bar{x} + \delta\hat{x}(t)$ [12, 13, 14]. As we operate in a regime where the mean values are much larger than the fluctuations, we can then drop all products involving more than one fluctuator. Additionally, the phase of the input field $\bar{s}_{\text{in}}$ is chosen such that $\bar{a}$ is real and we assume a strong coherent drive $\bar{a} \gg 1$.

1.2.3   Static backaction

The mutual coupling of the mechanical and optical modes is first described in the simple particular case of a static phenomenon.

The mean values of both modes are affected by the optomechanical coupling characterized by the Hamiltonian operator $\hat{H}_{\text{int}}$ expressed in (1.6). Using the linearization procedure previously introduced, the mean field terms of the coupled equations (1.14) and (1.15) when noise terms are dropped become

$$\Omega_{\text{m}}^2 \bar{x} = -\frac{\hbar G}{m_{\text{eff}}} \bar{a}^2, \tag{1.17}$$

$$\left(-i(\Delta - G\bar{x}) + \frac{\kappa}{2}\right)\bar{a} = \sqrt{\kappa_{\text{ex}}}\,\bar{s}_{\text{in}}. \tag{1.18}$$

Equation (1.17) denotes a shift in the mean position of the moving mirror, proportional to the value of the radiation pressure. Reciprocally, equation (1.18) shows that the optical resonance frequency is shifted by an amount proportional to the mechanical displacement. Since the static mechanical displacement is proportional to the intracavity photon number $\bar{a}^2$, the latter effect is equivalent to a change of optical path resulting from a third order non-linear optical susceptibility. As a consequence, a bistable regime appears upon sweeping the pump field with regards to the resonator resonance frequency. This spectacular phenomenon has been experimentally demonstrated in a pioneering experiment in an optical Fabry-Perot cavity in the group of Walther in 1983 [26]

In the following study however, only the effect the backaction has on the detuning of the pump field $\bar{s}_{\text{in}}$ compared to the resonator resonance frequency is considered. The corresponding normalized detuning is thus defined as

$$\bar{\Delta} = \Delta - G\bar{x}. \tag{1.19}$$

1.2.4   Dynamical backaction

The main focus in this work is on the dynamical effects leading to the dynamical backaction of the light's radiation pressure onto the mirror. Indeed, this phenomenon is responsible for the optical spring and damping effects as first described by Braginsky in 1967 [3] and for the quantum backaction: those effects will be especially studied in the experimental part of this work.

To describe these phenomena, we study the time-dependent terms introduced in section 1.2.2. Keeping the modified detuning introduced in the previous section, we obtain

$$\frac{d^2}{dt^2}\delta\hat{x}(t) = -\Omega_\mathrm{m}^2\delta\hat{x}(t) - \Gamma_\mathrm{m}\delta\frac{d}{dt}\hat{x}(t) - \frac{\hbar G}{m_\mathrm{eff}}\bar{a}\left(\delta\hat{a}^\dagger(t) + \delta\hat{a}(t)\right) + \sqrt{\Gamma_\mathrm{m}}\hat{\xi}_\mathrm{th}(t), \quad (1.20)$$

$$\frac{d}{dt}\delta\hat{a}(t) = \left(+i\bar{\Delta} - \frac{\kappa}{2}\right)\delta\hat{a}(t) - iG\bar{a}\delta\hat{x}(t) + \sqrt{\kappa_\mathrm{ex}}\delta\hat{s}_\mathrm{in}(t) + \sqrt{\kappa_0}\delta\hat{s}_\mathrm{vac}(t), \quad (1.21)$$

$$\frac{d}{dt}\delta\hat{a}^\dagger(t) = \left(-i\bar{\Delta} - \frac{\kappa}{2}\right)\delta\hat{a}^\dagger(t) + iG\bar{a}\delta\hat{x}(t) + \sqrt{\kappa_\mathrm{ex}}\delta\hat{s}_\mathrm{in}^\dagger(t) + \sqrt{\kappa_0}\delta\hat{s}_\mathrm{vac}^\dagger(t). \quad (1.22)$$

After Fourier transform[1], the set of equations becomes

$$-\Omega^2\delta\hat{x}(\Omega) = -\Omega_\mathrm{m}^2\delta\hat{x}(\Omega) + i\Omega\Gamma_\mathrm{m}\delta\hat{x}(\Omega) - \frac{\hbar G}{m_\mathrm{eff}}\bar{a}\left(\delta\hat{a}^\dagger(\Omega) + \delta\hat{a}(\Omega)\right) + \sqrt{\Gamma_\mathrm{m}}\delta\hat{\xi}_\mathrm{th}(\Omega), \quad (1.23)$$

$$-i\Omega\delta\hat{a}(\Omega) = \left(+i\bar{\Delta} - \frac{\kappa}{2}\right)\delta\hat{a}(\Omega) - iG\bar{a}\delta\hat{x}(\Omega) + \sqrt{\kappa_\mathrm{ex}}\delta\hat{s}_\mathrm{in}(\Omega) + \sqrt{\kappa_0}\delta\hat{s}_\mathrm{vac}(\Omega), \quad (1.24)$$

$$-i\Omega\delta\hat{a}^\dagger(\Omega) = \left(-i\bar{\Delta} - \frac{\kappa}{2}\right)\delta\hat{a}^\dagger(\Omega) + iG\bar{a}\delta\hat{x}(\Omega) + \sqrt{\kappa_\mathrm{ex}}\delta\hat{s}_\mathrm{in}^\dagger(\Omega) + \sqrt{\kappa_0}\delta\hat{s}_\mathrm{vac}^\dagger(\Omega), \quad (1.25)$$

where the property of the Fourier transform $\delta\hat{a}^\dagger(\Omega) = (\delta(-\Omega))^\dagger$ was used as well as the property $\delta\hat{x}^\dagger(\Omega) = \delta\hat{x}(\Omega)$ for a Hermitian operator. The correlation functions of the noise operators are given by

$$\langle\delta\hat{s}_\mathrm{in}(\Omega)\delta\hat{s}_\mathrm{in}^\dagger(\Omega')\rangle = 2\pi\delta\left(\Omega + \Omega'\right), \quad (1.26)$$

$$\langle\delta\hat{s}_\mathrm{vac}(\Omega)\delta\hat{s}_\mathrm{vac}^\dagger(\Omega')\rangle = 2\pi\delta\left(\Omega + \Omega'\right), \quad (1.27)$$

for the electromagnetic noise operators and

$$\langle\delta\hat{\xi}_\mathrm{th}(\Omega)\delta\hat{\xi}_\mathrm{th}^\dagger(\Omega')\rangle = 2\pi\delta\left(\Omega + \Omega'\right)\hbar\, m_\mathrm{eff}^{-1}\,\Omega\left(\coth\left(\frac{\hbar\Omega}{2k_\mathrm{B}T_\mathrm{m}}\right) + 1\right), \quad (1.28)$$

for the mechanical noise operator, k_B being the Boltzmann constant and T_m the mechanical bath temperature. Note that this double sided-spectrum is not an even function of Ω. It can be shown that the antisymmetric part of the noise spectrum is due to the (small) contribution of the quantum noise to the total Brownian force [27].

From Eq. (1.8), the dynamical radiation pressure force fluctuations acting on the movable mirror become

$$\delta\hat{F}_\mathrm{rp}(\Omega) = -\hbar G\bar{a}\left(\delta\hat{a}^\dagger(\Omega) + \delta\hat{a}(\Omega)\right). \quad (1.29)$$

The derivation from expressions (1.24) and (1.25) subsequently gives

$$\delta\hat{a}(\Omega) = \frac{-iG\bar{a}}{-i(\bar{\Delta} + \Omega) + \frac{\kappa}{2}}\delta\hat{x}(\Omega) + \frac{1}{-i(\bar{\Delta} + \Omega) + \frac{\kappa}{2}}\left(\sqrt{\kappa_\mathrm{ex}}\delta\hat{s}_\mathrm{in}(\Omega) + \sqrt{\kappa_0}\delta\hat{s}_\mathrm{vac}(\Omega)\right), \quad (1.30)$$

$$\delta\hat{a}^\dagger(\Omega) = \frac{+iG\bar{a}}{+i(\bar{\Delta} - \Omega) + \frac{\kappa}{2}}\delta\hat{x}(\Omega) + \frac{1}{+i(\bar{\Delta} - \Omega) + \frac{\kappa}{2}}\left(\sqrt{\kappa_\mathrm{ex}}\delta\hat{s}_\mathrm{in}^\dagger(\Omega) + \sqrt{\kappa_0}\delta\hat{s}_\mathrm{vac}^\dagger(\Omega)\right), \quad (1.31)$$

---

[1]The Fourier transform used here is $f(\Omega) = \int_{-\infty}^{+\infty} f(t)e^{+i\Omega t}\, dt$.

where the intracavity field fluctuations depend on the mechanical coordinate fluctuations $\delta\hat{x}(\Omega)$, and on the pump and vacuum field fluctuations. Therefore, by recasting Eqs. (1.30) and (1.31) into Eq. (1.29), the radiation pressure force fluctuations evaluate to

$$
\begin{aligned}
\delta\hat{F}_{\text{rp}}(\Omega) = & - \hbar G^2\bar{a}^2 \left(\frac{\bar{\Delta}+\Omega}{(\bar{\Delta}+\Omega)^2+(\kappa/2)^2} + \frac{\bar{\Delta}-\Omega}{(\bar{\Delta}-\Omega)^2+(\kappa/2)^2} \right) \delta\hat{x}(\Omega) \\
& + i\hbar G^2\bar{a}^2 \left(\frac{\kappa/2}{(\bar{\Delta}+\Omega)^2+(\kappa/2)^2} - \frac{\kappa/2}{(\bar{\Delta}-\Omega)^2+(\kappa/2)^2} \right) \delta\hat{x}(\Omega) \\
& - \hbar G\bar{a} \frac{1}{-i(\bar{\Delta}+\Omega)+\frac{\kappa}{2}} \left(\sqrt{\kappa_{\text{ex}}}\delta\hat{s}_{\text{in}}(\Omega) + \sqrt{\kappa_0}\delta\hat{s}_{\text{vac}}(\Omega) \right) \\
& - \hbar G\bar{a} \frac{1}{+i(\bar{\Delta}-\Omega)+\frac{\kappa}{2}} \left(\sqrt{\kappa_{\text{ex}}}\delta\hat{s}_{\text{in}}^{\dagger}(\Omega) + \sqrt{\kappa_0}\delta\hat{s}_{\text{vac}}^{\dagger}(\Omega) \right).
\end{aligned}
\tag{1.32}
$$

This expression shows that the radiation pressure force $\delta\hat{F}_{\text{rp}}(\Omega)$ originating from the intracavity electromagnetic field is partly dependent on the displacement $\delta\hat{x}(\Omega)$ of the movable mirror. This force has three distinct components:

- The first line of equation (1.32) corresponds to the component of $\delta\hat{F}_{\text{rp}}$ that is in phase with the mechanical coordinate $\delta\hat{x}(\Omega)$. The light therefore acts as a spring obeying the Hooke's law and the corresponding effect is called the *optical spring effect.*

- The second line corresponds to the component of $\delta\hat{F}_{\text{rp}}$ that is in quadrature with the mechanical coordinate $\delta\hat{x}(\Omega)$. It is therefore proportional to the velocity of the mechanical oscillator and acts as a viscosity. It is the *optical damping effect.*

- The third and fourth lines correspond to the radiation pressure force resulting from the fluctuations of the pump field and of the intracavity vacuum field, coupled through the two loss channels. Experimentally, we will use optical lasers exhibiting quantum noise limited fluctuations both on the phase and amplitude quadratures. Consequently, the only source of fluctuations introduced by the radiation pressure force will be of quantum nature, and the effects of the fluctuations described here are responsible for the *quantum backaction.*

Note that if the cavity has an very large bandwidth κ compared to the mechanical displacement angular frequency Ω_{m}, it will respond almost instantaneously and therefore the intracavity field induced radiation pressure force will not have any significant in-quadrature component, leading to a negligible optical damping effect.

Optical spring and damping effects are the two manifestations of the *dynamical backaction* of the intracavity electromagnetic field onto the mechanical oscillator. Furthermore, the cooling of the mechanical oscillator results from the optical damping and a simultaneous introduction of reduced force fluctuations from the coherent optical field. Hence, the detailed description of the dynamical backaction in the next sections will set the theoretical ground for the cooling work.

1.2.5 Optical spring and damping effects

To get a precise understanding, the equation of motion of the mechanical oscillator Eq. (1.23) is rearranged to

$$\chi_{\mathrm{m}}^{-1}(\Omega)\delta\hat{x}(\Omega) = \delta\hat{F}_{\mathrm{rp}}(\Omega) + \delta\hat{F}_{\mathrm{th}}(\Omega) \tag{1.33}$$

with

$$\chi_{\mathrm{m}}(\Omega) = m_{\mathrm{eff}}^{-1}\left(\Omega_{\mathrm{m}}^2 - \Omega^2 - i\Gamma_{\mathrm{m}}\Omega\right)^{-1} \tag{1.34}$$

being the intrinsic mechanical susceptibility of the movable mirror and

$$\delta\hat{F}_{\mathrm{th}}(\Omega) = m_{\mathrm{eff}}\sqrt{\Gamma_{\mathrm{m}}}\hat{\xi}_{\mathrm{th}}(\Omega) \tag{1.35}$$

the thermal Langevin force.

Recasting Eq. (1.32) into Eq. (1.33) gives

$$\chi_{\mathrm{eff}}^{-1}(\Omega)\delta\hat{x}(\Omega) = \delta\hat{F}_{\mathrm{rp}}^{\mathrm{qba}}(\Omega) + \delta\hat{F}_{\mathrm{th}}(\Omega), \tag{1.36}$$

where the effective susceptibility is defined as

$$\chi_{\mathrm{eff}}(\Omega) = m_{\mathrm{eff}}^{-1}\left(\left(\Omega_{\mathrm{m}}^2 + \frac{k_{\mathrm{dba}}}{m_{\mathrm{eff}}}(\Omega)\right) - \Omega^2 - i\left(\Gamma_{\mathrm{m}} + \Gamma_{\mathrm{dba}}(\Omega)\right)\Omega\right)^{-1}. \tag{1.37}$$

The additional spring and damping induced by the dynamical backaction "dba" have been included. $\delta\hat{F}_{\mathrm{rp}}^{\mathrm{qba}}(\Omega)$ corresponds to the radiation pressure force fluctuations resulting from the quantum backaction effect

$$
\begin{aligned}
\delta\hat{F}_{\mathrm{rp}}^{\mathrm{qba}}(\Omega) = &- \hbar G\bar{a}\frac{1}{-i(\bar{\Delta}+\Omega)+\frac{\kappa}{2}}\left(\sqrt{\kappa_{\mathrm{ex}}}\delta\hat{s}_{\mathrm{in}}(\Omega) + \sqrt{\kappa_0}\delta\hat{s}_{\mathrm{vac}}(\Omega)\right)\\
&- \hbar G\bar{a}\frac{1}{+i(\bar{\Delta}-\Omega)+\frac{\kappa}{2}}\left(\sqrt{\kappa_{\mathrm{ex}}}\delta\hat{s}_{\mathrm{in}}^{\dagger}(\Omega) + \sqrt{\kappa_0}\delta\hat{s}_{\mathrm{vac}}^{\dagger}(\Omega)\right).
\end{aligned}
\tag{1.38}
$$

Because of its stochastic nature, arising from the quantum noises, $\delta\hat{F}_{\mathrm{rp}}^{\mathrm{qba}}(\Omega)$ acts as a fluctuating force driving the mechanical oscillator during the cooling process.

The expressions of the additional mechanical parameters are given by

$$k_{\mathrm{dba}}(\Omega) = \hbar G^2\bar{a}^2\left(\frac{\bar{\Delta}+\Omega}{(\bar{\Delta}+\Omega)^2+(\kappa/2)^2} + \frac{\bar{\Delta}-\Omega}{(\bar{\Delta}-\Omega)^2+(\kappa/2)^2}\right), \tag{1.39}$$

$$\Gamma_{\mathrm{dba}}(\Omega) = \frac{\hbar G^2\bar{a}^2}{m_{\mathrm{eff}}\Omega}\left(\frac{\kappa/2}{(\bar{\Delta}+\Omega)^2+(\kappa/2)^2} - \frac{\kappa/2}{(\bar{\Delta}-\Omega)^2+(\kappa/2)^2}\right). \tag{1.40}$$

If the induced changes of the mechanical parameters are small compared to Ω_{m} and κ, the susceptibility can be simplified for the range of interest $\Omega \approx \Omega_{\mathrm{m}}$. Thus, the effective frequency Ω_{eff} and damping Γ_{eff} accounting for the dynamical backaction are given by [28]

$$\Omega_{\mathrm{eff}} \approx \Omega_{\mathrm{m}} + g_0^2\bar{a}^2\left(\frac{\bar{\Delta}+\Omega_{\mathrm{m}}}{(\bar{\Delta}+\Omega_{\mathrm{m}})^2+(\kappa/2)^2} + \frac{\bar{\Delta}-\Omega_{\mathrm{m}}}{(\bar{\Delta}-\Omega_{\mathrm{m}})^2+(\kappa/2)^2}\right), \tag{1.41}$$

$$\Gamma_{\mathrm{eff}} \approx \Gamma_{\mathrm{m}} + 2g_0^2\bar{a}^2\left(\frac{\kappa/2}{(\bar{\Delta}+\Omega_{\mathrm{m}})^2+(\kappa/2)^2} - \frac{\kappa/2}{(\bar{\Delta}-\Omega_{\mathrm{m}})^2+(\kappa/2)^2}\right). \tag{1.42}$$

In the context of cooling, we are mostly interested in maximizing the optical damping. From Eq. (1.42), it is shown that in the limit $\kappa/\Omega_{\mathrm{m}} \to 0$ this happens for the optimum detuning $\bar{\Delta} = -\Omega_{\mathrm{m}}$.

1.2.6   Quantum backaction

Besides dynamical backaction, when the quantum nature of the optical field is considered quantum fluctuations come into play and are responsible for the *quantum backaction* described in this section. It can be simply understood as a stochastic radiation pressure force that acts on the movable mirror.

From the expression of the radiation pressure force fluctuations (1.38), the quantum backaction force spectral density[2] reads

$$S_{FF}^{\mathrm{qba}}(\Omega) = \hbar^2 G^2 \bar{a}^2 \kappa \left(\frac{1}{(\bar{\Delta} + \Omega)^2 + (\kappa/2)^2} \right), \tag{1.43}$$

where the relations (1.26) and (1.27) on the correlations of the pump field and intracavity field noise operators and Eq. (1.16) are used. Once again, the double-sided spectrum associated with this quantum noise is not symmetric with respect to the Fourier frequency Ω.

1.2.7   Dynamical backaction cooling

The optical damping derived in (1.42) leads to the optical cooling of the mechanical mode of angular frequency Ω_{m}, in a process known dynamical backaction cooling or also cold damping, which is detailed here. Indeed, according to the fluctuation-dissipation theorem, a net cooling of the mechanical mode is achieved when reduced force fluctuations are introduced during the damping mechanism. The fundamental limitation of the process arises however from the quantum fluctuations (1.43) introduced by the optical field. We show here also that the resulting minimum occupancy is brought close to zero in the resolved-sideband configuration.

When the mechanical oscillator is subjected to the dynamical backaction force and the Langevin force, the mean value of its mechanical coordinate fluctuations evaluates to

$$\langle \delta \hat{x}^2 \rangle = \int_{-\infty}^{+\infty} |\chi_{\mathrm{eff}}(\Omega)|^2 \left(S_{FF}^{\mathrm{th}}(\Omega) + S_{FF}^{\mathrm{qba}}(\Omega) \right) \frac{d\Omega}{2\pi} \tag{1.44}$$

$$= 2 \int_0^{+\infty} |\chi_{\mathrm{eff}}(\Omega)|^2 \left(\bar{S}_{FF}^{\mathrm{th}}(\Omega) + \bar{S}_{FF}^{\mathrm{qba}}(\Omega) \right) \frac{d\Omega}{2\pi}, \tag{1.45}$$

where the symmetrized spectra $\bar{S}_{FF}(\Omega) = (S_{FF}(\Omega) + S_{FF}(-\Omega))/2$, and the optical spring and damping effects are included in the effective susceptibility $\chi_{\mathrm{eff}}(\Omega)$. The symmetrized

---

[2]The definition of the double-sided spectral density $S_{ff}(\Omega)$ given by $2\pi\delta(\Omega+\Omega')S_{ff}(\Omega) = \langle \delta\hat{f}(\Omega)\delta\hat{f}(\Omega') \rangle$ is used here [29].

thermal force fluctuation spectral density is derived from the correlator presented in Eq. (1.28) and from Eq. (1.35). It is given by

$$\bar{S}_{FF}^{\text{th}}(\Omega) = m_{\text{eff}}\Gamma_{\text{m}}\hbar\Omega\coth\left(\frac{\hbar\Omega}{2k_{\text{B}}T_{\text{m}}}\right). \tag{1.46}$$

This noise spectrum can be easily rewritten as a function of the Bose occupation number of the bath at temperature T_{m}, $\bar{n}_m = \frac{1}{e^{\frac{\hbar\Omega}{k_B T_{\text{m}}}}-1}$, evaluating to

$$\bar{S}_{FF}^{\text{th}}(\Omega) = 2m_{\text{eff}}\Gamma_{\text{m}}\hbar\Omega\left(\bar{n}_m + 1/2\right). \tag{1.47}$$

We introduce the simplified notations of the expressions (1.42) and (1.43):

$$\Gamma_{\text{eff}} = \Gamma_{\text{m}} + A_- - A_+ \tag{1.48}$$

$$\bar{S}_{FF}^{\text{qba}}(\Omega) \approx \bar{S}_{FF}^{\text{qba}}(\Omega_{\text{m}}) = \hbar m_{\text{eff}}\Omega_{\text{m}}\left(A_- + A_+\right), \tag{1.49}$$

with

$$A_{\pm} = g_0^2\bar{a}^2\kappa\left(\frac{1}{(\bar{\Delta} \mp \Omega_{\text{m}})^2 + (\kappa/2)^2}\right). \tag{1.50}$$

The coefficients A_+ and A_- are proportional respectively to the Stokes and anti-Stokes scattering rates of intracavity photons, as explained in detail in section 1.2.9. Cooling then occurs when $A_- > A_+$ and heating occurs in the opposite situation.

For small fluctuations around the mechanical frequency, we evaluate

$$\langle\delta\hat{x}^2\rangle = (2m_{\text{eff}}\Gamma_{\text{m}}(\bar{n}_{\text{m}} + 1/2)\hbar\Omega_m + \hbar m_{\text{eff}}\Omega_{\text{m}}\left(A_- + A_+\right))\int_{-\infty}^{+\infty}|\chi_{\text{eff}}(\Omega)|^2\frac{d\Omega}{2\pi}$$
$$= \frac{(\bar{n}_{\text{m}} + 1/2)\hbar}{m_{\text{eff}}\Omega_{\text{m}}}\left(\frac{\Gamma_{\text{m}}}{\Gamma_{\text{eff}}}\right) + \frac{\hbar}{2m_{\text{eff}}\Omega_{\text{m}}}\left(\frac{A_- + A_+}{\Gamma_{\text{eff}}}\right), \tag{1.51}$$

where the integral has been simply calculated with the approximation $\Omega_{\text{eff}} \approx \Omega_{\text{m}}$, thus giving

$$\int_{-\infty}^{+\infty}|\chi_{\text{eff}}(\Omega)|^2\frac{d\Omega}{2\pi} = \frac{1}{2m_{\text{eff}}^2\Omega_{\text{m}}^2\Gamma_{\text{eff}}}. \tag{1.52}$$

The equipartition of the mean energy $\langle E\rangle$ of the movable mirror is then used to get

$$\langle E\rangle = m_{\text{eff}}\Omega_{\text{m}}^2\langle\delta\hat{x}^2\rangle, \tag{1.53}$$

where the mean energy is considered equally distributed among the kinetic and the potential energy [30].

Since $\langle E\rangle = \hbar\Omega_{\text{m}}(\bar{n} + 1/2)$ (1.9), the mean value of the phonon occupancy can be deduced from (1.51) the expression

$$\bar{n} = \bar{n}_{\text{m}}\frac{\Gamma_{\text{m}}}{\Gamma_{\text{eff}}} + \frac{A_+}{\Gamma_{\text{eff}}}. \tag{1.54}$$

By increasing the value of Γ_{eff} when detuning the laser to the cavity's red side ($\omega_{\text{l}} < \omega_{\text{c}}$), one modifies the temperature and therefore the phonon occupancy of the mechanical oscillator. Importantly, this process cools the mechanical mode because the fluctuations introduced are comparatively low. Interestingly, the contribution of the total quantum backaction driving the oscillator is indissociable from the zero-point motion of the mechanical oscillator and it is simultaneously responsible for the minimum phonon occupancy achieved by laser cooling.

For a significant cooling such that $\Gamma_{\text{eff}} \gg n_{\text{m}}\Gamma_{\text{m}}$, the final phonon occupancy saturates to a minimum value given by

$$\bar{n}_{\text{min}}(\bar{\Delta}) = -\frac{1}{4}\frac{(\bar{\Delta} + \Omega_{\text{m}})^2 + (\kappa/2)^2}{\bar{\Delta}\Omega_{\text{m}}}, \tag{1.55}$$

which is the limit imposed by the quantum backaction. A detailed physical insight of this phenomenon is given in section 1.2.9 by comparing the laser cooling presented here with the case of laser cooling of ions. The laser optimally detuned to

$$\bar{\Delta}_{\text{opt}} = -\Omega_{\text{m}}\sqrt{1 + \frac{(\kappa/2)^2}{\Omega_{\text{m}}^2} + 1} \tag{1.56}$$

leads to a minimum phonon occupancy of

$$\bar{n}_{\text{min}}(\bar{\Delta}_{\text{opt}}) = \frac{1}{2}\left(\sqrt{\frac{(\kappa/2)^2}{\Omega_{\text{m}}^2} + 1} - 1\right). \tag{1.57}$$

In this configuration, the minimum saturation occupancy goes to zero only if the relation $\kappa \ll \Omega_{\text{m}}$ holds. This condition is called the *resolved-sideband* condition and is fundamentally necessary to reach the ground state of the mechanical oscillator with the dynamical backaction cooling process described along this section [12, 13, 14]. Under this condition, the minimum phonon occupancy reads

$$\bar{n}_{\text{min}}(\bar{\Delta}_{\text{opt}}) \simeq \frac{\kappa^2}{16\Omega_{\text{m}}^2}, \tag{1.58}$$

indeed going to zero whereas in the opposite configuration $\kappa \gg \Omega_{\text{m}}$ it reads

$$\bar{n}_{\text{min}}(\bar{\Delta}_{\text{opt}}) \simeq \frac{\kappa}{4\Omega_{\text{m}}} \tag{1.59}$$

and precludes reaching the motional ground state.

Within the introduced framework additional conditions have to be considered:

- The thermal occupation of the electromagnetic field in the case of an optical laser is $k_{\text{B}}T/\hbar\omega_{\text{l}} \ll 1$ and is therefore neglected [31]. Experiments using a microwave field are, on the contrary, affected by this thermal occupation.

- To avoid obtaining an overdamped mechanical oscillator during the cooling process, the condition $\Omega_{\mathrm{m}} > \Gamma_{\mathrm{m}}\bar{n}_{\mathrm{m}}$ [13] must be fulfilled.

- The condition $\kappa > \Gamma_{\mathrm{m}}\bar{n}_{\mathrm{m}}$ precludes cooling limited by the decay rate of the cavity [31]. This effect appears when the approximation $\Gamma_{\mathrm{m}} \ll \kappa$ introduced in (1.41) and (1.42) breaks down.

1.2.8 Dynamical backaction heating and amplification

At a positive laser detuning close to $+\Omega_{\mathrm{m}}$, the optically-induced damping is negative, reducing the effective damping. As long as $\Gamma_{\mathrm{eff}} > 0$, the mechanical oscillator is in a thermal state and it is possible to use equation (1.54) to estimate the corresponding phonon occupation number, which increases. In this regime, the dynamical backaction provides gain to the mechanical oscillator: the oscillator's response to a force increases with increasing intracavity power. Consequently, this phenomenon is called dynamical backaction amplification.

The limiting situation $\Gamma_{\mathrm{eff}} \to 0$ is achieved for an input field beyond the threshold

$$|\bar{s}_{\mathrm{in}}|^2_{\mathrm{threshold}} = \frac{\kappa}{\kappa_{\mathrm{ex}}} \frac{\Gamma_{\mathrm{m}}\kappa}{16 g_0^2 \Omega_{\mathrm{m}}} \left(\Omega_{\mathrm{m}}^2 + (\kappa/2)^2\right) \left(4\Omega_{\mathrm{m}}^2 + (\kappa/2)^2\right) \tag{1.60}$$

at a positive detuning of $\bar{\Delta} = +\Omega_{\mathrm{m}}$. In this regime, the mechanical oscillator undergoes self-induced sinusoidal oscillations. This is demonstrated by solving the equations of motion (1.14) and (1.15) in this particular case. Even when the thermal noise is not considered, the motion of the movable mirror is oscillatory at an angular frequency Ω_{m} [32].

There, the description of the evolution of the body's trajectory is non-linear and multi-stability of the amplitude of the oscillator with change of the intracavity power is observed, leading to the onset of a complex array of attractors [33]. Eventually, upon high enough intracavity power, the phase space trajectory of the movable mirror becomes erratic, corresponding to a chaotic behavior of the canonical variables of the mechanical oscillator [34].

1.2.9 The sideband picture - analogy with atomic cooling

Cooling a movable mass using the radiation pressure of the light was actually initially studied, predicted and performed in the context of laser cooling of atoms. It is therefore worthwhile to introduce the *sideband picture* used to describe this process and to highlight the analogy with the optomechanical case.

In the context of atomic spectroscopy, it is of interest to reduce the thermal motion of the atoms. In 1975, two independent proposals from Wineland and Dehmelt for ionized atoms [9] and from Hänsch and Schawlow for a gas of neutral atoms [7] described the phenomenon of laser cooling. Soon after, the experimental demonstration of the technique was performed by Wineland in 1978 [10] for ionized atoms and by Andreev for neutral atoms in 1981 [8].

Sideband cooling of trapped ions

To underline the analogy with optomechanics, we consider the particular case of the laser cooling of a trapped ion [35, 36]. The motion of its center of mass in the harmonic trap with a frequency Ω_m is analog to the motion of the movable mirror.

Due to this sinusoidal movement, the ion exhibits absorption sidebands at $\omega_\mathrm{c} \pm m\Omega_\mathrm{m}$ with $m \in \mathbb{N}$ [37], where ω_c is the ion's atomic transition of lifetime κ^{-1}. When the laser is detuned to $\omega_\mathrm{l} = \omega_\mathrm{c} - \Omega_\mathrm{m}$, the first absorption sideband is driven. Consequently, the ion absorbs a photon of energy $\hbar(\omega_\mathrm{c} - \Omega_\mathrm{m})$ but spontaneously re-emits one of higher energy $\hbar\omega_\mathrm{c}$ (neglecting the recoil). The emitted photon thus removes energy from the ion and the phenomenon leads to *motional sideband cooling* of the ion. In this process, a phonon of energy $\hbar\Omega_\mathrm{m}$ is annihilated, leading to the reduction of the mechanical excitation. Like in the optomechanical case, the motional ground state of the ion can only be reached in the resolved-sideband regime $\kappa \ll \Omega_\mathrm{m}$. The resulting limiting mechanical occupation number is given by

$$\bar{n}_\mathrm{min} = \frac{1}{16}\frac{\kappa^2}{\Omega_\mathrm{m}^2},\tag{1.61}$$

which goes to zero in the strong resolved-sideband regime, analogously to the optomechanics case expressed in Eq. (1.58). Resolved-sideband cooling has led to the first observation of the ground state of a single trapped $^{198}\mathrm{Hg}^+$ ion by Wineland in 1989 [38].

Sideband cooling in optomechanics

The same description of sideband cooling applies in optomechanics. It corresponds then to the enhancement by the cavity of the anti-Stokes sideband upon adequate detuning of the cooling laser to $\bar{\Delta} = -\Omega_\mathrm{m}$. The scattering rates of the Stokes and anti-Stokes first sidebands are given respectively by $(\bar{n} + 1)A_+$ and $\bar{n}A_-$, as illustrated in Fig. 1.2, with $A_\pm$ defined in equation (1.50) and $\bar{n}$ being the phonon occupation number. They can be directly derived from Fermi's Golden Rule [13, 27] applied to the interaction Hamiltonian $\hat{H}_\mathrm{int}$. The rates' dependency on laser detuning illustrates the scattering enhancement provided by the optical cavity and modeled by the Lorentzian profile on Fig. 1.2. Cooling of the mechanical oscillator occurs when $\bar{n}A_- > (\bar{n} + 1)A_+$, corresponding to a positive optical damping, leading to $\Gamma_\mathrm{eff} > \Gamma_\mathrm{m}$. The ultimate limit on the occupancy imposed by quantum backaction can be simply understood in this scattering picture: when both scattering rates are equal, the phonon occupancy saturates to $\bar{n}_\mathrm{min} = A_+/(A_- - A_+)$.

Importantly, optically probing the strength of the Stokes and anti-Stokes sidebands (which are proportional to the scattering rates) gives direct access to the measurement of the phonon occupancy number of the mechanical oscillator. When a resonant laser is used ($\bar{\Delta} = 0$), $A_+ = A_-$ therefore the sideband strengths differ by a factor of $(\bar{n} + 1)/\bar{n}$. For $\bar{n} \to 0$, the contrast diverges, constituting an ultimate proof of ground state cooling of the massive mirror. A similar method, called sideband spectroscopy, has been used to experimentally demonstrate the first ground state cooling of a trapped ion [38]. It should
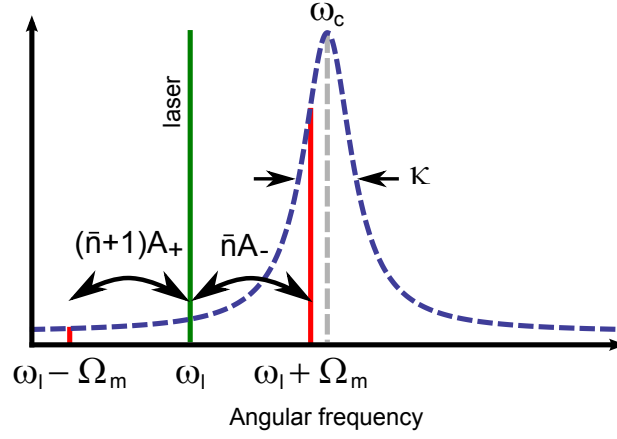
Figure 1.2: *Sideband picture of the optomechanical cooling. Stokes and anti-Stokes scattering at the angular frequency $\omega_l - \Omega_m$ and $\omega_l + \Omega_m$ of the carrier at ω_l, weighted by the optical cavity Lorentzian. The scattering rates of the carrier into the Stokes and anti-Stokes sideband are respectively $(\bar{n} + 1)A_+$ and $\bar{n}A_-$. Maximum cooling is achieved when the anti-Stokes sideband is resonant with the cavity at ω_c.*

also be noted that the process of backaction amplification introduced in the section 1.2.8 also applies in the case of trapped ions [39].

1.3   Detection sensitivity

The coupling of a cavity optical mode and a mechanical mode was initially studied in the context of highly sensitive position detection, such as in gravitational wave interferometers. The detection principle is based on the phase shift acquired by the reflected field $\hat{s}_{\text{out}}$ close to the cavity resonance. As shown in figure 1.3, the mechanical fluctuations of the movable mirror modulate the intracavity optical path. As a consequence, the resonant probe beam experiences a phase modulation: by comparing the output field phase fluctuations with a phase reference, like in a homodyne interferometer, the mechanical motion is detected.

In this section, the measurement quantum imprecision and the measurement backaction resulting from the quantum fluctuations of the probing field are introduced. The total uncertainty of the measurement process is detailed and the optimum measurement configuration, leading to a minimum uncertainty called the standard quantum limit, is explained.

1.3.1   Measurement imprecision and measurement backaction

Figure 1.3 represents the output field amplitude (upper panel) and phase (lower panel) for $\kappa_{\text{ex}} = \kappa$ and $\kappa_{\text{ex}} = \kappa/2$, respectively, when compared to the input field. Those different coupling conditions illustrate the visible effect of the resonance condition on the output field: full extinction for the output intensity and π phase shift for the phase difference. These are calculated using equations (1.18) - (1.19) and using the output field expression

$$\hat{s}_{\text{out}} = \hat{s}_{\text{in}} - \sqrt{\kappa_{\text{ex}}}\hat{a}. \tag{1.62}$$

We intentionally omit the π-shift acquired upon reflection for the case of a Fabry-Perot cavity as it does not influence the physical interpretation of the detection sensitivity.

As described in section 1.2.6, quantum intensity fluctuations of the input field and of the intracavity vacuum field are responsible for the radiation pressure fluctuations leading to a minimum achievable phonon number for the cooling process expressed in equation (1.57). Simultaneously, the quantum phase fluctuations of the output field set a limit on the minimum mechanical motion detectable. We first describe these phenomena in the restricted case of resonant probing of the cavity $\bar{\Delta} = 0$. Using equations (1.62), (1.30) and (1.31) and the definition of the spectral density given in footnote 2, the spectral density of the phase of the output field reads

$$\bar{S}_{qq}^{\hat{s}_{\text{out}}}(\Omega) = 1 + \frac{16G^2|\bar{s}_{\text{in}}|^2}{\Omega^2 + (\kappa/2)^2} \left(\frac{\kappa_{\text{ex}}}{\kappa}\right)^2 \bar{S}_{xx}(\Omega). \tag{1.63}$$

We use here the usual definitions of the quadratures with the intracavity field taken as the phase reference [21] and the properties of the correlators (1.26) and (1.27). The first term on the right-hand side of equation (1.63) corresponds to the phase noise background coming from the quantum noises of the input and intracavity fields, and the second term
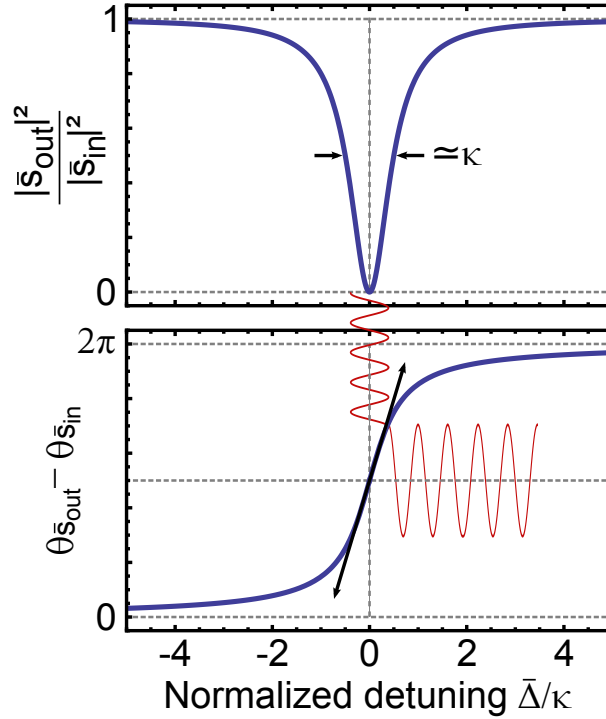
Figure 1.3: *Squared amplitude (upper panel) and phase (lower panel) of the output field $\hat{s}_\text{out}$ relative to the input field $\hat{s}_\text{in}$, representing the two experimentally accessible quantities. The squared amplitude shows full extinction at $\bar{\Delta} = 0$ for the critical coupling condition $\kappa_\text{ex} = \kappa/2$. For the phase difference, the maximum shift upon scanning of the detuning $\bar{\Delta}$ occurs for a strongly overcoupled cavity, where the external coupling losses are dominant over all other source of losses ($\kappa_\text{ex} \to \kappa$). The mechanical displacement of the movable mirror modulates the cavity optical path that transduces into a phase modulation detectable with conventional homodyne interferometry.*

denotes the transduction of the mechanical motion filtered out by the cavity bandwidth. Thus, the minimum detectable mechanical displacement spectral density is given by

$$\bar{S}_{xx}^\text{qi}(\Omega) = \frac{\Omega^2 + (\kappa/2)^2}{16G^2|\bar{s}_\text{in}|^2}\left(\frac{\kappa}{\kappa_\text{ex}}\right)^2, \tag{1.64}$$

corresponding to the *measurement imprecision* due to the fundamental quantum noise, or quantum imprecision "qi". The minimum detectable displacement decreases with increasing input power, as expected from a phase measurement limited by the quantum phase noise of the measuring coherent field.

However, upon increasing the readout laser power, the intracavity photon number fluctuations augment and perturb the movable mirror due to the radiation pressure. This unavoidable disturbance corresponds to the *measurement backaction* previously described and initially discussed by Braginsky [1] and Caves [2] in the context of gravitational wave detectors. Due to its quantum nature, this is called the *quantum backaction* "qba", the expression of which is given in Eq. (1.43). By disturbing the conjugate variable (momentum),

the continuous measurement of the position leads to an unavoidable backaction on the system. As required by the principles of quantum mechanics, the product of the imprecision and backaction in the measurement verifies the inequality:

$$\bar{S}_{xx}^{\mathrm{qi}}(\Omega) \times \bar{S}_{FF}^{\mathrm{qba}}(\Omega) = \left(\frac{\hbar}{2}\right)^2 \left(\frac{1}{\kappa_{\mathrm{ex}}/\kappa}\right) \geq \left(\frac{\hbar}{2}\right)^2. \tag{1.65}$$

1.3.2   Total measurement uncertainty

The *total* uncertainty on the position measurement of the mechanical oscillator reads

$$\bar{S}_{xx}^{\mathrm{tot}}(\Omega) = \bar{S}_{xx}^{\mathrm{qi}}(\Omega) + |\chi_{\mathrm{m}}(\Omega)|^2 \bar{S}_{FF}^{\mathrm{qba}}(\Omega), \tag{1.66}$$

with the mechanical susceptibility $\chi_{\mathrm{m}}(\Omega)$ given by Eq. (1.34). It corresponds to the total noise measured by the phase detector when the quantum noises from the optical probe are taken into account. Expression (1.66) is then rearranged into

$$\bar{S}_{xx}^{\mathrm{tot}}(\Omega) = \bar{S}_{xx}^{\mathrm{min}}(\Omega) \frac{1}{2} \left(p(\Omega) + \frac{1}{p(\Omega)} \right), \tag{1.67}$$

with $\bar{S}_{xx}^{\mathrm{min}}(\Omega) = \hbar|\chi_{\mathrm{m}}(\Omega)|(\kappa/\kappa_{\mathrm{ex}})^{1/2}$ and $p(\Omega) = \frac{8\hbar G^2}{\Omega^2 + (\kappa/2)^2}|\chi_{\mathrm{m}}(\Omega)||\bar{s}_{\mathrm{in}}|^2 (\kappa_{\mathrm{ex}}/\kappa)^{3/2}$. At the optimum input power $p(\Omega)_{\bar{\Delta}=0} = p(\Omega)^{\mathrm{opt}} = 1$, $\bar{S}_{xx}^{\mathrm{tot}}(\Omega) = \bar{S}_{xx}^{\mathrm{min}}(\Omega)$, and for an overcoupled cavity where $\kappa_{\mathrm{ex}} \to \kappa$

$$\bar{S}_{xx}^{\mathrm{tot}}(\Omega) = \bar{S}_{xx}^{\mathrm{SQL}}(\Omega) = \hbar|\chi_{\mathrm{m}}(\Omega)|. \tag{1.68}$$

In this situation, the values of the measurement quantum imprecision and backaction are optimized and the total uncertainty in the measurement of the mechanical oscillator's position corresponds to the *standard quantum limit* (SQL) [2]. However, when evaluated at the mechanical resonance frequency $\Omega = \Omega_{\mathrm{m}}$, the total noise spectral density at the SQL is exactly equal to the zero point fluctuations "zpf" as expressed in Eq. (1.12). The corresponding displacement spectral density evaluates then to

$$\bar{S}_{xx}^{\mathrm{SQL}}(\Omega_{\mathrm{m}}) = \bar{S}_{xx}^{\mathrm{zpf}}(\Omega_{\mathrm{m}}) = \frac{\hbar}{m_{\mathrm{eff}}\Gamma_{\mathrm{m}}\Omega_{\mathrm{m}}}. \tag{1.69}$$

Note that this calculation assumes no correlations between the 2 terms limiting the displacement sensitivity, which is the case when studying a cavity probed at resonance. There exists a more fundamental limit, called the ultimated quantum limit [40], which can be achieved when exploiting existing quantum correlations between the noise terms.

   Figure 1.4 shows the total position uncertainty normalized to the SQL uncertainty when the normalized coupling power $p(\Omega)/p^{\mathrm{opt}}(\Omega)$ is swept. At low normalized power $p(\Omega) \ll p^{\mathrm{opt}}(\Omega)$, the total uncertainty is dominated by the measurement imprecision induced by the phase noise (negative slope asymptote). On the contrary, at high normalized power $p(\Omega) \gg p^{\mathrm{opt}}(\Omega)$, the total position measurement is dominated by the measurement backaction (positive slope asymptote).
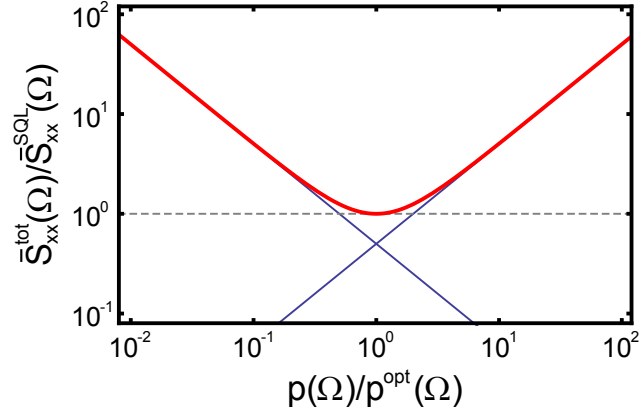
Figure 1.4: *Total uncertainty on the position measurement normalized to the value at optimum normalized power (red curve) at detuning $\bar{\Delta} = 0$.*

In experimental situations, where the cooling laser detuned to $\bar{\Delta} = \bar{\Delta}_{\mathrm{opt}}$ is used as the measurement field, the expression of the measurement imprecision calculated using the same previous procedure is given by

$$\bar{S}_{xx}^{\mathrm{qi}}(\Omega_{\mathrm{m}}) = \frac{\Omega_{\mathrm{m}}^2}{4G^2|\bar{s}_{\mathrm{in}}|^2}. \tag{1.70}$$

Similarly, the measurement backaction is given by

$$\bar{S}_{FF}^{\mathrm{qba}}(\Omega_{\mathrm{m}}) = \frac{2G^2\hbar^2|\bar{s}_{\mathrm{in}}|^2}{\Omega_{\mathrm{m}}^2}, \tag{1.71}$$

evaluated for simplicity at the mechanical resonance frequency $\Omega = \Omega_{\mathrm{m}}$ and for $\kappa_{\mathrm{ex}} \gg \kappa_0$ [41]. It should be pointed out that the imprecision-backaction product at this detuning is at least a factor of two higher than in the optimum case where the cavity is resonantly probed (Eq. (1.65)). However, evaluating the total uncertainty as in the case of resonant pumping is much more complex, since the modification of the mechanical susceptibility has to be taken into account. It is even possible to beat the SQL expressed in equation (1.68) with a detuned cavity, under the condition of a large cavity bandwidth $\kappa \ll \Omega_{\mathrm{m}}$, as it has been shown both theoretically [42] and experimentally [43] in the group of A. Heidmann. Other schemes involving multiple optical resonances reduce the input power required to reach the SQL [44].

The fundamental quantum limits described in this section are imposed by the coherent readout field: indeed, the presence of additional classical noise in the field quadratures deteriorates the sensitivity which is circumvented in this work by the use of quantum limited lasers.

Finally, it is important to note that the SQL presented here corresponds to the optimum sensitivity of a continuous linear measurement type known as *amplitude-and-phase mea-surements* [45]. This type of measurement introduces quantum backaction to the system resulting from the non-commutation and the time-variation of the generalized coordinate

$\hat{x}(t)$ and momentum $\hat{p}(t)$ of the mechanical oscillator being measured. When measuring $\hat{x}(t)$ with a certain precision, $\hat{p}(t)$ is simultaneously randomly kicked and after time evolution, this random kick is fed back into $\hat{x}(t)$. Several schemes have been proposed to perform what is called a *quantum non-demolition* measurement [45, 46].

By quadratically coupling the mechanical displacement to the cavity resonance frequency, it is possible to perform *quantum counting* measurements [47], where the observable $\hat{n}_{\mathrm{p}} = \hat{a}^{\dagger}\hat{a}$ is measured rather than the mechanical quadrature $\hat{x}$. Experimental implementations of such a coupling have been recently done in the group of J. Harris [48, 49] by replacing the generic optomechanical system sketched in fig Fig. 1.1 by a "membrane-in-the-middle" setup.

Another scheme relies on the measurement of constants of the motion of the mechanical oscillator, so that random kicks are never fed back into the measured variable [45, 46]: this can be achieved by monitoring either the sine or the cosine quadrature of the oscillator [50, 46, 18]. This scheme can even lead to the quadrature noise squeezing of the mechanical oscillator, since the measurement uncertainty is only randomly kicking the non-monitored quadrature. Experimentally, this is achieved by simultaneously pumping an optomechanical cavity with two input fields detuned at $-\Omega_{\mathrm{m}}$ and Ω_{m} respectively, as already demonstrated in the group of K. Schwab [51].

Chapter 2

Silica toroidal microresonators as candidates for cavity optomechanics

2.1 Introduction

The theoretical framework given in chapter 1 was described using a unidimensional Fabry-Perot cavity as a model system. Thought, the interaction has been experimentally implemented during the past two decades in a myriad of different optomechanical systems. Indeed, dynamical backaction cooling using radiation pressure was recently performed in various experimental systems such as a Fabry-Perot cavity with a back mirror mounted on a microcantilever [52, 53], a silica microtoroidal cavity [54, 55] and a silica microsphere cavity [56] with movable boundaries, a Fabry-Perot cavity with a mechanical membrane in the middle [48], an optomechanical crystal [57], and a superconducting microwave cavity capacitively coupled to a mechanical nanobeam [58] or to a mechanical membrane [59]. Additionally, a similar optomechanical configuration was used in other systems to dynamically detect the oscillator's position and apply an external viscous force to cool the mechanical mode [60, 61, 62]. In fact, the radiation pressure force can even be used as viscous force to perform this "feedback" cooling [63, 64, 65, 66].

The optomechanical system used in this work is a silica[1] microtoroidal resonator supporting optical whispering-gallery modes of a Q factor exceeding 10^8. This type of optical mode, initially studied in 1989 in silica microspheres in the group of Braginsky [67], has shown record values of optical Q exceeding 10^9 and micron-size modal confinement, making this kind of structure particularly well-adapted for the observation of non-linear optical effects in glass [67, 68, 69]. It is the unique fabrication method based on the melting of a glass fiber or rod to form a solid droplet of vitreous silica that allows to reach surface roughness on the nm-scale, consequently leading to reduced scattering and long photon storage time in the visible and near infrared range, as allowed by the transparency of glass [70]. Combining the remarkable optical properties of whispering-gallery modes with the

---

[1]To take into account today's usual nomenclature, throughout this thesis the term "silica" refers to vitreous silicon dioxide whereas "quartz" refers to its crystalline form.

geometrical control provided by microfabrication was achieved in 2003 in the group of Vahala [71] and lead to the first fabrication of on-chip silica microtoroidal cavities.

These systems have also supported the observation of various optical non-linear effects such as the Kerr effect [72, 73] which can result in the generation of frequency combs [74, 75], stimulated Raman scattering [76, 77, 78] and thermal bistable behavior [79]. It was, however, the first measurements of the mechanical vibrations of the toroid [80] and of dynamical backaction amplification [81, 82] that triggered the work on dynamical backaction cooling of toroidal microresonators. Moreover, the mechanical control over the structure provided by the tools of microfabrication makes it a promising candidate for the implementation of cavity optomechanics. It makes dynamical backaction cooling to the motional ground state of a mechanical mode of silica microtoroids conceivable: their intrinsic properties put them in the resolved-sideband regime, and their on-chip implementation facilitates integration in a cryogenic environment.

This chapter introduces the optical and mechanical properties of silica toroidal microresonators. In section 2.2, starting with the analytical derivation in spheres, the optical whispering-gallery modes are calculated using the accurate oblate spheroidal approximation. The sources of optical losses for spheres and toroids are reviewed and discussed in the context of optomechanics. The tapered-fiber technique used to couple light in these structures is also briefly introduced. In section 2.3, calculations of the mechanical modes supported by spheres are presented, and we show that, despite the reduced number of symmetries in toroids, numerical simulations allow precise predictions of their resonance properties. Finally, we show in section 2.4 that the complex spatial extension of the mechanical radial breathing modes and the optical whispering-gallery modes can be simply parametrized to an effective displacement and an effective mass equivalent to the generic system described in chapter 1.

2.2 Optical modes in silica toroidal resonators

At St Paul's cathedral in London, the gallery under the dome exhibits a particular acoustic phenomenon: whispers from a person speaking along the gallery's walls can be clearly heard again as coming from the person's back. This phenomenon was studied by Lord Rayleigh [83] who called this effect whispering-gallery phenomenon: in essence, the acoustic wave creeps along the walls of the gallery made of stone, undergoing total internal reflections over the circumference of the gallery.

In this section, we review the similar phenomenon occurring for electromagnetic waves undergoing total internal reflections in a dielectric sphere. The supported modes are thus named whispering-gallery modes (WGM) and exhibit resonance condition when the trajectory of the optical wave following the perimeter of the sphere is equal to an integer number of the optical wavelength, thus leading to constructive interference.

2.2.1 Analytic derivation of optical modes in spheres

To calculate the mode profile in the sphere of diameter R, we consider the propagation of an electromagnetic wave in spherical coordinates of variables (r, θ, φ). The details of the resolution can be found in [84, 85, 86]. The jth eigenmode's electric field at the vector coordinate $\vec{r}$ is expressed as $\vec{\tilde{E}}_j(\vec{r}, t) = \vec{E}_j(\vec{r})e^{-i\omega_j t}$ with ω_j being the angular frequency of the mode. Its complex spatial amplitude obeys the Helmholtz equation (the mode identification number j is dropped for readability)

$$\Delta \vec{E}(\vec{r}) + k^2(\vec{r}) \cdot \vec{E}(\vec{r}) = 0, \tag{2.1}$$

with $\vec{\nabla} \cdot \vec{E}(\vec{r}) = 0$ and $k(\vec{r}) = n(\vec{r})\omega/c$. $n(\vec{r})$ is the position dependent refractive index and c is the speed of light in vacuum. $n(\vec{r})$ equals the refractive index of silica n inside the sphere and the refractive index of air $n_{\text{air}} \simeq 1$ outside.

For a homogeneous medium, the solutions for the field are calculated using the Debye potentials [85] or by resolving the eikonal equation [84, 86]. Both methods lead to an exact solution for spheres. For its similarity with the problem in toroids, it is interesting to remind the main solutions and to describe the particular case of the WGM that will be used in the context of optomechanics.

The calculated modes can be separated in two classes, transverse electric (TE) and transverse magnetic (TM), characterized by their integer mode numbers (q, l, m). The azimuthal mode number m denotes the sinusoidal dependence of the electric field on the azimuthal angle which is proportional to $(e^{im\varphi})$. Thus, m is the number of full azimuthal train waves and for a WGM pumped at resonance, with $m \simeq 2\pi Rn/\lambda$ where λ denotes the wavelength in vacuum. The polar dependence of the field is given by the Legendre polynomials $P_l^m(cos\theta)$, with $m \in [-l; +l]$. Therefore, the number of field nodes in the polar direction is given by $|l - m|$. Finally, the radial mode number q denotes the number of solutions of the characteristic equation of the TE and TM fields and $q - 1$ corresponds to the number of nodes in the radial direction.

The class of TM and TE modes of interest is the WGM type with $q = 1$ (no nodes in the radial direction) and $|l-m| = 0$ (no nodes in the polar direction). The complete description shows that the field is proportional to the Bessel function of the first kind $J_{l+\frac{1}{2}}(k(\vec{r})r)$ for $r \leq R$ inside the sphere, and the Hankel function of the first kind $H^{(1)}_{l+\frac{1}{2}}(k(\vec{r})r)$ for $r > R$, thus outside the sphere [85]. Consequently, since the WGM ideally "clings" on the internal surface of the sphere, this corresponds to $l \gg 1$. Due to the significant spatial extension outside the sphere, WGMs can be coupled with a waveguide. We show also that their spatial position allows significant coupling to strain waves.

2.2.2   Approximated derivation of optical modes in toroids

For toroids with reduced number of symmetries as compared to spheres, there are no analytic solutions for all supported modes. Using perturbation analysis [87], it is however possible to get accurate analytical results that are very close to numerical simulations obtained with a finite element method (FEM) [88].
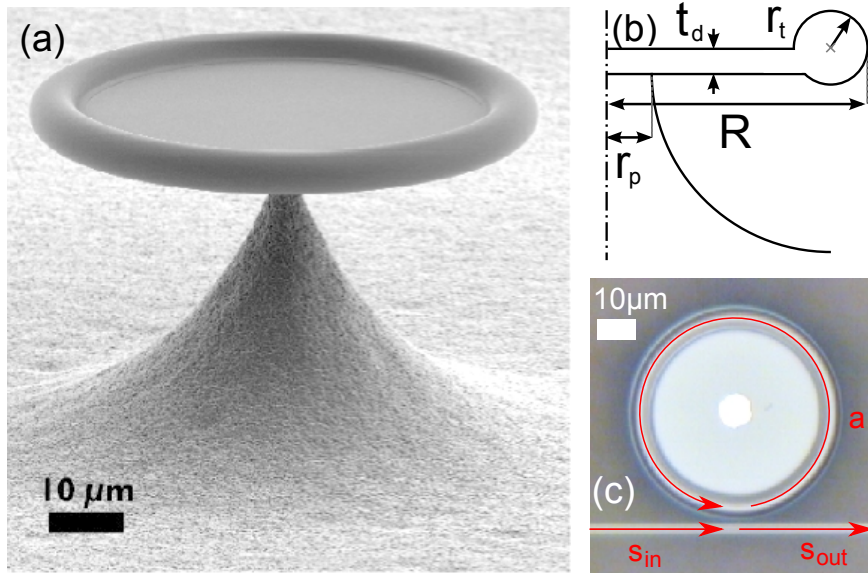
Figure 2.1: *(a) Scanning electron microscope (SEM) picture of a toroidal silica microcavity supporting both optical whispering-gallery modes and mechanical modes. (b) Schematic illustration of the profile of the toroid structure and its important parameters: the major diameter R, the toroid's minor diameter r_t, the disk's oxide thickness t_d and the supporting pillar radius r_p. (c) Optical micrograph of a toroid. The tapered fiber used to externally couple the optical mode is visible. The arrows represent the trajectory of the driving field s_in, the intracavity field a and the output field s_out in analogy with the generic scheme of Fig. 1.1. Adapted from Ref. [89].*

Another accurate approach is to calculate the optical mode *only* in the particular case of WGM where the geometrical structure of the torus can be safely approximated by an oblate spheroidal [90, 91, 92]. The problem has then a cylindrical symmetry (spatial coordinates

(r, θ, z)) facilitating the approximate analytical expression of the mode [21]. Considering the typical representation of toroids in Fig. 2.1, the electric field is given by [93]

$$
E_\zeta = \begin{cases}
E_0 e^{-\frac{z^2}{2r_z^2}} J_m\left(T_{m1} r/\bar{R}\right) e^{im\varphi} & r < R, \\
\frac{1}{P} E_0 e^{-\frac{z^2}{2r_z^2}} J_m\left(T_{m1} r/\bar{R}\right) e^{im\varphi} e^{-\alpha(r-R)} & r > R,
\end{cases}
\tag{2.2}
$$

with $\bar{R} = R + \frac{P}{k_0\sqrt{n^2-1}}$ being the effective radius and T_{m1} denoting the first zero[2] of J_m [94, 95]. The wave number in vacuum is $k_0 = 2\pi/\lambda$. Although optical modes in spheroids are not pure TE or TM, those from the present approximation can be safely treated as such with $\zeta \simeq z$ and $P = 1$ for TE-like modes and $\zeta \simeq \rho$ and $P = 1/n^2$ for TM-like modes. The mode width r_z in the z direction is given by

$$
r_z = \frac{R^{3/4} r_t^{1/4}}{\sqrt{m}} \frac{m}{(1 - R/(4m^2 r))^{1/4}},
\tag{2.3}
$$

illustrating the significant mode confinement inherent to toroids responsible for a smaller modal volume than for spheres. Importantly, the meridional confinement depends on the major radius R. The decay length of the evanescent field in the radial direction is then

$$
\alpha^{-1} \simeq \frac{\lambda}{2\pi\sqrt{n^2 - 1}},
\tag{2.4}
$$

where we note the role of the refractive index in the mode confinement and the scaling with λ. In the same approximation, the mode number m of the fundamental mode is expressed using $nk_0 R = \sqrt{T_{m1}^2 + m\sqrt{R/r_t}} - Pn/\sqrt{n^2 - 1}$ which leads to the same approximation for a WGM as already explained for spheres.

A numerical simulation of the localization of the TE and TM WGM in a toroid with a radius of $16\,\mu$m is displayed in Fig. 2.2. It shows that the mode profile is "pressed" against the dielectric interface and evanescently extends outside. In Ref. [21], it is shown that the predictions from the analytical approximation and the numerical simulations deviate by only a few percent.

2.2.3 Analysis of whispering-gallery mode losses in microtoroids

In equation (1.16), the total decay rate κ of the optical mode is defined as the sum of the intrinsic decay rate of the cavity κ_0 and the external decay rate due to the coupling to the output mode κ_{ex}. The description valid for the Fabry-Perot cavity used in chapter 1 holds for a toroid and the details of the coupling using a tapered fiber will be explained in section 2.2.4. The reflow of the silica disk during the microfabrication produces toroids with small surface asperities (few nm surface roughness). Consequently, surface scattering is reduced and the storage time of WGMs reaches a record value of tens of ns. In the

---

[2]For WGMs, the approximation $T_{m1} \simeq m + 1.8558m^{1/3} + O(m^{-1/3})$ can be used, as $m \gg 1$.
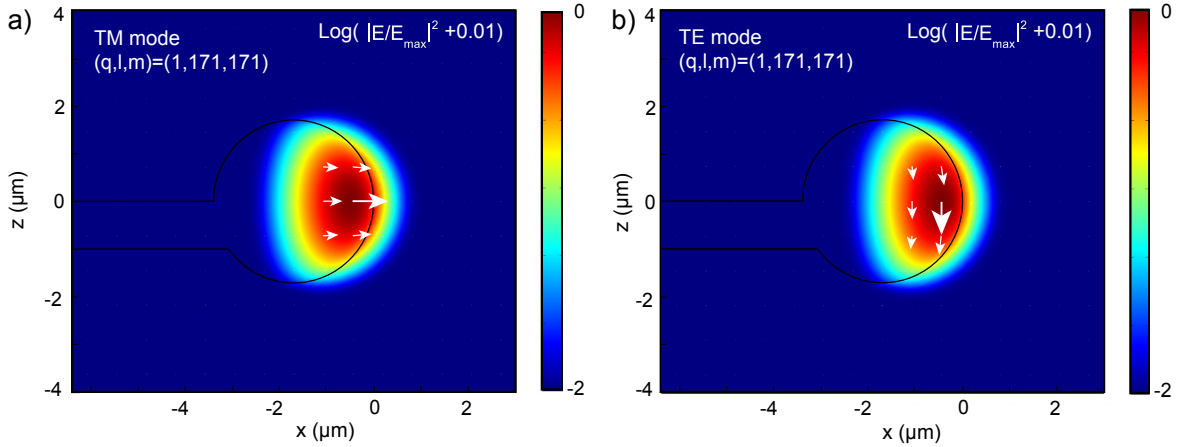
Figure 2.2: *Finite element method (FEM) simulation of a normalized electric field squared amplitude of a WGM illustrating the equatorial localization of the mode near the surface, as well as the evanescent part of the field outside of the dielectric torus, for TM (a) and TE (b) mode types. The arrows corresponds to the field direction and amplitude. Adapted from [21].*

context of optomechanics, it is nonetheless crucial to thoroughly characterize the losses as they influence the resolved-sideband parameter and the absorption heating.

For the intracavity decay rate κ_0, several mechanisms contribute to the losses:

$$\kappa_0 = \kappa_{\mathrm{rad}} + \kappa_{\mathrm{mat}} + \kappa_{\mathrm{wat}} + \kappa_{\mathrm{sca}}. \tag{2.5}$$

The intrinsic quality factor is then given by

$$Q_0^{-1} = Q_{\mathrm{rad}}^{-1} + Q_{\mathrm{mat}}^{-1} + Q_{\mathrm{wat}}^{-1} + Q_{\mathrm{sca}}^{-1}. \tag{2.6}$$

- The reflection of the WGM optical field on the inner curved surface of the resonator is not total. Part of the field is radiated outside. The resulting radiation losses are analytically estimated following the calculation of the mode profile and its associated eigenvalues as detailed in Ref. [85] for a sphere or in Ref. [92] for a spheroid, or using perturbation analysis as in Ref. [87]. The latter provides an estimation of $Q_{\mathrm{rad}} > 10^{11}$ for a torus of dimensions of $R > 40\,\mu\mathrm{m}$ and $r_{\mathrm{t}} > 2\,\mu\mathrm{m}$ as typically used in this work.

- Material losses are expressed by $Q_{\mathrm{mat}} = 2\pi n/\alpha\lambda$, where α is the loss due to absorption by the silica material and Rayleigh scattering induced by bulk inhomogeneities. At visible and near-infrared wavelengths, fused silica is very transparent, leading to an estimated $Q_{\mathrm{mat}} \simeq 10^{10}$ for a sphere at $630\,\mathrm{nm}$ [96] and more than 10^{11} for higher wavelengths [97]. Moreover, the fabrication method of the silica itself strongly influences its absorption properties. To grow silica from silicon wafers, two distinct methods are employed: *wet oxidation* where the oxidation is mediated by water and *dry oxidation* using dioxygen [98]. Unavoidably, water and hydroxyl group OH incorporates in the silica structure grown from wet oxidation [99] typically used for our samples. This leads to extra material absorption compared to the dry method [100].

- Another important source of losses originates from the absorption by the water layer that unavoidably deposits on the surface of the resonator. Indeed, the fabrication method leaves the fused silica subjected to adsorption of H_2O molecules from the ambient air within typically $100\,s$ after formation [96]. The layer couples to the evanescent part of the external field and absorbs power, thereby heating the structure. Experimental results demonstrate that this phenomenon significantly contributes to the overall loss mechanism at $1550\,nm$ for silica toroids (typical Q of 10^8) [101] and spheres (typical Q of a few times 10^8) [101], together with bulk absorption.

- At lower wavelengths, the total losses are dominated by light scattering from the surface inhomogeneities [102, 101]. The surface scattering quality factor is $Q_{\mathrm{sca}} \propto \lambda^3/\sigma^2 B^2$, where σ is the root-mean-square surface roughness and B the correlation length [97], which were measured to be $2\,nm$ and $5\,nm$ respectively for a typical silica sphere employing a similar fabrication method as in this work [102]. For toroids, the stronger polar confinement leads to a Q factor more strongly dominated by Q_{sca} compared to spheres since the field couples to the interface over a larger surface. This explains why toroids reach scattering-limited $Q \simeq 10^8$ [101] while spheres exhibit higher values up to $8 \cdot 10^9$ [96, 102], close to theoretical estimations [97] at $780\,nm$.

In the context of optomechanics, it is then justified to work at lower wavelengths where the losses are dominated by surface scattering. There, experimentally achieved optical Q are similar to those obtained at higher wavelength but losses by absorption are comparatively reduced, avoiding extra heating.

2.2.4   Optical fiber taper coupling to optical resonator modes

In the model presented in chapter 1, the Fabry-Perot cavity is pumped using a free space laser. For simplicity, overlapping of the cavity and laser modes is assumed and the external coupling rate κ_{ex} comes from the input mirror's transmission. Although free space coupling is used for spheres [103], deformed spheres [104], even in the context of optomechanics [56], waveguide coupling is normally employed with WGMs. Historically, the prism coupling technique was initially used [67] but the bulkiness of the setup and the multimode operation of the system is penalizing for applications in sensitive optical detection. For eroded optical fibers, single mode coupling is achieved with large spheres' WGM, although with low efficiency [105]. It is then the tapered fiber coupling method, which combines efficient single-mode coupling with limited setup dimensions, that is more appropriate for sensitive optomechanics experiments. Its fundamental properties are briefly reviewed in this section. On the experimental side, the fabrication technique of tapered fibers used in our group is described in Appendix B.

Taper coupling

The tapered fiber is obtained by melting a standard silica optical fiber with a flame while stretching it until the melted waist reaches a diameter of the order of the wavelength.

The taper supports then single mode waveguide propagation in the glass rod, where the surrounding air constitutes the cladding medium. As expected from a highly confined waveguide, part of the field propagates evanescently outside the tapered fiber and can be coupled to the WGM. For a tapered region of diameter r_f, the radial dependence of the expression of the electric field $E_f(r)$ is proportional to [106]

$$E_f(r) \propto \begin{cases} J_0(k_f r)/J_0(k_f r_f) & r \leq r_f, \\ \exp\left(-\gamma_f(r - r_f)\right) & r > r_f, \end{cases} \tag{2.7}$$

with the radial evanescent decay constant given by

$$\gamma_f = \alpha_f \frac{K_1(\alpha_f r_f)}{K_0(\alpha_f r_f)}, \tag{2.8}$$

with K_0 and K_1 denoting the modified Hankel functions of zero and first order. The term α_f is equal to $\sqrt{\beta_f^2 - k^2 n_{cl}^2}$, with $k_f = \sqrt{k^2 n_f^2 - \beta_f^2}$, n_f and n_{cl} being the refractive index of the tapered fiber and the cladding respectively, the latter being air in this case ($n_{cl} \simeq 1$).

For typical taper radii r_f of the order of λ used in our work, the propagation constant simply approximates to [107]

$$\beta_f \simeq \sqrt{k^2 n_f^2 - (2.405)^2/r_f^2}. \tag{2.9}$$

Coupling of the fiber taper mode to the WGM is achieved not only by spatial overlapping but also by matching the propagation constants of both, as efficient excitation of the WGM requires that both fields remain in phase across the interaction region. In the approximation given by equation (2.9), the propagation constant is varied with the radius of the taper. Experimentally, phase-matching is achieved by displacing the toroid along the axis of the tapered region, until the optimum taper radius r_f is reached. For typical toroids ($R > 10 \, \mu$m) and tapers ($r_f \lesssim \lambda$), the phase-matching region extends over hundreds of μm along the taper which makes the condition particularly easy to fulfill [90, 108].

Coupling regimes

Unlike for usual Fabry-Perot resonators, the external coupling rate of WGM resonators can be varied by changing the distance d between the waveguide and the resonator. In this case, the external coupling rate is expressed by $\kappa_{ex} \propto \exp\left(-\gamma_f(d - r_f)\right)$ [106]. Different coupling regimes can therefore be accessed over a displacement of the order of λ using commercially available positioners [109]. For convenience, the coupling parameter

$$\eta_c = \kappa_{ex}/\kappa \tag{2.10}$$

is introduced, with $\eta_c \in [0; 1]$.

By varying d, typical toroids can be undercoupled ($\eta_c < 1/2$, incident field mostly transmitted), critically coupled ($\eta_c < 1/2$, full destructive interference of the input and cavity field) or undercoupled ($\eta_c > 1/2$, intracavity field mostly transmitted).

Ideality

When approaching the taper to the near-field of the cavity, it is desirable to achieve coupling only to the fundamental mode of the waveguide. Unavoidably, in usual experimental situations, the taper propagates higher order "ho" modes that may couple to the WGM, This additional coupling to a lossy waveguide mode (that does not propagate out of the taper) leads to an extra decay rate κ_{ho}. In addition, the taper may scatter light when approached in the vicinity of the optical mode, inducing an additional decay κ_{rad}. Therefore, the "ideality" of the coupling is defined as

$$I = \frac{\kappa_{\mathrm{ex}}}{\kappa_{\mathrm{ex}} + \kappa_{\mathrm{ho}} + \kappa_{\mathrm{rad}}}, \tag{2.11}$$

quantifying the relative coupling of the WGM to the fundamental mode of the waveguide. The possibility to fabricate tapers supporting only the fundamental mode and the adiabatic nature of the fiber to taper transition allows to reach idealities of more than 99.97%, while simultaneously having a strongly coupled fundamental mode $\kappa_{\mathrm{ex}} \simeq 10^4(\kappa_{\mathrm{ho}} + \kappa_{\mathrm{rad}} + \kappa_0)$ [110].

2.3   Mechanical modes in silica toroidal resonators

In contrast with the generic scheme introduced in chapter 1, optomechanical coupling in our monolithic cavities arises between the whispering-gallery mode and an internal mode of vibration of the structure. Microtoroids, however, support a large number of mechanical modes that cannot be simply derived analytically. For their similarities with modes in toroids, the analytical derivation of acoustic modes in spheres is first presented in this section. The results of numerical simulations are introduced and we show next that they accurately predict the resonance frequency values experimentally measured [89]. We focus on the radial breathing mode corresponding to a peripheral oscillation that couples the strongest to the optical whispering-gallery mode and we briefly discuss its different loss mechanisms.

2.3.1   Supported mechanical modes in toroids

Analytical derivation in the case of spheres

The derivation of acoustic modes in silica microspheres is reminded here. The following calculations are based on Ref. [20] and are summarized in Ref. [111] where analytical derivations, finite element method (FEM) simulations and experimental measurements are shown to agree satisfyingly. The deformation of a sphere induced by an acoustic wave is described by the displacement vector $\vec{u}(\vec{r}, t)$ that denotes the displacement of a point to the coordinate $\vec{r}$ at a time t. In an isotropic homogeneous medium (such as silica), the equation of motion of the displacement field reads [112]

$$\rho \ddot{\vec{u}}(\vec{r}, t) = (\lambda + 2\mu)\, \vec{\nabla} \cdot \left(\vec{\nabla} \cdot \vec{u}(\vec{r}, t) \right) - \mu \vec{\nabla} \times \left(\vec{\nabla} \times \vec{u}(\vec{r}, t) \right), \tag{2.12}$$

with ρ being the material density and with the Lamé coefficients defined as

$$\lambda = \frac{\sigma E}{(1 + \sigma)(1 - 2\sigma)}, \tag{2.13}$$

$$\mu = \frac{E}{2(1 + \sigma)}. \tag{2.14}$$

σ is the Poisson's ratio and E the Young's modulus of the material.

Equation (2.12) admits a discrete number of solutions within the sphere. These acoustic modes are decomposed as [20]

$$\vec{u}(\vec{r}, t) = \sum_n \vec{u}_n(\vec{r}, t) = \sum_n c_n(t) \vec{u}_n^0(\vec{r}) = \sum_n \bar{c}_n \vec{u}_n^0(\vec{r}) e^{-i\Omega_n t}, \tag{2.15}$$

where $\bar{c}_n$ is the displacement amplitude of a mode of index n oscillating at an angular frequency Ω_n and $\vec{u}_n^0(\vec{r})$, is the displacement pattern normalized such that

$$\frac{\int_V \vec{u}_n^0(\vec{r}) \vec{u}_{n'}^0(\vec{r}) d^3 r}{\int_V d^3 r} = \delta(n - n'). \tag{2.16}$$

To solve the equation of motion (2.12), the scalar potential $\phi_q(\vec{r}, t)$ and the vector potential $\vec{\Phi}_q(\vec{r}, t)$ defining the displacement vector are introduced [113]

$$\vec{u}(\vec{r}, t) = \vec{\nabla}\phi_0(\vec{r}, t) + \vec{\nabla} \times \vec{\Phi}_1(\vec{r}, t) + \vec{\nabla} \times \vec{\nabla} \times \vec{\Phi}_2(\vec{r}, t). \tag{2.17}$$

The potentials are given in spherical coordinates by

$$\vec{\Phi}_q(\vec{r}, t) = r\phi_q(\vec{r}, t)\vec{e}_{\rm r} \text{ for } q = 1, 2 \tag{2.18}$$

and

$$\phi_q(\vec{r}, t) = \sum_{l,m} A_{qnlm} j_l\left(\frac{\Omega_{nlm}r}{v_q}\right) Y_l^m(\theta, \varphi)e^{-i\Omega_{nlm}t}, \tag{2.19}$$

where j_l is the spherical Bessel function of index l, Y_l^m the spherical harmonic function, A_{qnlm} a normalization constant and $\vec{e}_r$ the radial unity vector. $v_0 = \sqrt{(\lambda + 2\mu)/\rho}$ is the longitudinal sound velocity and $v_1 = v_2 = \sqrt{\mu/\rho}$ is the transverse sound velocity. The acoustic modes are characterized by their integer mode numbers comprising the radial mode number n ($n = 0, 1, 2, \ldots$), the angular mode number l ($l = 0, 1, 2, \ldots$), and the azimuthal mode number m ($m \in [-l, l]$) and by their angular eigenfrequencies Ω_{nlm}.

The mode of interest realizing the strongest optomechanical coupling to the WGM is the radial breathing mode (RBM) characterized by $(n, l, m) = (1, 0, 0)$, for which the displacement field is purely radial. Its displacement pattern reads

$$\vec{u}^0(\vec{r}) = \frac{A}{r^2}\left(\sin(kr) - kr\cos(kr)\right)\vec{e}_{\rm r}, \tag{2.20}$$

where the mode numbers are dropped for readability, and where $k = \Omega_{\rm m}/v_0$ is the wavenumber given by the characteristic equation. We take $\Omega_{\rm m}$ as the mechanical angular frequency of the mode of interest for consistency with chapter 1. Thus, we have

$$\left(1 - \frac{1}{4}\frac{v_0^2}{v_1^2}k^2R^2\right)\frac{\tan(kR)}{kR} - 1 = 0 \tag{2.21}$$

from the calculation of the strain tensor, for a sphere of radius R [20]. For fused silica, this equation is solved for $kR \simeq 2.4005$ and gives the mechanical angular frequency of the RBM of the sphere $\Omega_{\rm m} \simeq 2.4005 v_0/R$. It estimates to $91.2\,{\rm MHz}$ for a sphere of diameter $50\,\mu{\rm m}$. The resonance frequency estimated by FEM simulation is less than 1% different, proving the relevance of the numerical model to estimate the parameters of the mechanical modes supported by the spheres.

Numerical modeling in the case of silica toroids

Using FEM simulation tools, acoustic modes can be accurately estimated in toroids despite the absence of analytical derivations due to their reduced number of symmetries. Figure 2.3 shows FEM simulation results illustrating the displacement pattern of the various mechanical modes supported by the structure, with exaggerated displacement [89]. As in
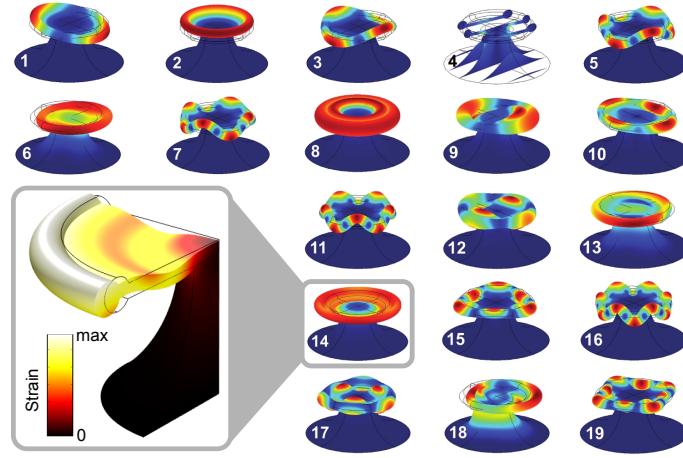
Figure 2.3: *Three dimensional FEM simulations of the 19 first mechanical modes showing the exaggerated and color-coded displacement patterns. Mode 14 is the RBM, which couples the strongest to the optical mode. Adapted from Ref. [89]. Inset: RBM displacement on a different geometry closer to the type of samples used in chapter 3. Adapted from Ref. [55].*

the case of spheres, the acoustic mode that couples the most strongly to the WGM is the RBM, numbered 14 in Fig. 2.3. Its displacement pattern is illustrated in the inset, with a frequency $\Omega_m/2\pi = 75\,\text{MHz}$ for a radius $R = 22\,\mu\text{m}$.

The experimental values of 19 different modes ranging from 1 to 100 MHz deviate by less than 2% when compared to numerically simulated values. The FEM simulation therefore appears as a powerful tool for investigating the mechanical properties of toroids. It is used in section 3.2.2 for the engineering of mechanical losses of the RBM induced by the coupling to other supported modes.

In silica microtoroids, typical RBM resonance frequencies are much larger than typical optical linewidths at 780 nm (on the order of 1 MHz). When the cavity is close to critically coupled, the optomechanical system is then in the resolved-sideband regime. Silica microtoroids satisfy therefore the fundamental condition required to reach the motional ground state.

2.3.2   Mechanical losses

The mechanical mode under consideration is subject to several types of mechanical losses adding up. The total mechanical damping rate yields

$$\Gamma_m = \Gamma_{gas} + \Gamma_{clamp} + \Gamma_{mat} + \Gamma_{other}, \tag{2.22}$$

leading to a mechanical quality factor given by

$$Q_m^{-1} = \Omega_m/\Gamma_m = Q_{gas}^{-1} + Q_{clamp}^{-1} + Q_{mat}^{-1} + Q_{other}^{-1}. \tag{2.23}$$

The contributions to the damping from the surrounding gas (Q_{gas}^{-1}), from the clamping of the moving mass (Q_{clamp}^{-1}) and from the material (Q_{mat}^{-1}) require particular attention in the context of optomechanics and are described in section 3.2.

Although not dominant in our system at room and low temperatures, other fundamental contributions are responsible for Q_{other}^{-1} and are summarized in Ref. [21]:

- Thermoelastic damping comes from delayed flow of the heat generated by the strain field propagating in the medium [114].

- Surface effects such as oxidation, adsorption, and irregularities constitute also another source of dissipation [115].

2.4   Optomechanical coupling

The complex 3D geometry of the system makes its parametrization less straightforward than in the case of the linear Fabry-Perot cavity depicted in Fig. 1.1. Consequently, in this section, we introduce the effective displacement and the effective mass parametrically equivalent to $x(t)$ and m_{eff} for the simplified case, allowing to apply the theoretical considerations given in chapter 1 to the non-trivial geometrical structures of the microtoroids.

2.4.1   Effective displacement

To map the complex three-dimensional vectorial displacement $\vec{u}_n(\vec{r}, t)$ onto a simple one-dimensional scalar displacement $x(t)$, we introduce the weighting function $\vec{w}(\vec{r})$ and define the displacement as

$$x(t) = \int_V \vec{w}(\vec{r}) \cdot \vec{u}(\vec{r}, t) d^3r = \sum_n c_n(t) \int_V \vec{w}(\vec{r}) \cdot \vec{u}_n^0(\vec{r}) d^3r$$

$$\equiv \sum_n c_n(t) \langle \vec{w}(\vec{r}) \cdot \vec{u}_n^0(\vec{r}) \rangle. \tag{2.24}$$

The integral $\langle \vec{w}(\vec{r}) \cdot \vec{u}_n^0(\vec{r}) \rangle$ defines the relative *spatial* overlap of the strain wave and the optical field. The frequency shift induced by this scalar displacement is however determined by the optomechanical coupling constant $G = d\omega_c/dx$.

In experiments using the Fabry-Perot cavity configuration where the back mirror moves as a whole, the weighting function is simply defined using the Gaussian profile of the intracavity mode, which can be analytically derived [19]. For WGMs in toroids, an accurate approximation can be made by considering the mechanical displacement as a perturbation of the electromagnetic mode due to the displacement of polarizable material (we consider here a magnetic permeability of glass close to unity). The weighting function then reads [20]

$$\vec{w}(\vec{r}) \approx \frac{1}{2\pi R} \delta(z - z_0) \delta(r - R) \vec{e}_r, \tag{2.25}$$

where $z = z_0$ is the coordinate of the equatorial plane. This expression approximates the spatial overlap to be confined to the periphery of the toroid at $r = R$ with zero transverse extension. Recasting Eq. (2.25) in Eq. (2.24) shows that for a toroid the scalar displacement is simply the change of the cavity radius and the optomechanical coupling constant is then given by $G = -\omega_c/R$. It should be noted additionally that the change of refractive index induced by the strain accounts for less than 20% of the frequency shift [20, 82].

2.4.2   Effective mass

The scalar displacement $x(t)$ changes the angular resonance frequency of the cavity Ω_c by an amount quantified by the optomechanical coupling parameter G. Similarly, the spatial overlap of the optical and mechanical mode redefines the mechanical susceptibility of the mechanical mode through the effective mass m_{eff} introduced here.

We consider the potential energy U_n of the n-th mode of interest

$$U_{\mathrm{n}} = \frac{1}{2}M_n\Omega_n(c_n(t))^2 \tag{2.26}$$

with

$$M_{\mathrm{n}} = \int_V \rho|\vec{u}_n^0(\vec{r})|^2 dV \tag{2.27}$$

simply being the moving mass of the n-th mechanical mode. We then use the normalized displacement defined in Eq. (2.24) in the case of the n-th mode and recast it into Eq. (2.26) $U_{\mathrm{n}} = \frac{1}{2}m_{\mathrm{eff},n}\Omega_n(x_n(t))^2$ with the effective mass defined by

$$m_{\mathrm{eff},n} = \frac{M_n}{\langle \vec{w}(\vec{r}) \cdot \vec{u}_n^0(\vec{r})\rangle^2}. \tag{2.28}$$

For the typical toroidal resonators used, the values of the effective mass range from 0.5 to 2×10^{-11} kg.

The optomechanical system presented in this chapter is parametrized to the unidimensional system of chapter 1, with an effective displacement $x(t)$ and an effective mass m_{eff} taking into account the complex spatial extensions of both optical and mechanical modes. In addition, it is shown that the electromagnetic radiation pressure force within the classical framework of the propagating mode exerts a force in the radial direction exactly equivalent to the radiation pressure force derived in Eq. (1.8) [20]. Hence, the theoretical framework introduced using the simple unidimensional model can be directly applied with the parametrization of the structure described in this chapter.

Chapter 3

Optomechanical cooling to low phonon occupancy

3.1 Introduction

In the two previous chapters, it has been theoretically demonstrated that silica microtoroids are promising candidates for the implementation of dynamical backaction cooling mediated by radiation pressure: their intrinsic properties make the preparation and detection of the mechanical radial breathing mode in its quantum ground state conceivable.

A proof-of-principle experiment demonstrated the phenomenon in silica microtoroids in the group in 2006 by reducing the phonon occupancy of a 58-MHz mechanical radial breathing mode from more than $100\,000$ at room temperature down to $\sim 4\,000$. Diverse factors have limited the performance: the equation describing the mean number of final phonons (1.54)

$$\bar{n} = \bar{n}_\mathrm{m}\frac{\Gamma_\mathrm{m}}{\Gamma_\mathrm{eff}} + \bar{n}_\mathrm{min}$$

allows us to analyze those factors separately. Nevertheless, this pioneer accomplishment does not answer the question of whether it is experimentally possible to use dynamical backaction to cool the mechanical oscillator to its motional ground state and to subsequently detect a genuine quantum signature. By proving a phonon occupancy of 9 ± 1 solely limited by simple technical issues, the experimental work presented here strongly suggests that the aim is within reach. Moreover, very recent follow-up measurements performed in our group combining the optimizations suggested here demonstrated an occupancy of 1.7 ± 0.1 [54], offering convincing evidence for the relevance of the approach used here. All experimental efforts that have paved the way to the aforementioned results are presented in this chapter.

In section 3.2, the coupling of the mechanical oscillator to the thermal environment is studied by looking at the various mechanisms that contribute to the mechanical dissipation Γ_m. The damping related to the surrounding gas and the intermodal coupling are negated, respectively, by placing the sample in a low-vacuum chamber and by modifying

the geometrical structure to incorporate spokes, making use of the mechanical engineering control provided by microfabrication technologies [116]. The mechanical dissipation, after these optimizations, is dominated by the material dissipation mostly due to silica defect states. The temperature dependence of the mechanical properties induced by these two-level systems are thoroughly studied.

In section 3.3, the quantum aspect of the cooling process leading to the minimum occupation $\bar{n}_{\mathrm{min}}$ is considered more deeply. The fundamentally required resolved-sideband configuration is experimentally demonstrated for the first time in the context of optomechanics [117].

In section 3.4, the influence of the thermal environment at the average occupancy $\bar{n}_{\mathrm{m}}$ is reduced by cryogenically refrigerating the sample using a ^{4}He cryostat. Due to this successful implementation, it is possible to explore novel optical dispersive properties intrinsic to the whispering-gallery mode configuration of the silica resonators [118], and to study the thermodynamical aspects of the cryogenic cooling [119]. The success of this technical achievement is proven by laser cooling the mechanical mode down to a phonon occupancy of 63 ± 20 [41], providing the first demonstration of cavity optomechanics at cryogenic temperatures and achieving a phonon occupancy on par with other similar experiments [56, 53].

The final optimization of the experiment using a ^{3}He refrigeration technology is demonstrated in section 3.5 by measuring a final phonon occupancy of 9 ± 1 using a purpose-built balanced homodyne interferometer [55]. Although the cooling in this case is still limited by the excess heating resulting from the absorption of the light transversely scattered by the tapered fiber, this result demonstrates that the experiment set up for this analysis can host the dynamical backaction cooling down to the motional ground state of the macroscopic oscillator.

Finally, section 3.6 reports on the effect of the mutual optomechanical interaction on the optical properties of the resonator. Because this phenomenon shares strong similarities with atomic electromagnetically induced transparency, it is referred to as optomechanically induced transparency; its first observation is reported here [120].

3.2 Reduction of the mechanical dissipation

The reduction of the mechanical damping of mechanical oscillators is a crucial aspect that has received significant considerations, especially in the field of atomic force microscopy (AFM). Since its inception in 1986 [121], the most common AFM principle resides on the detection of the change of frequency of a mechanical oscillator probing the atomic force gradient of a sample's surface. To improve the detection sensitivity, experimental efforts have focused on increasing the oscillator's mechanical Q. The performances achieved had a major impact on recent successful mechanical detection of single spin magnetic force [122], single adsorbed gold atom masses [123] and single adsorbed protein masses [124].

Similarly, in the context of optomechanics, it is crucial to the reduce the mechanical dissipation to augment the sensitivity and to lower the thermal noise level (see equation (1.46)). This section presents the efforts required to produce optomechanical systems whose mechanical dissipations are dominantly limited by the intrinsic properties of the material used. By operating at low pressures below 1 mbar, gas friction is rendered negligible and allows to study the acoustic emission in spectrally-close modes responsible for the clamping damping. By proper mechanical engineering of the vibrating structure, the contribution due to intermode coupling is negated and the dissipations inherent to silica thus becomes the dominant mechanism, at both room and cryogenic temperatures.

3.2.1 Gas damping

When a mechanical object oscillates in its surrounding gas, it experiences a force proportional to its velocity adding extra friction Q_{gas} to the oscillating movement (see Eq. (2.23)). Depending on the pressure, three regimes corresponding to three different damping mechanisms occur [125]:

- *Viscous regime.* When the mean free path of molecules is smaller than the characteristic dimension of the device, the interaction rate between molecules is very high and the damping mechanism is usually described by introducing a gas viscosity. Simultaneously, the inertial force of the gas modifies the resonant frequency of the mechanical oscillator.

- *Molecular regime.* In the opposite situation, molecules of the gas are non interacting among each others and damping of the motion solely comes then from collisions with independent molecules [115].

- *Intrinsic regime.* When the number of gas molecules is low enough to neglect their influence on the motion, damping mechanisms are dominated by the intrinsic properties of the mechanical oscillator.

Construction of the vacuum chamber

To reach the intrinsic regime, the experimental coupling setup – including the toroid, the tapered fiber on the holder and the positioners – is placed in a vacuum chamber.
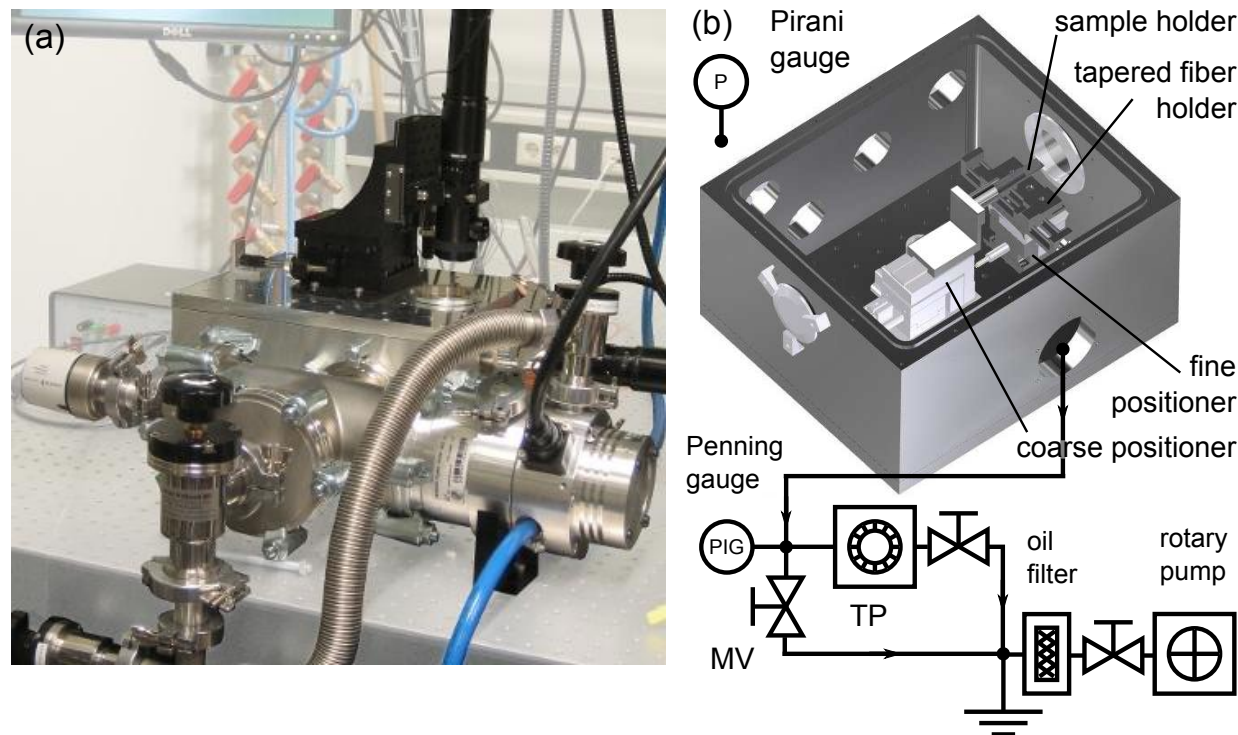
Figure 3.1: *Picture (a) and 3D rendering (b) of the vacuum chamber designed to host a full coupling stage. The vacuum construction allows to reach a base pressure of 6×10^{-3} mbar using only the rotary pump (Leybold DB16) and below 10^{-5} mbar using a turbomolecular pump (TP) (Leybold TD20) backed by the rotary pump. Coupling in vacuum is enabled by the combined use two 3-axes displacement stages using piezoelectric stepper motors (New Focus 8302-UHV) for coarse positioning and a piezoelectric flexural stage (Physik Instrument P-611 series) for fine positioning. The toroid-taper distance is monitored with two appropriate high working distance microscopes located outside the chamber imaging through the top (non represented) and the side vacuum-tight windows. MV: manual valve.*

In Fig. 3.1, the chamber is evacuated using a turbomolecular pump backed by a rotary pump, allowing a significant pumping speed at a pressure below 10^{-5} mbar. ISO-standard (Viton ®) vacuum joints are used for the chamber as the best compromise among ease of operation, cost, and targeted pressure residing in the high vacuum regime.

To maintain low oil contamination within the pumping circuit, an activated alumina trap is placed before the rotary pump to avoid back diffusion of the lubricating oil. The turbomolecular pump bearings are ceramics-based, avoiding the use of oil for lubrication and therefore keeping the chamber free of contamination from this pump. Measurements of optical quality factors of silica toroids in the evacuated chamber show no contamination.

After thorough pumping of the chamber, a base pressure below 10^{-5} mbar is reached. Under usual experimental conditions, the chamber is evacuated to the base pressure, then the valves are closed. The pressure is then slowly made to rise thus allowing to measure the mechanical Q factor versus the pressure spanning over 8 orders of magnitude.

Measurements of mechanical quality factors

Measuring the mechanical Q of toroids placed in the vacuum chamber enables to characterize the intrinsic regime of the mechanical oscillator. For experimental practicality, the technique of the side-of-the-fringe detection technique is employed.
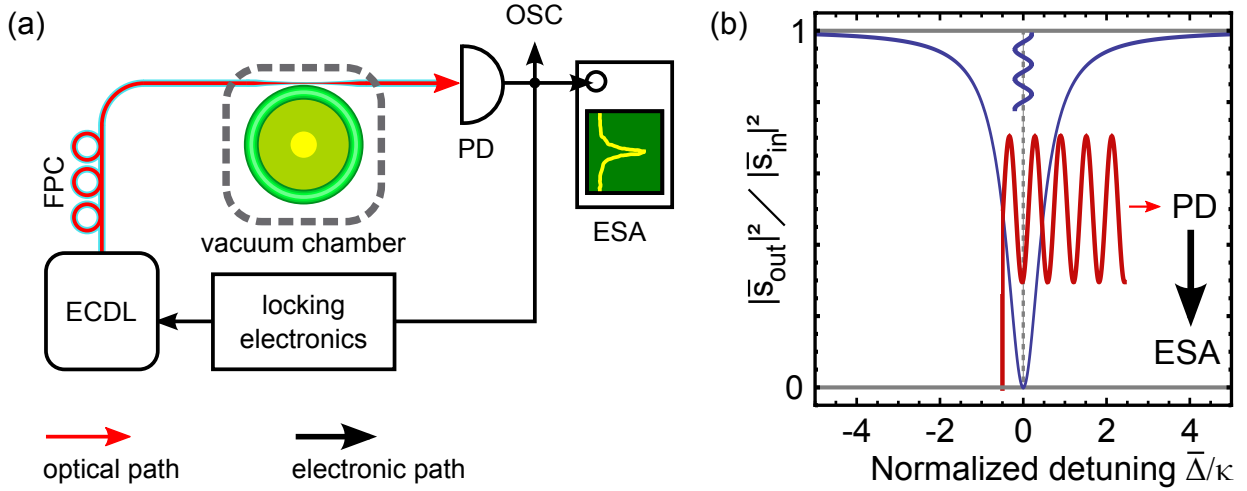
Figure 3.2: *(a) Side-of-the-fringe detection setup. A 1550 nm fiber-coupled external cavity diode laser (ECDL) (New Focus Velocity series) probes the toroid placed inside the vacuum chamber. Matching of the polarization is ensured using a fiber polarization controller (FPC). The photodetected transmission signal (New Focus 1811 InGaAs, fiber coupled) provides the error signal for the locking electronics. The photodetector's (PD) bandwidth is of 125 MHz, larger than the typically detected mechanical fluctuations below 100 MHz. OSC: oscilloscope. ESA: electrical spectrum analyzer. (b) Side-of-the-fringe detection principle. When the laser is detuned by $\pm \kappa/2$, thermally driven mechanical vibrations modulate the intensity of the output field s_{out}. Electrical spectrum analysis of the photodetected intensity allows to infer the mechanical parameters.*

As depicted in Fig. 3.2 (a), a 1550 nm external cavity diode laser (ECDL) is used for characterization. The large mode-hop free detuning range of the Littman-Metcalf configuration allows to quickly address the desired optical resonance frequency of the toroid. Using the positioners, the critical coupling condition $\eta_{\mathrm{c}} = 1/2$ is reached for better contrast in the transmission signal. Then, when the appropriate DC electric signal is subtracted, the transmission signal is directly used as an error signal to be fed back into the electric input of the ECDL frequency tuning port. An appropriate electronic closed-loop circuit ensures the locking mechanism. Thus, the laser is locked at a detuning $\bar{\Delta} = |\kappa/2|$ with a locking bandwidth limited by the actuator at ~ 2 kHz. This bandwidth is sufficiently large at low input powers to maintain locking even in the presence of the detuning non-linearity induced by absorption heating.

The principle of this detection is described in Fig. 3.2 (b). When the readout laser is detuned from the optical cavity resonance frequency, mechanical fluctuations are directly transduced into intensity fluctuations that are spectrally analyzed. This technique is particularly convenient for the rapid test of many samples at room temperature and

its construction is simple. From the parity of Ω_{eff} and Γ_{eff} (Eqs. (1.41) and (1.42)), radiation pressure effects that unavoidably affect the mechanical parameters can be simply subtracted from two successive measurements at $\bar{\Delta} = -\kappa/2$ and $\bar{\Delta} = +\kappa/2$. In addition, at room temperature, this technique is sensitive enough to enable low input power measurements precluding thermal effects.

The measurements of the mechanical quality factor $Q_{\text{m}} = \Omega_{\text{m}}/\Gamma_{\text{m}}$ when the environmental pressure is varied from atmospheric pressure (ca. 1000 mbar) to less than 0.1 mbar are presented in Fig. 3.3 for a typical toroid (a) and for a disk (b). The clamping-induced damping is optimized for these samples as explained in the next section. The intrinsic damping regime is reached for a pressure below 1 mbar.
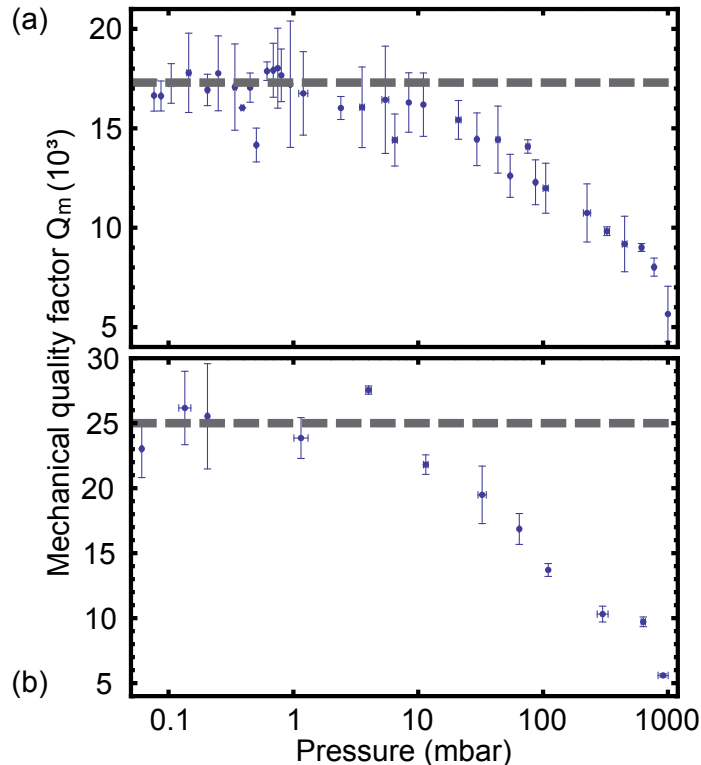
Figure 3.3: *Mechanical quality factor of the radial breathing mode of a silica toroid (a) and of a silica disk (b) versus pressure. The mechanical frequency is 47.4 MHz for the toroid and 37.1 MHz for the disk. The vertical error bars account for the radiation pressure induced change of Q_{m}. The horizontal error bars account for the slow pressure drift between two consecutive measurements. As pressure drops, Q_{m} of the toroid increases from 5600 to 17300. The regime of intrinsic dissipation is achieved at a pressure below 1 mbar, symbolized by the dashed gray asymptote. A similar behavior is observed for the disk.*

For the cryogenic implementation, it is therefore possible to use exchange gas pressures of 1 mbar to thermalize the sample without degrading the mechanical Q.

3.2.2 Clamping-induced damping

The mechanical attachment of the moving mass to the environment results in clamping-induced damping. Particular attention has been given to this type of losses in the community of cantilever-based detection [126] and of gravitational wave interferometers [127], where high mechanical Q oscillators are desirable for improved sensitivity. For toroids, clamping losses can be addressed due to the control over the geometrical parameters of the structure using microfabrication.

In this section, we measure the mechanical quality factor versus the size of the pillar and show that it exhibits a non-linear dependency [116]. This is explained by mechanical mode coupling, leading to the hybridization of the mechanical parameters of the radial breathing mode with contiguous modes, especially with the flexural mode of the central disk. Using a novel microfabrication technique, "spoke" toroids are designed to reduce this coupling. These structures exhibit a measured mechanical Q reaching up to 50000 at a frequency above 20 MHz, solely limited by damping due to the material at room temperature.

Measurement of the coupling to the neighboring modes

To study the influence of the attachment of the mechanical structure to the substrate, the mechanical Q of the RBM is measured for varying pillar diameters. Between each measurements, the toroid is placed in the etching chamber introduced in appendix A and a controlled train of etching pulses is applied to progressively reduce the pillar radius r_p to the desired value. Figure 3.4 (a) shows the results of these measurements for six different toroids at room pressure. A reproducible drop of the mechanical Q is clearly observed at specific undercuts $u = (R - r_\mathrm{p})/R$ (Fig. 2.1), with R being the major radius of the toroid.

An insight on this observation is given by comparing the measured RBM mechanical frequencies with the numerically simulated frequencies of the modes supported by the structure and spectrally adjacent to the RBM. The comparison depicted in Fig. 3.4 (b) shows that at specific undercuts, a neighboring mode is pulled spectrally closer to the RBM but avoids crossing, revealing a significant coupling.

To have a precise description at the phenomenon, we focus on the RBM "r" and flexural "f" mode of the disk (mode 8 in Fig. 2.3), and their mutual coupling. Both mechanical parameters of the modes have a strong linear dependency on the undercut that can be approximated as

$$\Omega_\mathrm{r,f} = \Omega_\mathrm{r,f}^{(0)} + \Omega_\mathrm{r,f}^{(1)}\, u \tag{3.1}$$

$$\Gamma_\mathrm{r,f} = \Gamma_\mathrm{r,f}^{(0)} + \Gamma_\mathrm{r,f}^{(1)}\, u. \tag{3.2}$$

They correspond to the bare values, experimentally unaccessible as u is varied because coupling has to be accounted for. We then parameterize the two modes by two coupled
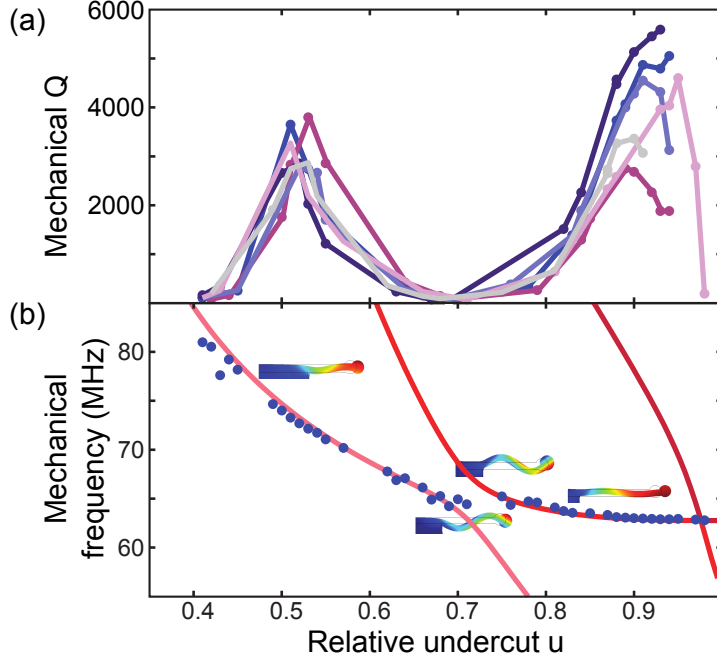
Figure 3.4: *Radial breathing mode's (RBM) mechanical Q and frequency versus relative undercut. (a) Measured mechanical Q of the RBM of 6 toroids versus undercut. A reproducible drop of mechanical Q is visible for undercuts $u \approx 0.7$ and $u \gtrsim \approx 0.95$. (b) Measured mechanical frequency of the RBM (blue dots) versus undercut showing the avoided crossing. The red lines correspond to the numerically simulated mechanical frequencies of the modes supported by the structure. The mode coupling phenomenon is illustrated by the corresponding evolution of the simulated displacement patterns, shown in inset. Adapted from Ref. [116].*

harmonic mechanical oscillators whose equations of motion are

$$\ddot{x}_r + \Gamma_r \dot{x}_r + \Omega_r^2 x_r + C^2 x_f = 0 \tag{3.3}$$

$$\ddot{x}_f + \Gamma_f \dot{x}_f + \Omega_f^2 x_f + C^2 x_r = 0, \tag{3.4}$$

with C being the coupling parameter. This system supports a couple of eigensolutions $(+, -)$ (normal modes) whose respective frequencies and dampings are given by

$$\Omega_\pm + \frac{i}{2}\Gamma_\pm = \frac{1}{2}(\Omega_r + \Omega_f) + \frac{i}{4}(\Gamma_r + \Gamma_f) \pm \sqrt{\left(\frac{1}{2}(\Omega_r + \Omega_f) + \frac{i}{4}(\Gamma_r - \Gamma_f)\right)^2 + \frac{C^4}{4\Omega_r \Omega_f}}. \tag{3.5}$$

Figure 3.5 shows a fit of the data to the model described by Eq. (3.5). The bare parameters given by expressions (3.1) and (3.2) are represented by the dashed lines. The fitted solid lines show an agreement with the experimental points, outputting as a fit parameter a coupling $C/2\pi = 14$ MHz. This is a significantly high value compared to the bare frequencies. This important coupling of the oscillatory motions of both modes originates from the particular geometry of the toroid. The torus is offset from the equatorial plane of symmetry of the disk, thus the radial motion induces vertical displacement. Additionally,
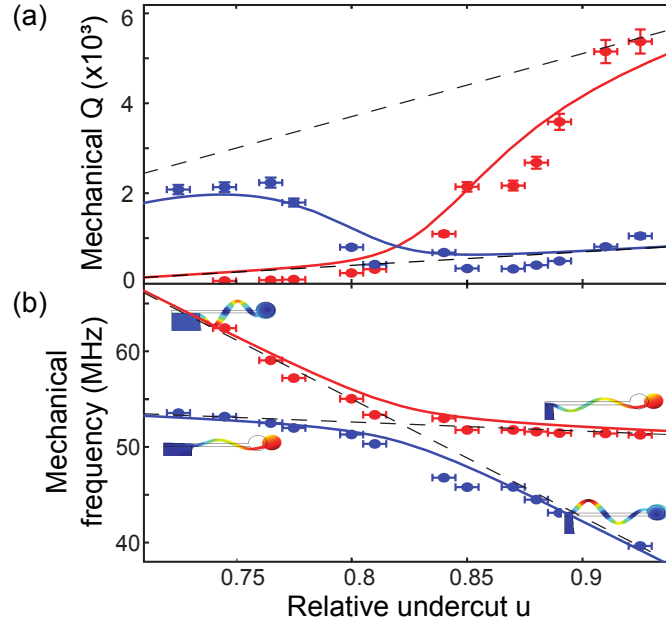
Figure 3.5: *Comparative mechanical Q (a) and frequency (b) versus relative undercut for the RBM and the flexural mode of a radius $R \approx 28\,\mu m$ and thickness $t_{\rm d} = 1\,\mu m$ toroid. The measured values (dots) are fitted with the analytical model of expression (3.5) (solid line) with Q factors $Q_{\pm} = \Omega_{\pm}/\Gamma_{\pm}$ and frequencies $\Omega_{\pm}$. The avoided crossing between the modes illustrate their mutual coupling. The dashed lines represent the bare values $\Gamma_{\rm r,f}$ and $\Omega_{\rm r,f}$. The numerically simulated displacement patterns illustrate the mode hybridization through the crossing. Adapted from Ref. [116].*

the disk is clamped only on its bottom side, therefore enhancing the vertical displacement under radial oscillations.

When u is varied, the bare frequencies get closer until hybridization becomes important. The two coupled eigenmodes mix frequencies and dampings, and both measured mechanical Qs drops, as observed in Figs. 3.4 (a) and 3.5 (a).

To increase the mechanical Q, the geometrical parameters of the structure are scanned to find a toroid combining reduced intermode coupling and a small attachment section. The optimum geometry is hit for toroids supported by a "needle pillar" exhibiting an intrinsic mechanical Q of 31000 for a pillar diameter close to 500 nm as shown in Fig. 3.6. This type of structure, which is relatively easy to fabricate, will be used in a cryogenic environment to perform the dynamical backaction cooling.

Mechanical Q engineering

Inspired by the work performed in the context of fundamental studies of mechanical dissipations [128], the clamping losses are quantified using numerical tools. The results are subsequently used to perform geometrical optimization of the structure.

When hybridizing to other modes, the mechanical energy of the RBM is ultimately
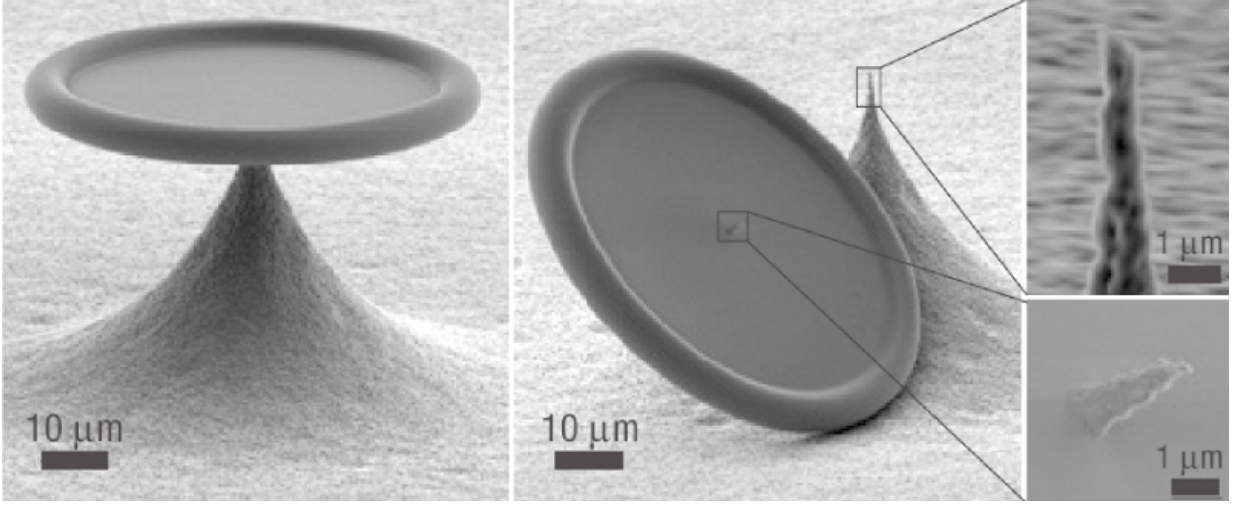
Figure 3.6: *Scanning electron microscope picture of a needle-pillar supported structure exhibiting an intrinsic mechanical Q of 31000 at 73.5 MHz. During the imaging, the structure was broken close to its weakest point, revealing the top of the supporting needle pillar. Adapted from Ref. [117].*

radiated through the pillar. To quantify this loss, the power P_{mech} carried by the emitted mechanical wave is numerically evaluated and the parameter D is introduced [116]

$$D = \frac{\Omega_{\text{m}} E_{\text{mech}}}{P_{\text{mech}}} = E_{\text{mech}} \left(\rho c_{\text{s}} \Omega_{\text{m}} \int_{A_{\text{p}}} |\Delta z(r)|^2 dA \right)^{-1}, \qquad (3.6)$$

where E_{mech} is the total stored mechanical RBM energy, ρ the material density, c_{s} the sound velocity and $\Delta z(r)$ the vertical displacement of the pillar/disk interface of section A_{p}. This parameter is the ratio of the energy stored to the energy radiated per cycle and is homogeneous with a Q factor. Comparisons of simulated D and experimental results reveal a proportionality $Q_{\text{clamp}} = \alpha_{\text{clamp}} D$ [116] where the prefactor $\alpha_{\text{clamp}} \approx 3$ accounts for the impedance mismatching that cannot be simulated with the current model. Thus, experimental mechanical Q limited by clamping-induced damping can be numerically quantified.

Engineering of the coupling parameter C is technically difficult because its value is inherent to the fabrication technique employed to produce the toroids. However, frequency mismatching of the RBM with neighboring modes is controllable over the size of the structure. It is moreover directly affecting $\Delta z(r)$ and can therefore be numerically quantified by D. To increase D, the central disk is cut into smaller geometrical forms whose eigenfrequencies are mismatching the RBM frequency. An implementation of this optimization is to have the outer rim carried by spokes (Fig. 3.7) of defined lengths and widths controlled during the microfabrication process.

The fabrication process of the spoke toroids is detailed in Fig. 3.8. It is adapted from the conventional process presented in appendix A allowing the fabrication of high optical finesse cavities. Importantly, optical quality factors are not affected by the newly developed
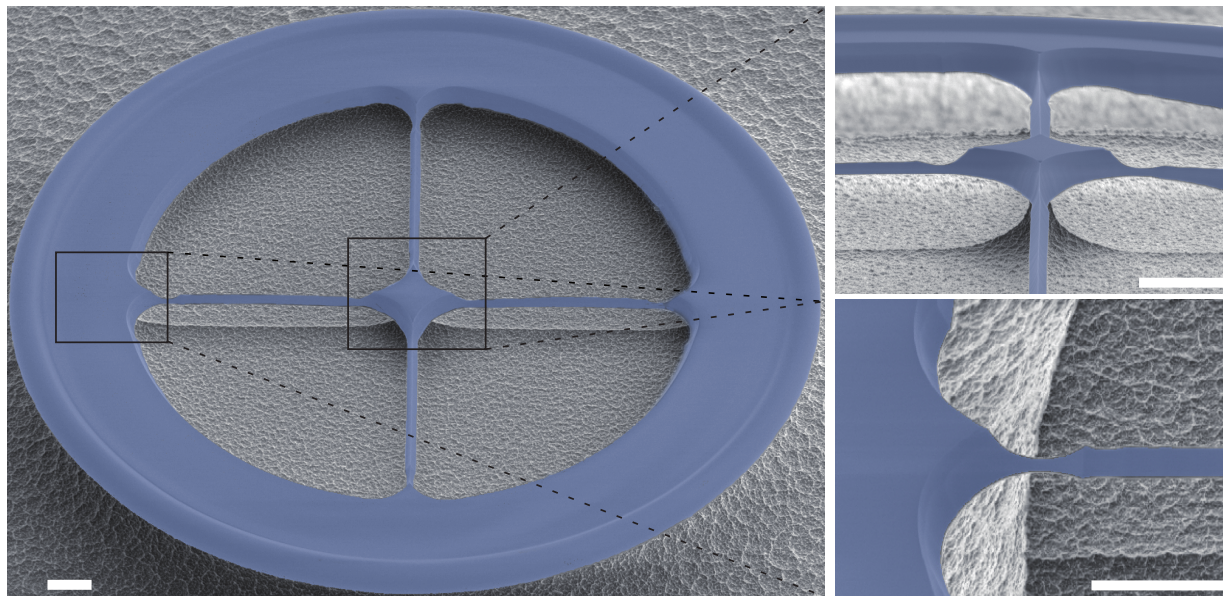
Figure 3.7: *Scanning electron micrograph of a $R \simeq 45\,\mu m$ spoke toroid (scale bars of $5\,\mu m$ each). The insets show the deviation from ideal pattern transfer, resulting from both incorrect optical projection (rounding of the corners) and SiO_2 chemical etching isotropy (curved vertical steps). Adapted from Ref. [116]*

process, therefore decoupling optical and mechanical performance engineering on the same optomechanical system.

Spoke toroids with mechanical Q as high as 50000 are measured for RBM frequencies above 20 MHz. Experimentally, it is shown that these samples do not see their mechanical Q strongly affected by the further reduction of the pillar diameter, additionally proving that mode hybridization is strongly controlled and optimized. Figure 3.9 (a) shows a numerically simulated displacement pattern of the RBM of an optimized spoke toroid illustrating the localization of the mechanical displacement to the outer rim. Negligible power is carried by the outcoupled mechanical wave, thus leading to a high mechanical Q of the RBM.

Although very high values of D are numerically simulated, measurements show that the value of $Q_m \simeq 50000$ cannot be exceeded at room temperature. Indeed, it corresponds to the limit set by the material dissipation, as illustrated in Fig. 3.9 (a). The blue points are measurements of the mechanical Q of various spoke structures, plotted versus their parameter D numerically evaluated after estimation of the geometry of the structure. Clearly, the mechanical Qs saturate at a value determined by Q_{mat} and estimated using the model presented in the next section. The solid line is a fit of the experimental points with the model $Q_m = \left((\alpha_{clamp}D)^{-1} + Q_{mat}^{-1}\right)^{-1}$. The fit parameter α_{clamp} is slightly lower than previously estimated because impedance mismatching conditions are modified by the use of different oxide thicknesses t_d.

It can be thus concluded that clamping-induced damping is made quantitatively neg-
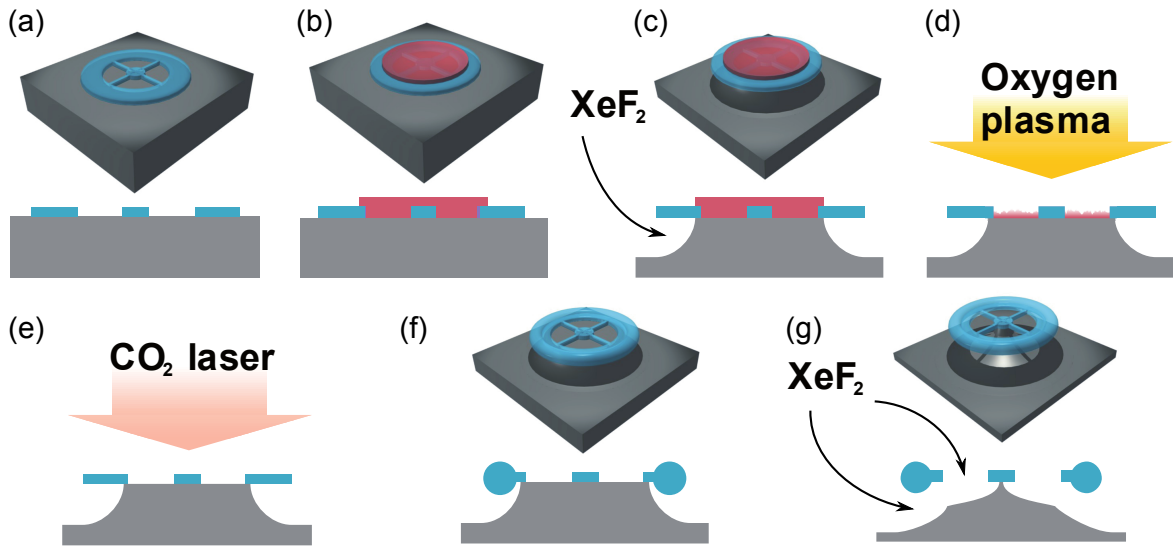
Figure 3.8: *Microfabrication steps of a spoke toroid, adapted from the fabrication steps of a normal toroid presented in appendix A.*

(a) After optical photolithography, the patterns of the spoke disks are chemically etched in the SiO_2 layer, eventually using a Süss MA6 mask aligner for its better imaging and pattern transfer performance compared to the MJB3 model. (b) A second photoresist pad is deposited onto the first etched structure, blanking the spoke openings. (c) The isotropic etching with gaseous XeF_2 pulses releases the outer rim, since the etching reactant is highly selective with both SiO_2 and photoresist. Contact between the outer rim and the formed silicon pillar is ensured by stopping the etching accordingly. (d) The remaining photoresist pad is thoroughly removed using cycles of acetone, isopropanol, DI water and oxygen plasma ashing. (e),(f) Using a CO_2 laser reflow technique, the toroid is formed according to the same principle as for normal toroids, as thermal contact of the melting region to the Si pillar is ensured (see appendix A). Previous considerations for the reflow process still hold. (g) A second train of XeF_2 pulses is applied, releasing the spokes without measurably affecting the toroid's optical properties. Adapted from Ref. [116].
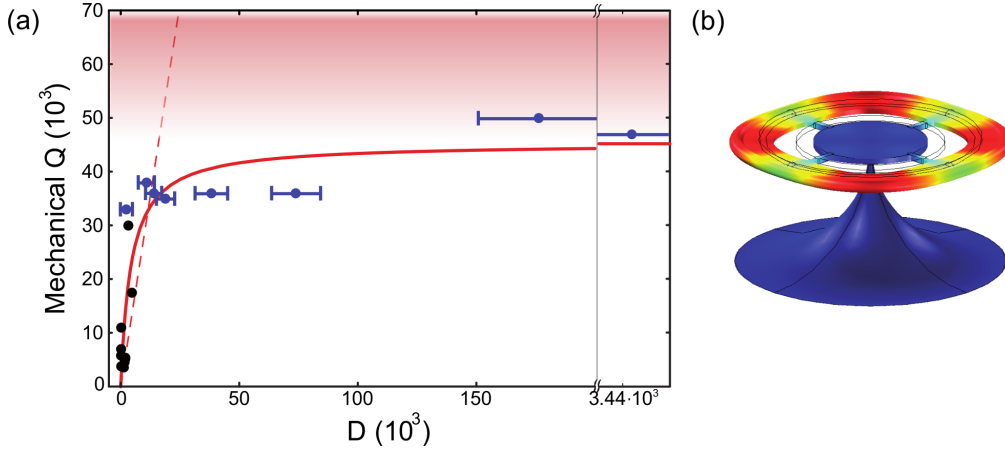
Figure 3.9: (a) Measured mechanical Q versus parameter D for spoke toroids (blue dots) and normal toroids (black dots). The dashed line represents the mechanical Q versus the parameter D as previously estimated. The experimental mechanical Q saturates to $Q_{\mathrm{m}} \simeq 50000$ as expected when material dissipation is taken into account. The horizontal error bars come from the uncertainty of the simulated D-parameter due to the deviations of the simulated geometry with reality. b) Displacement pattern of a geometrically-optimized spoke toroid simulated using FEM simulations, revealing the very low acoustic emission of the RBM to the central part. The simulated structure corresponds to the measured spoke exhibiting $Q_{\mathrm{m}} = 50000$ at 24 MHz. Adapted from Ref. [116]

ligible at room temperature compared to material damping, by using proper fabrication engineering assisted with numerical estimation of the clamping losses. It leaves the mechanical Q solely limited by material losses with values comparable with specifically designed oscillators, such as tensioned silicon nitride beams [129] for frequencies above 20 MHz. Importantly, this is achieved without affecting the optical quality factor of the optomechanical device. Other approaches to describe the clamping-induced damping consider the phonon tunneling through the pillar [130] and the destructive interference of the radiated mechanical waves [131]. Recently, experimental results in the context of optomechanics reported an equivalent numerical prediction and experimental mechanical Q of 51000 for a frequency around 2 MHz [132].

3.2.3 Material damping

Using a Peltier heater placed in the vacuum chamber directly underneath the chip, the temperature of a spoke toroid is varied from room temperature to 400 K. The measured Q_{m} then grows from 32000 to 80000 for a 38 MHz RBM [116]. This increase results from the temperature dependence of the material dissipations and their estimations reveal the following contributions at room temperature:

- *Network viscosity*: the mechanical wave modulates the thermally excited modes and therefore their effective temperature. Return to equilibrium with a finite delay is

responsible for material damping and stiffness [133]. This phenomenon can also be referred to as *anharmonicity* induced by the mechanical wave to the vibrational bath. It is shown that this is a limiting source of dissipation, on the same order of magnitude as two-level-system-induced losses [116].

- *Thermally activated relaxation of two-level system (TLS)*: the mechanical wave couples to the glass defects parametrized as energy TLS; delayed relaxation is responsible for damping and frequency shift [134].

Quantitatively, TLS-induced dissipation dominates at cryogenic temperatures. It is therefore thoroughly studied in this section. The three main regimes of dissipation, the thermally activated regime (TAR), the tunneling regime (TR) and the resonant interaction regime (RIR) are presented. Experimental data spanning from room temperature down to liquid ^{3}He temperatures are discussed, and the different contributions from the three damping mechanisms are detailed. The implementation of the cryogenic experiment using ^{4}He and ^{3}He technology is discussed in sections 3.4.1 and 3.4.7, respectively.

Two-level-system induced damping

The physics of the TLS in amorphous solids derives from the simplified model of the tunneling of an atom across a potential barrier. In 1927, the vibrational spectrum of amonia was explained by Hund from the quantum tunneling of the nitrogen atom from one position to the symmetric one across the plane formed by the three hydrogen atoms [135]. The atom occupies two energetically-similar positions separated by a potential barrier lifting the energy degeneracy. The energy diagram can therefore be described by a two-level system also referred to as a tunneling state. The same phenomenon was considered in solids by Pauling in 1930 [136] and in glasses in 1972, to explain the anomalous thermodynamical properties observed [137, 138]. This model is currently accepted for explaining the mechanical properties of glasses from cryogenic temperatures to room temperature and we present here the discussion from Enss and Hunklinger [139], focusing on silica.

In a theoretically perfect crystalline lattice of quartz (Fig. 3.10 (a)), each atom occupies only one site, corresponding to the coordinate where its energy is minimized. For vitreous silica however, due to the loss of long-range order, bonding angles may vary within the lattice. Consequently, atoms or groups of atoms can occupy several local energy-minimum positions, as depicted by A, B and C in Fig. 3.10 (b). Although simplified, this illustration still provides a clear picture of the phenomenon. The problem is parametrized by an energy TLS and the particle considered (which is not restricted by the model to be a unique atom) may tunnel through the potential barrier of height V between the two levels separated by a distance d and of initial energy asymmetry Δ_0 (Fig. 3.10 (c)). The corresponding tunnel energy splitting is given by

$$\Delta_1 = \hbar\Omega_1 e^{-\lambda}, \tag{3.7}$$

for the intrinsic oscillation angular frequency within the individual atomic sites Ω_1, and
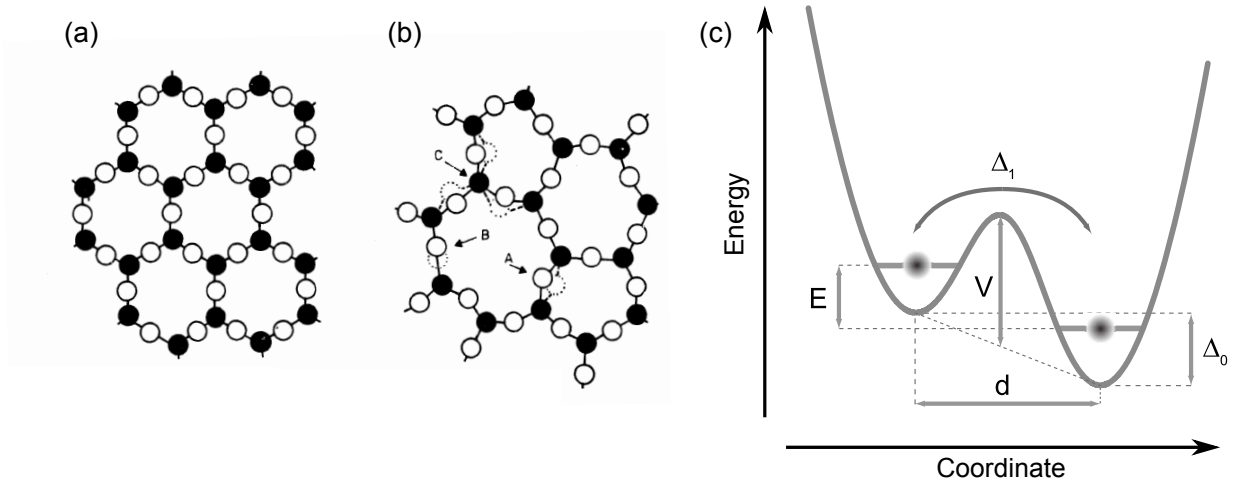
Figure 3.10: *2D structure of crystalline and glassy SiO_2 and two-level system configuration. (a) Crystalline structure of quartz. (b) Vitreous structure of silica in which atoms (A,B) or group of atoms (C) can occupy energetically-similar conformations. Adapted from Ref. [140]. (c) Each site is parametrized by a double-well potential, each well being separated by a distance d and shifted by an energy Δ_0. The potential barrier of height V is responsible for the tunneling coupling strength Δ_1 within the two sites of splitting energy levels E. Adapted from Ref. [55].*

with the corresponding tunneling parameter

$$\lambda \approx \sqrt{\frac{2mV}{\hbar^2}} \frac{d}{2}, \tag{3.8}$$

depending on the mass m of the tunneling particle. Due to the tunneling, the new eigenmodes of the coupled system exhibit an energy splitting of

$$E = \sqrt{\Delta_0^2 + \Delta_1^2}. \tag{3.9}$$

Strain fields deform the TLS potential, altering Δ_0 and Δ_1 in quantitative different ways and subsequently perturb the thermal equilibrium in the population of the two energy levels. Relaxation towards equilibrium occurs after a relaxation time τ and the delayed response yields a complex susceptibility of the medium, leading to a strain field velocity shift and attenuation. Electromagnetic fields also couple to TLS and are affected similarly.

For TLS in glasses, the main channel of relaxation is the coupling to thermal phonons. Transitions between the two levels are governed by different mechanisms as the temperature is varied:

- At high temperatures, thermally activated transitions between the two levels occur, involving many thermal phonons. The relaxation time follows the Arrhenius law for this *thermally activated regime*.

- For intermediate temperatures such as $k_B T \gtrsim E$, the thermal energy is generally too low for activating jumps, and the main transition mechanism is tunneling through the barrier V. This process is the *tunneling regime*.

- For low temperatures such as $k_B T \lesssim E$, the thermal energy is too low to induce the two relaxation processes previously described. Simultaneously, the population imbalance given by $\Delta N \propto \tanh\left(\frac{E}{2k_B T}\right)$ augments; therefore, direct resonant absorption of phonons of angular frequency $\Omega_m = E/\hbar$ is the main mechanism responsible for the transitions. Although not being a relaxation process, this transition mechanism is responsible for damping and shift of the speed of sound at very low temperatures.

General expression of the relaxation

If relaxation is the dominant process, the general expression of the mean free path of phonons is given by

$$l^{-1}(T) = \frac{1}{\rho c_s^3} \iint \left(-\frac{\partial n_0}{\partial E}\right) 4B^2 \frac{\Delta_0^2}{E^2} \frac{\Omega_m^2 \tau}{1 + \Omega_m^2 \tau^2} \bar{P}(\Delta_0, \lambda) \, \mathrm{d}\Delta_0 \, \mathrm{d}\lambda, \tag{3.10}$$

with

$$n_0 = \frac{1}{e^{E/k_B T} + 1} \tag{3.11}$$

being the Boltzmann repartition function, τ the relaxation time of the individual TLS, c_s the speed of sound, ρ the mass density of the solid and B is the coefficient linking a deformation δe to a change of E via $\delta E = 2B(\Delta_0/E)\delta e$. Because of the irregularity of the amorphous structure, a distribution of the different TLS potential parameters is introduced with $\bar{P}(\Delta_0, \lambda)$. This is the volume density of TLS with an energy asymmetry between Δ_0 and $\Delta_0 + \mathrm{d}\Delta_0$ and a with tunnel parameter between λ and $\lambda + \mathrm{d}\lambda$. The integration is performed on all interacting TLSs. The corresponding mechanical quality factor is given by

$$Q_m^{-1}(T) = \frac{c_s l^{-1}(T)}{\Omega_m}. \tag{3.12}$$

From the Kramers-Kronig relations, the change of the speed of sound is calculated and the corresponding shift in mechanical resonance frequency is given by

$$\delta\Omega_m(T) = -\frac{\Omega_m}{2\rho c_s^2} \iint \left(-\frac{\partial n_0}{\partial E}\right) 4B^2 \frac{\Delta_0^2}{E^2} \frac{1}{1 + \Omega_m^2 \tau^2} \bar{P}(\Delta_0, \lambda) \, \mathrm{d}\Delta_0 \, \mathrm{d}\lambda. \tag{3.13}$$

The frequency dependent terms in expressions (3.12) and (3.13) describe a Debye relaxator. Hence, the maximum damping is observed when the condition $\Omega_m \tau = 1$ is fulfilled.

The thermally activated regime

For silica glass and at the mechanical frequency of interest for the RBM (tens of MHz range), the dominant relaxation process is the thermally activated transition for temperature above 10 K. The relaxation time is given by [141, 134]

$$\tau_{\text{TAR}} \approx \tau_1 e^{V/k_\text{B}T}, \tag{3.14}$$

where τ_1 represents the period of oscillation in individual wells.

Fig. 3.11 shows the measurements of Q_m^{-1} and of the relative frequency shift $(\Omega_\text{m} - \Omega_0)/\Omega_0$ of two toroid RBMs, with Ω_0 arbitrarily measured, for a temperature range from room temperature down to 1.65 K. The inverse mechanical Q exhibits a significant increase of two orders of magnitude at a temperature $T \approx 50$ K, as expected from mechanical losses dominated by TLS relaxation in glass. The shape of the inverse mechanical Q curve can be interpreted from the temperature dependence of τ_{TAR}. When T is varied, the TLSs with potential barrier V satisfying the Debye relaxator condition $\Omega_\text{m}\tau_{\text{TAR}} = 1$ participate dominantly to the mechanical losses.
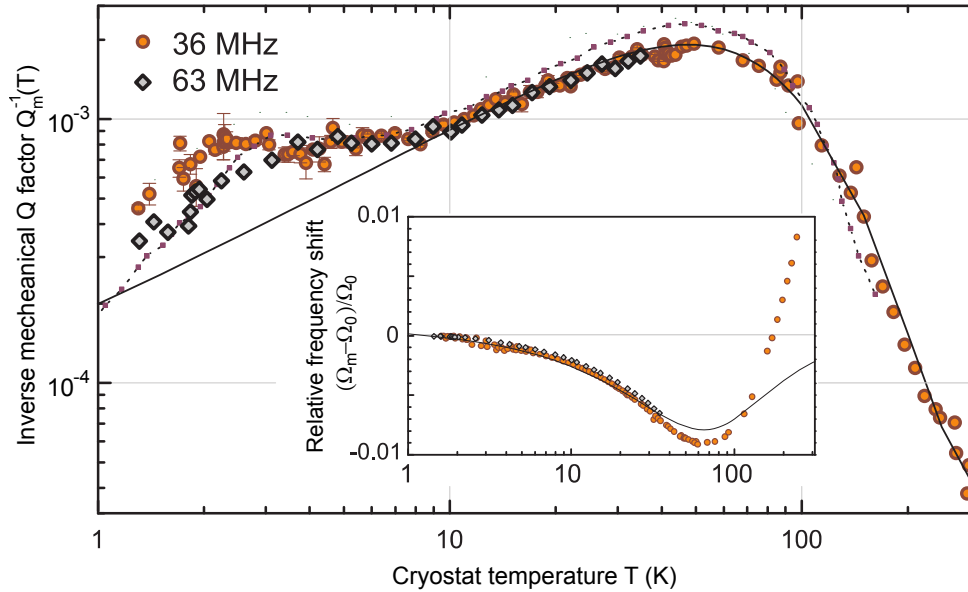
Figure 3.11: *TLS-induced variation of the inverse mechanical Q (main figure) and mechanical frequency (inset) from room temperature down to liquid ^4He temperature. The two figures show the experimental points measured from the radial breathing mode of two different toroids. The solid line of the main figure is a fit according to the expression of Q_m^{-1} (3.15). The data measured from Ref. [142] are superimposed on the graph, illustrating the quantitative correspondence with a dedicated acoustic wave attenuation experiment. The inset shows the corresponding relative frequency shift, where the solid line is a plot of the equation (3.17) using the same values as in the main figure. Adapted from Ref. [118].*

In the main part of Fig. 3.11, the solid line is a fit to the expression

$$Q_\text{m}^{-1} = Q_\text{clamp}^{-1} + Q_{\text{TAR}}^{-1}, \tag{3.15}$$

using only the inverse clamping Q as a fit parameter. The simplified expression of the inverse mechanical Q governed by thermally activated relaxation is [134]

$$Q_{\text{TAR}}^{-1} = C\Phi\left(\frac{\sqrt{2}k_{\text{B}}T}{\Delta_{\text{C}}}\right)\frac{1}{k_{\text{B}}T}\int_0^\infty \left(\frac{V}{V_0}\right)^{-\zeta} e^{-\frac{V^2}{2V_0^2}}\frac{\Omega_{\text{m}}\tau_1 e^{V/(k_{\text{B}}T)}}{1 + \Omega_{\text{m}}^2\tau_1^2 e^{2V/(k_{\text{B}}T)}}dV, \tag{3.16}$$

where $\Phi(z)$ is the error function $\Phi(z) = \frac{2}{\sqrt{\pi}}\int_0^z e^{-x^2}dx$ and C the tunneling strength. The TLS potential parameter distributions are simplified and Δ_{C} and V_0 are introduced as the asymmetry cutoff value and the potential barrier cutoff value respectively [134]. The values of τ_0, V_0, V_0/Δ_{C}, ζ and C given in this article are directly used in the fit of Fig. 3.11. The agreement above $10\,\text{K}$ proves that Q_{m} can be quantified using the presented model in this temperature range.

The associated frequency shift is given by

$$\delta\Omega_{\text{TAR}} = -\frac{\Omega_{\text{m}}C}{2}\Phi\left(\frac{\sqrt{2}k_{\text{B}}T}{\Delta_{\text{C}}}\right)\frac{1}{k_{\text{B}}T}\int_0^\infty \left(\frac{V}{V_0}\right)^{-\zeta} e^{-\frac{V^2}{2V_0^2}}\frac{1}{1 + \Omega_{\text{m}}^2\tau_1^2 e^{2V/(k_{\text{B}}T)}}dV. \tag{3.17}$$

Although fitting correctly at low temperature, the evident failure at temperature above $\sim 30\,\text{K}$ comes from the previously introduced network viscosity contribution that is not included in the model.

The tunneling regime

Below $10\,\text{K}$, the thermal activation of TLS transitions decreases. The level transition process is here dominated by the tunneling of the particle through the barrier at temperatures between $\sim 0.1\,\text{K}$ and $\sim 10\,\text{K}$ for frequencies of tens of MHz. In this regime, the relaxation time is

$$\tau_{\text{tun}} = \tau_{\text{m}}\frac{E^2}{\Delta_1^2}, \tag{3.18}$$

with the (inverse) maximum relaxation rate

$$\tau_{\text{m}}^{-1} = \frac{3}{c_{\text{s}}^5}\frac{B^2}{2\pi\rho\hbar^4}E^3\coth\left(\frac{E}{2k_{\text{B}}T}\right). \tag{3.19}$$

Parametrizing expressions (3.12) and (3.13) in terms of energy splitting E and parameter $u = \tau_{\text{tun}}^{-1}/\tau_{\text{m}}^{-1}$ yields [139, 143]

$$Q_{\text{tun}}^{-1}(T) = \frac{2\bar{P}B^2}{\rho c_{\text{s}}^2}\int_0^\infty \left(-\frac{\partial n_0}{\partial E}\right)\Omega_{\text{m}}\tau_{\text{m}}\int_0^1 \frac{\sqrt{1-u}}{u^2 + \Omega_{\text{m}}^2\tau_{\text{m}}^2}\,du\,dE \tag{3.20}$$

and

$$\delta\Omega_{\text{tun}}(T) = -\frac{\Omega_{\text{m}}\bar{P}B^2}{\rho c_{\text{s}}^2}\int_0^\infty \left(-\frac{\partial n_0}{\partial E}\right)\int_0^1 \frac{u\sqrt{1-u}}{u^2 + \Omega_{\text{m}}^2\tau_{\text{m}}^2}\,du\,dE,$$

where it is assumed that $\bar{P}(E,\lambda) = \bar{P}$ is constant, which is experimentally consistent.

Two asymptotic behaviors can be distinguished:

- for T of typically a few kelvin, $Q_{\mathrm{tun}}^{-1}(T)$ is independent of T and follows a plateau value given by

$$Q_{\mathrm{plateau}}^{-1} = \frac{\pi}{2} \frac{\bar{P}B^2}{\rho c_{\mathrm{s}}^2}. \tag{3.21}$$

In this temperature range, there is always a significant amount of TLSs satisfying the Debye relaxator condition.

- for T lower than typically a few kelvin however, the condition $\Omega_{\mathrm{m}}\tau_{\mathrm{m}} \gg 1$ holds and the mechanical absorption therefore decreases with T, yielding [143]

$$Q_{\mathrm{slope}}^{-1} \approx \frac{9\zeta(3)}{\pi} \frac{\Omega_{\mathrm{m}}\bar{P}B^4}{\rho^2 c_{\mathrm{s}}^7 \hbar^4} \left(k_{\mathrm{B}}T\right)^3, \tag{3.22}$$

with $\zeta(s)$ being the Riemann zeta function of s. Notably, the inverse Q factor exhibits a cubic temperature dependence. This justifies going from a commercial ^{4}He cryostat (base temperature of $\sim 1.65\,\mathrm{K}$) to a ^{3}He cryostat (operated at a temperature of $\sim 0.85\,\mathrm{K}$) as an improvement of more than three for a mechanical Q solely limited by TLS losses is reachable.

Figure 3.12 shows the measurement of the inverse Q and the relative mechanical frequency for a span of temperatures addressing the TR and the RIR for $\Omega_{\mathrm{m}}/(2\pi) = 76.3\,\mathrm{MHz}$. The fit model is

$$\Omega_{\mathrm{m}}(T) = \Omega_{\mathrm{upt}} + \delta\Omega_{\mathrm{tun}}(T) + \delta\Omega_{\mathrm{res}}(T), \tag{3.23}$$
$$Q_{\mathrm{m}}^{-1}(T) = Q_{\mathrm{cla}}^{-1} + Q_{\mathrm{tun}}^{-1}(T) + Q_{\mathrm{res}}^{-1}(T), \tag{3.24}$$

where Ω_{upt} is the unperturbed angular frequency in the absence of TLS-induced effects, and $Q_{\mathrm{res}}^{-1}(T)$ and $\delta\Omega_{\mathrm{res}}(T)$ are the contributions from the RIR expressed in Eqs. (3.25) and (3.26), respectively. For the frequency shift, the resonant interaction contribution dominates up to $\sim 2\,\mathrm{K}$ whereas it plays a minor role on the inverse Q thermal dependence. Since the effects are governed by two different regimes, one expects two different densities of contributing TLSs interceding in the dissipation and the frequency shift. The fit to the data then gives for the mechanical Q: $\bar{P}_{Q_{\mathrm{m}}} = 4.6 \times 10^{45}\,\mathrm{m}^{-3}$ and for the frequency shift: $\bar{P}_{\Omega_{\mathrm{m}}} = 2.5 \times 10^{45}\,\mathrm{m}^{-3}$ with $B = 1.1 \times 10^{-19}\,\mathrm{J}$, showing reasonable agreement with values given in the literature [144].

The resonant interaction regime

What has been presented up to now in term of TLS damping is a relaxation mechanism. When working at lower temperatures or higher oscillation frequencies, the relaxation contribution is reduced so that one can observe the regime where the phonons resonantly interact with a few TLSs. This is called the resonant interacting regime, and corresponds to a situation where the phonon energy is close to the TLS energy so that coherent processes take place. This has been first observed and subsequently widely studied in the field
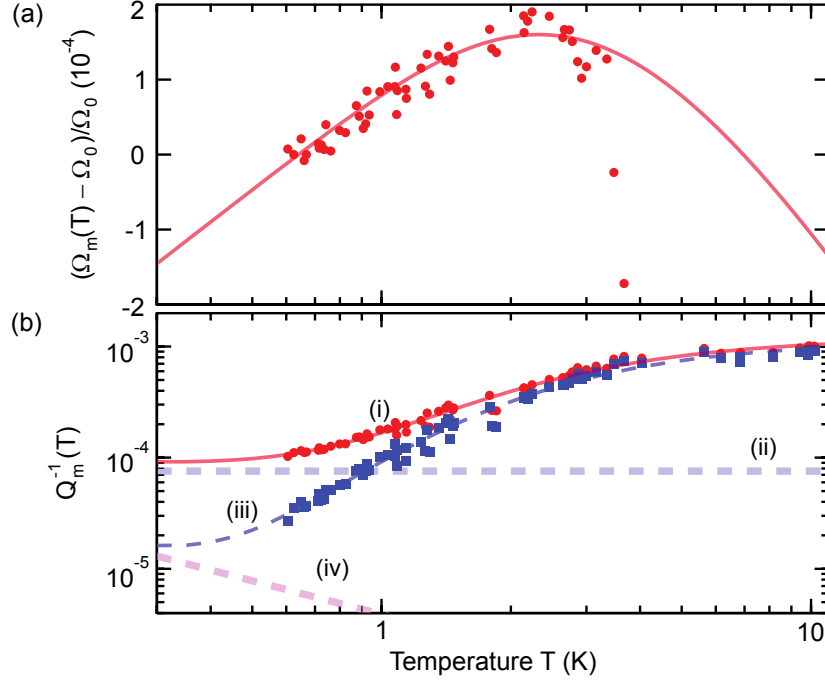
Figure 3.12: *Variation of mechanical frequency (a) and inverse mechanical Q (b) from 10 K down to liquid ^{3}He temperature due to TLS for a 76.3 MHz toroid. Solid lines are uncoupled fits of the model (3.23) and (3.24). The agreement holds in the tunneling and resonant regime. The temperature-independent Q_{clamp}^{-1} extracted from the fit is plotted in line ii). Its subtraction from measured data yields to the possible damping limited solely by TLS-induced effect, materialized by the squares and by the line iii). At temperatures below the ones shown, damping by resonant interaction with TLS (line iv) becomes dominant. Ω_0 is measured at the temperature $T = 620\,mK$. Adapted from Ref. [55].*

of acoustic wave propagation in amorphous medium [139]. This interaction is responsible for an additional damping term as well as a modified frequency shift, whose expressions are given by:

$$Q_{\text{res}}^{-1}(T) = \frac{\pi \bar{P} B^2}{\rho c_{\text{s}}^2} \tanh \left(\frac{\hbar \Omega_{\text{m}}}{2 k_B T} \right) \tag{3.25}$$

$$\delta \Omega_{\text{res}}(T) = \frac{\Omega_{\text{m}} \bar{P} B^2}{\rho c_{\text{s}}^2} \ln \left(\frac{T}{T_0} \right), \tag{3.26}$$

where T_0 is a reference temperature. Note that the damping term increases when working at lower temperatures or higher frequencies, which is due to the increased population imbalance between the two states of the TLS resonantly interacting. The logarithmic frequency shift is clearly visible in Fig. 3.13, which suggests that resonant interaction have to be considered in our experiments. Importantly, it is possible to saturate the TLSs with phonons, and finally equilibrate the populations of the two levels, thus reducing the
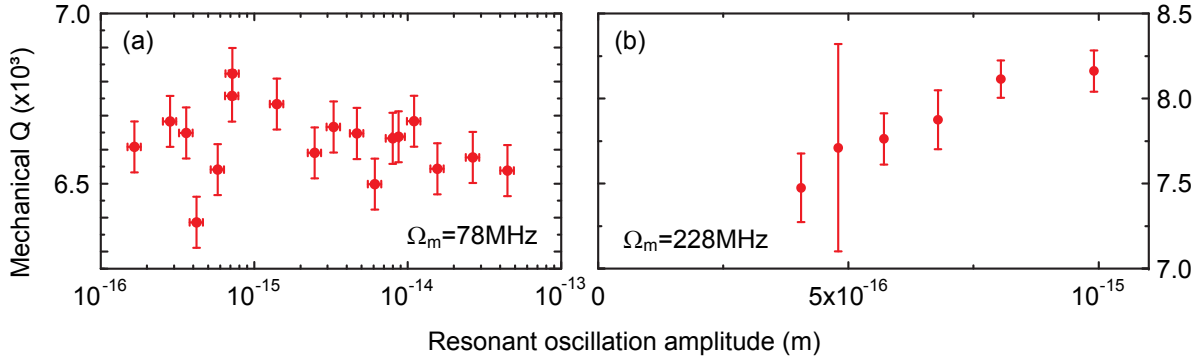
Figure 3.13: *Mechanical Q versus resonant driving for a 1st (a) and 3rd-oder (b) mechanical RBM at 0.6 K. Vertical error bars correspond to the fitting uncertainty, horizontal error bars to the displacement calibration error. The increase of mechanical Q at high frequency is attributed to a saturation phenomenon from the mechanical drive.*

resonant phonon absorption. One then expects to observe an increase of the mechanical quality factor when increasing the driving amplitude of the system, as it has been observed in acoustic waves propagation. This would represent a signature of coherent mechanical interaction between the oscillator and the TLS.

For higher mechanical frequencies, the population imbalance for a given temperature is higher. For a 228 MHz 3rd-order mechanical RBM at 0.6 K, the resonant contribution on the mechanical Q is expected to have the same order of magnitude as the tunneling contribution. It is estimated to account for $\sim 10\%$ of the measured Q_{m}^{-1} [145]. By coherently driving the mode, it is possible to augment the TLS excitation and to populate the excited level until reaching equal population, or saturation of the TLS. The contribution on the mechanical dissipation then decreases.

Figure 3.13 compares the mechanical Q values of two oscillators at 78 (a) and 228 MHz (b) subjected to a coherent drive. The mechanical Q of the 78 MHz oscillator does not visibly change over 3 orders of driving magnitude, the material dissipations being here dominated by the tunneling regime. When reproducing this measurement on the higher frequency mode (228 MHz), one can observe a trend in which the mechanical quality factor increases with the driving amplitude, as expected from resonant TLS interaction. Note that additional measurements will be necessary to confirm this observation. However, both the saturation amplitude and the change in mechanical damping are of the same order of magnitude as theoretically expected [143]. The ultra-low amplitude at which one expects to see the saturation underlines the difficulty of this experiment and the degree of control required. For the 228 MHz mode, the theoretical estimation shows that the resonant oscillation amplitude required to saturate the TLSs corresponds to the observation [145].

The description of the TLS model in glass gives here a complete characterization of the mechanical dissipation (and dispersion) at the temperature range of interest. The strong thermal dependence described here will prove to be an extra tool to characterize the increase of temperature due to intracavity light absorption [55]. This "TLS thermometer" provides

an additional way to estimate the mechanical mode temperature, since localized heating consecutive to light absorption is difficult to estimate using conventional thermometers. In addition, by going to lower temperatures or higher mechanical frequencies, it is possible to study the resonant interaction of a phonon with a TLS and to perform similar experiments as in electrodynamics: population saturation [146] and phonon echoes [147].

3.3 The resolved-sideband regime

In the classical picture, the phonon occupancy can be reduced to arbitrarily low values by simply increasing the red-detuned input field $\bar{s}_{\mathrm{in}}$ and thus maximizing the optical damping effect. However, when reaching low phonon occupancy $\bar{n}$ the quantum optical noises interfering in the process significantly influence the cooling dynamics and have to be considered. Ultimately, they are responsible for the minimum occupancy expressed in Eq. (1.57) at optimum detuning. The limit imposed by quantum backaction on the phonon occupancy is minimized in the resolved-sideband (RSB) regime where the oscillation angular frequency Ω_{m} strongly exceeds the cavity decay rate κ [12, 14, 13].

In this section, it is experimentally demonstrated that laser cooling in a microtoroidal cavity is performed in this regime. Although measuring a large optical damping in this experiment, the occupancy achieved is limited by the classical noise in the cooling diode laser. To avoid this, we use for the rest of the cooling work a Ti:sapphire laser exhibiting quantum-noise limited operation at the experimental parameters of interest.

Reduction of the required intracavity power

Fig. 3.14 illustrates the technical advantage of performing cooling in the RSB regime. The plotted curve shows the normalized average intracavity photon number $\bar{a}^2$ required to cool an optomechanically coupled mechanical oscillator down to $\bar{n} = 1$ versus the RSB factor $\Omega_{\mathrm{m}}/\kappa$. The detuning is always taken optimum as expressed in Eq. (1.56). An increase of the RSB factor results in a significant decrease of the required intracavity photon number, for the same phonon occupancy achieved. Unavoidable non-linearities consequent to high intracavity intensities are then strongly reduced. Heating due to intracavity absorption by the silica toroid is also lowered and its influence on the final phonon occupancy reduced accordingly. This aspect is particularly important when thermalizing the sample in a cryostat with cooling power on the order of a mW. At $\Omega_{\mathrm{m}}/\kappa \approx 0.18$, the divergence shows that quantum backaction prevents cooling down to a phonon occupancy $\bar{n} = 1$.

Experimental demonstration of the resolved-sideband regime

The study pursued in chapter 2 reveals that typical silica microtoroids can reach a RSB factor of more than 10. In this configuration, the reduction of the phonon occupancy by dynamical backaction cooling saturates to $\bar{n}_{\mathrm{min}}(\Delta_{\mathrm{opt}}) < 10^{-3}$. To experimentally prove this regime, the transmission spectrum of a vibrating microtoroidal cavity is recorded.

From the equation of motion of the intracavity field, the output field is first calculated using the theoretical framework introduced in chapter 1. For an intense coherent input field, the quantum operators introduced are identified with their expectation values and the noise terms are dropped. For simplicity, the time evolution of the mechanical displacement is considered sinusoidal:

$$x(t) = x_0 \sin\left(\Omega_{\mathrm{m}} t\right). \tag{3.27}$$
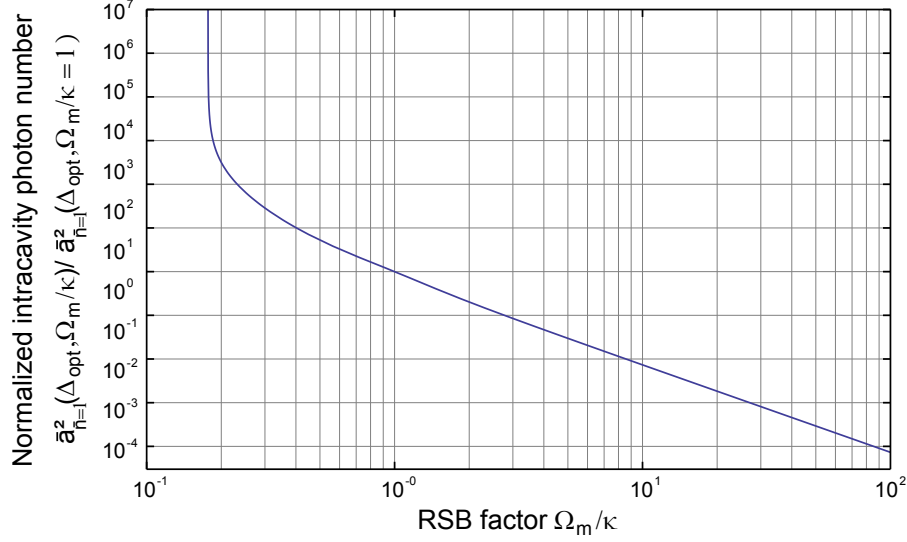
Figure 3.14: *Normalized mean intracavity photon number required to obtain a cooling to an occupancy $\bar{n} = 1$ versus resolved-sideband factor Ω_m/κ. The cavity is pumped at optimum detuning, ensuring the lowest input power.*

The equation of motion of the intracavity field is

$$\dot{a}(t) = \left(-i\omega_\mathrm{c} - \kappa/2 - iGx_0\sin\left(\Omega_\mathrm{m}t\right)\right)a(t) + \sqrt{\eta_\mathrm{c}\kappa}\bar{s}_\mathrm{in}e^{-i\omega_\mathrm{l}t}. \tag{3.28}$$

The solution is then given by [117]

$$a(t) = \sqrt{\eta_\mathrm{c}\kappa}\bar{s}_\mathrm{in}\sum_{n=-\infty}^{+\infty}\frac{i^nJ_n(\beta)}{-i(\Delta - n\Omega_\mathrm{m}) + \kappa/2}e^{-i(\omega_\mathrm{l} - n\Omega_\mathrm{m})t - i\beta\cos(\Omega_\mathrm{m}t)}, \tag{3.29}$$

after a time $t \gg \kappa^{-1}$ allowing for intracavity field build-up, with $\beta = \frac{\omega_\mathrm{c}}{R}\frac{x_0}{\Omega_\mathrm{m}} = -G\frac{x_0}{\Omega_\mathrm{m}}$ being the modulation factor used in the Jacobi-Anger expansion and J_n being the Bessel function of the first kind and of index n.

The output field is measured with a photodetector giving a signal proportional to

$$|s_\mathrm{out}|^2 = |\bar{s}_\mathrm{in}e^{-i\omega_\mathrm{l}t} - \sqrt{\eta_\mathrm{c}\kappa}a(t)|^2. \tag{3.30}$$

The signal is filtered with a low-pass filter of bandwidth much lower than the mechanical frequency $\Omega_\mathrm{m}/(2\pi)$. Thus, only the DC terms are kept in expression (3.30) in which expression (3.29) is integrated. The measured signal is then proportional to [20]

$$|s_\mathrm{out}|^2_\mathrm{DC} \propto |\bar{s}_\mathrm{in}|^2\sum_{n=-\infty}^{+\infty}\frac{J_n^2(\beta)}{(\Delta - n\Omega_\mathrm{m})^2 + (\kappa/2)^2}. \tag{3.31}$$

The measured transmission spectrum is a symmetric succession of motional sidebands of individual linewidth κ equally spaced by Ω_m. The relative weight of the sidebands is determined by the modulation index β.

For a mechanical oscillator thermally driven at room temperature, the oscillation amplitude is small enough to consider $\beta \ll 1$ and to neglect terms in (3.29) in order of β higher than 1. Taking $J_0(\beta) \approx 1$ and $J_{\pm 1}(\beta) \approx \pm \beta/2$, the intracavity field can thus be expanded into

$$a(t) = \sqrt{\eta_c \kappa} \bar{s}_{\text{in}} \frac{1}{-i\Delta + \kappa/2} e^{-i\omega_l t}$$
$$+ \sqrt{\eta_c \kappa} \bar{s}_{\text{in}} \frac{\beta \Omega_m/2}{-i\Delta + \kappa/2} \left(\frac{e^{-i(\omega_l - \Omega_m)t}}{-i(\Delta - \Omega_m) + \kappa/2} - \frac{e^{-i(\omega_l + \Omega_m)t}}{-i(\Delta + \Omega_m) + \kappa/2} \right). \qquad (3.32)$$

The vibrating cavity builds up a pair of Stokes and anti-Stokes sidebands in the intracavity field at $\omega_l - \Omega_m$ and $\omega_l + \Omega_m$ that are weighted by the cavity Lorentzian profile.

Interestingly, the relative weights of the sidebands in the recorded output signal power is analog to the relative scattering rates of the sidebands introduced in section 1.2.9 for $\bar{n} \gg 1$. As described previously, this analogy breaks down for low phonon occupancy ($\bar{n}$ on the order of smaller than 1) and the deviation from the classical case is a direct proof of the quantum aspect of the mechanical oscillator.

Figure 3.15 shows the transmission spectrum of a toroid recorded with a scanning diode laser of low input power. The cavity is subjected to another strong blue-detuned laser to amplify the mechanical oscillations as described in section 1.2.8. The input field is kept above the threshold given by expression (1.60) to ensure coherent self-oscillation of the mechanical oscillator. Clearly, the sidebands are resolved, proving that experimentally the optomechanical system is in the RSB regime.

Next, dynamical backaction cooling is performed on another sample exhibiting a RSB factor of 7. At an input power $P_{\text{in}} = \hbar\omega_l |\bar{s}_{\text{in}}|^2 = 2.7\,\text{mW}$, an effective damping of $\Gamma_{\text{eff}} = 2\pi \times 1.56\,\text{MHz}$ is achieved on a radial breathing mode of intrinsic damping $\Gamma_m = 2\pi \times 1.3\,\text{kHz}$ (needle-pillar toroid in vacuum) [117]. Due to the high RSB factor, this is achieved with a small fraction of intracavity power. It is then estimated that the environmental temperature of the sample is not affected by absorption induced heating. Simply calculating the resulting phonon occupancy $\bar{n} \simeq \bar{n}_m \Gamma_m / \Gamma_{\text{eff}}$ gives an average final occupancy of less than 200, starting from room temperature. Measurements reveal however a much higher final occupancy of 5900. A detailed analysis reveals that the diode laser [148] used for cooling carries excess classical frequency noise at the Fourier frequency of interest. The resulting intracavity radiation pressure fluctuations act as a source of *classical* backaction responsible for an extra heating of the mechanical oscillator during the cooling process. To avoid this effect, the cooling is performed in the following with a Ti:sapphire laser with quantum limited fluctuations.

Quantum limited laser: Ti:sapphire laser

The continuous-wave Ti:sapphire laser used in this work exhibits shot-noise limited operation [149, 150] for both field quadratures, for Fourier frequencies above $1\,\text{MHz}$ and for the power of interest on the order of the mW, as experimentally measured. The long-range
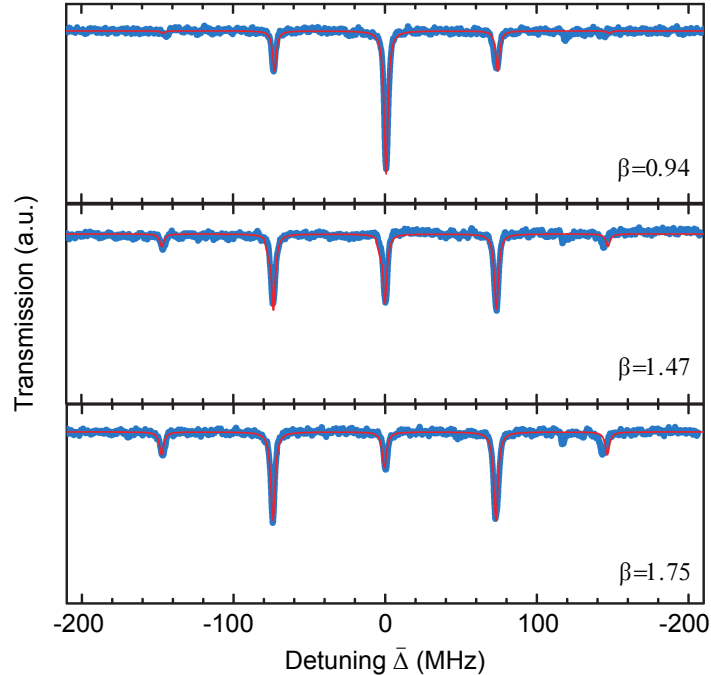
Figure 3.15: *Motional sidebands on the transmission spectrum of a toroidal cavity subjected to an external 1064 nm-Nd:YAG blue-detuned laser (amplification regime beyond the self-oscillation power threshold). The blue points are experimental data recorded from DC photodetection of the transmission of a scanning diode laser. The red line is a fit of the model (3.31) with the modulation index β as free parameter. The linewidth of each motional sideband is κ and the spacing is Ω_{m}, thus illustrating the deep RSB factor of more than 20 of this optomechanical system. Mechanical frequency: $\Omega_{\mathrm{m}}/(2\pi) = 73.5$ MHz, optical linewidth: $\kappa/(2\pi) = 3.2$ MHz. Adapted from Ref. [117].*

tunability makes the laser additionally convenient for probing toroidal cavities with a large free spectral range of ~ 2.5 nm at wavelengths close to 780 nm.

Figure 3.16 depicts the optical layout of the laser. Because of the homogeneous broadening of the gain medium, the laser oscillation is single-mode. The strongest mode imposes itself and a set of cascaded optical filters (birefringent filter, thin étalon and thick étalon, successively) selects the desired longitudinal mode. Due to the broadband gain of the Ti:sapphire crystal, the wavelength of the emitted mode can be selected within the span allowed by the optics set (750 nm to 870 nm). Two piezoelectrically positionable mirrors (slow and fast PZT) and an electro-optical modulator (EOM) are used for fast wavelength actuation, spanning up to 30 GHz without readjustment of the mode-selective components.

Both analog and digital locking of the frequency-selecting parts proved to be robust in a normal laboratory environment including acoustically noisy devices such as vacuum pumps. Using the slow and fast PZT and the EOM, the output TEM$_{00}$ mode can be locked to the resonance of a stable reference cavity (finesse of $\sim$300) to reduce its drift and its linewidth down to 50 kHz rms [151].
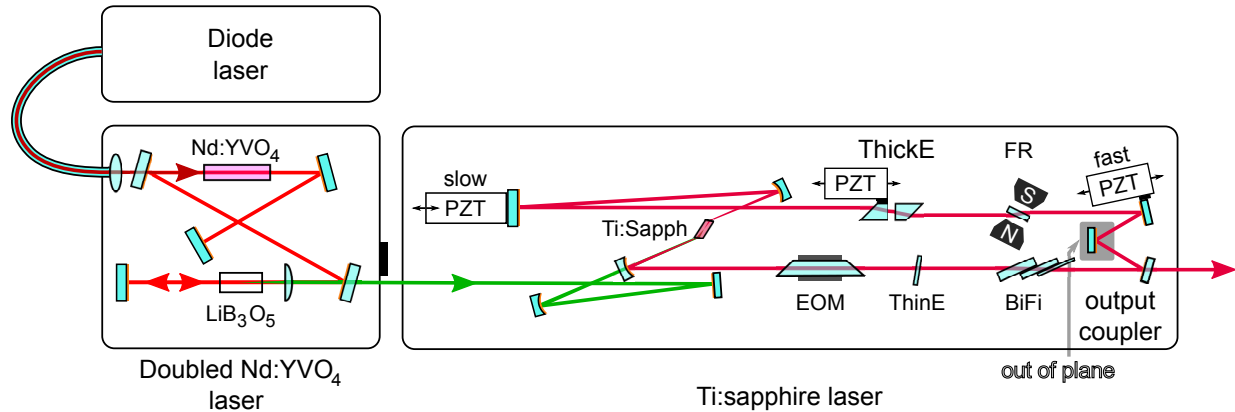
Figure 3.16: *Optical layout of the quantum-limited Ti:sapphire laser used in the experiment. The Ti:sapphire crystal is pumped with a 1064 nm light from a $Nd:YVO_4$ crystal that is frequency doubled to 532 nm using a LiB_3O_5 (or LBO) crystal outputting 6 W (Spectra Physics Millenia 6s laser). The $Nd:YVO_4$ crystal is pumped with a diode laser. The present configuration allows optical output of a TEM_{00} at a wavelength comprised between 750 and 870 nm, at a maximum output power of 800 mW. The length of the Ti:sapphire cavity is adjusted using the slow and fast piezoelectric positioners (PZT) to displace the mirrors. The single longitudinal mode is selected successively by the birefringent filter (BiFi or Lyot filter), the thin étalon (ThinE) and the thick étalon (ThickE), that are mechanically controlled. Spatial hole burning is avoided by favoring one propagation direction in the ring cavity using a Faraday rotator (FR) and the out of plane mirror acting as an polarization selective element. Fast actuation of the optical path is provided by an extra electro-optic modulator (EOM) of large bandwidth compared to piezoelectrically transduced actuators. Adapted from Ref. [151].*

It can then be concluded that due to the high resolved-sideband factor of the toroidal microcavities and to the quantum noise limited laser used for the cooling, limitations from the classical and quantum backaction of the cooling field are reduced down to a negligible level.

3.4   Reduction of the environmental temperature

Placing the optomechanical system in a cryogenic environment is a straightforward way to lower its phonon occupancy by more than two orders of magnitude. Exploiting the mature technology of cryogenics to reduce the bath occupation $\bar{n}_\mathrm{m}$ constitutes a leap towards the ground state, without jeopardizing benefits from laser cooling.

Placing a toroidal microcavity in a cryostat, thermalizing it to its base temperature of $1.65\,\mathrm{K}$ and coupling light using a tapered fiber is an endeavor that was first accomplished in our group. Additionally, only few studies [68, 152] have been performed on the behavior of silica whispering-gallery mode microresonators at cryogenic temperatures. The technical success of this implementation at low temperatures therefore allows the study of unexplored domains that reveals intriguing optical properties of silica resonators.

In this section, the *prototype* cryostat using ^{4}He as a coolant is presented, along with the technical modifications on the cryohead hosting the toroidal cavity and the coupling device: indeed, the fiber taper coupling technique used at room temperature is modified to a *cryotaper*. Next, the dispersive and thermodynamical properties of the silica microtoroids are quantified and the laser cooling down to an occupancy of 63 ± 20 is presented. Finally, motivated by the studies of the mechanical properties of silica described in section 3.2.3 and the success of the developed prototype setup, the final *experimental* ^{3}He cryostat is constructed, with its details and performances being described here.

3.4.1   The prototype helium-4 cryostat

A previous unsuccessful attempt to thermalize a $4.5\,\mu\mathrm{m}$ AlGaAs microdisk to the base pressure of a ^{4}He continuous flow cryostat [153] was convincing enough to consider implementing our experiment in a cryostat of larger cooling power. This poor performance was attributed to the low heat extraction mechanism from the sample placed in high vacuum, based on thermal conduction through the supporting structure attached to a "cold finger". Even by enlarging the thermal anchoring to the cooled part of the cryostat using copper braids, the effective cooling power on the sample was too small in this case to ensure efficient thermalization. In our case, the shaping of the supporting disk of the toroid to spokes in our case further reduces the thermal anchoring of the hot spot being here the modal volume in which the intracavity light is absorbed. Consequently, another paradigm is used for cryogenically cooling our sample, based on thermalization to a low pressure *exchange* gas, itself cooled by the cryogenic device. A gas pressure on the order of $1\,\mathrm{mbar}$ is used since it has been demonstrated in section 3.2.1 that at this pressure range, the gas does not damp the mechanical oscillator.

The cryostat

The prototype cryostat is a low-pressure ^{4}He exchange gas cryostat based on Oxford Instrument OptistatSXM. The cooling process is named *static* exchange gas cooling since the volume into which the cryoprobe is inserted is not subjected to any gas circulation apart

from unavoidable gas convection. This class of device provides a cooling power exceeding a mW and the generated vibrations are low enough to perform sensitive experiments such as atomic force microscopy.

Figure 3.17 shows an on-scale simplified drawing of the cryostat. This device does not have a liquid N_2 shield as a first cooling stage because it would be a source of extra vibrations due to the boiling of the liquid nitrogen (according to the manufacturer). Instead, radiation shields made of a stack of insulating layers are directly cooled by the exhaust gas from the 4.3-L liquid ^{4}He tank.

From this reservoir, the *cooling* liquid ^{4}He is admitted into a capillary tube through a needle valve that allows very fine control of the liquid's flux and therefore of the cooling power of the cryostat. The coolant is then circulated using a rotary pump (Oxford Instrument EPS40) of $40\,\mathrm{m}^3$/h and evaporated at an adjustable rate, thus adjusting the vapor pressure, the working temperature and the cooling power of the cryostat. The heat is extracted by the flux of *cooling* helium from the experimental chamber via the heat exchanger. Thereafter, the evaporated *cooling* ^{4}He gas is pumped away. Inside the experimental chamber, the *exchange* ^{4}He gas thermalizes the sample with the chamber's cooled walls. By using a built-in electric heater and a temperature sensor, the cryostat temperature is locked to $\pm 0.1K$ accuracy over 10 min for the temperature range of interest down to $1.65\,\mathrm{K}$.

The specific mechanical construction provided by the manufacturer ensures low vibration level of the whole device. In addition, because of its rather small size (82 cm to the top of the experimental tube), the cryostat is placed on a usual optical table and benefits from its acoustic isolation. To cut off extra vibrations from the rotary pump, the connecting hose is firmly clamped to the ground.

Two separated vacuum circuits are connected to the setup: one for pumping the insulation vacuum prior to cool down and another one to regulate the pressure of the *cooling* and *exchange* ^{4}He gas. For the former, an oil filter is added to the rotary pump (Leybold D16B) to avoid contamination via diffusion. The simplified piping presented in Fig. 3.17 allows to fill the experimental chamber with *exchange* ^{4}He gas directly from the evaporation port of the capillary tube, therefore providing a very pure source of gas. This technique avoids the contamination of the chamber with unwanted gases such as H_2O or N_2 that may freeze on the sample and deteriorate its properties. Eventually, frozen contaminants can be sublimated by pointing a 5 W Coherent Verdi laser (532 nm) directly onto the sample through the optical windows of the cryostat.

A set of mechanical, Pirani and capacitance gauges monitors the relevant pressures. The latter (Pfeiffer CMR 361) is the most precise utilized to record the environmental pressure of the sample under study.

Under the normal conditions presented in Appendix C, the holding time of the cryostat is ∼8 h at a temperature around $4.2\,\mathrm{K}$. Prior to cool down, careful purging of the cooling circuit must be performed with gaseous ^{4}He filtered using a liquid N_2 trap to avoid icing the fragile needle valve. Below $4.2\,\mathrm{K}$, excellent temperature stability is reached solely using the needle valve opening to regulate the pumping pressure of the dry rotary pump.
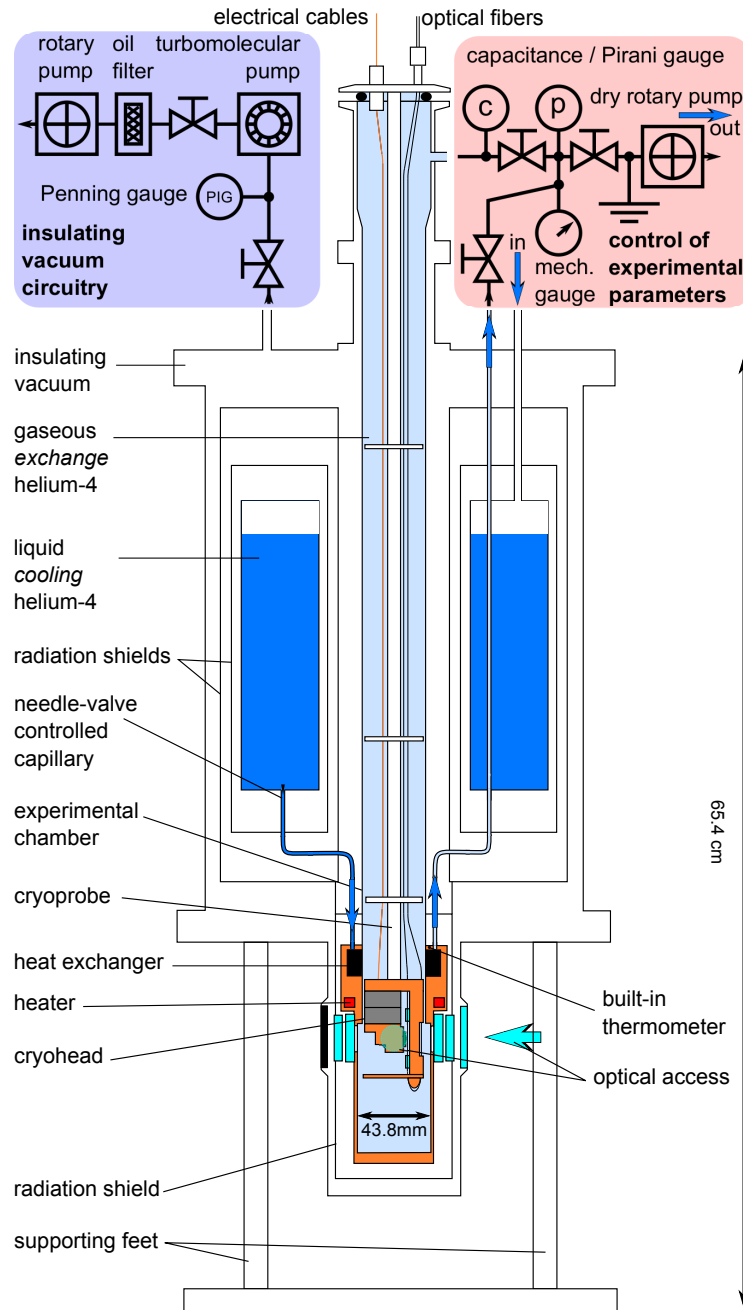
Figure 3.17: *Technical layout of the helium-4 cryostat describing the commercial Oxford Instrument OptistatSXM static exchange gas cryostat (on scale), the modified top-loading cryoprobe, the optical fiber and electrical cable layout, the optical access and the simplified vacuum circuit.*

The cryohead

This cryostat model is designed to host microscopy experiments. To adapt it to our configuration involving a silica microtoroid coupled with a tapered fiber, specific engineering was required.

The cryoprobe already shown in Fig. 3.17 is a probe from the manufacturer, modified to host the cryohead comprising the whole coupling setup (Fig. 3.18). It is compacted to fit into the experimental chamber of diameter 43.8 mm. To avoid that elements of the head vibrate under excitation from the rotary pumps, the cryohead is specifically designed in a compact way, avoiding floppy mechanical elements of low resonance frequencies. The present design proves to be outstandingly stable and coupling can be successfully performed in an acoustically noisy laboratory environment.

Figures 3.18 (a) and (b) show a photograph and a 3D rendering of the cryohead, respectively. The sample is clamped using a mechanical claw onto a holder that can be smoothly slided and attached to the piezoelectric displacers without risk for the nearby cryotaper. Opposite to the sample chip, the cryotaper (detailed in the next section) is attached to a mechanical slide that allows adjusting the position to ensure proper phase-matching (see section 2.2.4) prior to cooling, by scanning longitudinally the taper region until finding the correct position. Under normal experimental conditions, it does not need further adjustment at low temperatures. Figure 3.18 (c) symbolically represents the translation axis allowed on the cryohead to ensure optimum coupling.

To accurately measure the temperature as close as possible from the sample, two Si and RuO_2 diodes are attached to the cryohead. The latter, an Oxford Instruments T1-202 diode (not represented on Fig. 3.17), allows the most precise temperature measurement. Using an Agilent 34401A digital multimeter, its temperature-dependent resistivity is measured with an uncertainty close to ± 10 mK.

This mechanism proves to successfully allow coupling of silica microtoroid in a cryogenic environment and its principle is reused in the ^{3}He cryostat (section 3.4.7).

3.4.2 Taper coupling at low temperature

The fiber taper coupling technique presents the advantage of single-mode and high coupling efficiency to whispering-gallery modes, and tunable coupling from the under- to the overcoupled regime. To preserve those advantages at low temperature, the tapered fiber used at room temperature is adapted as a *cryotaper*.

The cryotaper

To keep the it straightly tensioned after cool down, the fiber taper is glued, using UV epoxy glue, to a C-shaped piece of glass presented in Fig. 3.19 (a) and (b). Since it is made of essentially the same material as the taper, the fiber remains properly tensioned at all temperatures, as experimentally verified. The UV epoxy glue is used because it does not contract when cured. Thus, the taper tension properly adjusted during the
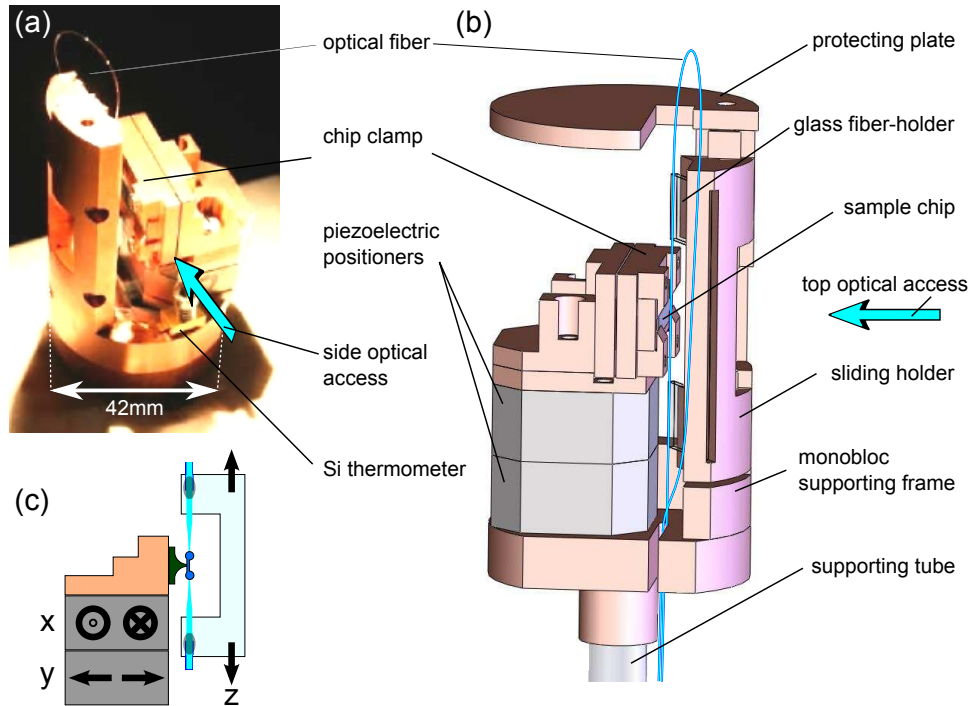
Figure 3.18: *Picture and technical layout of the cryohead. (a) Picture of the cryohead without the protecting plate. The thermometer is a Lakeshore DT-670B-CO Si. (b) 3D rendering of the cryohead showing the piezoelectric positioners (Attocube Systems ANPx101/LT/HV, "low temperature high vacuum" version) supporting the 3-part sample holder and the cryotaper placed on the mechanical slide, supported by the rigid frame. The protecting plate avoids damaging shocks during the cryoprobe insertion. (c) Not on-scale symbolic drawing of the coupling mechanism. The two piezoelectric positioners displace the clamped chip so as to approach the desired toroid in the near-field of the mechanical-slide supported cryotaper when the cryoprobe is inserted and cooled down in the cryostat.*

fabrication process remains unchanged during the gluing and thereafter during the cool down operation. On Fig. 3.19 (c), the geometrical arrangement of the cryotaper is schemed, showing the trench in the glass slide hosting the acrylate buffer of the glass fiber.

Fabrication

This novel construction requires a specific fabrication technique (Fig. 3.20) adapted from the successful fiber taper fabrication protocol presented in Appendix B. By adjusting the flame at the position described in Fig. 3.20 (a), high transmission ($> 95\%$) tapers are obtained. Pulling the flame further or closer to the fiber allows to define the glass fiber length subjected to the H_2 flame and therefore the final length of the taper region. Hence, the tapered fiber is crafted to ensure gluing the acrylate buffer to the C-shaped glass, improving the overall mechanical robustness. In Fig. 3.20 (c), the tension of the taper is tested by approaching a dummy toroid, snapping it to the taper, retracting it and
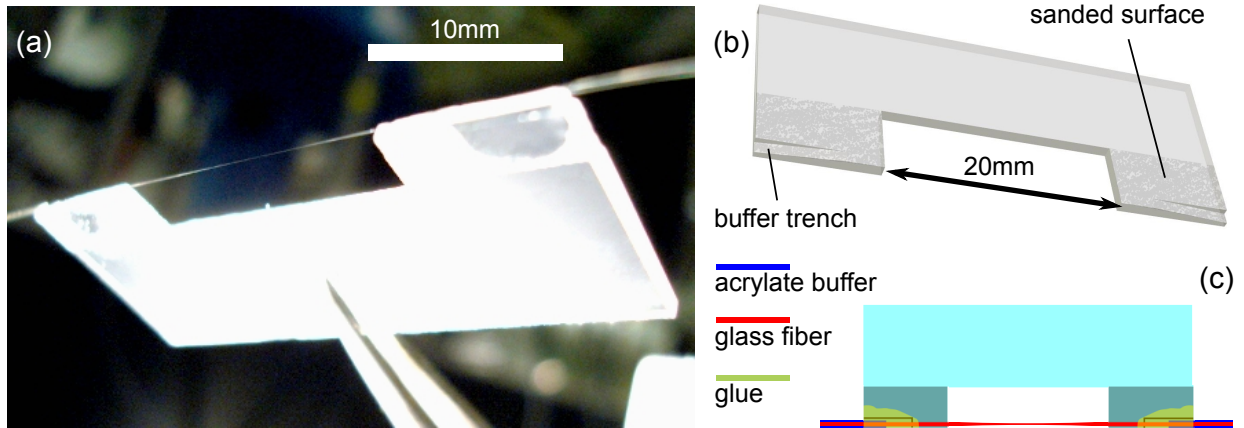
Figure 3.19: *Picture and technical layout of the cryotaper. (a) Picture of a finalized cryotaper. (b) On-scale 3D rendering of the cryotaper showing the trench for hosting the buffer of the optical fiber (245 µm diameter) and the sanded surface for better glue adhesion. (c) Technical layout describing the usual configuration of the cryotaper. To avoid shearing of the glass fiber during manipulation, the taper is crafted to dimensions such that the acrylate buffer is glued to the glass slide with simultaneously the uncovered central part of the glass fiber being still in contact with the support to avoid having a long suspended length subjected to large amplitude vibrations.*

measuring the "snap-back distance" [20]. Until this reaches less than a typical toroid radius, the taper is tensioned further using the micrometer screw displacing the fiber holder. Cleaning, using droplets of liquid acetone or isopropanol, can safely be performed to remove dusts that may aggregate during the previous steps. After approaching and gluing under microscope monitoring (Fig. 3.20 (e) and (f)), the cryotaper is released (Fig. 3.20 (g)) and placed on the cryohead. The taper is normally fabricated using one long optical fiber to avoid having fragile fiber splices inside the cooled experimental chamber

3.4.3 Thermalization

The previously described engineering efforts to couple a toroidal microcavity in a cryogenic environment aim to thermalize the mechanical radial breathing mode to the base temperature of the cryostat. By measuring the effective temperature of the mode at low input power, we show that the sample is efficiently thermalized. This proves the relevance of the exchange gas pre-cooling technique for whispering-gallery resonators.

To experimentally prove the thermalization, this section introduces the Pound-Drever-Hall (PDH) detection technique that allows to measure and quantify the mechanical motion of the mechanical mode with a significant sensitivity. The effective temperature is then measured and the resulting measurements of the thermalization are detailed, demonstrating a thermal phonon occupancy of ~ 600.

(a) flame positioning
side view
laser in
laser out
H₂ flame

(b) tapering
side view
≃780nm
side view

(c) tension adjustment
top view
fixed
μm screw

(d) cleaning
side view
isopropanol and/or acetone

(e) approaching
side view

(f) gluing
top view
UV curing
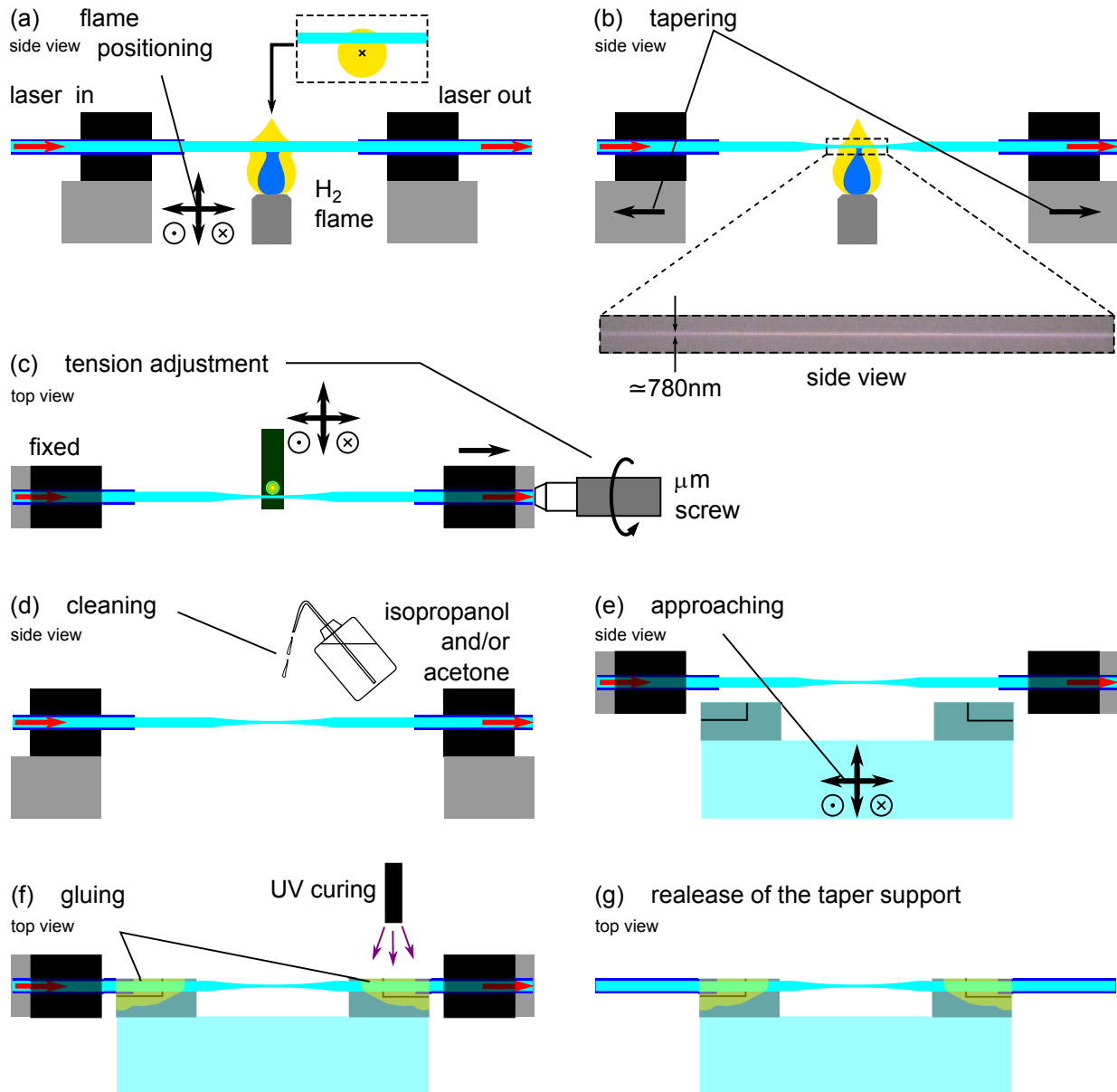
(g) realease of the taper support
top view

Figure 3.20: *Fabrication and installation steps of the cryotaper.*

The Pound-Drever-Hall detection technique

Although the method ultimately employed for detecting low occupancy is the balanced homodyne interferometer (section 3.5.1), a simple way to measure the phase fluctuations induced by the thermal motion is to use the PDH phase detection [154]. Compared to the side-of-the-fringe technique presented in section 3.2.1, this one uses an on-resonance probing laser therefore precluding any dynamical backaction effects that modify the measured mechanical spectrum. We remind here the principle of this method [155].

Figure 3.21 (a) shows the important parts of the optical and electronics setup. The laser $s_0(t)$ oscillating at ω_l is sent through a phase modulator (EOM) driven at a frequency $\Omega_{\mathrm{pdh}}/(2\pi)$, usually several times larger than the cavity linewidth κ. Modulation sidebands build up at $\omega_l \pm \Omega_{\mathrm{pdh}}$ and the expression of the field out of the EOM is given by

$$s_{\mathrm{in}}(t) = s_0(t) \left(J_0(\beta) + iJ_1(\beta)e^{i\Omega_{\mathrm{pdh}}t} + iJ_1(\beta)e^{-i\Omega_{\mathrm{pdh}}t} \right), \tag{3.33}$$

where the first order Jacobi-Anger expansion is used for small modulation indices β. When $s_{\mathrm{in}}(t)$ is coupled to the cavity with $\omega_l \simeq \omega_c$, only the carrier resonantly interacts with it. The output field $s_{\mathrm{out}}(t)$ is then phase-shifted compared to $s_{\mathrm{in}}(t)$ by an amount that gives information on the detuning: it is approximated to be linearly proportional to the detuning Δ. If only the carrier is measured, the phase shift information is lost as the photodetection only provides a signal proportional to the squared amplitude of the field.

Here, the two sidebands are non-resonant with the cavity and are consequently mostly transmitted. The photodetection voltage , which is the squared amplitude of the sum of the carrier and the two sidebands, therefore carries a term oscillating at Ω_{pdh} corresponding to the beat of the two sidebands with the carrier.

Next, the demodulation of the output voltage of the photodetector at Ω_{pdh} with the proper phase shift and low-pass filtering (of bandwidth much smaller than Ω_{pdh}) keeps only the DC signal linearly proportional to the carrier. It switches sign at the detuning $\Delta = 0$ and can be directly used as a locking signal.

Figure 3.21 (b) shows a broadband error signal for a modulation frequency $\Omega_{\mathrm{pdh}}/(2\pi) = 100\,\mathrm{MHz}$ and a cavity linewidth of $\sim 10\,\mathrm{MHz}$. The frequency range where locking can be achieved is much larger than the cavity linewidth, comprised in between $-\Omega_{\mathrm{pdh}}$ and Ω_{pdh} [155]. This signal is then fed back into the laser frequency control (here the piezoelectrically displaced external mirror of the cavity) to lock it on resonance. The part of the error function centered in $\Delta = 0$ can be approximated as a linear function of slope $\frac{dV_{\mathrm{err}}}{d\Delta} = -8J_0(\beta)J_1(\beta)|\bar{s}_0|^2\frac{\eta_c}{\kappa}$ [19]. The mechanically induced phase fluctuations are therefore transduced into voltage fluctuations that are detected by the electrical spectrum analyzer (Fig. 3.21 (a)).

A detailed derivation shows that the detected voltage spectral density is given by [19]

$$\bar{S}_{VV}^{err}(\Omega) = (8|\bar{s}_0|^2 J_0(\beta)J_1(\beta)\frac{\eta_c}{\kappa})^2 \frac{G^2}{1+(\frac{\Omega}{\kappa/2})^2}\bar{S}_{xx}(\Omega). \tag{3.34}$$

This formula demonstrates that the mechanical fluctuations filtered by the cavity are transduced by the PDH detection technique.
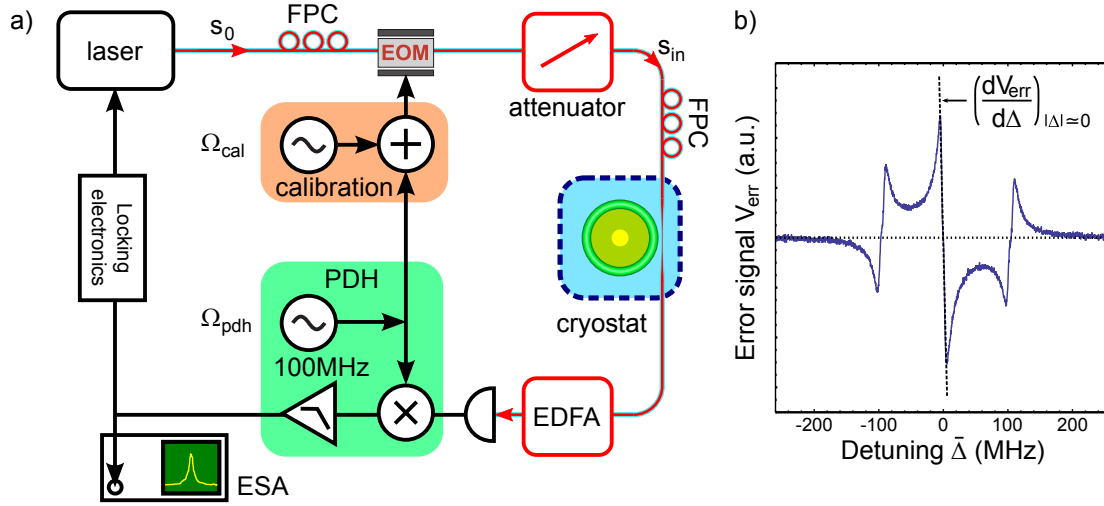
Figure 3.21: *Pound-Drever-Hall (PDH) detection scheme. (a) In-fiber optical and electronic scheme of the PDH locking and detection. EOM: electro-optic modulator, EDFA: erbium-doped fiber amplifier, ESA: electrical spectrum analyzer. (b) PDH error signal feedback into the laser for locking to the cavity resonance. Close to resonance, the mechanically-induced intracavity phase fluctuations are transduced into voltage fluctuations according to the central linear transduction slope.*

Practically, the implementation of this technique is simpler than a homodyne detection. In addition, the proper use of an optical attenuator and an erbium-doped fiber amplifier (EDFA) to amplify the optical output signal allows to perform measurements at low input powers to avoid intracavity absorption heating. With this method, the thermalization of the RBM can be entirely characterized.

Measurement of the thermalization to the cryostat's base temperature

The measured mechanical spectra are calibrated by adding a coherent phase modulation of modulation depth β_{cal} at an angular frequency Ω_{cal} close to Ω_{m}. The phase fluctuations induced by the thermally driven mechanical fluctuations are compared to this controlled phase modulation. The frequency difference of the two must be comprised well within the bandwidth of the cavity to ensure equivalent transduction but must also be higher than several times Γ_{m} to avoid coherent driving of the mechanical mode.

The driven EOM modulates the phase of the incoming field $\omega_{\mathrm{l}} t + \beta_{\mathrm{cal}}\sin(\Omega_{\mathrm{cal}}t)$, giving the instantaneous angular frequency $\omega_{\mathrm{l}}(t) = \omega_{\mathrm{l}} + \beta_{\mathrm{cal}}\Omega_{\mathrm{cal}}\cos(\Omega_{\mathrm{cal}}t)$ of variance

$$\langle \delta\omega_{\mathrm{l}}^2 \rangle = \beta_{\mathrm{cal}}^2 \Omega_{\mathrm{cal}}^2/2. \tag{3.35}$$

After photodetection and demodulation, this variance is plotted as a peak of area $A \times RBW \propto \langle \delta\omega_{\mathrm{l}}^2 \rangle$ by the spectrum analyzer, with A being the height of the peak and
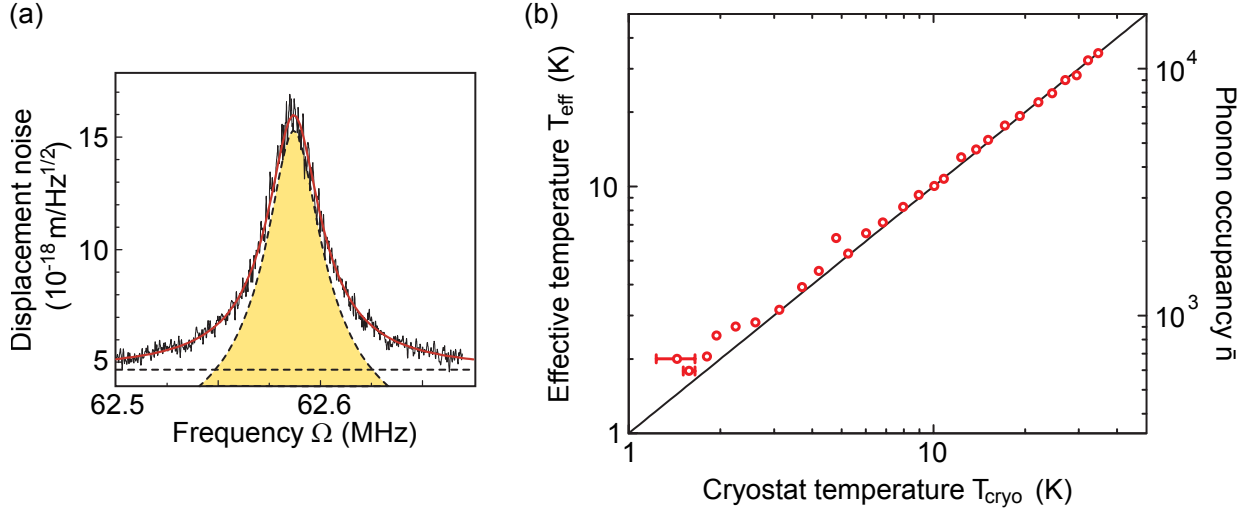
(a)

(b)

Figure 3.22: *Thermalization in the ^{4}He cryostat. (a) Mechanical displacement noise spectrum taken at $T_{\mathrm{cryo}} \simeq 1.65\,K$ and a pressure of 4 mbar. The red line is a fit of the mechanical spectrum with the background, each separately represented by the dashed lines. The effective temperature of the mechanical mode is extracted from the mechanical trace. (b) Effective temperature of the RBM versus the cryostat's temperature measured with the commercial Si diode. The correspondence with the guide to the eye illustrates the thermalization of the mechanical mode to the cryostat.*

RBW the given effective resolution bandwidth[1]. The mechanical fluctuations also give rise to a frequency variance of

$$\langle \delta \omega_{\mathrm{c}}^2 \rangle = G^2 \langle \delta x^2 \rangle \tag{3.36}$$

that is also recorded by the spectrum analyzer, with $G = -\omega_{\mathrm{c}}/R$. Thus, a simple estimation of the toroid's radius R (for example with a microscope) and of the cavity resonance frequency $\omega_{\mathrm{c}}/(2\pi)$ allows to estimate G and subsequently allows to calibrate the mechanical displacement noise measured (Fig. 3.22 (a)), knowing the root mean square of the applied voltage source and the calibration of the EOM.

The effective temperature $T_{\mathrm{eff}} = m_{\mathrm{eff}}\Omega_{\mathrm{m}}^2 \langle \delta x^2 \rangle / k_{\mathrm{B}}$ (for $T_{\mathrm{eff}} \gg \hbar\Omega_{\mathrm{m}}/(2k_{\mathrm{B}})$) is extracted from the Lorentzian integral of the calibrated spectrum (Fig. 3.22 (a)). The effective mass of the mode is estimated similarly, from the calibrated displacement noise spectrum of a thermalized mechanical mode such that $T_{\mathrm{eff}} = T_{\mathrm{m}}$, with T_{m} measured independently with an external thermometer.

Figure 3.22 (b) shows the effective temperature of a 62-MHz RBM versus the temperature of the exchange gas of the experimental chamber of the cryostat measured with the Si diode. The excellent thermalization is clearly marked by the agreement of the experimental points to the linear guide to the eye, from 40 K down to 1.8 K, the latter corresponding to a phonon occupancy of 600. From 1.8 K down to 1.65 K, the thermalization is proven despite the inaccuracy if the Si diode (points removed from Fig. 3.22).

---

[1] The effective resolution bandwidth is independently given by the device to directly calculate the area of the peak by knowing its height, for any used spectral filter.

The cryogenic cooling of a toroidal microcavity is successfully achieved down to liquid [4]He temperatures, therefore enabling the exploration of optical properties of those structures.

3.4.4 Optical cryogenic properties of silica microtoroids

The optical dissipative properties of the silica microtoroids are unaltered at cryogenic temperatures. The study of their dispersive response is, on the other hand, of particular interest in the context of laser cooling. Indeed, the heating resulting from intracavity absorption induces a shift in the optical resonance frequency responsible for the bistable behavior of the intracavity power versus detuning [79]. Consequently, one side of the cavity spectrum is stable when subjected to a pump laser since the resonance frequency follows the fluctuations of the laser frequency whereas the other side is instable. At cryogenic temperatures, the situation is opposite to room temperature [68]: the red side ($\omega_l < \omega_c$) is stable, allowing to optimally red-detune the cooling laser and to perform cooling without the need for complex fast locking devices.

In this section, the measurements of the static frequency shift from the cryostat base temperature to $40\,\mathrm{K}$ is analyzed, and the signature of a deposited film of liquid [4]He is subsequently observed.

Static thermal frequency shift

The shift of the optical resonance frequency for temperatures from $40\,\mathrm{K}$ down to $1.65\,\mathrm{K}$ is presented in Fig. 3.23 (main figure). Notably, the slope of the thermal dependency switches sign at $T^* = 13.3\,\mathrm{K}$. We attribute this behavior to the temperature dependence of the refractive index of silica [68] and to the refractive index of the surrounding gaseous [4]He.

For a homogeneously thermalized toroidal cavity (we use here optical powers sufficiently low to preclude parasitic effects), the frequency shift results from a change of optical length $L \approx 2\pi R$ for a whispering-gallery mode and from a change of effective refractive index n_{eff} given by

$$\frac{1}{\omega_c(T)}\frac{d\omega_c(T)}{dT} = -\alpha_{\mathrm{SiO_2}}(T) - \frac{1}{n_{\mathrm{eff}}}\frac{dn_{\mathrm{eff}}}{dT}, \tag{3.37}$$

where $\alpha_{\mathrm{SiO_2}}(T)$ is the expansion coefficient of silica that becomes negligible for $T \lesssim 5\,\mathrm{K}$ [156, 157]. The effective refractive index takes into account the fact that the optical field propagates not only inside the silica toroid but also outside, in the external environment (see section 2.2.2). Consequently, the evanescent field (the energy of which corresponds to few percent of the total mode energy for pump wavelengths close to $1550\,\mathrm{nm}$ [158]) probes the thermal dependence of the refractive index of the surrounding exchange [4]He gas.

At low temperatures, a liquid layer containing superfluid [4]He deposits on the surface of the microtoroid and significantly alters the dispersion of the evanescent field. The inset of Fig. 3.23 is a zoom on the low temperature part of a frequency shift trace taken with thermodynamic conditions favoring such a deposition (high pressure and low temperature).
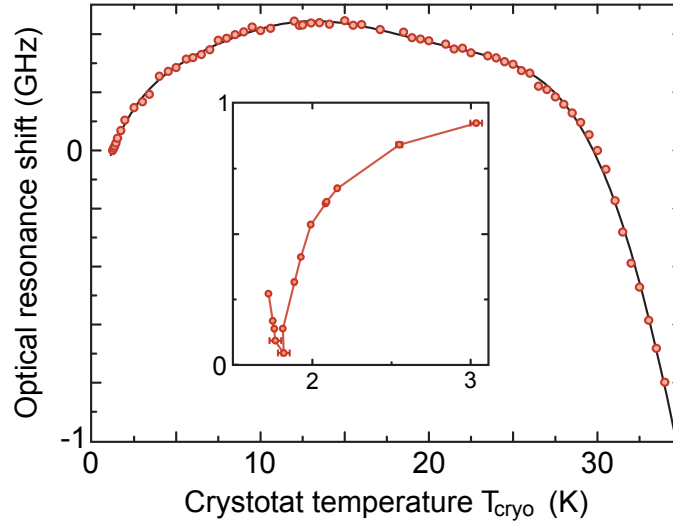
Figure 3.23: *Optical resonance shift for varying temperatures down to* 1.65 K. *The main figure shows the optical resonance frequency* $\omega_c(T)$ *for varying cryostat temperature* T_{cryo} *from 40 K down to the base temperature 1.65 K, there at a pressure of the order of a mbar. The thermal dependence of the resonance frequency varies from* $\frac{d\omega_c(T)}{dT} = 2\pi \times (+120\,\mathrm{MHz/K})$ *at 2 K to* $2\pi \times (-200\,\mathrm{MHz/K})$ *at 30 K through 0 at* $T^* \simeq 13.3$ K. *The inset zooms on the region below 3 K for a pressure ten times higher and shows the factor of 5 increase of the slope* $\frac{d\omega_c(T)}{dT}$. *The slope switches sign upon further cooling, signaling the preponderant contribution of superfluid* ^{4}He. *Adapted from [118].*

For T_{cryo} just above 1.8 K, the slope of the frequency shift is four times larger compared to the main figure (pressure one order of magnitude lower and low temperature). This is attributed to the influence of the larger density of gaseous ^{4}He and the corresponding increase of dn_{He}/dT. At $T_{cryo} \simeq 1.8$ K, a film of helium II (conceptual "mixture" of normal and superfluid ^{4}He, according to the two-fluid model [159]) deposits and the slope abruptly changes from +500 MHz/K to -500 MHz/K as expected from the particular dispersive property of the layer [160].

Principle of the thermal bistability

The thermal dependence of the resonance frequency shift leads to a non-linear behavior of the intracavity power for a varying laser detuning known as thermal bistability [67].

The mean intracavity power, proportional to $\bar{a}^2$, is absorbed at a rate κ_{abs} and provides the heat source term describing the following Fourier equation of the subsequent increase in temperature $\delta T(\vec{r}, t)$ at the coordinate vector $\vec{r}$

$$\delta \dot{T}(\vec{r}, t) - D\Delta T(\vec{r}, t) = \frac{\kappa_{abs}}{\rho c_p} \hbar \omega_l |a(t) \cdot \vec{v}(\vec{r})|^2, \tag{3.38}$$

with $D = k/(\rho c_p)$ being the diffusion constant, k the thermal conductivity, ρ the density and c_p the specific heat capacity. $\vec{v}(\vec{r})$ is the normalized spatial distribution of the optical mode [20].

Considering very slow time-variations of the heat source compared to the time constants involved (typically below 1 ms at both room [161] and low temperatures), the temperature of the toroid homogeneously increases. Neglecting the influence of the spatial extension of the mode, the increase of temperature due to absorption is approximated to

$$\delta T = \chi_{\text{th}}^{\text{stat}} \kappa_{\text{abs}} \hbar \omega_{\text{l}} \bar{a}^2, \tag{3.39}$$

with $\chi_{\text{th}}^{\text{stat}}$ given in K/W standing for the static coefficient of temperature increase per absorbed intracavity power.

At room temperature, the thermal dependence of the frequency shift is approximated to be linear. The expression of the resonance frequency is therefore given by

$$\omega_{\text{c}}(T + \delta T) = \omega_{\text{c}}(T) + \frac{d\omega_{\text{c}}(T)}{dT} \delta T, \tag{3.40}$$

with $\frac{d\omega_{\text{c}}(T)}{dT} = -1.28 \, \text{GHz/K}$ [20]. The expression of the static intracavity photon number is then

$$\bar{a}^2 = \frac{\eta_{\text{c}} \kappa |\bar{s}_{\text{in}}|^2}{(\kappa/2)^2 + (\omega_{\text{l}} - \omega_{\text{c}}(T) - \frac{d\omega_{\text{c}}(T)}{dT} \chi_{\text{th}}^{\text{stat}} \kappa_{\text{abs}} \hbar \omega_{\text{l}} \bar{a}^2)^2}. \tag{3.41}$$

If the induced distortion of the resonance frequency is larger than $\kappa/2$, this expression supports three real solutions in $\bar{a}^2$ leading to two turning points corresponding to infinite slopes $\frac{d\bar{a}^2}{d\Delta(T)}$ which are the particular signatures of the bistable behavior. Figure 3.24 shows this three real solutions and the corresponding resonance frequency distortion compared to the "cold" case, reproducing the qualitative behavior encountered at room temperature. The distortion of the resonance frequency and the consequent evolution of the intracavity power follows the evolution of the laser when scanning from the *blue side* ($\omega_{\text{l}} > \omega_{\text{c}}$) of the cavity. On the contrary, it evolutes oppositely to the laser when scanning from the *red side*. Consequently, the cavity is responding unstably to a laser pumping its red side. In the context of laser cooling, this effect obliges to lock the laser on the red side with complex fast feedback systems.

Low-temperature thermal multistability

Because of the switch of sign of the thermal shift, the situation is opposite for $T < T^*$, the red side becoming stable upon pumping. Complex locking devices fast enough to compensate the thermal instability are then not required to perform the laser cooling. Figure 3.25 (a) shows the measurement and the simulation of the reversed bistability for $T < T^*$ for an input power low enough to still approximate a linear thermal shift of the resonance frequency as in Eq. (3.40). Upon increase of the input power, the temperature elevation due to absorption becomes too strong and the approximation breaks down: the resonance frequency does not shift linearly with detuning and the bistable triangle distorts (Fig. 3.25 (b)). From the plot in Fig. 3.23, the frequency is then approximated by the polynomial function of fourth order in T

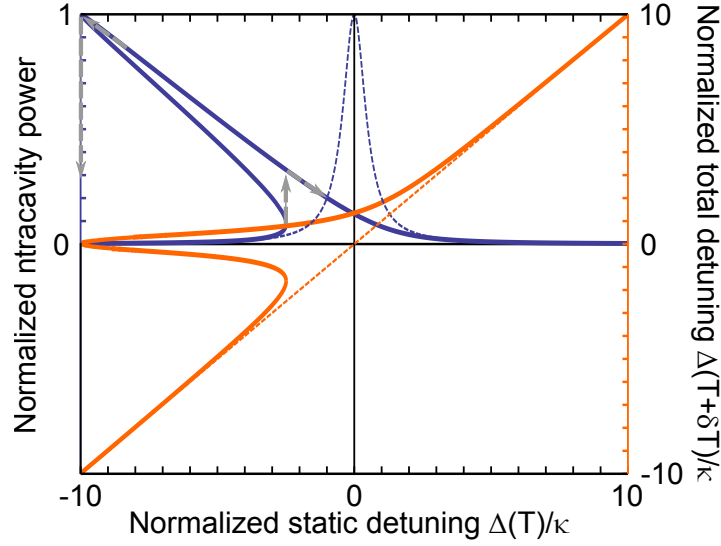$$\omega_{\text{c}}(T) = \sum_{i=0}^{4} \mu_i \delta T^i, \tag{3.42}$$

Figure 3.24: *Bistable intracavity power in the case of a linear frequency decrease upon absorption heating (solid blue line) compared to the same cavity in the absence of any absorption (dashed blue line). The corresponding cavity detuning is plotted with absorption (orange solid line) and without (orange dashed lines). The sign and strength of the deviation from the "cold" cavity is proportional to the thermal dependency of $\omega_c(T)$, in this case linear. The arrows denote the scan jumps at the turning points.*

with $\mu_i = \{-214.9, 157.2, 15.32, 0.6512, -0.0104\}$ in MHz/K^i.

The expression of the intracavity photon number then reads

$$\bar{a}^2 = \frac{\eta_c \kappa |\bar{s}_{\mathrm{in}}|^2}{(\kappa/2)^2 + (\omega_l - \sum_{i=0}^{4} \mu_i (T + \chi_{\mathrm{th}}^{\mathrm{stat}} \kappa_{\mathrm{abs}} \hbar \omega_l \bar{a}^2)^i)^2}, \tag{3.43}$$

using the approximation given in expression (3.39). This highly non-linear equation describes the optical multistability. Note that for an input power sufficiently high to heat the cavity to $T + \delta T > T^*$, the resonance distortion changes sign and two more branches appear.

The multistable mechanism allows to quantify the parameter $\chi_{\mathrm{th}}^{\mathrm{stat}}$ relating the absorbed intracavity power to the elevation of temperature. The fact that this parameter doubles when the pressure is decreased by one order of magnitude from 5 to 0.5 mbar emphasizes the importance of the thermalization through gas at these pressures. This result is of particular interest for the laser cooling operations as static heating due to intracavity powers is undesired.

The same measurement performed in the presence of a helium II layer clearly shows an alteration of the bistable trace in Fig. 3.25 (d). The apparition of the shoulder in the scan and the observed strong splitting (≈ 70 MHz) are both attributed to the presence of the liquid layer.
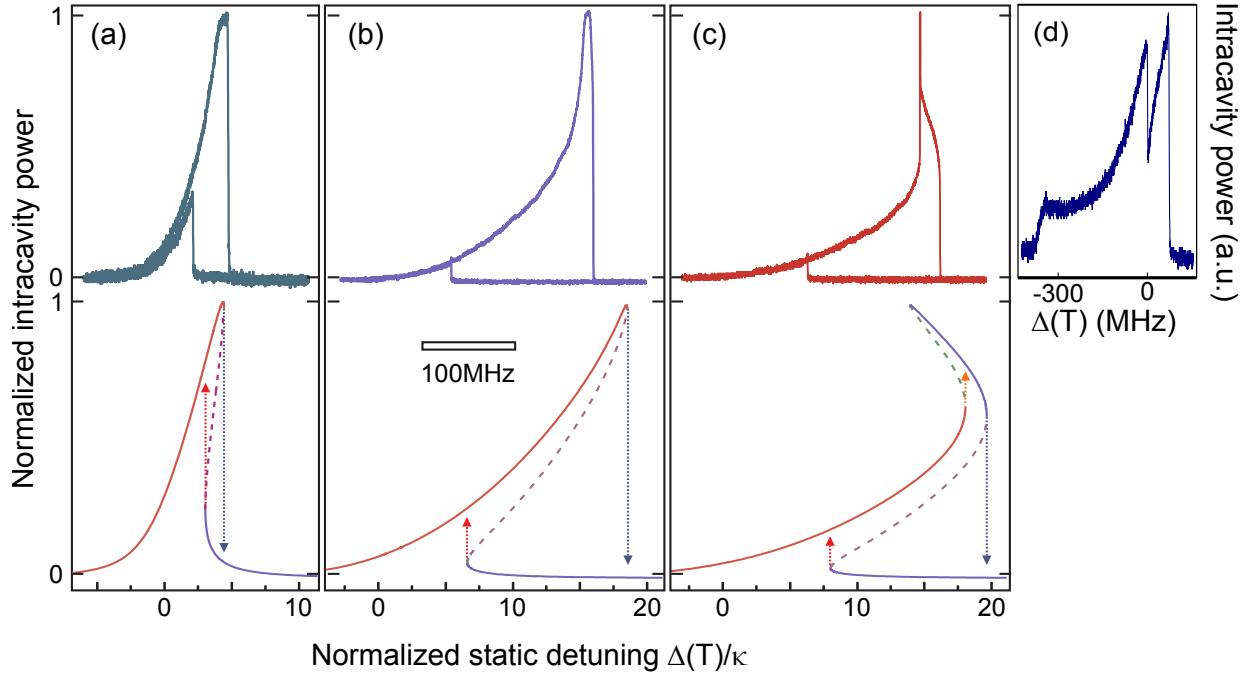
Figure 3.25: *Multistable intracavity power for pump powers 13 (a), 131 (b) and 260 μW (c) at T = 2.3 K (higher panels). The corresponding simulations according to Eqs. (3.42-3.43) with the same input power ratio are shown in the lower panels. The cold cavity linewidth is κ/(2π) = 14 MHz. (d) Typical bistable intracavity power in the presence of a helium-II film. The splitting is accredited to be genuine to the deposition of a fluid layer onto the torus surface.*

3.4.5   Thermal response

Although showing the influence of the exchange gas on the static absorption, the optical measurements presented in the previous section do not give an insight on the dynamics of the propagation of the absorption-induced heat inside the toroid. To analyze this, the dynamical thermal response is recorded using a pump-and-probe experimental scheme. An amplitude-modulated pump laser is locked on one resonance and induces a propagating thermal wave evanescently extending in the structure. The elevation of temperature along this propagation length modulates the resonance frequency that is recorded and demodulated, characterizing the thermal response of the toroid.

This section presents the setup used to characterize the toroid's thermal response at varying cryogenic temperatures. The observed influence of the surrounding exchange ^{4}He in the heat extraction mechanism is discussed. In addition, when a layer of helium II deposits, the response trace shows a clear signature of a resonance effect attributed to the generation of a superfluid "third sound" [162].

Diffusion in silica

The temporal dynamics of the heat extraction mechanisms in toroids are fully characterized using a pump-and-probe scheme. The heat generated from the absorbed intracavity light can flow via two media: the silicon pillar after diffusion in the silica disk or the surrounding ^{4}He gas. The former phenomenon is analytically presented in the simple case where the latter is neglected.

The heat propagation through silica is governed by the equation of heat diffusion given in Eq. (3.38). As expected from a temperature source [163] oscillating at an angular frequency Ω, the generated thermal wave propagates and decays over a characteristic length $l_c = \sqrt{D/\Omega}$. The resulting oscillating elevation of temperature δT changes the cavity's length and refractive index, therefore inducing a modulation of the optical path detected by a resonant probe laser using the PDH frequency detection technique.

For low modulation frequencies, l_c is much larger than the toroid's periphery-pillar distance $L = R - r_p$. The thermal wave thus extends to the strongly thermally anchored silica region above the silicon pillar, for which δT is assumed to be equal to zero. The flow of heat through the pillar prevents additional elevation of temperature per cycle, resulting in a flat thermal response when decreasing Ω, transduced as a measured response's amplitude plateau. The phase difference between the heat source and temperature oscillation in this regime is close to zero. In essence, the structure "thermalizes" at each cycle.

On the contrary, for modulation frequencies such that l_c is much smaller than L, the thermal front wave cannot reach the pillar at each cycle. Hence, the amount of deposited energy per cycle decreases for increasing frequency and leads to a decreasing elevation of temperature. This is the frequency-dependent amplitude response. The modulation frequency at the junction of these two regimes is the cutoff frequency of the diffusion phenomenon.

To analytically derive the complex temperature response from the equation (3.38), the geometry of the system is simplified by considering a disk of radius R and thickness t_d supported by a pillar of radius r_p. The disk can be considered thermally insulated from the surrounding medium. The localization of the heat source, the optical mode, is approximated to the peripheral wall of the disk, simplifying Eq. (3.38) after Fourier transform to (in polar coordinates)

$$i\Omega\delta T(r,\Omega) - D\frac{1}{r}\frac{\partial}{\partial r}\left(r\frac{\partial}{\partial r}\right)\delta T(r,\Omega) = \frac{\kappa_{abs}}{\rho c_p}\frac{\delta_K(r-R)}{2\pi R t_d}\hbar\omega_l\bar{a}^2. \tag{3.44}$$

The analytical solution for the elevation of temperature at $r = R$ reads [20]

$$\delta T(R,\Omega) \approx \frac{\delta T_1}{1 + i\Omega/\Omega_1}, \tag{3.45}$$

with

$$\delta T_1 = -\hbar\omega_l\kappa_{\text{abs}}\bar{a}^2\frac{1}{2\pi k t_{\text{d}}}\ln(r_{\text{p}}/R), \tag{3.46}$$

$$\Omega_1 = \frac{4\ln(r_{\text{p}}/R)}{1 - (r_{\text{p}}/R)^2 + 2\ln(r_{\text{p}}/R)(1 + \ln(r_{\text{p}}/R))}\frac{D}{R^2}. \tag{3.47}$$

For large frequencies $\Omega \gg \Omega_1$, l_{c} becomes comparable to the radius r_0 of the optical mode. The radial extension of the heat source must then be taken as non-zero. It is approximated as a circle of radius r_0 localized at $r \approx R$. As in the previous case, at low frequencies the elevation of temperature is small and localized whereas at high frequencies the heat wave propagates and the elevation on the center of the disk saturates. The elevation of temperature at $r \approx R$ is then given by

$$\delta T(R, \Omega) \approx \frac{\delta T_2}{1 + i\Omega/\Omega_2}, \tag{3.48}$$

with

$$\Omega_2 = D/r_0^2. \tag{3.49}$$

For a toroid of minor diameter much larger than several wavelengths, the mode radius is $r_0 \approx 1.8\,Rm^{-2/3}$ [20], where m is the azimuthal mode number. The two derived cutoff frequencies characterize the diffusion mechanism in silica for a given geometry. Measured deviations from the presented ideal model additionally inform on the presence of gas thermalization breaking down the assumed analytical approximations.

Pump-and-probe measurements

Figure 3.26 (a) depicts the setup used to perform the pump-and-probe measurements. The amplitude-modulated pump laser is thermally locked on one resonance of the toroid and provides the modulated heat source. The probe laser is locked on a spectrally distant mode. Demodulation of the probe laser's PDH error signal by the network analyzer provides the amplitude and phase thermal responses of the toroid's resonance frequency. It thus allows to record and characterize the cutoff frequencies and amplitudes of the different heat extraction mechanisms (Fig. 3.26 (b)).

The total variation of the cavity's resonance frequency is given by [20]

$$\delta\omega_{\text{c}}(\Omega) = (\delta\omega_{\text{th}}(\Omega) + \delta\omega_{\text{K}} + \delta\omega_{\text{rp}}(\Omega)), \tag{3.50}$$

where $\delta\omega_{\text{rp}}$ relates to the radiation pressure force coming from the modulated intracavity light. The responses are studied here at frequencies below $10\,\text{MHz}$, lower than the cavity bandwidth of $25\,\text{MHz}$. The cavity low-pass filtering effect on the pump and the probe modulations has thus an insignificant influence on the presented results. For the radiation-pressure induced frequency shift modeled by $\delta\omega_{\text{rp}}(\Omega)$, the RBM is estimated to vibrate at a frequency above $50\,\text{MHz}$ and is also not taken into account in the present discussion. In
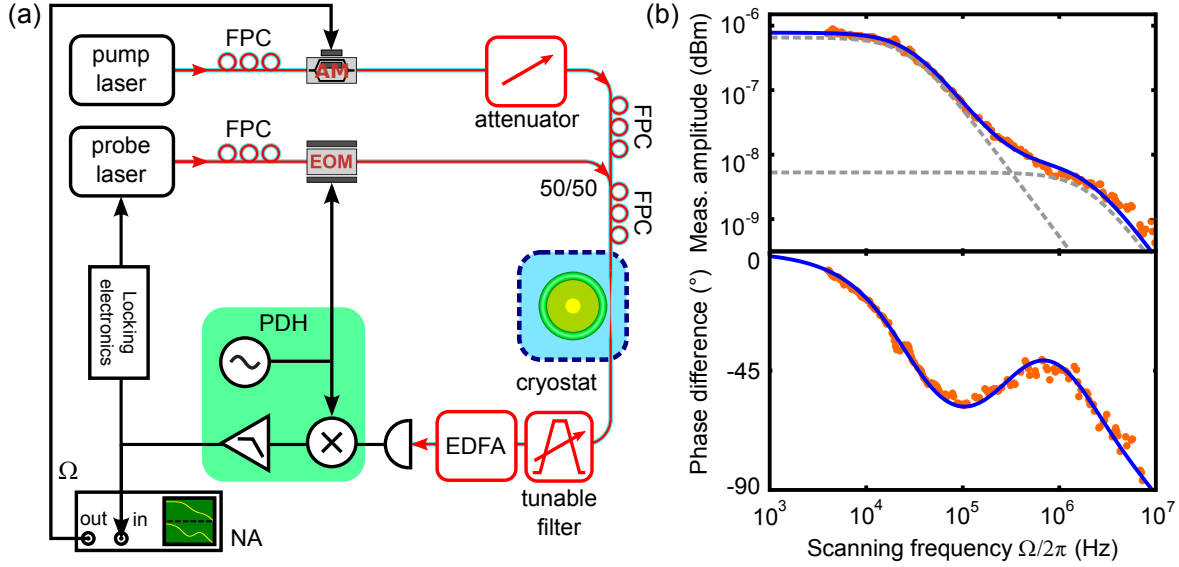
Figure 3.26: *Pump-and-probe setup (a) and recorded amplitude and phase-difference traces (b). (a) The network analyzer (NA) modulates the amplitude of the thermally-locked pump laser at the scanning angular frequency Ω and demodulates the AC part of the PDH signal, recording the amplitude and phase responses. The cross-talk between the two lasers is reduced using a tunable étalon filter. The input powers and wavelengths of the pump and probe are $10\,\mu W$ and $1521\,nm$ and $20\,\mu W$ and $1563\,nm$, respectively. (b) Measured amplitude and phase-difference (orange dots) of the thermal response of a $60\,\mu m$-diameter toroid cooled to $9.9\,K$ using $\sim 2\,mbar$ of gaseous ^4He. The fitted curve (blue line) corresponds to a two-pole response of $29\,kHz$ and $2.0\,MHz$ cutoff frequencies. Each of them is separately represented by a dashed gray line in the amplitude trace.*

the context of dynamical backaction cooling, it has been estimated that the influence of the thermal effect at typical mechanical frequencies of the radial breathing mode is two orders of magnitude lower than the radiation pressure effect [28]. Finally, the instantaneous contribution of the Kerr effect $\delta\omega_{\mathrm{K}}$ is simply taken as a frequency-independent background in the frequency range considered.

The variation of the optical resonance frequency due to the thermal modulation reads

$$\delta\omega_{\mathrm{th}}(\Omega) \approx -\omega_{\mathrm{c}} \left(\int_0^R \alpha\,\delta T(r,\Omega)\,dr/R + \int_{R-r_0}^{R+r_0} \frac{1}{n}\frac{dn}{dT}\delta T(r,\Omega)\,dr/(2r_o) \right). \tag{3.51}$$

The integrals account for the different spatial influences of the elevation of temperature on the change of optical resonance frequency. The effects on the surrounding gas are neglected. At $r \approx R$ where the probe mode is localized, $\delta T(r,\Omega)$ is the sum of both contributions expressed in Eqs. (3.46) and (3.48).

Figure 3.27 shows the fitted cutoff frequencies for cryostat temperatures varying from 5 to 37 K, with pressures varying from 2 to 46 mbar (low pressure measurements) and from 80 to 260 mbar (high pressure measurements).

The approximated model given by Eq. (3.51) suggests to fit two low-pass filters to account for the diffusion in glass only. For T_{cryo} above 13 K, the fitted cutoff frequencies

follow the trend given by the theoretical expressions for the first pole (Eq. (3.47)) and the second pole (Eq. (3.49)) estimated using the tabulated values of silica's thermal properties [164, 165, 166]. A first manifestation of the influence of the surrounding gas onto the thermal response is the systematic increase by a factor of two of the cutoff frequency of the first pole at high pressures. For T_{cryo} below $13\,K$ and high pressures, however, the first pole approximation expressed by Eq. (3.45) breaks down and cannot be analytically estimated as a first-order low-pass filter. Numerical simulations currently on-going in the group show that both phenomena can be accurately predicted when the diffusion through the gaseous ^{4}He is included in the model. Another intriguing aspect discovered at low temperature is
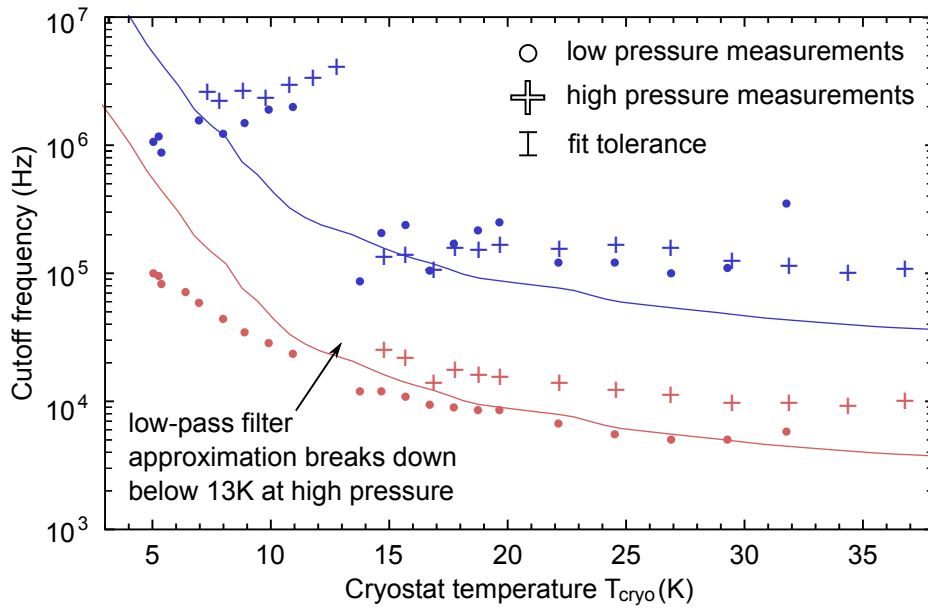
Figure 3.27: *Response cutoff frequencies versus cryostat temperature for low and high pressures (more than one order of magnitude difference). The red and blue lines correspond respectively to the estimation of the cutoff frequencies given by Eqs. (3.47-3.49) using tabulated thermal transport coefficients of silica [164, 165, 166]. The cutoff frequencies are obtained by fitting a two-pole model plus background for which the amplitude and frequencies are fitted parameters. The fit tolerance is an average estimation from several fit processes outputting fitted traces of similar confidence coefficients. For the high pressure measurements, the first low-pass filter approximation breaks down below 13 K.*

the fact that the cutoff frequency of the second pole reaches high values (more than 1 MHz) and evolves inversely than theoretically expected.

Those observations highlight the preponderant role of the exchange ^{4}He at low temperatures in the heat dynamics of the sample, whereas the gas plays a negligible role at room temperature [20]. This conclusion justifies the *exchange gas* technology used for thermalizing the toroidal microcavity and confirms the relevance of this type of cryostat design when going to even lower temperatures, using an exchange gas ^{3}He cryostat.

Finally, another interesting aspect revealed by the pump-and-probe measurements is

that the different contributions to the variation of the resonance frequency strongly cancel each other at T_{cryo} close to T^*, reducing the amplitude of the thermal response by more than $20\,\mathrm{dB}$ up to $10^7\,\mathrm{MHz}$. This phenomenon can be exploited in the context of stabilized cavities [167]. The pressure dependency of the cancellation temperature suggests furthermore that a significant role is played by the gaseous $^4\mathrm{He}$.

Superfluid $^4\mathrm{He}$ signature

When decreasing the temperature below $\sim 2\,\mathrm{K}$, a film of helium II deposits. In the response amplitude curve, its contribution manifests itself as the oscillatory trace shown in Fig. 3.28. Cancellation peaks of similar free spectral ranges are detected, suggesting that the generated heat transport wave undergoes a cavity effect with a cavity dispersion of $-40\,\mathrm{kHz/MHz}$. From the thermal dispersion of $\sim -500\,\mathrm{kHz/K}$, it is supposed that the type of wave generated is intrinsic to helium II films, known as the "third sound" [162]. Its existence has been theoretically derived [168] and experimentally demonstrated [169] by Atkins five decades ago. Since trace (i) is a convolution of trace (ii) with an extra interferometric term, it could signify that this thermal surface wave dispersively modulates the propagation medium of the optical wave. Measurements performed with a $980\,\mathrm{nm}$ pump laser show a significantly modified spectrum. This suggests additionally that the spatial boundary conditions of the third sound cavity partially depend on the wavelength and could be due to the regularly spaced hot spots generated by the standing pump wave.
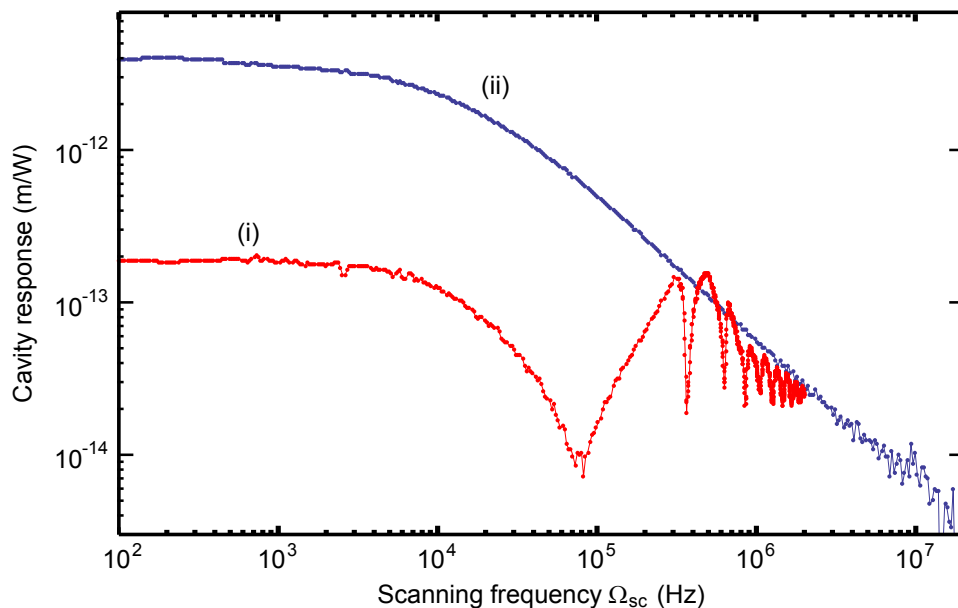

Figure 3.28: *Calibrated amplitude response in the presence of a film of superfluid $^4\mathrm{He}$ (i) and of normal liquid $^4\mathrm{He}$ (ii) at a pressure of a few tens of mbar and a temperature of $2.17\,\mathrm{K}$. The cancellation effect observed is attributed to the destructive interference of a generated superfluid third sound wave in a cavity-like spatial confinement.*

3.4.6   Dynamical backaction cooling in the helium-4 cryostat

The studies performed in previous sections on the reduction of the mechanical dissipations (section 3.2), on the classical and quantum backaction (section 3.3) and on the reduction of the environmental temperature (sections 3.4.1 to 3.4.5) aim towards the reduction of the phonon occupancy. Implementation of cryogenic pre-cooling and resolved-sideband optomechanical cooling came to the fore in 2008 with the first ever reported cryogenic cooling results from our group [41], quickly followed by other groups using microspheres [56] and beam nanoresonators [53].

Laser cooling

Here, the experiment is performed in the cryostat at a temperature close to $T_{\mathrm{cryo}} = 1.65\,\mathrm{K}$, with an exchange gas pressure of tens of mbar to ensure significant thermalization. The study pursued on silica two-level-systems in section 3.2.3 shows that the mechanical Q drops by one order of magnitude when cryogenically cooling from room temperature to the cryostat's base temperature. Spoke optimization in this regime is useless and the simple needle-pillar samples are therefore superfluous as optomechanical systems, with a TLS-limited mechanical Q of ~ 2000 at $66\,\mathrm{MHz}$.

The detection of the phase fluctuations of the output field is performed using a balanced homodyne interferometer detailed in section 3.5.1. Subsequent calibrated spectral analysis directly provides the mechanical spectrum from which the effective temperature T_{eff} of the radial breathing mode is extracted. The Ti:sapphire laser is thermally locked to the red side of the optical cavity and serves as both cooling and readout laser.

Starting at room temperature, the mechanical spectrum of the RBM of a $30-\mu\mathrm{m}$ radius toroid is recorded (Fig. 3.29 (a), red trace). With an optical linewidth $\kappa/(2\pi) \approx 19\,\mathrm{MHz}$ in normal experimental conditions (slightly overcoupled), the ratio $\Omega_{\mathrm{m}}/\kappa$ is larger than three. The resolved-sideband regime is then reached and the cooling process therefore benefits from both a reduced limitation due to quantum backaction and a reduced intracavity heating (section 3.3). Measured with a low input power, the effective temperature of the RBM is first cryogenically reduced to reach a phonon occupancy of 530 at the cryostat's base temperature (Fig. 3.29 (a), green traces). Thereafter, laser cooling is performed by simultaneously increasing the power of the laser, detuned to $\bar{\Delta}_{\mathrm{opt}}$, to $200\,\mu\mathrm{W}$ (Fig. 3.29 (a), blue traces) to reach an effective mechanical linewidth of $\Gamma_{\mathrm{eff}}/(2\pi) = 370\,\mathrm{kHz}$. The corresponding phonon occupancy averaged from several measurements is $\bar{n} = 63 \pm 20$ for an effective temperature of $T_{\mathrm{eff}} = 200 \pm 60\,\mathrm{mK}$.

Intracavity absorption estimation

This cooling performance is limited by the intracavity light absorption that unavoidably elevates the environmental temperature of the mechanical oscillator. Its influence is quantified here.

In Fig. 3.30, the measured effective temperatures are plotted versus the measured effective linewidths (blue points) obtained when the laser power is increased. The deviation
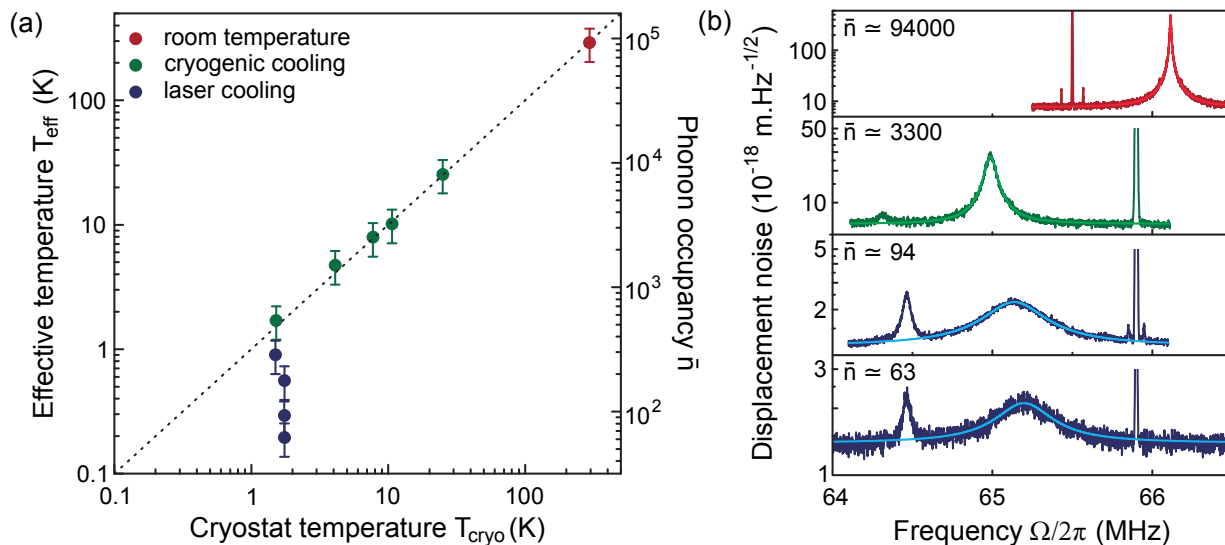
Figure 3.29: *Cryogenic pre-cooling and laser cooling. (a) Effective temperature $T_{\rm eff}$ of a 65.1-MHz mechanical RBM versus cryostat temperature $T_{\rm cryo}$ starting at room temperature (red), then subjected to cryogenic cooling (green) and finally to laser cooling (blue), down to an occupancy $\bar{n} = 63 \pm 20$. The dashed line is a guide to the eye denoting perfect thermalization to the ^4He cryostat. Each value is an average of several measurements. The varying experimental conditions are responsible for scattered values denoted by the error bars ($< 30\%$). Global heating of the experimental chamber by the laser is responsible for the measured increase of $T_{\rm cryo}$. (b) Recorded and Lorentzian-fitted mechanical spectra for various points in (a) for which noise thermometry is used to infer $T_{\rm eff}$. The model includes the shift of the intrinsic mechanical parameters resulting from the silica two-level system when the temperature increases because of absorption. For the blue traces, laser cooling is performed to increase the effective linewidth $\Gamma_{\rm eff}$ at input powers of 190 and $200\,\mu W$. The sharp peak is the calibration peak, the other peak on the red side of the RBM is an unaffected mechanical resonance.*

from the ideal case without absorption (blue solid lines) is modeled by the fit taking into account the absorption-induced elevation of temperature (dashed green lines). For increasing input powers, $\Gamma_{\rm eff}$ increases but the concomitant increase of the environmental temperature due to intracavity absorption leads to a saturation of the total effective temperature. In trace (a), the corresponding increase of the environmental temperature estimated from the deviation is denoted by the red dashed line. The temperature dependence of the intrinsic mechanical parameters (strongly dominated by silica two-level systems) is taken into account. From the study of section 3.2.3, it is clear that the elevation of temperature penalizes additionally the cooling performance by degrading the intrinsic mechanical parameters of the oscillator. This illustrates the dramatic effect of the intracavity absorption on the cooling process in the cryogenic environment.

The beneficial effect of the deep resolved-sideband (RSB) regime on this issue, explained in section 3.3, is nevertheless illustrated by performing laser cooling on another sample exhibiting a smaller RSB factor close to 1 (Fig. 3.30 (b)). The deviation in this case is
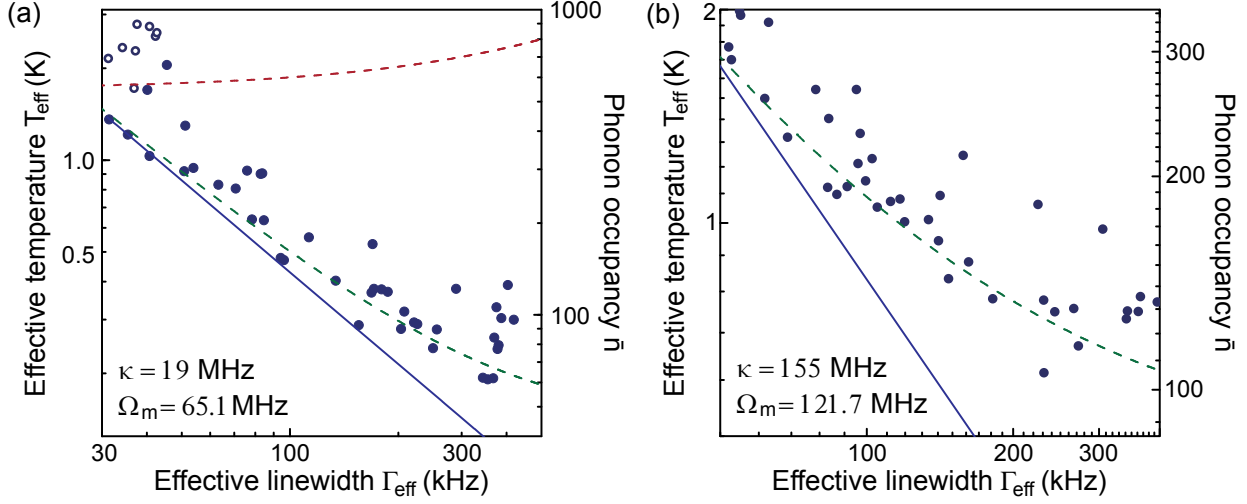
Figure 3.30: *Quantification of intracavity absorption heating for two different samples of resolved-sideband factor 3 (a) and 1 (b), subjected to laser cooling. Both graphs show $T_{\rm eff}$ versus $\Gamma_{\rm eff}$ and compare the ideal case (blue line) with measurements (filled points). The fit (green dashed line) accounts for the intracavity laser absorption and for the TLS mechanical effects (the latter only for (a)). Open points are measurements in the absence of laser cooling. The extracted corresponding environment temperature is denoted by the red dashed line in (a).*

much more important and demonstrates experimentally the advantage of using samples with high RSB factors in cryogenic environments with limited thermalization capabilities. This aspect will be pushed further to achieve an even lower phonon occupancy in the ^{3}He cryostat.

Imprecision-backaction product

The experiment is considered from the quantum measurement perspective theoretically introduced in section 1.3. The extracted raise of temperature for the high RSB ratio sample allows to calculate the total thermal force fluctuations $\bar{S}^{\rm th}_{FF}(\Omega_{\rm m}) \approx (8 \times 10^{-15}\,{\rm N}/\sqrt{\rm Hz})^2$ from expression (1.46). Subtracting the contribution of the cryostat temperature, the *classical backaction* mostly resulting from the measurement field absorption heating is estimated to be $\bar{S}^{\rm cba}_{FF}(\Omega_{\rm m}) \approx (4 \times 10^{-15}\,{\rm N}\sqrt{\rm Hz})^2$. Indeed, the quantum contribution $\bar{S}^{\rm qba}_{FF}(\Omega_{\rm m})$ from expression (1.71) is one order of magnitude smaller and therefore neglected.

Consequently, the imprecision-backaction product resulting from the sole contribution of the optical measurement field is estimated to be $\bar{S}^{\rm qi}_{xx}\bar{S}^{\rm cba}_{FF} \approx (100)^2\,(\hbar/2)^2$. The quantum imprecision measured from the background of the calibrated mechanical spectra is $\bar{S}^{\rm qi}_{xx}(\Omega_{\rm m)} \approx (1.4 \times 10^{-18}\,{\rm m}/\sqrt{\rm Hz})^2$, formally expressed by Eq. (1.70). From the measurement perspective, reducing the intracavity laser absorption allows to reduce the classical backaction that alters the total measurement uncertainty. This point is analyzed when implementing the experiment in the next cryostat.

As a conclusion, the experimental work undertaken to implement the coupling setup in the prototype cryostat has proven to be successful and sets the ground for the next cryostat using ^{3}He. All technical innovations reviewed in this section can simply be adapted and the studies pursued on the thermalization and on the material dissipations are still of prime relevance in the new experimental setup.

3.4.7   The experimental helium-3 cryostat

The study conducted in section 3.2.3 predicts a decrease by a factor of more than 3 of the mechanical dissipations dominated by silica two-level system by going from 1.65 K to 850 mK. At this ^{3}He temperature, the characterization of a 76.3 MHz oscillator demonstrates a mechanical Q of ~ 7100 (Fig. 3.12), more than three times higher than measured in the prototype cryostat's base temperature during the cooling run [41]. Combined with the large effective damping $\Gamma_{\text{eff}} > 1.5$ MHz already experimentally achieved in the deep resolved-sideband regime at room temperature (section 3.3), operating at such a modest pre-cooling temperature would lower the phonon occupancy of the mechanical oscillator close to 1. The motional sideband asymmetry would then reach an experimentally clearly visible ratio of almost 3 dB. This statement justifies the implementation of the coupling setup into the *experimental* ^{3}He exchange gas cryostat presented in this section, using the technical knowledge obtained during the construction of the prototype cryostat. The relevance of the similar refrigeration principle is proven by thermalizing the mechanical mode to a phonon occupancy below 200 at 600 mK. Laser cooling experiments in this setup are nevertheless performed at 850 mK to benefit from a significant thermalization of the sample at the vapor pressure of ^{3}He of 2.8 mbar.

^{3}He vaporizes at 3.19 K, hence at lower temperature than ^{4}He at room pressure. Thus, a cryostat with an equivalent vacuum technology vaporizing a bath of ^{3}He reaches a lower base temperature. This is the principle of the employed Oxford Instruments HelioxTL cryostat. In essence, the construction is the same as the previously described ^{4}He cryostat except that the experimental chamber is filled with ^{3}He that liquefies and drops at the bottom. There, its vaporization is strongly forced by a mounted charcoal pump leading to a lowering of the bath temperature down to 400 mK and thermalizing the mounted cryoprobe to 600 mK.

Figure 3.31 (a) depicts the ^{3}He cryostat with the on-scale drawings of the different reservoirs and the symbolic drawings of the tubings[2]. As for the previous one, this cryostat is designed to host mechanically sensitive experiments and is therefore particularly adapted for our sensitive coupling setup.

A Leybold TMP 361 turbomolecular pump ensures that high vacuum is reached in the insulation vacuum space before cryogenic operation. For the refrigeration process itself, a liquid N_2 shielding provides the first cooling stage and reduces the evaporation rate of the second cooling stage which is the 24-L liquid ^{4}He reservoir. The latter is connected through a needle valve to the "1-K pot" that fills with 4.2-K liquid ^{4}He. This sub-reservoir

---

[2]See Ref. [170] for the standard vacuum graphic symbols used.

optical feedthrough

cryoprobe

electrical feedthrough

vacuum lock

(a)

1K POT CONTROL

rotary pump

oil filter

gate valve

turbo-molecular pump

SORB CONTROL

(b)

cryotaper

chip

mechanical slide

capacitance gauge

Ca

sample holder

Penning gauge

PIG

piezoelectric positioners

high vacuum

liquid N₂ shield

liquid ⁴He reservoir

heater

heat exchange

cryosorption pump

1K pot

gaseous ³He

37.5mm

baffle

49.2cm

cryohead + protecting cup

heater

optical access

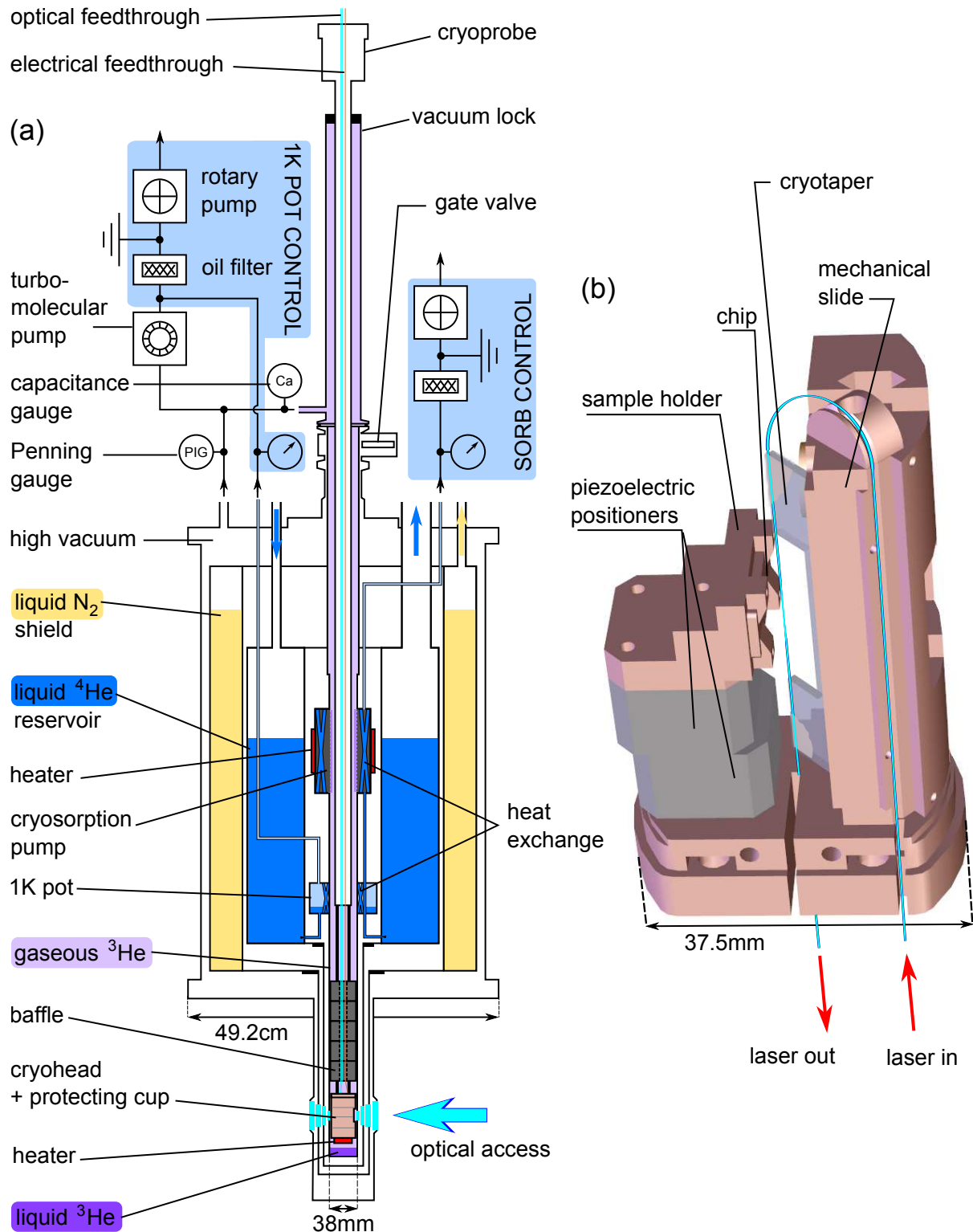liquid out   laser in

liquid ³He

38mm

Figure 3.31: *On-scale drawing of an Oxford Instrument HelioxTL helium-3 exchange gas cryostat (a) and 3D-rendered drawing of the cryohead without the protecting cup (b). The inner circuitry is symbolically represented, since not disclosed by the manufacturer.*

is thermally anchored to the experimental chamber. Appropriate pumping with a rotary pump lowers its temperature to $\sim 1.3\,\mathrm{K}$, simultaneously lowering the temperature of the experimental chamber and liquefying the ^{3}He residing inside. When a sufficient bath of liquid ^{3}He forms at the bottom of the chamber, its temperature is lowered even more by pumping it with a charcoal "cryosorption" pump of maximum pumping speed of $2200\,\mathrm{m^3/h}$, providing a cooling rate of more than a mW at the working temperature of the experiment ($850\,\mathrm{mK}$) for a holding time of $\sim 6\,\mathrm{h}$.

The pumping speed of the cryosorption pump is adjusted by varying its temperature, therefore controlling the cryostat's base temperature. To this end, a digital feedback loop controls a heater and provides a temperature stability below $1\,\mathrm{mK}$ at an operating temperature below $1.2\,\mathrm{K}$.

The cryoprobe construction allows to remove the sample while the cryostat is kept at low temperature (typically ^{4}He temperature) using a vacuum lock that can be evacuated to high vacuum (see Fig. 3.31). A full swap normally requires $24\,\mathrm{h}$ as the evacuation of the lock before cooling necessitates long turbomolecular pumping to remove contaminating species such as N_2 or organic materials unavoidably depositing during manipulation.
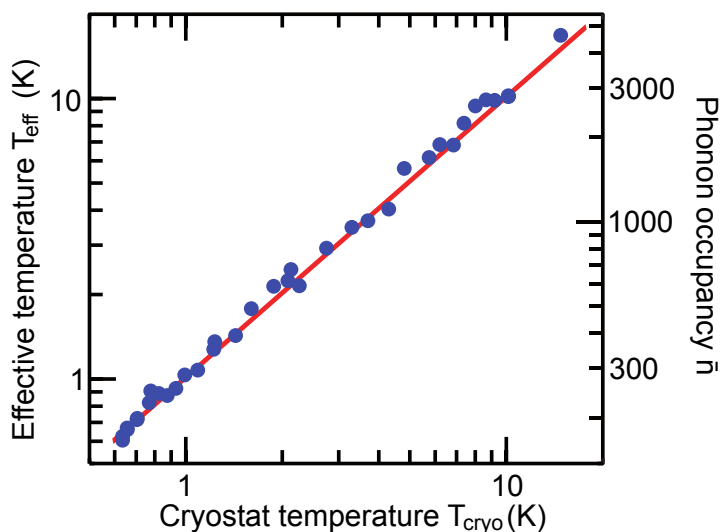
Figure 3.32: *Mechanical radial breathing mode thermalization curve in the helium-3 cryostat, reaching an occupancy below 200 at 600 mK confirming the efficiency of the exchange gas technique for toroidal microresonators. The data points are taken with a Koheras 1550 nm erbium fiber laser at a power below 1 μW locked to the resonance of a WGM.*

The cryohead (Fig. 3.31 (b)) is designed to adapt the one of the ^{4}He cryostat (Fig. 3.18 (b)) to the even more confined space of $38\,\mathrm{mm}$ in diameter of the current cryostat. An additional constraint is to leave enough passage to ensure a significant pumping speed across the cryohead to evaporate the bath of the liquid ^{3}He residing at the bottom of the chamber. Additionally, a protecting cup covers the whole cryohead to ensure that the gaseous stream of the evaporation does not mechanically drive the cryotaper into motion. The spatial approach of the resonator to the cryotaper is ensured by two slip-

stick motion piezoelectric displacers (Attocube Systems AG ANPx51/LT) and the phase matching is adjusted at room temperature using the same type of mechanical slide as previously described. The temperature of the cryohead T_{cryo} is measured with a Lakeshore CX-1010-CI-0.3L Cernox sensor resistively readout with a Model 336 controller.

The setup proved to be appropriately designed, allowing stable coupling of the resonator and thermalization down to 600 mK or less than 200 phonons for the 76.3-MHz RBM investigated, as depicted on Fig. 3.32. The excellent agreement of the experimental points (blue dots) with the line (red guide to the eye) proves the thermalization of the mechanical mode with the cryogenic device.

3.5 Measurement of low phonon numbers

The previous sections of this chapter introduced the various improvements intended to lower the phonon occupancy of the mechanical radial breathing mode subjected to dynamical backaction cooling. The performance leap achieved with the ^{3}He setup makes it particularly relevant to envisage observing quantum signatures of the mechanical oscillator in the near future. Previously, quantum effects were observed in a simply thermodynamically cooled HF oscillator piezoelectrically coupled to a superconducting qubit [171]. Although scientifically interesting, this cooling scheme is confined to the material spectrum usable with superconducting qubits and to mechanical oscillators with resonance frequencies high enough to exhibit a quantum temperature reachable by conventional cryogenics. Other attempts to reach an occupancy below one were limited by the intrinsic thermal noise of the optical field used at radio frequencies [58], that were only recently overcome [59]. Recently, at optical frequencies, a phonon occupancy of 0.85±0.04 [57] was very recently measured in an optomechanical crystal.

This section presents the proof-of-principle of optomechanical cooling of a toroidal resonator close to its quantum ground state in the experimental cryostat. Using a specifically built homodyne detection, mechanical spectra are recorded with a sensitivity down to $3.2 \times 10^{-19}\,\mathrm{m}/\sqrt{\mathrm{Hz}}$. The effective temperature is extracted from the optical spring and damping effects and compared with the independent estimation given by calibrating noise spectra, allowing to estimate a cooling down to 9 ± 1 phonon occupancy. Importantly, intracavity light absorption is significantly reduced compared to the previous cooling attempt due to a resolved-sideband factor more than three times higher. In addition, the imprecision-backaction product is lowered closer to the Heisenberg limit, as expected from the measurement improvement. The thermal dependence of the two-level system induced damping is exploited to quantify the excess heating resulting from the absorption of the light transversely scattered from the coupling waveguide. This relatively basic effect is shown to be the main limitation of the cooling performance of this experimental run.

3.5.1 The balanced homodyne detection

To detect small fluctuations of the mechanical oscillator subjected to cooling, the detecting field should carry the least classical fluctuations. For this reason, we are using the quantum-limited Ti:sapphire laser (section 3.3) to simultaneously cool and probe the optomechanical system. In addition, the phase quadrature of the output field should be detected and amplified above any other sources of detection noise for any arbitrary input power. The side-of-the-fringe technique introduced in section 3.2.1 does not satisfy the last condition, as its sensitivity scales with the intracavity power. For the PDH detection technique detailed in section 3.4.3, the amplification of the signal also requires to increase the input field s_0, therefore suffering from the same limitation.

The best detection technique in terms of sensitivity is achieved with a balanced homodyne interferometer which directly addresses and amplifies the phase quadrature of the output field s_{out}. Conceptually, the laser field is split into two parts: the signal field which

probes the cavity and the strong local oscillator (LO) field s_{LO}. Each field runs along a different arm of the interferometer. After running each path and acquiring a controlled phase difference, the two fields mix on a beam splitter. The AC component of the subtraction of the photodetected signals from both ports is then the product of the mean strong LO field and the fluctuations of the signal field's quadrature oscillating in phase with the LO field. Varying the phase difference thus allows to address and amplify the desired quadrature of the signal field probing the cavity.

The fundamentals of the detection are detailed here, and the experimental implementation is described, along with the various additions relevant to the cooling experiment.

Principle of the detection

The principle of the balanced homodyne detector is simplified in Fig. 3.33 [172]. In this Mach-Zehnder type interferometer, the laser source is split into two fields: the signal field and the local oscillator field. They acquire a phase difference ϕ due to the difference of optical path lengths of the two arms controlled by the positioner. The output field exiting the cavity s_{out} carrying the mechanically induced phase fluctuations is reflected by the polarizing beam splitter PBS$_1$, whereas the strong local oscillator field s_{LO} is transmitted. The two fields are then spatially co-located but of orthogonal polarizations and do not interfere on PBS$_1$. Then, the $\lambda/2$ waveplate rotates both polarizations by 45° and makes them interfere on PBS$_2$. The reflected "r" and transmitted "t" fields then read (the fields' mean values are taken real in this section)

$$s_{\text{r}}(t) = \frac{1}{\sqrt{2}} \left(s_{\text{out}}(t) - s_{\text{LO}}(t)e^{i\phi} \right), \tag{3.52}$$

$$s_{\text{t}}(t) = \frac{1}{\sqrt{2}} \left(s_{\text{out}}(t) + s_{\text{LO}}(t)e^{i\phi} \right). \tag{3.53}$$

The subtracted "-" photodetected optical power is given by

$$P_-(t) = P_{\text{t}}(t) - P_{\text{r}}(t) = s_{\text{out}}(t)s_{\text{LO}}^*(t)e^{-i\phi} + s_{\text{out}}^*(t)s_{\text{LO}}(t)e^{i\phi}, \tag{3.54}$$

$$\tag{3.55}$$

giving rise to the measured voltage at the photodiode $V_-(t)$.

The linearization procedure gives for the mean value

$$\bar{V}_- \propto 2\bar{s}_{\text{out}}\bar{s}_{\text{LO}}\cos(\phi), \tag{3.56}$$

and for the time dependent fluctuations

$$\delta V_-(t) \propto \bar{s}_{\text{LO}} \left(\delta s_{\text{out}}(t)e^{-i\phi} + \delta s_{\text{out}}^*(t)e^{i\phi} \right) + \bar{s}_{\text{out}} \left(\delta s_{\text{LO}}(t)e^{i\phi} + \delta s_{\text{LO}}^*(t)e^{+i\phi} \right). \tag{3.57}$$

For a strong local oscillator $\bar{s}_{\text{LO}} \gg \bar{s}_{\text{out}}$ in Eq. (3.57), the signal $\delta V_-(t)$ is proportional to the fluctuation of one quadrature of the output field s_{out} amplified by the strong field. The measured signal is then proportional to

$$\delta V_-(t) \propto \bar{s}_{\text{LO}} \left(\delta s_{\text{out}}(t)e^{-i\phi} + \delta s_{\text{out}}^*(t)e^{i\phi} \right). \tag{3.58}$$
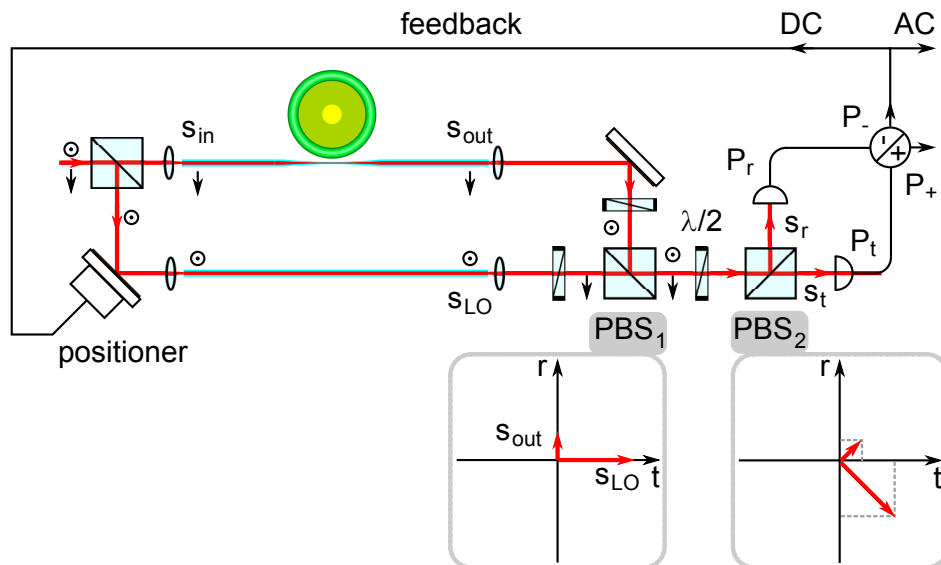
Figure 3.33: *Simplified scheme of the balanced homodyne detection principle. The polarization of each field is symbolically represented, and their projection on the axis of the polarizing beam splitters (PBS) are given in insets. "r": reflection, "t" transmission.*

The phase difference ϕ determines the quadrature angle of the field fluctuations that is amplified by the local oscillator's mean field $\bar{s}_{\mathrm{LO}}$. Thanks to the strong amplification by the factor $\bar{s}_{\mathrm{LO}}$, the quantum noise of the signal $\bar{s}_{\mathrm{out}}$ can be made dominant over all sources of technical noise, allowing to reach the best detection sensitivity authorized by quantum mechanical limitations.

Practically, the mean value of the subtracted photovoltage Eq. (3.56) provides an error signal proportional to $\cos(\phi)$ to the feedback loop, stabilizing then the phase difference ϕ. Locking the LO phase in order to get a zero value for $\bar{V}_-$, one gets a value of $\phi = \pi/2$, for which the detector measures the phase quadrature fluctuations of the output field.

Experimental setup

The experimental setup of the balanced homodyne detector is depicted in Fig. 3.34.

From the Ti:sapphire laser described in section 3.3, a small portion of the 780 nm collimated beam is collected. It is then directed to a Pound-Drever-Hall detection setup (section 3.4.3) to lock the frequency of the longitudinal mode of interest to the frequency of the TEM$_{00}$ mode of a thermally stabilized and vacuum-operated external Fabry-Perot cavity (RefCell). The locking error signal is recorded and the output optical mode imaged with a CCD camera (picture inset) to ensure proper locking. The main beam is directed through an electro-optic modulator and various beam attenuation units before being fed to the Mach-Zehnder interferometer using a polarization-maintaining fiber (dark blue coating). In addition, a 780 nm diode laser can be coupled to the signal arm to quickly determine the resonator's resonance. The beat with the Ti:sapphire beam indicates its detuning, thus allowing proper frequency adjustment. The mixed fields outputting the interferometer are
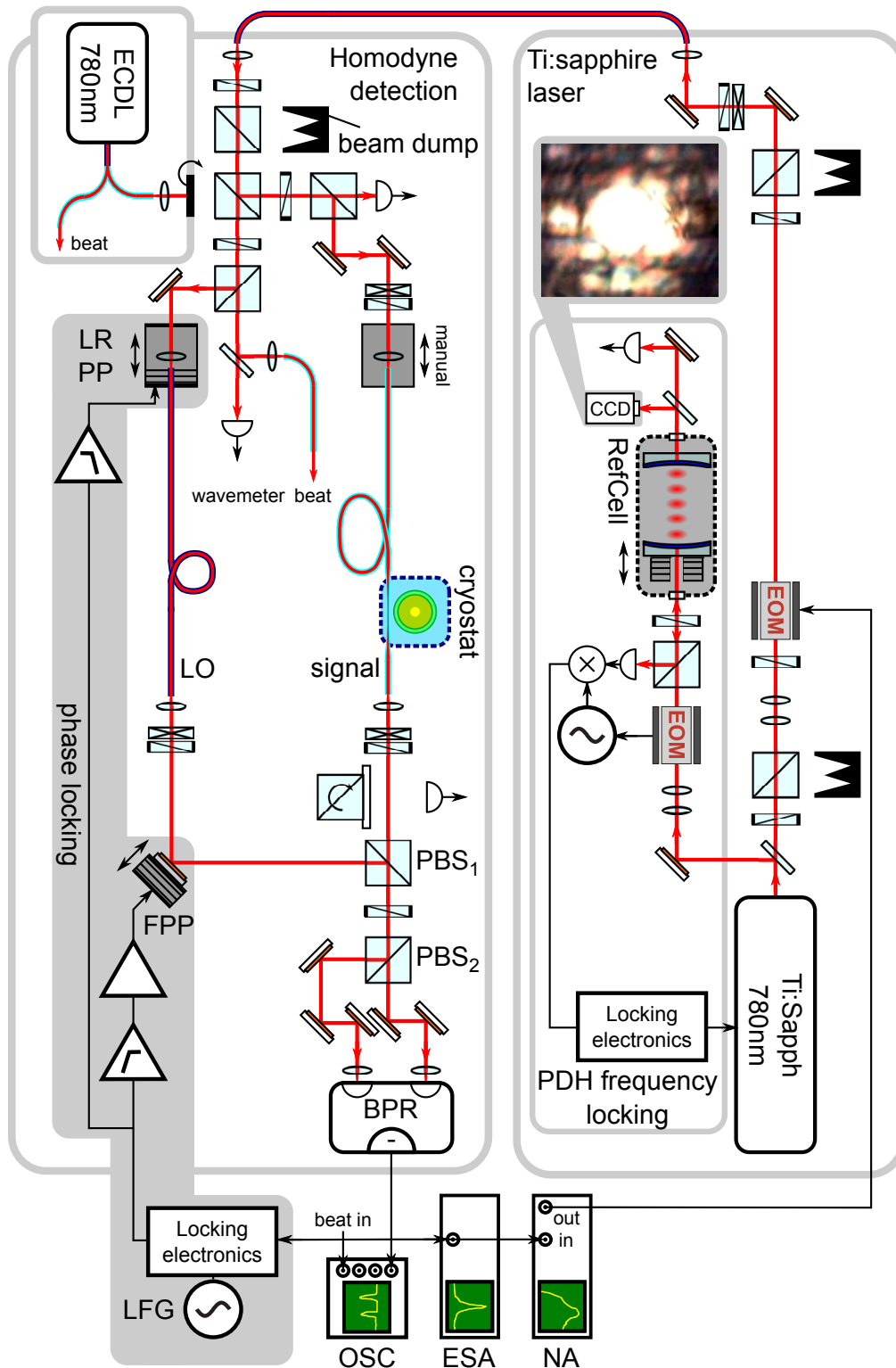
Figure 3.34: *Optical and electronic layout of the Ti:sapphire laser and the balanced homodyne detection. OSC: oscilloscope, ESA, electrical spectrum analyzer, NA: network analyzer, ECDL: external cavity diode laser, BPR: balanced photoreceiver, PP: piezoelectric positioner (LR: long range, F: fast), LFG: low frequency generator, EOM: electrooptic modulator.*

focused on the two photodetectors of a 80 MHz balanced photoreceiver (BPR, New Focus 1807-FS). After proper spectral selection using a digital filter (Stanford Research Systems SR560), the mean value of the subtracted photosignal is fed back to the two piezoelectric positioners providing a slow long-range (low-pass bandwidth of 0.3 Hz) and fast (band-pass bandwidth from 0.1 Hz to 100 kHz) displacement to keep the phase difference $\pi/2$, maintaining the mean value of the homodyne signal to 0. The former compensates slow thermal drifts whereas the latter compensates fast acoustic vibrations, their tuning ranges being respectively 950 and $\sim 10\,\mu$m. Along the beam path, various stages of power measurements are included. Ideally, the detector should be configured so that light collected from the signal arm is reflected from the polarizing beam splitter PBS_1 as in Fig. 3.34 to avoid that the intrinsic higher losses in transmission reduces the amount of light collected. The sensitivity of the current non-ideal configuration allows nevertheless satisfying detection of the mechanical modes.

The spatial overlap of the signal and LO beams on PBS_2 is calculated from the interference fringes by scanning the optical path difference with the low frequency generator (LFG) [173]. Experimental values of 85% overlap are typically obtained. The balancing of the interferometer is performed by simply phase modulating the input beam and modifying the length of the LO fiber until the interference fringes vanish. Even more accurate balancing is achieved by minimizing the fringes detected with an electrical spectrum analyzer (ESA).

Demodulation of the signal phase fluctuations with an ESA (Agilent MXA N9020A) gives after proper averaging the mechanical spectrum that is further analyzed to quantify the optical spring and damping effect. Under optimum conditions and after cryogenic pre-cooling, the sensitivity of the detector at the mechanical frequency of interest around 70 MHz reaches $3.2 \times 10^{-19}\,\mathrm{m}/\sqrt{\mathrm{Hz}}$ as detailed in the next section, a value that permits to envisage detection of the zero point motion of the mechanical oscillator. The amplification provided by the LO ensures that the optical shot noise is at least 10 dB higher than the electronic noise of the detections circuit under normal operation.

The calibration of the mechanical spectrum is equivalent to the description given in section 3.4.3. The network analyzer in zero-span configuration provides the calibration tone being applied to the Ti:sapphire's EOM and detected using the homodyne signal.

Additionally, by scanning the phase modulation of the calibration with the network analyzer, the optical transmission of the cavity is measured. Essentially, the phase modulation generates an upper and lower sideband from the detuned laser. When the laser is detuned to $-\Omega_{\mathrm{m}}$ and in the RSB regime, only the former interacts with the cavity after passing through the signal arm. Then, upon demodulation of the beat with the LO carrier, the NA measures a signal proportional to the transmission of the cavity, therefore plotting the transmission of the toroidal cavity relevant for the optomechanically induced transparency measurements detailed in section 3.6.

3.5.2   Dynamical backaction cooling

Measurements of dynamical backaction effects

Dynamical backaction cooling on the mechanical radial breathing mode of a toroid placed in the cryostat down to a phonon occupancy of 9 ± 1 is now performed. First, the optical spring and damping effects are characterized from the mechanical spectra detected with the balanced homodyne detector. Besides, the estimated elevation of temperature due to intracavity absorption is shown to be strongly reduced as a consequence of the record resolved-sideband factor of more than 10 achieved. Then, using this novel thermometry method based on the thermal dependence of TLS-induced dissipation, the elevation of temperature due to scattering from the taper is characterized. This phenomenon is shown to limit the cooling performance and the imprecision-backaction product.

Figure 3.35 shows the effective frequency Ω_{eff} and linewidth Γ_{eff} of the radial breathing mode of a needle-pillar microtoroid when the cooling laser is scanned across the lower sidebands of the two split resonances. The experiment is performed at $850\,\mathrm{mK}$ with a measured pressure of $2.8\,\mathrm{mbar}$, ensuring significant thermalization.

The double dispersive and dissipative signature of the radiation pressure effect comes from the split of the whispering-gallery mode, as represented on the inset. Backscattering of the light couples the counter-clockwise "ccw" and clockwise "cw" modes, therefore lifting the degeneracy of the eigenmodes of the system. The expression of the radiation pressure force acting on the mechanical mode is then modified. Since the fields are classical and coherent, the operators introduced in expressions (1.13) to (1.15) are identified with their expectation values, and the quantum optical noises are dropped. The equations of motion of the two counter-propagating modes are then given by

$$\dot{a}_{\mathrm{ccw}}(t) = (i(\Delta - Gx(t)) - \kappa/2)a_{\mathrm{ccw}}(t) + i\frac{\gamma}{2}a_{\mathrm{cw}}(t) + \sqrt{\eta_{\mathrm{c}}\kappa}s_{\mathrm{in}}(t), \qquad (3.59)$$

$$\dot{a}_{\mathrm{cw}}(t) = (i(\Delta - Gx(t)) - \kappa/2)a_{\mathrm{cw}}(t) + i\frac{\gamma}{2}a_{\mathrm{ccw}}(t). \qquad (3.60)$$

with γ being the coupling rate between the two modes. The eigenmodes of the steady-state of this set of equations are given by the following linear combinations

$$a_+ = (a_{\mathrm{ccw}}(t) + a_{\mathrm{cw}}(t))/\sqrt{2}, \qquad (3.61)$$

$$a_- = (a_{\mathrm{ccw}}(t) - a_{\mathrm{cw}}(t))/\sqrt{2}. \qquad (3.62)$$

The exerted radiation pressure force is then [55]

$$F_{\mathrm{rp}} = -\hbar G(|a_+(t)|^2 + |a_-(t)|^2), \qquad (3.63)$$

since the spatial projection of the cross-terms proportional to $\cos(m\varphi)\sin(m\varphi)$ on the rotationally symmetric mechanical RBM cancels (m is the azimuthal mode number of the WGM). The radiation pressure forces from the light in both eigenmodes simply add.
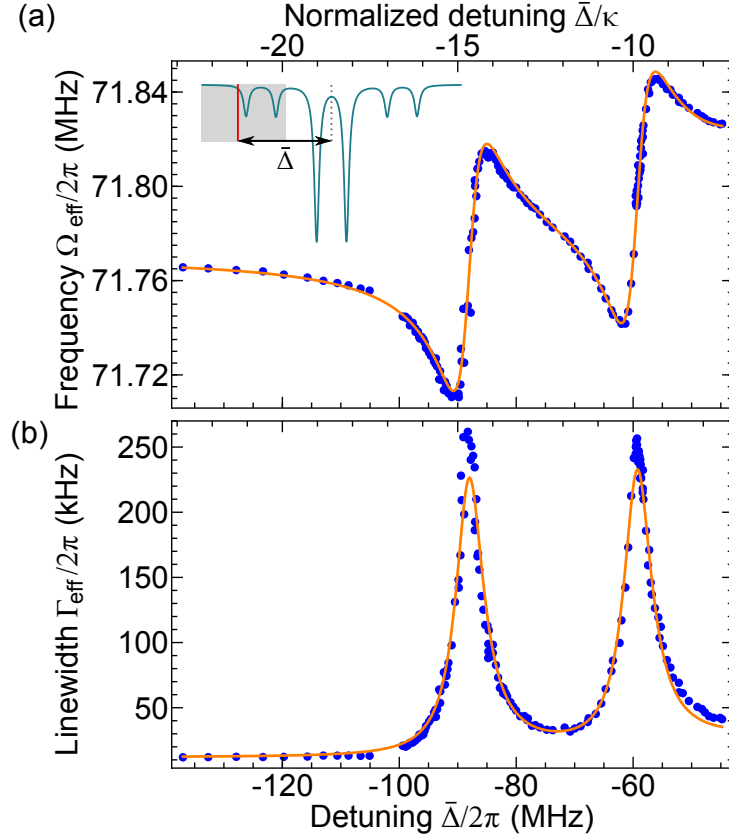
Figure 3.35: *Effective mechanical frequency (a) and linewidth (b) recorded when the 2 mW-power laser is scanned through the lower motional sideband of the split optical mode (modeled in inset). The sample is a $25 - \mu m$ radius needle-pillar microtoroid supporting a mechanical RBM of effective mass of 20 ± 5 ng and exhibiting a coupling factor $G \approx 2\pi \times 16$ GHz/nm. Blue points are the output parameters of the Lorentzian fits performed on the mechanical spectra, the orange line is a coupled fit to Eqs. (3.69 - 3.70). Adapted from Ref. [55].*

The equations of motion then read

$$\ddot{x}(t) = -\Omega_{\mathrm{m}}^2 \hat{x}(t) - \Gamma_{\mathrm{m}}\dot{x}(t) - \frac{\hbar G}{m_{\mathrm{eff}}}(|a_+(t)|^2 + |a_-(t)|^2) + \sqrt{\Gamma_{\mathrm{m}}}\xi_{\mathrm{th}}(t), \qquad (3.64)$$

$$\dot{a}_+(t) = \left(i(\Delta + \gamma/2 - Gx(t)) - \frac{\kappa}{2}\right)a_+(t) + \sqrt{\frac{\eta_{\mathrm{c}}\kappa}{2}}s_{\mathrm{in}}(t), \qquad (3.65)$$

$$\dot{a}_-(t) = \left(i(\Delta - \gamma/2 - Gx(t)) - \frac{\kappa}{2}\right)a_-(t) + \sqrt{\frac{\eta_{\mathrm{c}}\kappa}{2}}s_{\mathrm{in}}(t). \qquad (3.66)$$

Using the linearization procedure of the small fluctuations of parameters around their mean values introduced in section 1.2.2, the expression of the effective mechanical susceptibility is given by

$$\chi_{\mathrm{eff}}^{-1}(\Omega) = \chi_{\mathrm{m}}^{-1}(\Omega) - i\Omega_{\mathrm{m}}m_{\mathrm{eff}}h(\Omega). \qquad (3.67)$$

The radiation pressure induced modification of the susceptibility is then given by

$$h(\Omega) = 2g_0^2 \sum_{\sigma=\pm} |\bar{a}_\sigma|^2 \left(L_\sigma(\bar{\Delta} + \Omega) - L_\sigma^*(\bar{\Delta} - \Omega) \right), \tag{3.68}$$

considering the high-Q approximation, and after Fourier transform. The function $L_\pm(\bar{\Delta}) = \left(-i(\bar{\Delta} \pm \gamma/2) + \kappa/2 \right)^{-1}$ is the Lorentzian expression of each eigenmodes' mean value $\bar{a}_\pm = \sqrt{\eta_c \kappa/2} L_\pm(\bar{\Delta}) \bar{s}_{\mathrm{in}}$ [55]. $\bar{\Delta}$ is the laser detuning accounting for the static mechanical shift of the resonance.

When the cooling laser is scanned, the modification of the intracavity power results in a detuning dependent elevation of temperature due to absorption. Because of the silica two-level systems, it changes the intrinsic mechanical properties of the RBM. The total effective change therefore reads

$$\Omega_{\mathrm{eff}} \simeq \Omega_{\mathrm{m}}(T) + \mathrm{Re}[f(\Omega_{\mathrm{m}})], \tag{3.69}$$
$$\Gamma_{\mathrm{eff}} \simeq \Gamma_{\mathrm{m}}(T) + \mathrm{Im}[f(\Omega_{\mathrm{m}})]/2, \tag{3.70}$$

where $\Omega_{\mathrm{m}}(T)$ and $\Gamma_{\mathrm{m}}(T)$ are given by expressions (3.23) and (3.24), respectively. This model is used to perform a coupled fit of the effective frequency and linewidth of the RBM varying with detuning (orange line in Fig. 3.35). Since the determination of the mechanical resonance frequency is less prone to fit errors, its weight in the coupled fit is a factor of ten higher. Excellent agreement is found when accounting for an elevation of temperature δT_{WGM} dependent on the (detuning dependent) intracavity power according to $\delta T_{\mathrm{WGM}} = \chi_{\mathrm{th}}^{\mathrm{stat}} \kappa_{\mathrm{abs}}(|a_+|^2 + |a_-|^2)\hbar\omega_{\mathrm{l}}$. The total environmental temperature of the RBM is therefore given by

$$T \approx T_{\mathrm{cryo}} + \delta T_{\mathrm{WGM}} + \delta T_{\mathrm{stray}}. \tag{3.71}$$

The last term is the elevation of temperature determined by monitoring the change of $Q_{\mathrm{m}}^{-1}(T)$ at high detunings and negligible intracavity power. The heating is here attributed to the absorption of the stray light transversely scattered from the tapered fiber by dusts aggregating on the taper region.

For the run described in Fig. 3.35, $\delta T_{\mathrm{WGM}} \approx 70\,\mathrm{mK}$ on the lower sideband and $\delta T_{\mathrm{stray}}$ is estimated to be $220\,\mathrm{mK}$. Although small in absolute terms, the stray light heating deteriorates the mechanical quality factor from $Q_{\mathrm{m}}(T_{\mathrm{cryo}}) \simeq 8700$ to $Q_{\mathrm{m}}(T_{\mathrm{cryo}} + \delta T_{\mathrm{stray}}) \simeq 5970$ at $71.76\,\mathrm{MHz}$, therefore contributing significantly to the reduction of the performance of the cooling process. The fitted parameters κ, γ and s_{in} are found to be in good agreement with the independent estimations from the measurements of the transmission of the cavity, giving $\kappa \approx 2\pi \times 6\,\mathrm{MHz}$, $\gamma \approx 2\pi \times 30\,\mathrm{MHz}$ and $P_{\mathrm{in}} = |\bar{s}_{\mathrm{in}}|^2 \hbar\omega_{\mathrm{l}} \approx 2\,\mathrm{mW}$.

Phonon occupation

The previous analysis of the optical spring and damping effects allows to extract the phonon occupation by using expression (1.54), taking into account the elevation of temperature due to absorption. The minimum phonon occupation is less than 10^{-3} for the RSB factor of
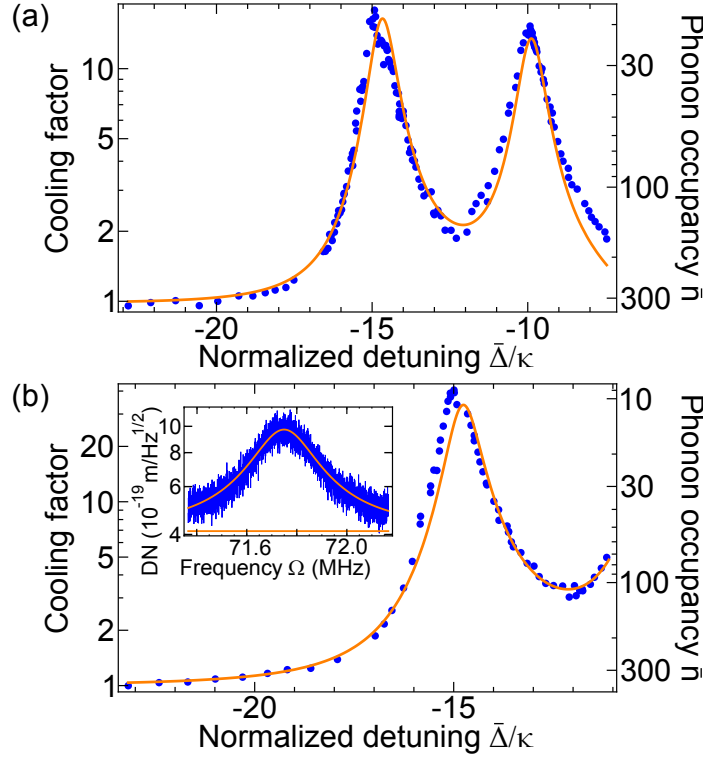
Figure 3.36: *Cooling factor $(T_{\mathrm{cryo}} + \delta T_{\mathrm{stray}})/T_{\mathrm{eff}}$ and phonon occupancy $\bar{n}$ versus detuning of the cooling laser for 2 mW (a) and 4 mW (b) input power. Blue points are occupancy derived directly from the noise spectrum whereas the orange lines show the occupancy extracted from the fitted optical spring and damping effect depicted in Fig. 3.35. The inset shows the displacement noise (DN) at optimum detuning $\bar{\Delta}_{\mathrm{opt}} = -\Omega_{\mathrm{m}} - \frac{\gamma}{2}$ in (a). Adapted from Ref. [55].*

more than 10 for the present experiment. Figure 3.36 (a) shows the calculated cooling factor $(T_{\mathrm{cryo}} + \delta T_{\mathrm{stray}})/T_{\mathrm{eff}}$ and the corresponding phonon occupation for the previously described run (orange line). To test the consistency of the estimation of $T_{\mathrm{eff}} = T \times \Gamma_{\mathrm{m}}(T)/\Gamma_{\mathrm{eff}}$, it is compared with the effective temperature extracted from noise thermometry directly performed on relatively calibrated mechanical spectra, as explained in section 3.4.3. The good agreement demonstrates the correctness of the model used to characterize the different sources of heating. Optomechanical amplification of the phase modulation (oscillating at a frequency close to Ω_{m} although away from the mechanical bandwidth) is taken into account according to the model described in Ref. [43].

Figure 3.36 (b) shows this comparison for a 4 mW input power for which the stray light heating elevation of temperature evaluates to $\delta T_{\mathrm{stray}} = 400$ mK whereas the elevation due to intracavity absorption is too small to be discerned. With an intrinsic mechanical quality factor of $Q_{\mathrm{m}}(T_{\mathrm{cryo}} + \delta T_{\mathrm{stray}}) = 4880$, the estimation from the coupled fit of the optical spring and damping effect yields $\bar{n} = 10$. The inferred noise temperature gives an even lower occupancy of 9 ± 1, the uncertainty being dominated by systematic errors estimated from the deviations of both methods.

Imprecision-backaction product

In the context of quantum measurements introduced in section 1.3, the amount of back-action introduced by the measurement is quantified. The imprecision-backaction product expressed in Eq. (1.65) considers only quantum fluctuations of the probing laser, exhibiting a minimum of $(\hbar/2)^2$. Upon experimental measurements, the laser unavoidably introduces excess force fluctuations via intracavity and stray light absorption heating. This is quantified here at the optimum detuning leading to the lowest occupancy.

The imprecision of the measurement is straightforwardly estimated from the calibrated background of the recorded mechanical spectrum, as the one showed in the inset of Fig. 3.35. It evaluates to

$$\bar{S}_{xx}^{\text{imp}} \equiv \bar{S}_{xx}^{\text{imp}}(\Omega_{\text{m}}) = (3.2 \times 10^{-19}\,\text{m}/\sqrt{\text{Hz}})^2.$$

Its measured linear dependence on the laser input power P_{in} shows that it is strongly dominated by the quantum noise of the input laser. Consequently, the quantum imprecision expressed in Eq. (1.64) is approximated by $\bar{S}_{xx}^{qi}(\Omega_{\text{m}}) \approx \bar{S}_{xx}^{\text{imp}}$.

From expression (1.46), the total thermal force noise at a temperature T (for $\frac{k_{\text{B}}T}{\hbar\Omega_{\text{m}}} \gg 1$) is expressed as

$$\bar{S}_{FF}^{\text{th}} \approx 2m_{\text{eff}}k_{\text{B}}T\Gamma_{\text{m}}(T), \tag{3.72}$$

leading to

$$\bar{S}_{FF}^{\text{th}} \approx 2m_{\text{eff}}k_{\text{B}}T_{\text{eff}}\Gamma_{\text{eff}}, \tag{3.73}$$

in the presence of optical spring and damping effects, simply using the expression of the effective temperature given by $T_{\text{eff}} \approx T \cdot \Gamma_{\text{m}}(T)/\Gamma_{\text{eff}}$. It evaluates to

$$\bar{S}_{FF}^{\text{th}} = ((8 \pm 2) \times 10^{-15}\,\text{N}/\sqrt{\text{Hz}})^2,$$

where Γ_{eff} and T_{eff} are extracted from the fits to the detuning series, evaluated at the optimum detuning $\bar{\Delta}_{\text{opt}} = -\Omega_{\text{m}} - \frac{\gamma}{2}$. This value gives a conservative estimate of the *classical measurement backaction*, considering all force noise as a classical backaction. The classical backaction solely originating from the measurement (i.e. from the laser) is estimated by subtracting from the total thermal force noise the contribution of the nonzero temperature of the cryostat. The thermal force noise originating from this bath

$$\bar{S}_{FF}^{\text{cryo}} = 2m_{\text{eff}}k_{\text{B}}T_{\text{cryo}}\Gamma_{\text{m}}(T_{\text{cryo}}), \tag{3.74}$$

is estimated to

$$\bar{S}_{FF}^{\text{cryo}} = ((5 \pm 1) \times 10^{-15}\,\text{N}/\sqrt{\text{Hz}})^2.$$

T_{cryo} and $\Gamma_{\text{m}}(T_{\text{cryo}})$ are extracted from independent low input power measurements where the mechanical radial breathing mode is thermalized to the cryostat's temperature. Finally, the excess classical backaction force noise evaluates to

$$\bar{S}_{FF}^{\text{cba}} \simeq \bar{S}_{FF}^{\text{th}} - \bar{S}_{FF}^{\text{cryo}} = ((6 \pm 2) \times 10^{-15}\,\text{N}/\sqrt{\text{Hz}})^2,$$

accounting for 60% of the thermal force fluctuations driving the mechanical oscillator.

The quantum backaction expressed in (1.71) for optimum detuning is evaluated to $(10^{-15}\,\mathrm{N}/\sqrt{\mathrm{Hz}})^2$ in our case, therefore being negligible in the total imprecision-backaction product. It yields the (for $\frac{k_\mathrm{B}T}{\hbar\Omega_\mathrm{m}} \gg 1$)

$$\bar{S}^\mathrm{qi}_{xx}(\bar{S}^\mathrm{th}_{FF} + \bar{S}^\mathrm{qba}_{FF}) \approx \bar{S}^\mathrm{qi}_{xx}\bar{S}^\mathrm{th}_{FF} = (49 \pm 8)^2 \left(\frac{\hbar}{2}\right)^2.$$

Considering only the classical backaction as measurement backaction, the product is at least a factor of 2 smaller than for the cooling run performed in the ^{4}He cryostat. In an ideal measurement, this product is equal to $(\hbar/2)^2$, corresponding to the best compromise between the quantum imprecision and the quantum backaction. In this experimental run, the classical backaction is dominated by the light transversely scattering off the taper and being absorbed by the toroid. Upon resolution of this problem, it is then possible to perform measurements for which the measurement backaction would be dominated by quantum fluctuations.

Using dynamical backaction cooling via intracavity radiation pressure, the described experimental performance demonstrates the feasibility of refrigerating a silica microtoroid to the quantum ground state after pre-cooling in the experimental ^{3}He cryostat and using the quantum-limited Ti:sapphire laser combined with the balanced homodyne detection. The technical obstacle that limits the reported performance can be simply removed by fabricating the tapered fiber in a clean atmosphere and by avoiding the penetration of aggregating contaminants in the cryostat, as it is currently performed in the group. Although the final phonon occupancy of 9 ± 1 is still too high to observe quantum effects such as motional sideband asymmetry with a good accuracy, the achieved performance is still comparable to recent results reporting phonon occupancies of 3.8 ± 1.3 in 2010 [58], and 0.34 ± 0.05 [59] in electromechanics and 0.85 ± 0.04 [57] in optomechanics in 2011. The constructed experiment is therefore a promising candidate for the observation of dynamical backaction cooling down to the motional ground state. Very recently in the group, laser cooling of optimized spoke toroids with higher vacuum optomechanical coupling rates have led to the cooling of the mechanical mode down to 1.7 ± 0.1 phonon occupancy. Along these lines, another interesting approach is to perform feedback cooling and quantum limited detection on an external mechanical oscillator coupled to the evanescent part of the circulating field of a toroid. Complete decoupling of the two degrees of freedom allow efficient engineering the parameters of the system, eventually putting it into premier position for cooling to the quantum ground state [174, 175].

3.6 Optomechanically induced transparency

The study pursued so far on the optomechanical interaction has been focused on the resulting modification of the mechanical response and the deriving cooling effect. From the mutual aspect of this coupling, it is justified to expect a reciprocal modification of the dispersive and dissipative properties of the optical cavity. To observe this effect, a weak laser probes the optomechanical system subjected to another intense laser detuned at $\bar{\Delta} = -\Omega_m$ maximizing the optomechanical coupling. When the beat frequency of the two lasers is equal to the mechanical resonance frequency, a destructive interference renders the cavity transparent upon probing.

   The classical aspect of the phenomenon is explained here, starting from the coupled equations of motion of the optical and mechanical modes. The experimental manifestations of the optomechanically induced transparency are measured for the first time [120], demonstrating a transparency of more than 80% in the optimal configuration. Thereafter, the quantum analogy between this effect and the atomic electromagnetically induced transparency [176, 177] is demonstrated.

3.6.1 Principle of the optomechanically induced transparency

To obtain a physical understanding of the problem, the equations of motions introduced in section 1.2.2 are considered in more detail [120]. Since the fields are classical and coherent, the operators introduced in expressions (1.13) to (1.15) are identified with their expectation values, and the quantum and thermal noises are dropped. The driving field is here $s_{\mathrm{in}}(t) = (\bar{s}_{\mathrm{in}} + \delta s_{\mathrm{in}}(t))e^{-i\omega_l t}$. The equations of motion are solved for the perturbation term $\delta s_{\mathrm{in}}(t) = s_p\, e^{-i\Omega t}$ being the "probe" of the optical cavity subjected to the "coupling" field $\bar{s}_{\mathrm{in}}$. The probe field oscillates at an angular frequency $\omega_p = \omega_l + \Omega$.

   To proceed, the ansatz

$$\delta a(t) = A^- e^{-i\Omega t} + A^+ e^{+i\Omega t}, \tag{3.75}$$

$$\delta a^*(t) = (A^+)^* e^{-i\Omega t} + (A^-)^* e^{+i\Omega t}, \tag{3.76}$$

$$\delta x(t) = X e^{-i\Omega t} + X^* e^{+i\Omega t}, \tag{3.77}$$

is introduced. The problem is analyzed in the case where the coupling laser is detuned to the lower motional sideband $\bar{\Delta} \simeq -\Omega_m$, with the static shift of the resonance frequency included in the modified detuning $\bar{\Delta}$. The probe field's transmission at the angular frequency $\omega_l + \Omega$ depends on A^-; therefore, the equations of interest deduced from Eqs. (1.23) to (1.25) are

$$(-i(\bar{\Delta} + \Omega) + \frac{\kappa}{2})A^- = -iG\bar{a}X + \sqrt{\eta_c \kappa}s_p, \tag{3.78}$$

$$(+i(\bar{\Delta} - \Omega) + \frac{\kappa}{2})(A^+)^* = +iG\bar{a}X, \tag{3.79}$$

$$m_{\mathrm{eff}}(\Omega_m^2 - \Omega^2 - i\Gamma_m\Omega)X = -\hbar G\bar{a}(A^- + (A^+)^*). \tag{3.80}$$

The intracavity probe amplitude is then given by

$$A^- = F(\Omega)s_{\mathrm{p}} = \frac{1 + if(\Omega)}{-i(\bar{\Delta} + \Omega) + \kappa/2 + 2\bar{\Delta}f(\Omega)}\sqrt{\eta_{\mathrm{c}}\kappa}s_{\mathrm{p}}, \qquad (3.81)$$

with

$$f(\Omega) = \hbar g^2 \bar{a}^2 \frac{\chi_{\mathrm{m}}(\Omega)}{i(\bar{\Delta} - \Omega) + \kappa/2}, \qquad (3.82)$$

where χ_{m} is the mechanical susceptibility. $F(\Omega)$ denotes the absorption of the probe by the cavity.

The introduced system of coupled equations allows to approach the physical interpretation of the phenomenon. The beat of the intracavity coupling and probe fields generates a radiation pressure force oscillating at Ω. For Ω close to the mechanical resonance frequency Ω_{m}, the mechanical oscillator is coherently driven. The resulting mechanical oscillations subsequently generate Stokes and anti-Stokes scattering out of the intracavity coupling field. If the system is in the resolved-sideband regime, Stokes scattering is strongly off-resonance therefore only the anti-Stokes field builds up in the cavity at the angular frequency $\omega_{\mathrm{l}} + \Omega$. The scattered field is thus degenerate with the probe field, therefore interfering with it destructively. This phenomenon, called optomechanically induced transparency (OMIT), opens a transparency window centered at $\Omega_{\mathrm{m}} = \Omega$ in the cavity transmission.

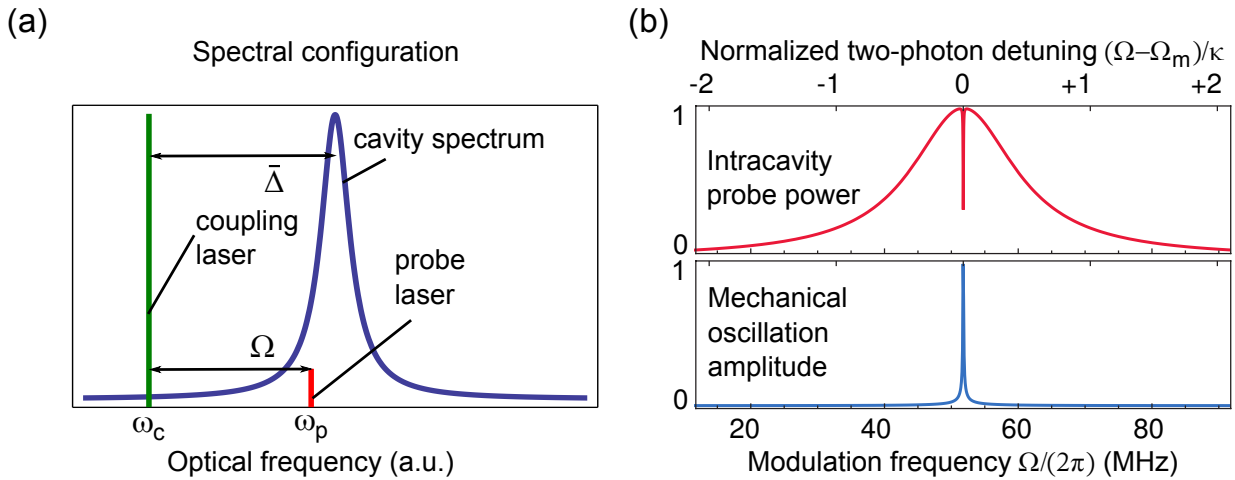**Figure 3.37:** *Optomechanically induced transparency principle. (a) OMIT configuration. The cavity subjected to a strong coupling laser at ω_{l} is probed by a weak laser at a frequency $\omega_{\mathrm{p}} = \omega_{\mathrm{l}} + \Omega$. (b) Normalized intracavity probe power and mechanical oscillation amplitude exhibiting the simultaneous optical transparency and mechanical coherent driving at the two-photon resonance condition $\Omega = \Omega_{\mathrm{m}}$. See text for details. Adapted from Ref. [120].*

Figure 3.37 describes the phenomenon in the resolved-sideband regime and for $\bar{\Delta} = -\Omega_{\mathrm{m}}$ (a), illustrating the coherent mechanical driving by the modulated intracavity radiation pressure beat (b, lower panel) leading to the optical transparency (b, upper panel) at

the condition $\Omega = \Omega_{\mathrm{m}}$. In analogy with atomic electromagnetically induced transparency (EIT), it is called the *two-photon resonance* condition.

To clarify our analysis of the OMIT phenomenon, the set of equations (3.75) to (3.77) is considered in the resolved sideband regime. For a coupling laser detuned at $\bar{\Delta} = -\Omega_{\mathrm{m}}$, the lower sideband is off-resonance; therefore, the term A^+ is neglected. The normalized mechanical coordinate amplitude $\tilde{X} = X/x_{\mathrm{zpf}}$ (see Eq. (1.11)) is introduced. Using the high-Q approximation for the mechanical oscillator, the equations of motion approximate then to

$$(\Omega_{\mathrm{m}} - \Omega - i\Gamma_{\mathrm{m}}/2)\,\tilde{X} + \Omega_{\mathrm{c}}/2\,A^- = 0, \tag{3.83}$$

$$\left(-\bar{\Delta} - \Omega - i\kappa/2\right) A^- + \Omega_{\mathrm{c}}/2\,\tilde{X} = -i\sqrt{\eta_{\mathrm{c}}\kappa}\,s_{\mathrm{p}}, \tag{3.84}$$

where $\Omega_{\mathrm{c}} = 2G\bar{a}x_{\mathrm{zpf}}$ is the field-enhanced coupling rate proportional to the square root of the mean field intracavity photon number. The rearrangement of the coupled equations of motion gives a different perspective of the physical principle. For $\bar{\Delta} < 0$, equations (3.83) and (3.84) suggest to consider the optical mode and the mechanical mode as two harmonic oscillators, with very different damping rates, coupled at a rate Ω_{c} controlled by the coupling field, as illustrated in Fig. 3.38 (a). By increasing the coupling rate such that $\Omega_{\mathrm{c}} \approx \sqrt{\kappa\Gamma_{\mathrm{m}}}$ (weak coupling regime), a sharp optical transparency window appears for a two-photon detuning close to the mechanical resonance (b). By increasing the pump power further, such that $\Omega_{\mathrm{c}} > \kappa$, two separated absorption peaks can be distinguished (strong coupling regime). These peaks are the consequence of the splitting between the two normal modes of the coupled system.
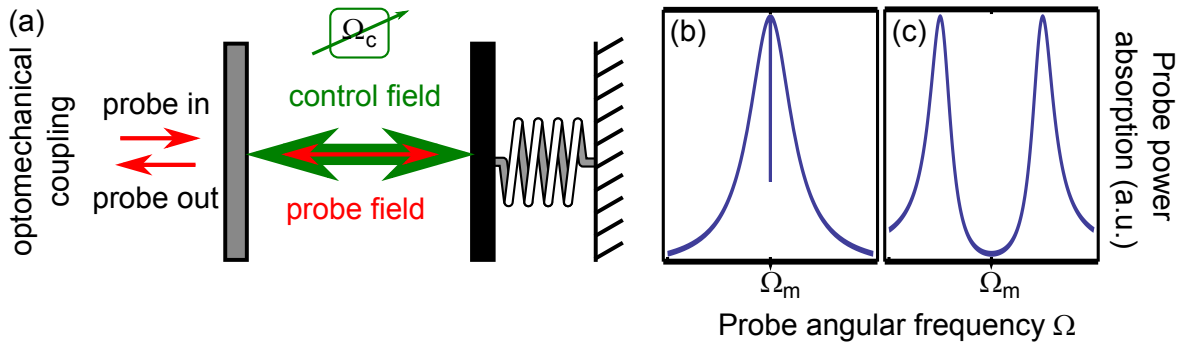

Figure 3.38: *(a) Optomechanical oscillators coupled at the rate Ω_{c}. Absorption of the optical cavity at the detuning $\bar{\Delta} = -\Omega_{\mathrm{m}}$ in the weak (b) and strong coupling regime (c).*

From expressions (3.83) and (3.84), the weak intracavity field can then be expressed by

$$A^- = F_{\mathrm{RSB}}(\Omega)s_{\mathrm{p}} = \frac{\sqrt{\eta_{\mathrm{c}}\kappa}}{-i(\bar{\Delta} + \Omega) + \kappa/2 + \dfrac{\Omega_{\mathrm{c}}^2/4}{-i(-\Omega_{\mathrm{m}} + \Omega) + \Gamma_{\mathrm{m}}/2}}\,s_{\mathrm{p}}, \tag{3.85}$$

where $F_{\mathrm{RSB}}(\Omega)$ is the absorption function of the cavity in the RSB regime.

3.6.2   Optomechanically induced transparency measurements

Measurement of the cavity transmission

The detection of the transmission of the optical cavity subjected to the strong detuned field is performed using the phase modulation-demodulation scheme already mentioned in section 3.5.1. Before entering the homodyne interferometer, the carrier is phase modulated at a frequency Ω. The resulting field is split in the two arms of the interferometers. The modulation frequency is swept in order for the upper sideband to be scanned through the optical resonance of the cavity.

The signal and local oscillator fields are entering the Mach-Zehnder combining element with the expressions

$$s_{\text{out}}(t) = \bar{s}_{\text{out}} \left(t_{\text{c}} + t_{\text{us}} i\frac{\beta}{2} e^{+i\Omega t} + t_{\text{ls}} i\frac{\beta}{2} e^{-i\Omega t} \right), \qquad (3.86)$$

$$s_{\text{LO}}(t) = \bar{s}_{\text{LO}} e^{i\phi} \left(1 + i\frac{\beta}{2} e^{+i\Omega t} + i\frac{\beta}{2} e^{-i\Omega t} \right), \qquad (3.87)$$

where t_{c}, t_{us} and t_{ls}, are the complex field cavity's transmission functions for respectively the carrier, the upper sideband and lower sideband. We use here the Jacobi-Anger expansion for modulation depth $\beta \ll 1$. ϕ is the locked phase difference between signal and local oscillator optical paths.

In the resolved-sideband regime, only the upper sideband close to resonance interacts with the cavity; therefore, $t_{\text{c}} \simeq t_{\text{ls}} \simeq 1$. For the upper sideband, the transmission function is $t_{\text{us}} = t_{\text{p}} = 1 - \sqrt{\eta_{\text{c}}\kappa}F(\Omega)$, with $F(\Omega)$ being the absorption function expressed in Eq. (3.81) in the general case and in Eq. (3.85) in the resolved-sideband regime, and t_{p} the transmission of the cavity. The phase difference between the signal and LO mean fields is actively locked to $\phi = \pi/2$ by maintaining the mean homodyne signal to 0. Neglecting terms of order higher than 1 in the small modulation index β, the voltage $V_-(t)$ measured across the photodetector's output is proportional to the photodetected power expressed in Eq. (3.54). Using expressions (3.86) and (3.87), it reads

$$V_-(t) \propto \cos(\Omega t)\left(1 - \text{Re}(t_{\text{p}})\right) + \sin(\Omega t)\left(\text{Im}(t_{\text{p}})\right). \qquad (3.88)$$

The network analyzer demodulates the recorded signal $V_-(t)$ at the angular frequency Ω and outputs a signal proportional to the square modulus of $1 - t_{\text{p}}^*$, therefore proportional to $|F(\Omega)|^2$, thus allowing the characterization of the OMIT.

Experimental results

The main feature of the measured OMIT effect is shown in Fig. 3.39. The normalized signal measured by the homodyne detector $|F'(\Omega)|^2$ is plotted versus the scanning frequency of the weak probe beam Ω for mean field detunings $\bar{\Delta}$ varying from -69.1 to -35.4 MHz. The recorded trace is normalized to isolate the OMIT effect versus coupling variations that may
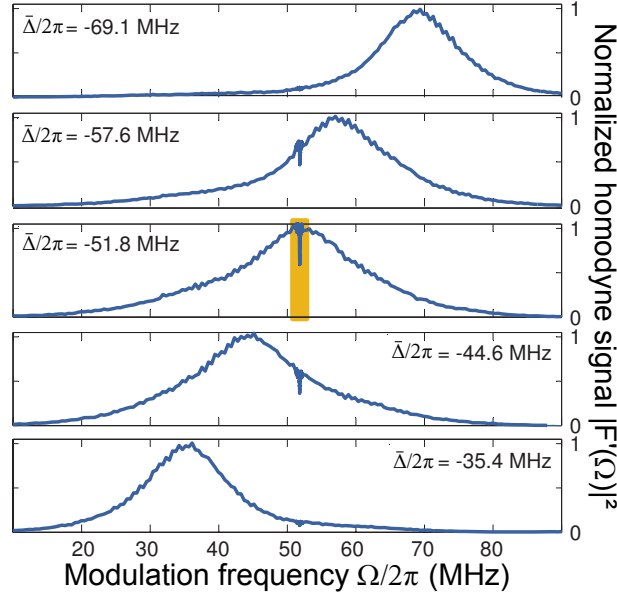
Figure 3.39: *Optomechanically induced transparency measurements. Normalized transmission plotted versus the modulation frequency Ω for various mean field detunings $\bar{\Delta}$. The measured optomechanical system is a needle-pillar toroid thermalized at $3.8\,K$ ($155\,mbar$ gaseous ^3He exchange gas pressure) and having a mechanical radial breathing mode resonance frequency of $51.8\,MHz$. The optical and mechanical dissipation rates are $\kappa/2\pi \approx 15\,MHz$ and $\Gamma_m/2\pi \approx 41\,kHz$, respectively. Adapted from Ref. [120].*

induce changes of the homodyne signal. The figure shows the transparency opening in the cavity's transmission at the two-photon resonance condition $\Omega = \Omega_m$ for each detuning.

The transmission window of the cavity is controllable with the coupling field. The detail of the transparency window highlighted in yellow in Fig. 3.39 is shown in Fig. 3.40, for varying coupling powers. In the weak coupling case Ω_c smaller or close to $\sqrt{\kappa\Gamma_m}$ and for $\bar{\Delta} = -\Omega_m$ the OMIT window is a *transmission* window t'_p corresponding to a Lorentzian function of linewidth [120]

$$\Gamma_{\mathrm{OMIT}} = \Gamma_m + \Omega_c^2/\kappa, \tag{3.89}$$

varying linearly with the input power and with a peak value

$$t'_p(\Omega = \Omega_m) = \left(\frac{\Omega_c^2/\kappa}{\Gamma_m + \Omega_c^2/\kappa}\right)^2. \tag{3.90}$$

The parameters of the Lorentzian transmission window are measured in Fig. 3.40 for input powers increasing from 0.125 to $6.5\,\mathrm{mW}$. They follow the expected behavior, showing a maximum transparency of 81%.

The dissipative feature of the transmission is simultaneously accompanied with a frequency dispersion. The group velocity of a resonant light pulse (of bandwidth much shorter than the optical cavity bandwidth) can be consequently significantly reduced [120]. The
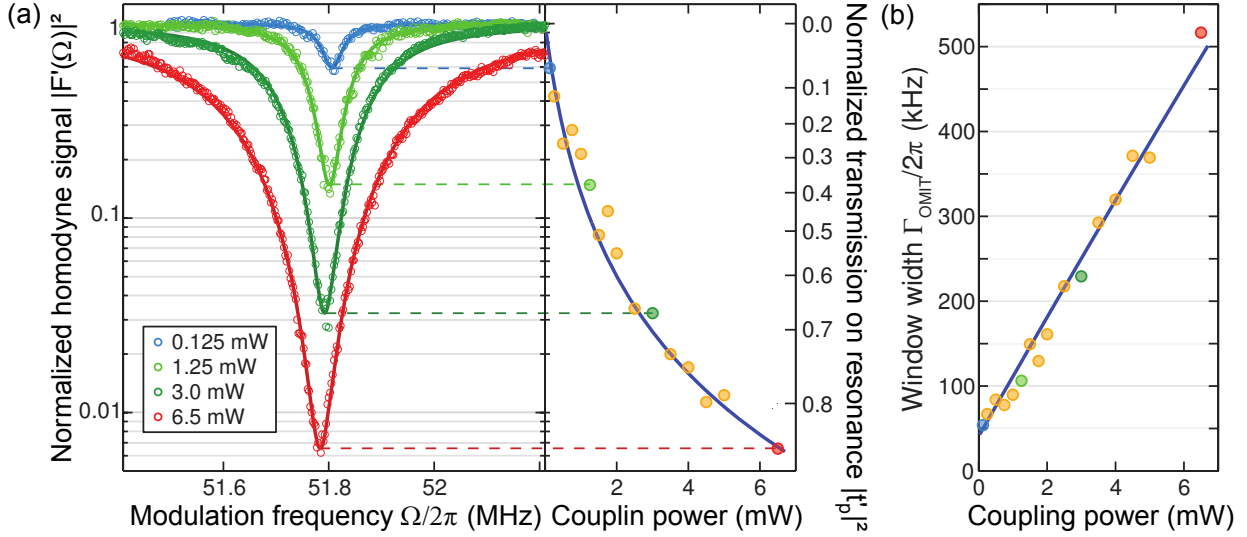
Figure 3.40: *Power dependence of the transparency parameters. (a) Zoom on the transparency window at the condition $\bar{\Delta} = -\Omega_\mathrm{m}$ (yellow highlight in Fig. 3.39) for varying input powers $\hbar\omega_\mathrm{l}\bar{s}_\mathrm{in}$ from 0.125 to 6.5 mW. The corresponding Lorentzian transparency peak value is plotted, agreeing with the model expressed in Eq. (3.90). (b) Lorentzian transparency linewidth versus input power, exhibiting the expected agreement with the model expressed in Eq. (3.89). Adapted from Ref. [120].*

acquired group delay is then given by

$$\tau_\mathrm{g} = -\frac{d}{d\omega}\left(\arg(t_\mathrm{p}(\omega))\right), \tag{3.91}$$

which leads to

$$\tau_\mathrm{g} = 2/\Gamma_\mathrm{OMIT}, \tag{3.92}$$

in the weak coupling regime and for $\Omega = \Omega_\mathrm{m}$. This group delay can be used to slow down optical pulses.

3.6.3 Analogy to atomic Electromagnetically Induced Transparency

The OMIT phenomenon is named in the same way as the atomic EIT based on their similarity. Therefore, considering the full quantum description of the optomechanical interaction using photons and phonons, the system can also be described as a three-level system exhibiting a similar configuration as for atomic EIT.

Atomic state coherence

The physics of atomic EIT, first demonstrated in 1991 in the group of S. E. Harris in a vapor of Sr atoms [178], involves the coherence of the atomic states [177]. To catch its fundamentals, the phenomenon of coherent population trapping (CPT) is described first.
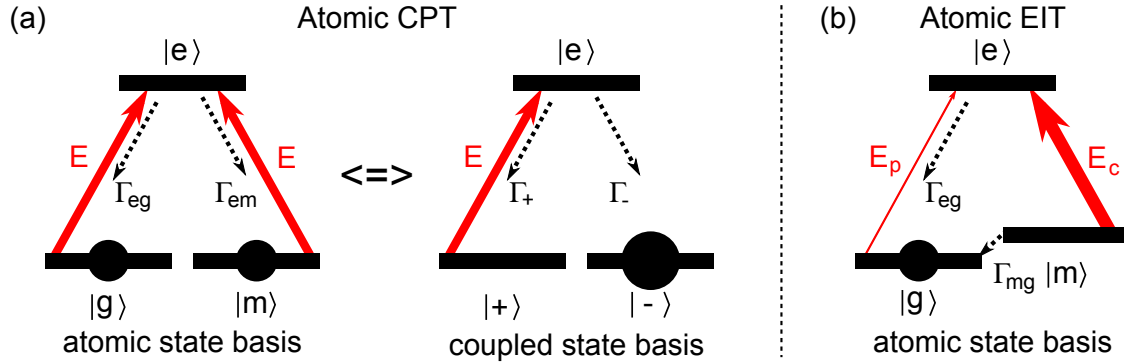
Figure 3.41: *Coherent population trapping example from a degenerate three-level atomic system. (a) Atomic state basis (left) and corresponding coupled state basis (right). The disk's area graphically represent the level populations. Adapted from Ref. [179]. (b) Specific configuration of the electromagnetically induced transparency. See text for details.*

For a degenerate atomic three-level system (Fig. 3.41 (a), left), we consider the usual atomic state basis with its fundamental levels $|g\rangle$ and $|m\rangle$ initially equally populated. Under two resonant optical fields E, it is possible to redefine the usual atomic state basis into a coupled basis with the two lower levels being the linear combinations $|\pm\rangle \propto \alpha|g\rangle \pm \beta|m\rangle$. α and β are proportional to the field applied on the $|m\rangle \to |e\rangle$ and $|g\rangle \to |e\rangle$ transitions, respectively. The configuration obtained corresponds to an optical pumping (Fig. 3.41, (a) right) to the coupled state $|-\rangle$ that does not couple to the field, trapping therefore the population into a dark state (other name of CPT). Consequently, the population is trapped in a state that is a coherent superposition of the two lower levels and which does not interact with the field [179]. Indeed, the dark state does not couple to the field as a consequence of the destructive interference of both transition routes to the excited state in the usual basis [25].

The EIT is a particular case of CPT for which the two lower levels are non degenerated and the coupling field E_{c} applied on the transition from the metastable state to the excited state $|m\rangle \to |e\rangle$ is strong compared to the probe field E_{p}.

Again here, the population is initially in the ground level $|g\rangle$. The transition from $|g\rangle$ to the metastable level $|m\rangle$ is dipole forbidden, with a corresponding decay rate Γ_{mg} being very small compared to the decay rate of the excited state to the ground state Γ_{eg}. As in the CPT case, the two possible transition routes destructively interfere when probed with E_{p}. Thereby, the process does not populate neither $|e\rangle$ nor $|m\rangle$ and trap the population to the ground state. Exact destructive interference occurs when the probe field is resonant (two-photon condition): in this case, the transparency achieved is limited by Γ_{mg} for a given power [177].

The atomic EIT analogy

The analogy between the atomic levels and the optomechanical levels is evident from the description given in Fig. 3.42. The energy levels of the optomechanical system are taken
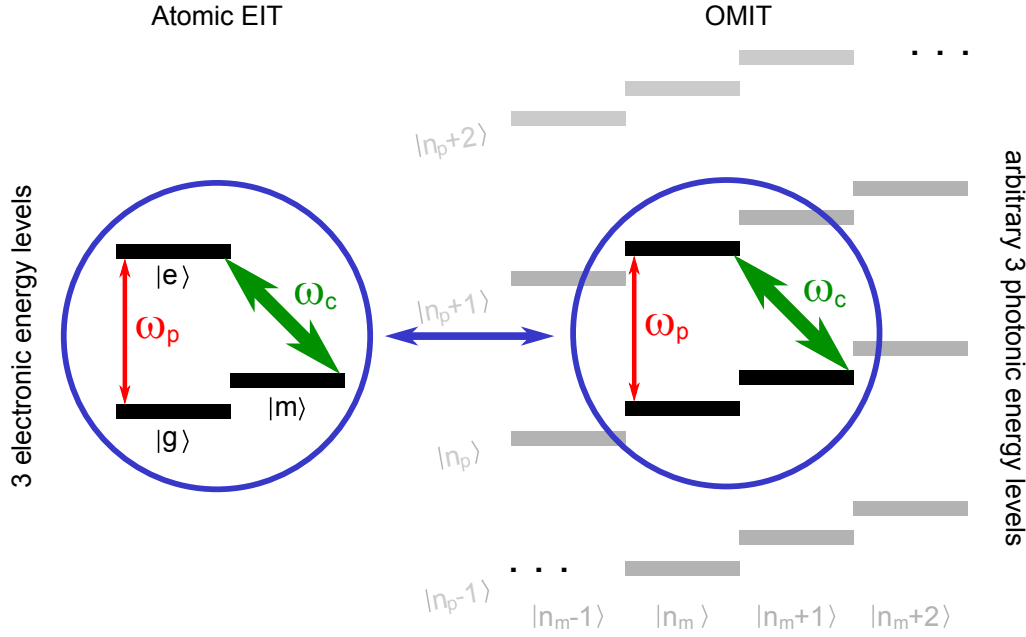
Figure 3.42: *Atomic EIT - OMIT energy level analogy. (Left) atomic EIT configuration in a Λ system. Similarly (right), an arbitrary set of three-level system equivalent to the atomic EIT case is considered in the optomechanical system.*

to be $|n_\mathrm{p}, n\rangle$, meaning the photon occupation of the optical resonator and the phonon occupation of the mechanical oscillator. Conceptually, three levels can be arbitrarily considered (Fig. 3.42, right) in pure analogy with the atomic EIT case (Fig. 3.42, left). In the resolved-sideband regime, the weak probe field oscillating at ω_p adds intracavity photons whereas the strong coupling field oscillating at ω_c adds an intracavity photons by annihilating mechanical phonons.

For the atomic case, the semi-classical model expressed in Ref. [176] shows that the coherence S_{ge} expressed in the relevant rotating frame of the coupling laser is given by

$$S_{ge} = \frac{i\mu_{ge}/(2\hbar)}{-i((\omega_\mathrm{c} - \omega_\mathrm{gm} - \omega_\mathrm{me}) + \Omega) + \Gamma_\mathrm{eg}/2 + \frac{\Omega_\mathrm{c}^2/4}{-i(-\omega_\mathrm{gm}+\Omega)+\Gamma_\mathrm{mg}/2}} E_\mathrm{p}. \quad (3.93)$$

This expression is analog to expression (3.85), the parameters given in table 3.1, with the explicit atomic level frequencies ω and dipole moment μ.

Atomic EIT	OMIT
main transition coherence S_{ge}	intracavity weak field amplitude A^-
forbidden transition coherence S_{gm}	normalized mechanical amplitude $\tilde{X}$
lower state energy difference $\hbar\omega_\mathrm{gm}$	phonon energy $\hbar\Omega_\mathrm{m}$
field-enhanced Rabi frequency $\Omega_\mathrm{c} = \mu_\mathrm{me}E_\mathrm{c}/\hbar$	optomechanical coupling $\Omega_\mathrm{c} = 2G\bar{a}x_\mathrm{zpf}$

Table 3.1: *Atomic EIT and OMIT parameter comparison. Adapted from Ref. [120]*

The analogy thus demonstrated is actually expected if the quantum interaction Hamiltonian expressed in Eq. (1.10) is rearranged by displacing the operators $\hat{a}$ and $\hat{b}$ by their steady-state values, yielding

$$\hat{H}_{\text{int}} = \hbar \frac{\Omega_{\text{c}}}{2} \left(\hat{a}^{\dagger} + \hat{a} \right) \left(\hat{b}^{\dagger} + \hat{b} \right). \tag{3.94}$$

In the resolved-sideband regime, with an intense laser tuned at the lowest sideband, the interaction Hamiltonian in the rotating wave approximation becomes

$$\hat{H}_{\text{int}} = \hbar \frac{\Omega_{\text{c}}}{2} \left(\hat{a}^{\dagger}\hat{b} + \hat{a}\hat{b}^{\dagger} \right). \tag{3.95}$$

The resulting Hamiltonian is the Beam Splitter Hamiltonian, analogous to the Jaynes-Cummings Hamiltonian except that it couples two harmonic oscillators [180, 31] via the term $(\hat{a}\hat{b}^{\dagger} + \hat{a}^{\dagger}\hat{b})$ instead of a harmonic oscillator and a two-level system via the product $(\hat{a}\hat{\sigma}_{+} + \hat{a}^{\dagger}\hat{\sigma}_{-})$ (where $\hat{\sigma}_{-}$, $\hat{\sigma}_{+}$ are the lowering and raising operators, respectively, in the two-level system).

The reported observations are the first demonstration of OMIT [120], measured also shortly after in an optomechanical crystal [181]. The phenomenon analyzed and experimentally observed in this section corresponds, however, to the case where the coupling, accounted for by the field-enhanced coupling rate Ω_{c}, is weak compared to the optical losses $(\Omega_{\text{c}}, \Gamma_{\text{m}} \ll \kappa)$. In this regime, the transparency phenomenon is similar to the atomic EIT. In the case where the coupling rate exceeds both damping rates κ and Γ_{m}, the optomechanical system enters in the strong coupling regime, in its classical interpretation. The peculiar manifestation of this regime is the splitting of the two normal modes of the strongly coupled system, proportional to Ω_{c}. In time domain, the amplitudes of the mechanical and optical modes subjected to a pulsed excitation undergo a Rabi-like periodic evolution, resulting from the beat of the normal modes. This strong coupling has been recently observed in the group in spoke structures optimized to increase the vacuum optomechanical coupling rate [54]. Previous experiments reported the same regime in the electromechanical [182] and optomechanical [183] context, the later experiment showing however only normal mode splitting of the mechanical spectrum.

Chapter 4

Summary and outlook

4.1 Summary of the doctoral work

In this thesis, the cooling of a macroscopic harmonic mechanical oscillator close to its quantum ground state was realized. We have thus demonstrated the feasibility to observe in the near-future purely quantum effects on objects whose dimensions are equivalent to those of tangible ones.

To realize this experimental challenge, we have chosen a platform that presents a coupling between a mechanical oscillator and the optical mode of a resonator, which enables us to exploit the principle of dynamical backaction cooling via the radiation pressure of the light. The vitreous silica microtoroidal cavities of dimensions typically comprised between 10 and 100 μm have been found to be a judicious candidate for diverse reasons. First, the high optical finesse – close to 10^6 – of the supported whispering-gallery modes allows an important intracavity power enhancement which makes the effect of radiation pressure larger. Moreover, due to the transparency of glass, these cavities support high quality optical modes in the visible and near infrared, thus permitting us to harness widely commercially available ultra-stable laser sources. Finally, this type of microstructures hosts mechanical modes oscillating in the frequency range from 30 to 120 MHz, where external parasitic acoustic noise is negligible. These properties have directly placed the selected system in a prominent position to observe the cooling to the ground state of motion.

In this doctoral work, the various experimental aspects limiting the aforementioned performance have all been addressed in the purpose of the final objective. First thing, the dynamical backaction cooling competes with the unavoidable thermalization of the mode with its mechanical environment. To favor the effect of cooling over the thermalization to the environment in order to achieve a low final mode temperature, two approaches were followed.

First, the sources of mechanical dissipations that determine the coupling rate of the mode to its environment have been carefully studied. This has permitted to engineer the system such as to reduce these losses by more than an order of magnitude, reaching a record mechanical quality factor value of 50 000 at 24 MHz at room temperature. By placing the

mechanical structure in a purpose-built vacuum chamber, the effect of the gas damping was diminished until the regime where intrinsic properties of the structure govern the dissipations was reached. This enabled us to highlight the major role played by intermode coupling, which was finally reduced by fabricating spoke-anchored microtoroids using a newly developed microfabrication method [116]. Thus, in this optimized structures, the mechanical damping is strongly dominated by the intrinsic properties of the glass materials, rather than its geometry.

Subsequently, the thermal fluctuations directly driving the mechanical oscillator were significantly reduced by placing it in a cryostat. First, the principle of cryogenic operation has been demonstrated in an exchange gas ^{4}He cryostat [41], and afterwards in a similar type of apparatus using ^{3}He. Thermalization of the sample to an operating temperature of $850\,\mathrm{mK}$ was achieved, using a pressure on the order of $1\,\mathrm{mbar}$. This corresponds to the optimal configuration in light of the trade-off between the thermalization of the structure at cryogenic temperatures and the properties of dissipation of amorphous silica [55]. In the course of this work, interesting properties of vitreous silica have been discovered, notably the inversion of the thermal bistable effect below $\sim 13\,\mathrm{K}$ which enabled us on the one hand to overcome laser locking problems on the red side of the optical cavity (corresponding to the cooling configuration) and on the other hand, to observe interesting non-linear properties conducting to measurable multistable effects [118].

Another aspect to take into account is the fluctuating radiation pressure force introduced by the laser itself that perturbs the cooling process, by providing extra driving to the mechanical oscillator. The pursued studies have revealed that the classical part of these fluctuations can be negated by employing a quantum-limited Ti:sapphire laser. Conveniently, parasitic acoustic fluctuations are negligible at the ultrasonic mechanical frequencies considered. Furthermore, the quantum nature of this phenomenon can be moderated only if – as in the case of the sideband cooling of ions – the resolved-sideband regime is reached, which we have directly observed experimentally [117].

The combination of all these experimental advances lead to the observation, using a dedicated balanced homodyne detection, of a phonon occupancy – figure of merit of the cavity optomechanics field – of 9 ± 1 [55]. This is more than two orders of magnitude lower than the proof-of-principle measurement [28] and we demonstrated in addition that this value is now limited by purely technical aspects such as the heating due to the absorption of the light scattering off the coupling tapered fiber. All other limitations considered in the course of this thesis have been reduced with success.

Finally, the realized experimental conditions permitted to measure another interesting aspect of the mutual optomechanical coupling on the optical properties of the cavity itself. By harnessing a phase modulation-demodulation technique authorized by the configuration of the detector, we measured the phenomenon of optomechanically induced transparency corresponding to the weak coupling of both mechanical and optical resonators, highlighting another perspective of the optomechanical coupling [120].

4.2   Outlook

The work described in this thesis has enabled us to make large improvements on the process of cooling a mechanical oscillator, bringing its phonon occupancy close to zero. Nonetheless, the quantum regime of the macroscopic mechanical oscillator can be unambiguously identified only through measurements reporting a pure quantum signature and for which classical theory fails to describe the observation.

An example of such measurements is the detection of the strength difference of the motional sidebands of the probed cavity that is expected for very small occupation numbers. In pure analogy with the detection of the motional ground state of trapped ions, the scattering rates of these Stokes and anti-Stokes sidebands are proportional to $\bar{n}+1$ and $\bar{n}$, respectively, where $\bar{n}$ is the average phonon occupancy of the oscillator subjected to laser cooling. This phenomenon is the direct consequence of the quantum formulation of the cooling process, obeying Fermi's Golden Rule. One possibility to measure the asymmetry is to resonantly probe the optical cavity with another weak laser and to subsequently heterodyne the output field, as in the experimental setup already installed in the group [117]. Such measurements are being currently investigated.

Another interesting aspect of the optomechanical coupling that will be of prime interest in the near future is to achieve the "quantum coherent coupling" condition for which the optomechanical coupling rate overcomes both decoherence rates of the optical and mechanical mode to their respective environment. This regime, which has recently been reached in our group by optimizing the spoke structures and measuring them in the ^{3}He cryostat [54], directly allows the study of quantum interactions, putting the optomechanical system into a class of experimental systems such as single atoms in high-finesse cavities [184]. This regime opens numerous perspectives by enabling the transfer of non-classical states of the light field onto the macroscopic oscillator [180]. Additionally, it makes it conceivable to use the optomechanical system as a transducer between a robust solid-state qubit attached to the mechanical mass and an optical communication channel conveying the quantum state on large distances [185]. The emerging field of *cavity quantum optomechanics* thus opens new perspectives in the application of counter-intuitive quantum concepts to macroscopic objects.

Appendix A
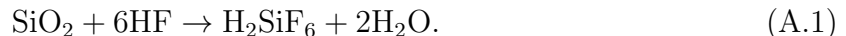
Microfabrication of silica microtoroids

The on-chip microtoroids previously described and used in this work are microfabricated in clean room facilities whereas the final steps such as silicon gaseous etching and laser reflow are performed in usual laboratory environment, such as in the Max-Planck-Institut für Quantenoptik. The process described here was implemented in the clean room of Prof. Jörg P. Kotthaus at the Ludwig-Maximilians-Universität in Munich. A similar process is implemented for the group at the Center of Micronanotechnology (CMI) at the Ecole Fédérale Polytechnique de Lausanne in Switzerland.

Photolithography and silica wet etch

The process uses widely commercially available $\langle 100 \rangle$-oriented. 3-inch diameter, $\sim 400 - \mu$m thickness, undoped (resistivity $> 20\,\Omega \cdot$ cm) Czochralski-grown silicon wafers. They come with a polished layer of thermally grown oxide using the wet (Virginia Semiconductor, Si-Mat) or dry (HLL Munich) growing method, of thickness typically between 1 to $3\,\mu$m.

The process is summarized in Fig. A.1. A droplet of photoresist is spun using a spincoater and softbaked to flatten the deposited layer (Fig. A.1 step (a)), enabling UV lithography through a predesigned quartz-Cr photomask to illuminate the desired surface. Compared to microspheres, microtoroids enable a wide range of geometries as photomasks (fabricated by ML&C) defining the patterns can be designed using commercial computer-aided design (CAD) software (AutoCAD). After development of the photactivated resist (figure A.1 step (b)), the remaining photoresist pads are hardbaked to ensure resistance during the etching using hydrofluoric acid in a buffered solution NH_4F:HF (Fig. A.1 step (b)).

Anistropic etching of the SiO_2 takes place following [186]

$$SiO_2 + 6HF \rightarrow H_2SiF_6 + 2H_2O. \tag{A.1}$$

Quarter circle etching profiles are observed only if adhesion promotion of the photoresist is used to avoid creeping of the HF at the SiO_2/photoresist interface. This phenomenon is
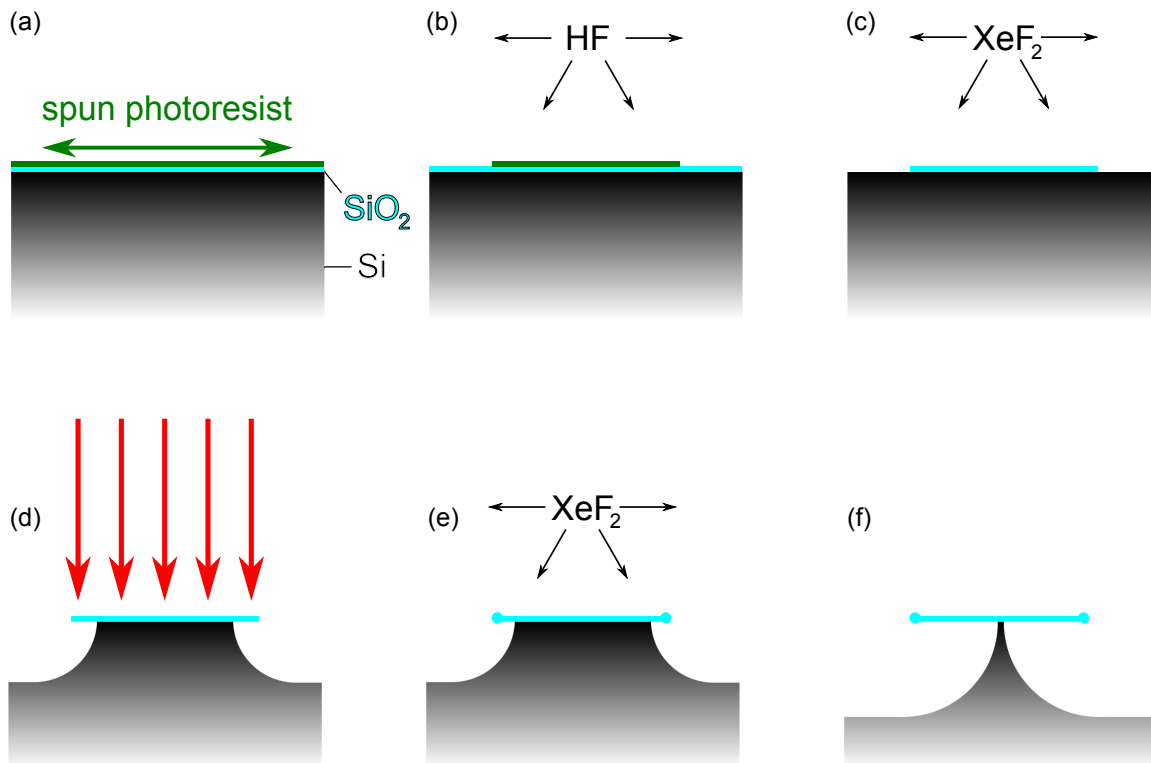
Figure A.1: *Microfabrication of the toroidal microcavities (a) Spinning of the photoresist (Shipley S-1813) on top of a crystalline Si wafer with a thermally-grown micron-thick polished SiO_2 layer. Potential irregularities in the photoresist's thickness are flattened by softbake at $110\,°C$ for $1\,min$. (b) A photoresist disk remains after photolithographic UV illumination (Karl Süss MJB3 mask aligner) through the photomask and proper development (Microposit MF-319) of the illuminated photoresist. After hardbake at $115\,°C$ for $10\,min$ for hardening the photoresit, the stack is subjected to buffered NH_4F:HF (12.5 or 7:1) isotropic wet etching that removes the unprotected SiO_2. (c) After thorough cleaning of the wafer using acetone, isopropanol, di-ionized (DI) water and compressed nitrogen for drying, the Si material of the photolithographed wafer is isotropically etched with pulses of gaseous XeF_2. (d) Using an out of focal plane illumination from a CW CO_2 laser emitting at $10.6\,\mu m$, the rim of the protruding glass is melted, forming the toroidal shape. (e) Eventually, a second run of isotropic XeF_2 etching is performed to reduce the attaching pillar diameter, without affecting the surface quality of the previously formed toroid, leading to the final shape of the structure (f).*

however exploited to produce sharp edged microdisks with enhanced light confinement of the WGM [187, 188].

After removal of the masking photoresist using conventional cleaning, the silica pads are ready for silicon under-etching (Fig. A.1 step (c)). The wafer is then cleaved along crystallographic axis using a diamond tip to prepare the chips in their final shape to enable further straight taper coupling. At the CMI, automatic trenching of the wafer is performed.

Silicon dry etch

To confine the light in the silica, the underlying silicon of higher refractive index is removed. XeF_2 in its gaseous form etches Si isotropically with a selectivity of more than $1000:1$ relative to SiO_2 [189], according to the reaction [190]

$$2XeF_2 + Si \rightarrow 2Xe_{(g)} + SiF_{4(g)}. \tag{A.2}$$
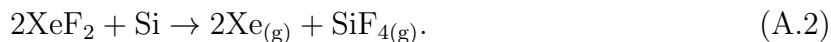
The etching takes place in a commercially available computer-controlled reaction chamber similar to the one described in Ref. [190]. Pulses of sublimated gaseous XeF_2 of controllable duration and pressure are admitted in the etching chamber. The etching progress is monitored through the control top-window of the etching chamber using a microscope. Several precautions have to be taken to ensure isotropic uniform etching: pulses have to be of low pressure ($< 140\,Pa$) and low duration ($30\,s$), the chip has to be ideally placed in an adjusted top-opened box to avoid side etching effects and the gas should be admitted slowly in the chamber using a needle valve to avoid turbulence effects. Etching rates are typically $< 1\,\mu m$/pulse. Importantly, the chip should be carefully dried before etching to avoid parasitic reactions involving H_2O.

Laser reflow

The edges of the wet etched disks are left with residual asperities that eventually couple to the whispering-gallery mode, inducing scattering losses. To smooth out the surface and to form the toroidal shape previously presented, an intense laser beam is applied one-by-one to each released disk using a CO_2 laser emitting at a wavelength of $10.6\,\mu m$, as detailed in Ref. [71].

The silica efficiently absorbs the light [70]. When the pulse of light is applied, the rim of the disk heats up strongly comparatively to the center of the disk, the silicon pillar evacuating the heat to the substrate with a conductivity 100 times higher than the silica. In addition, silicon is transparent at this wavelength and its thermal conductivity is 100 times larger than for silica. Therefore, the temperature of the rim of the disk dramatically increases compared to the center. The effect is additionally enhanced by the temperature-dependent absorption of SiO_2 [191]. Eventually, the disk periphery reaches the glass transition temperature, melts, and because of surface tension the droplet takes the form of a toroid. After toroid formation, the cross-section available for laser light absorption decreases, responsible for the cool down of the toroid and the self-termination of the reflow process. The central part of the disk is normally left undeformed after this step. The major diameter R and the minor diameter r_t of the formed toroid can be adjusted by varying the diameter of the the supporting pillar r_p at the previous etching step. For decreasing r_p, the amount of glass participating to the toroid's formation increases, thereby leading to a toroid with smaller R and larger r_t.

The used setup is depicted in Ref. [20] and comprises a Synrad 48-1 CO_2 laser emitting a Gaussian-shaped TEM_{00} optical mode that is directed to the desired microdisk using appropriate ZnSe optics and monitored using a microscope. The chip is placed out of the

focal plane of the focusing lens to avoid non-uniform intensity on the small-scale of the disk.

Although self-terminating, the process should be visually monitored, as extra heating of the disk may happen upon exaggerated illumination. This may lead to prejudicial deformation influencing further optimization of the mechanical properties of the disk. In addition, it has been realized after a second etching set (Fig. A.1, step (e)) that intense laser heating may lead to the post-formation of a thin layer of silicon oxide that deviates the resulting structure from its optimal shape depicted in Figs. 2.1 (a) and A.1 (e). The role of this second etch on the mechanical engineering of the structure is described in detail in section 3.2.2.

Appendix B

Fabrication of tapered optical fibers

Tapered fibers are fabricated using a flame from a H_2 torch to melt a commercial single-mode glass-fiber propagating 1550-nm (Corning SMF-28 or similar model from other manufacturers) or 780-nm (Nufern 780HP) light for the optomechanics experiment.

The buffer made of acrylate is removed using stripping device and the denuded part is thoroughly cleaned with isopropanol and lens wipes. It is then placed on a specially designed taper holder allowing axial elongation of the fiber with very small transverse motion. Next, the holder is positioned on a stage made of two counter-propagating computer controlled stepper motors used for stretching. Manual positioning allows to adjust the placement of the denuded fiber on top of the blue combustion cone of a H_2 flame so as to obtain homogeneous heating of the glass to be elongated and to avoid contamination from imperfect combustion. The transmission of the whole fiber is monitored at the appropriate wavelength, as well as the diameter of the melted region using a microscope mounted camera.

As detailed in Ref. [192], coupling of the fundamental mode with higher order modes upon reduction of r_f leads to oscillations of the transmission easily recorded in transmission. When the beat disappears, the fabricated taper is close to single mode propagation condition, although experimental verification is difficult in the presented configuration of the fabrication setup. After cool down, the taper holder elongation is manually adjusted to ensure optimum tensioning of the taper using the experimental procedure described in [20]. Tapers of more than 95% transmission are typically achieved using the previously described technique.

Taper fabrication methods may be varied to ensure better reproducibility, using electric resistance heating [192], CO_2 laser melting or chemical etching. In our group, we designed a final step of taper transfer to a glass holder, glued with low-contraction UV epoxy glue for having rigid tapers to be mounted in an acoustically noisy environment such as a cryostat. Since the fiber and the glass are made essentially of the same material, the tapered fiber remains properly tensioned upon thermal expansion or contraction during the cool down. The fabrication steps are described in figure 3.19 and successfully achieved coupling with usual cryogenic equipments running.

Appendix C

Manipulation procedure of the prototype helium-4 cryostat

This procedure chronologically describes the steps for reaching the base temperature of the prototype ^{4}He cryostat starting from room temperature. It is based on the manual of the Oxford Instruments (OI) OptistatSXM. The setup is detailed in section 3.4.1.

Preparation of the cryoprobe

1. The cryohead is prepared. The sample and the cryotaper are placed on the cryoprobe (Fig. C.1 (c)). The cryoprobe stands on the test setup (Fig. C.1 (b)).

2. Using non-powdered gloves, the cryoprobe is cleaned with optical lens tissue and isopropanol to remove organic species that may have deposited during previous manipulations.

3. The electrical connections are verified. The coupling is achieved on the desired toroid (Fig. C.1 (a)). Phase matching is achieved and the mechanical slide is screwed.

4. The optical fiber feedthrough is adjusted. Vacuum glue (Varian Torr seal) is used to seal any vacuum leak. More than 80% transmission is typically achieved throughout the whole cryostat.

Insertion of the cryoprobe at room temperature

1. The cryoprobe is carefully inserted in the experimental chamber using a lifting rope. Shocks are avoided as they may misalign the cryotaper.

2. The alignment of the optical accesses with the cameras is adjusted.

3. The cryoprobe is clamped to the tube. Alignment is re-checked as compression of the O-ring may displace the cryoprobe down by few mm. Everything is blocked after this step.

4. The experimental chamber is pumped with the rotary pump (OI EPS40) below 10^{-1} mbar to ensure evacuation of outgassing materials.

Cooling of the cryostat and the cryoprobe

1. The insulating vacuum is pumped with the turbomolecular pump below 10^{-5} mbar. Once reached, the valve is closed as the cryopumping of the cold cryostat maintain lower pressures (below 10^{-6} mbar as measured with the Penning gauge).

2. The cooling ^{4}He reservoir and the heat exchange circuit is cyclically purged with clean gaseous ^{4}He and pumped with the dry pump. The gas is cleaned from water and gaseous nitrogen using a liquid N_2 trap. This step ensures that no contaminants ice on the fragile needle valve (Fig. C.2 (b) and (c)). Precooling with liquid nitrogen is not recommended as it may contaminate the circuit and freeze inside.

3. The reservoir is filled directly with liquid ^{4}He. The level is regularly checked with a manual gauge.

4. Once filled to 100%, the transfer can is removed and a cold time range of ~ 8 hours is expected in normal experimental conditions.

5. The needle valve is opened to accelerate the cooling down of the experimental chamber. It can be achieved from room temperature typically in 2 hours. Ideally, no exchange gas is admitted during the process so that the cryoprobe thermalizes slower than the cooled inner walls of the experimental chamber. This ensures that contaminating materials preferentially adsorb on the walls.

6. Once 4.2 K is reached in the chamber, *exchange* ^{4}He gas is admitted in the chamber directly from the evaporated *cooling* ^{4}He using the vacuum tubings described in Fig. 3.17. This ensures that uncontaminated He gas is used for the heat exchange.

7. The temperature of the experimental chamber (as measured with the RuO_2 or Si diode) is determined by adjusting the pumping flux of the rotary pump. A compromise has to be found between cooling power, base temperature and vibrations induced by a large flux of *cooling* ^{4}He through the cooling circuit. Base temperature of 1.65 K in the experimental chamber is achieved and coupling the toroid is possible within the configuration described.

8. Heating up of the probe is typically achieved in ~ 24 hours by simply letting the whole cryostat thermalize to room temperature. It can be accelerated by using the built-in electric heater. During heat-up, contaminating species unavoidably deposit on the cryoprobe, especially if the process is accelerated using the heater.
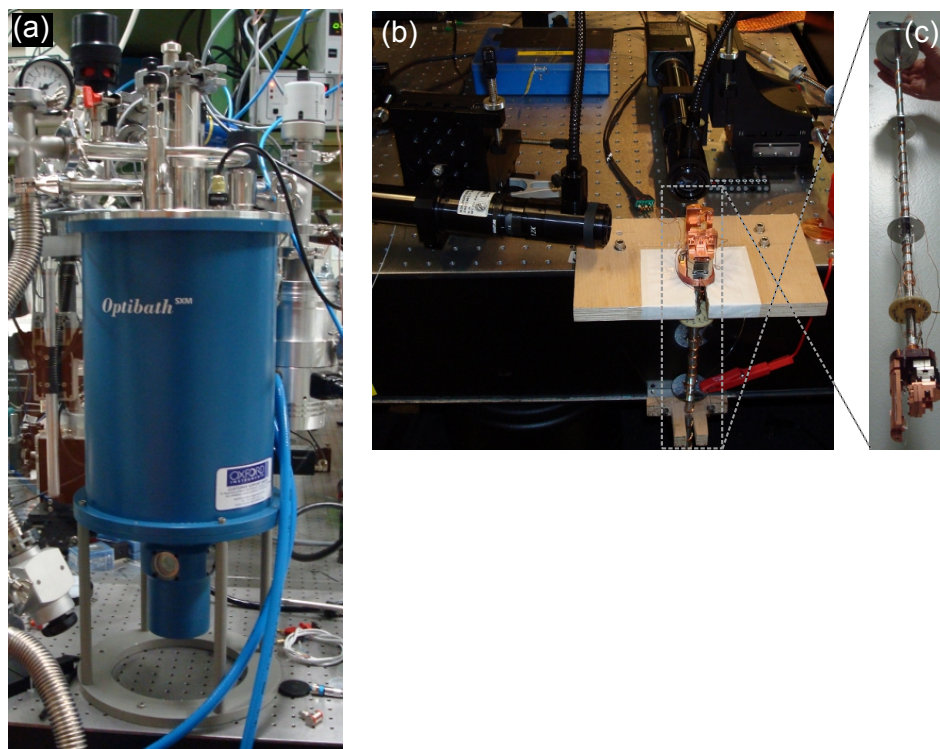
Figure C.1: *(a) The cryostat installed on top of the optical table. (b) The cryoprobe probe test setup. (c) The cryoprobe.*
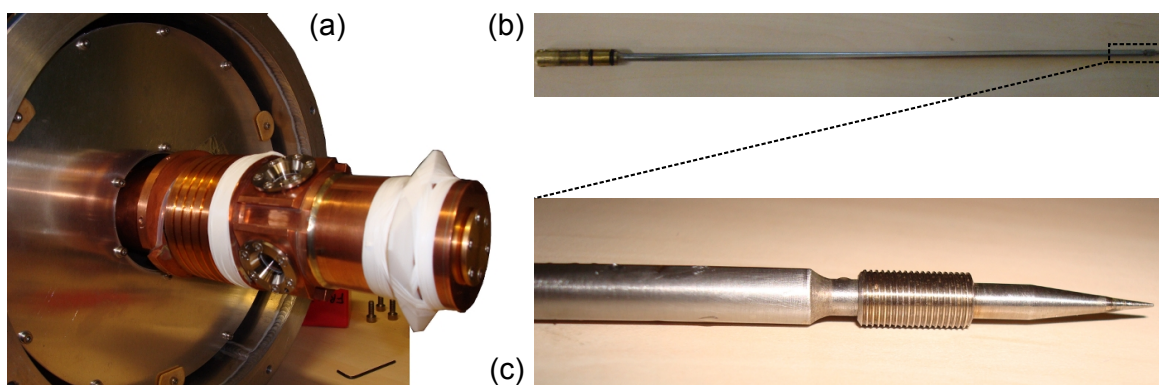

Figure C.2: *Photographs of the opened prototype cryostat. (a) The radiation shield comprising the experimental chamber. (b) The needle valve stick. (c) Zoom-in of the needle valve.*

Appendix D

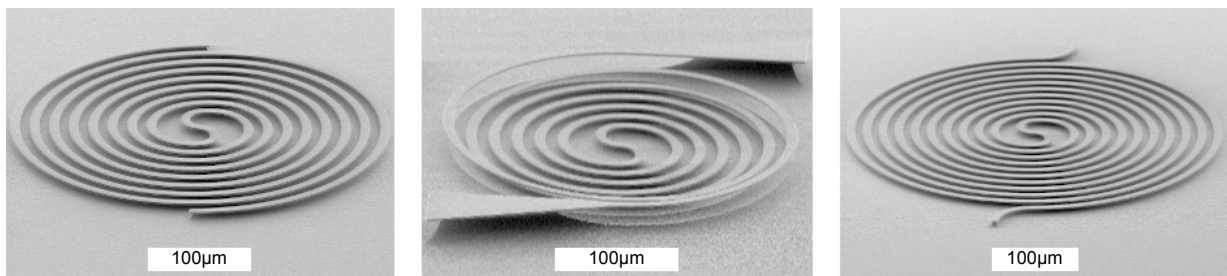# Gallery of on-chip optical microstructures

Figure D.1: *On-chip silica optical delay elements. Collaboration with the group of K. J. Vahala, California Institute of Technology.*
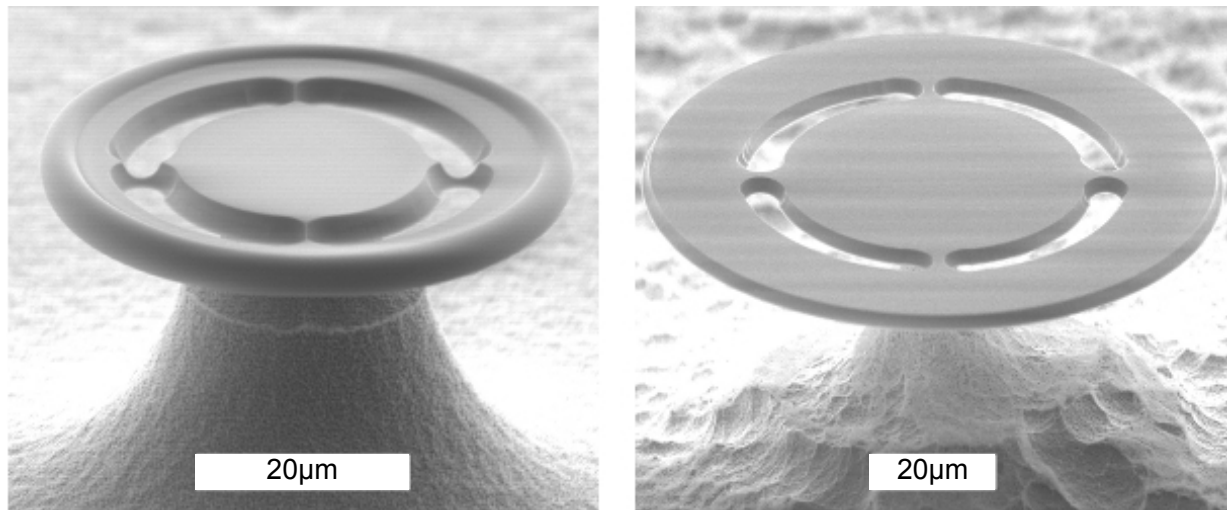

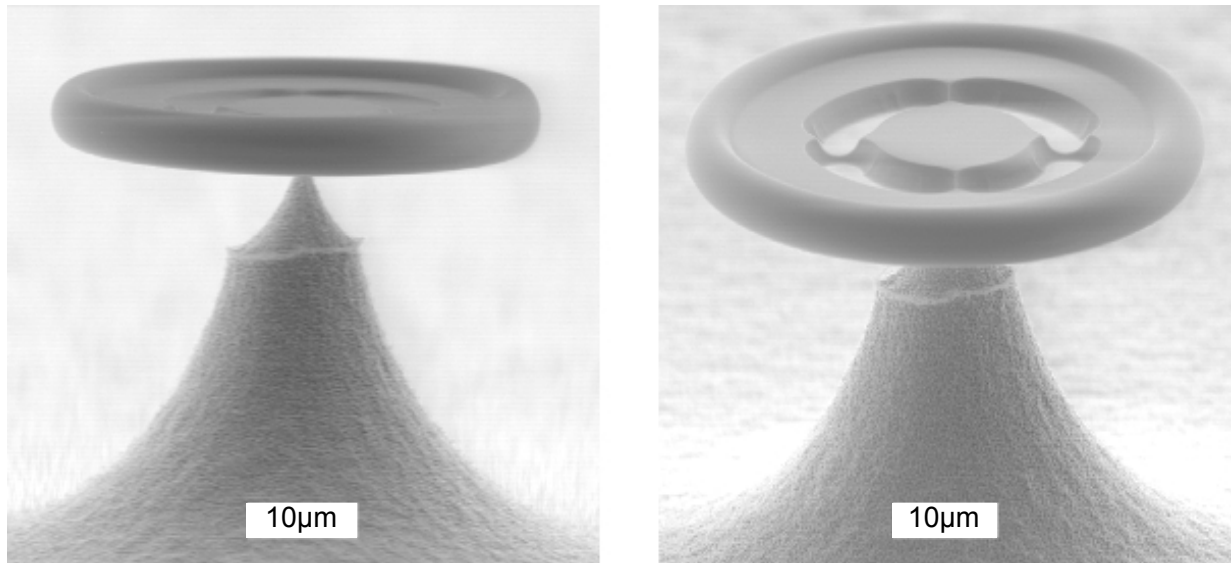**Figure D.2:** *Spoke silica toroidal and disk microresonators*

Figure D.3: *Spoke silica toroidal microresonator*

Bibliography

[1] Braginskii, V. B. and Vorontsov, Y. I., "Quantum-mechanical limitations in macroscopic experiments and modern experimental technique," *Soviet Physics Uspekhi* **17**, 644 (1975).

[2] Caves, C. M., "Quantum-mechanical radiation-pressure fluctuations in an interferometer," *Physical Review Letters* **45**, 75 (1980).

[3] Braginskii, V. B. and Manukin, A. B., "Ponderomotive effects of electromagnetic radiation," *Soviet Physics JETP* **25**, 653 (1967).

[4] Braginskii, V. B., Manukin, A. B., and Tikhonov, M. Y., "Investigation of dissipative ponderomotive effects of electromagnetic radiation," *Soviet Physics JETP* **31**, 829 (1970).

[5] Lebedew, P., "Untersuchung über die Druckkräfte des Lichtes," *Annalen der Physik* **311**, 433 (1901).

[6] Nichols, E. F. and Hull, G. F., "A preliminary communication on the pressure of heat and light radiation," *Physical Review* **13**, 307 (Nov 1901).

[7] Hänsch, T. W. and Schawlow, A. L., "Cooling of gases by laser radiation," *Optics Communications* **13**(1), 68 (1975).

[8] Andreev, S., Balykin, V., Letokhov, V., and Minogin, V., "Radiative slowing and reduction of the energy spread of a beam of sodium atoms to $1.5\,\mathrm{K}$ in an oppositely directed laser beam," *Journal of Experimental and Theoretical Physics Letters* **34**, 463 (1981).

[9] Wineland, D. J. and Dehmelt, H., "Proposed $10^{14}\delta\nu < \nu$ laser fluorescence spectroscopy on Tl^+ ion mono-oscillator," *Bulletin of the American Physical Society* **20**, 637 (1975).

[10] Wineland, D. J., Drullinger, R. E., and Walls, F. L., "Radiation-pressure cooling of bound resonant absorbers," *Physical Review Letters* **40**, 1639 (1978).

[11] Kippenberg, T. J. and Vahala, K. J., "Cavity optomechanics: back-action at the mesoscale," *Science* **321**, 1172 (2008).

[12] Wilson-Rae, I., Nooshi, N., Zwerger, W., and Kippenberg, T. J., "Theory of ground state cooling of a mechanical oscillator using dynamical backaction," *Physical Review Letters* **99**, 093901 (2007).

[13] Marquardt, F., Chen, J. P., Clerk, A. A., and Girvin, S. M., "Quantum theory of cavity-assisted sideband cooling of mechanical motion," *Physical Review Letters* **99**, 093902 (2007).

[14] Genes, C., Vitali, D., Tombesi, P., Gigan, S., and Aspelmeyer, M., "Ground-state cooling of a micromechanical oscillator: Comparing cold damping and cavity-assisted cooling schemes," *Physical Review A* **77**, 033804 (2008).

[15] Pinard, M., Dantan, A., Vitali, D., Arcizet, O., Briant, T., and Heidmann, A., "Entangling movable mirrors in a double-cavity system," *EPL (Europhysics Letters)* **72**, 747 (2005).

[16] Pirandola, S., Mancini, S., Vitali, D., and Tombesi, P., "Continuous-variable entanglement and quantum-state teleportation between optical and macroscopic vibrational modes through radiation pressure," *Physical Review A* **68**, 062317 (2003).

[17] Vitali, D., Gigan, S., Ferreira, A., Böhm, H. R., Tombesi, P., Guerreiro, A., Vedral, V., Zeilinger, A., and Aspelmeyer, M., "Optomechanical entanglement between a movable mirror and a cavity field," *Physical Review Letters* **98**(3), 030405 (2007).

[18] Clerk, A. A., Marquardt, F., and Jacobs, K., "Back-action evasion and squeezing of a mechanical resonator using a cavity detector," *New Journal of Physics* **10**(9), 095010 (2008).

[19] Arcizet, O., *Mesure optique ultrasensible et refroidissement par pression de radiation d'un micro-resonateur mécanique*, PhD thesis, Université Paris VI (2006).

[20] Schliesser, A., *Cavity Optomechanics and Optical Frequency Comb Generation with Silica Whispering-Gallery-Mode Mircroresonators*, PhD thesis, Ludwig-Maximilians-Universität (2009).

[21] Anetsberger, G., *Novel Cavity Optomechanical Systems at the Micro- and Nanoscale and Quantum Measurements of Nanomechanical Oscillators*, PhD thesis, Ludwig-Maximilians-Universität (2010).

[22] Haus, H. A., [*Waves and fields in optoelectronics*], Prentice-Hall (1984).

[23] Law, C. K., "Interaction between a moving mirror and radiation pressure: A Hamiltonian formulation," *Physical Review A* **51**, 2537 (1995).

[24] Gorodetsky, M. L., Schliesser, A., Anetsberger, G., Deléglise, S., and Kippenberg, T. J., "Determination of the vacuum optomechanical coupling rate using frequency noise calibration," *Optics Express* **18**, 23236 (2010).

[25] Scully, M. O. and Zubairy, M. S., [*Quantum Optics*], Cambridge University Press (2000).

[26] Dorsel, A., McCullen, J. D., Meystre, P., Vignes, E., and Walther, H., "Optical bistability and mirror confinement induced by radiation pressure," *Physical Review Letters* **51**, 1550 (1983).

[27] Clerk, A. A., Devoret, M. H., Girvin, S. M., Marquardt, F., and Schoelkopf, R. J., "Introduction to quantum noise, measurement, and amplification," *Reviews of Modern Physics* **82**, 1155 (2010).

[28] Schliesser, A., Del'Haye, P., Nooshi, N., Vahala, K. J., and Kippenberg, T. J., "Radiation pressure cooling of a micromechanical oscillator using dynamical backaction," *Physical Review Letters* **97**, 243905 (2006).

[29] Landau, L. D. and Lifshitz, J. S., [*Statistical Physics*], Butterworth Heinemann (1980).

[30] Feynman, R. P., Leighton, R. B., and Sands, M., [*The Feynman lectures on physics, Vol. I*], Addison-Wesley Publishing Company (1963).

[31] Dobrindt, J. M., Wilson-Rae, I., and Kippenberg, T. J., "Parametric normal-mode splitting in cavity optomechanics," *Physical Review Letters* **101**, 263602 (2008).

[32] Ludwig, M., Kubala, B., and Marquardt, F., "The optomechanical instability in the quantum regime," *New Journal of Physics* **10**, 095013 (2008).

[33] Marquardt, F., Harris, J. G. E., and Girvin, S. M., "Dynamical multistability induced by radiation pressure in high-finesse micromechanical optical cavities," *Physical Review Letters* **96**, 103901 (2006).

[34] Carmon, T., Cross, M. C., and Vahala, K. J., "Chaotic quivering of micron-scaled on-chip resonators excited by centrifugal optical pressure," *Physics Review Letters* **98**, 167203 (2007).

[35] Itano, W. M. and Wineland, D. J., "Laser cooling of ions stored in harmonic and Pkleckneenning traps," *Physical Review A* **25**, 35 (1982).

[36] Itano, W. M., Bergquist, J. C., Bollinger, J. J., and Wineland, D. J., [*Laser manipulation of atoms and ions*], ch. Laser cooling of trapped ions, 519–537S, North-Holland (1992).

[37] Wineland, D. J. and Itano, W. M., "Laser cooling of atoms," *Physical Review A* **20**, 1521–1540 (1979).

[38] Diedrich, F., Bergquist, J. C., Itano, W. M., and Wineland, D. J., "Laser cooling to the zero-point energy of motion," *Physical Review Letters* **62**, 403 (1989).

[39] Vahala, K. J., Hermann, M., Knünz, S., Batteiger, V., Saathoff, G., Hänsch, T. W., and Udem, T., "A phonon laser," *Nature Physics* **5**, 682 (2009).

[40] Jaekel, M. T. and Reynaud, S., "Quantum limits in interferometric measurements," *EPL (Europhysics Letters)* **13**(4), 301 (1990).

[41] Schliesser, A., Arcizet, O., Rivière, R., Anetsberger, G., and Kippenberg, T. J., "Resolved-sideband cooling and position measurement of a micromechanical oscillator close to the Heisenberg uncertainty limit," *Nature Physics* **5**(7), 509 (2009).

[42] Arcizet, O., Briant, T., Heidmann, A., and Pinard, M., "Beating quantum limits in an optomechanical sensor by cavity detuning," *Physical Review A* **73**(3), 033819 (2006).

[43] Verlot, P., Tavernarakis, A., Briant, T., Cohadon, P.-F., and Heidmann, A., "Back-action amplification and quantum limits in optomechanical measurements," *Physical Review Letters* **104**, 133602 (2010).

[44] Dobrindt, J. M. and Kippenberg, T. J., "Theoretical analysis of mechanical displacement measurement using a multiple cavity mode transducer," *Physical Review Letters* **104**, 033901 (2010).

[45] Braginsky, V., Vorontsov, Y. I., and Thorne, K. S., "Quantum nondemolition measurements," *Science* **209**, 547 (1980).

[46] Caves, C. M., Thorne, K. S., Drever, R. W. P., Sandberg, V. D., and Zimmermann, M., "On the measurement of a weak classical force coupled to a quantum-mechanical oscillator. I. Issues of principle," *Reviews of Modern Physics* **52**, 341 (1980).

[47] Milburn, G. J. and Walls, D. F., "Quantum nondemolition measurements via quantum counting," *Physical Review A* **28**, 2646 (1983).

[48] Thompson, J. D., Zwickl, B. M., Jayich, A. M., Marquardt, F., Girvin, S. M., and Harris, J. G. E., "Strong dispersive coupling of a high finesse cavity to a micromechanical membrane," *Nature* **452**, 72 (2007).

[49] Sankey, J. C., Yang, C., Zwickl, B. M., Jayich, A. M., and Harris, J. G. E., "Strong and tunable nonlinear optomechanical coupling in a low-loss system," *Nature Physics* **6**, 707 (2010).

[50] Thorne, K. S., Drever, R. W. P., Caves, C. M., Zimmermann, M., and Sandberg, V. D., "Quantum nondemolition measurements of harmonic oscillators," *Physical Review Letters* **40**, 667 (1978).

[51] Hertzberg, J. B., Rocheleau, T., Ndukum, T., Savva, M., Clerk, A. A., and Schwab, K. C., "Back-action evading measurements of nanomechanical motion," *Nature Physics* **6**, 213 (2009).

[52] Arcizet, O., Cohadon, P.-F., Briant, T., Pinard, M., and Heidmann, A., "Radiation-pressure cooling and optomechanical instability of a micromirror," *Nature* **444**, 71 (2006).

[53] Gröblacher, S., Hertzberg, J. B., Vanner, M. R., Gigan, S., Schwab, K. C., and Aspelmeyer, M., "Demonstration of an ultracold micro-optomechanical oscillator in a cryogenic cavity," *Nature Physics* **5**, 485 (2009).

[54] Verhagen, E., Deléglise, S., Weis, S., Schliesser, A., and Kippenberg, T. J., "Quantum-coherent coupling of a mechanical oscillator to an optical cavity mode," *Nature* **482**, 63 (2012).

[55] Rivière, R., Deléglise, S., Weis, S., Gavartin, E., Arcizet, O., Schliesser, A., and Kippenberg, T. J., "Optomechanical sideband cooling of a micromechanical oscillator close to the quantum ground state," *Physical Review A* **83**, 063835 (2011).

[56] Park, Y. S. and Wang, H. L., "Resolved-sideband and cryogenic cooling of an optomechanical resonator," *Nature Physics* **5**(7), 489 (2009).

[57] Chan, J., Mayer-Alegre, T. P., Safavi-Naeini, A. H., Hill, J. T., Krause, A., Gröblacher, S., Aspelmeyer, M., and Painter, O., "Laser cooling of a nanomechanical oscillator into its quantum ground state," *Nature* **478**, 89 (2011).

[58] Rocheleau, T., Ndukum, T., Macklin, C., Hertzberg, J. B., Clerk, A. A., and Schwab, K. C., "Preparation and detection of a mechanical resonator near the ground state of motion.," *Nature* **463**, 72 (2010).

[59] Teufel, J. D., Donner, T., Li, D., Harlow, J. H., Allman, M. S., Cicak, K., Sirois, A. J., Whittaker, J. D., Lehnert, K. W., and Simmonds, R. W., "Sideband cooling micromechanical motion to the quantum ground state," *Nature* **475**, 359 (2011).

[60] Poggio, M., Degen, C. L., Mamin, H. J., and Rugar, D., "Feedback cooling of a cantilever's fundamental mode below 5 mK," *Physical Review Letters* **99**, 017201 (2007).

[61] Vinante, A., Bignotto, M., Bonaldi, M., Cerdonio, M., Conti, L., Falferi, P., Liguori, N., Longo, S., Mezzena, R., Ortolan, A., Prodi, G. A., Salemi, F., Taffarello, L., Vedovato, G., Vitale, S., and Zendri, J.-P., "Feedback cooling of the normal modes of a massive electromechanical system to submillikelvin temperature," *Physical Review Letters* **101**, 033601 (2008).

[62] Hopkins, A., Jacobs, K., Habib, S., and Schwab, K., "Feedback cooling of a nanomechanical resonator," *Physical Review B* **68**, 235328 (2003).

[63] Cohadon, P. F., Heidmann, A., and Pinard, M., "Cooling of a mirror by radiation pressure," *Physical Review Letters* **83**, 3174 (1999).

[64] Kleckner, D. and Bouwmeester, D., "Sub-kelvin optical cooling of a micromechanical resonator," *Nature* **444**, 75 (2006).

[65] Corbitt, T., Wipf, C., Bodiya, T., Ottaway, D., Sigg, D., Smith, N., Whitcomb, S., and Mavalvala, N., "Optical dilution and feedback cooling of a gram-scale oscillator to 6.9 mK," *Physical Review Letters* **99**, 160801 (2007).

[66] Li, T., Kheifets, S., and Raizen, M. G., "Millikelvin cooling of an optically trapped microsphere in vacuum," *Nature Physics* **7**, 527 (2011).

[67] Braginsky, V. B., Gorodetsky, M. L., and Ilchenko, V. S., "Quality-factor and non-linear properties of optical whispering-gallery modes," *Physics Letters A* **137**, 393 (1989).

[68] Treussart, P., Ilchenko, V. S., Roch, J.-F., Hare, J., Lefèvre-Seguin, V., Raimond, J.-M., and Haroche, S., "Evidence for intrinsic Kerr bistability of high-Q microsphere resonators in superfluid helium," *European Journal of Physics D* **1**, 235 (1998).

[69] Spillane, S. M. and Kippenberg, T. J. Vahala, K. J., "Ultralow-threshold Raman laser using a spherical dielectric microcavity," *Nature* **415**, 621 (2002).

[70] Kitamura, R., L.Pilon, and Jonasz, M., "Optical constants of silica glass from extreme ultraviolet to far infrared at near room temperature," *Applied Optics* **46**, 8118 (2007).

[71] Armani, D. K., Kippenberg, T. J., Spillane, S. M., and Vahala, K. J., "Ultra-high-Q toroid microcavity on a chip," *Nature* **421**, 925 (2003).

[72] Kippenberg, T. J., Spillane, S. M., and Vahala, K. J., "Kerr-nonlinearity optical parametric oscillation in an ultrahigh-Q toroid microcavity," *Physical Review Letters* **93**, 083904 (2004).

[73] Rokhsari, H. and Vahala, K., "Observation of Kerr nonlinearity in microcavities at room temperature," *Optics Letters* **30**, 427 (2005).

[74] Del'Haye, P., Schliesser, A., Arcizet, O., Wilken, T., Holzwarth, R., and Kippenberg, T. J., "Optical frequency comb generation from a monolithic microresonator," *Nature* **450**, 1214 (2007).

[75] Del'Haye, P., *Chip-based Optical Frequency Combs*, PhD thesis, Ludwig-Maximilians-Universität (2011).

[76] Kippenberg, T. J., Spillane, S. M., Min, B., and Vahala, K. J., "Theoretical and experimental study of stimulated and cascaded Raman scattering in ultrahigh-Q optical microcavities," *IEEE Journal of Selected Topics in Quantum Electronics* **10**, 1219 (2004).

[77] Kippenberg, T. J., Spillane, S. M., Armani, D. K., and Vahala, K. J., "Ultralow-threshold microcavity Raman laser on a microelectronic chip," *Optics Letters* **29**, 1224 (2004).

[78] B.Min, Yang, L., and K.Vahala, "Controlled transition between parametric and raman oscillations in ultrahigh-Q silica toroidal microcavities," *Applied Physics Letters* **87**, 181109 (2005).

[79] Carmon, T.and Yang, L. and Vahala, K. J., "Dynamical thermal behavior and thermal selfstability of microcavities," *Optics Express* **12**, 4742 (2004).

[80] Rokhsari, H., Kippenberg, T. J., Carmon, T., and Vahala, K. J., "Radiation-pressure-driven micro-mechanical oscillator," *Optics Express* **13**, 5293 (2005).

[81] Carmon, T., Rokhsari, H., Yang, L., Kippenberg, T. J., and Vahala, K. J., "Temporal behavior of radiation-pressure-induced vibrations of an optical microcavity phonon mode," *Physical Review Letters* **94**, 223902 (2005).

[82] Kippenberg, T. J., Rokhsari, H., Carmon, T., Scherer, A., and Vahala, K. J., "Analysis of radiation-pressure induced mechanical oscillation of an optical microcavity," *Physical Review Letters* **95**, 033901 (2005).

[83] Strutt, J. W., "The problem of the whispering gallery," *Philosophical Magazine* **20**, 1001 (1910).

[84] Treussart, F., *Etude expérimentale de l'effet laser dans des microsphères de silice dopées avec des ions néodyme*, PhD thesis, Université Paris VI (1997).

[85] Oraevsky, A. N., "Whispering-gallery waves," *Quantum Electronics* **32**, 377 (2002).

[86] Long, R., *Couplage d'une microsphère accordable et d'une puce à atomes*, PhD thesis, Université Paris VI (2003).

[87] Min, B., Yang, L., and Vahala, K., "Perturbative analytic theory of an ultrahigh-Q toroidal microcavity," *Physical Review A: Atomic, Molecular, and Optical Physics* **76**, 013823 (2007).

[88] Oxborrow, M., "Traceable 2D finite-element simulation of the whispering-gallery modes of axisymmetric electromagnetic resonators," *IEEE Transactions on Microwave Theory and Techniques* **55**, 1209 (2007).

[89] Schliesser, A., Anetsberger, G., Rivière, R., Arcizet, O., and Kippenberg, T. J., "High-sensitivity monitoring of micromechanical vibration using optical whispering gallery mode resonators," *New Journal of Physics* **10**, 095015 (2008).

[90] Fomin, A. E. and Gorodetsky, M. L., "Spheroidal microresonators for the optoelectronics," *Proceedings of SPIE* **5948**, 594818 (2005).

[91] Gorodetsky, M. L. and Formin, A. E., "Geometrical theory of whispering-gallery modes," *IEEE Journal of Selectred Topics in Quantum Electronics* **12**, 33 (2006).

[92] Gorodetsky, M. L. and Formin, A. E., "Eigenfrequencies and Q factor in the geometrical theory of whispering-gallery modes," *Quantum Electronics* **37**, 167 (2007).

[93] Gorodetsky, M. L. Private communication.

[94] Ilchenko, V. S., Gorodetsky, M. L., Yao, X. S., and Maleki, L., "Microtorus: a high-finesse microcavity with whispering-gallery modes," *Optics Letters* **26**, 256 (2001).

[95] Gorodetsky, M. L., [*Optical microresonators with giant quality factors*], M. Fizmatlit (2010).

[96] Gorodetsky, M. L., Savchenkov, A. A., and S., I. V., "Ultimate Q of optical microsphere resonators," *Optics Letters* **21**, 453 (1996).

[97] Gorodetsky, M., Pryamiko, A. D., and Ilchenko, V. S., "Rayleigh scattering in high-Q microspheres," *Journal of Optical society of America B* **17**, 1051 (2000).

[98] Plummer, J., Deal, M. D., and Griffin, P. B., [*Silicon VLSI Technology: Fundamentals, Practice, and Modeling*], Prentice Hall (2000).

[99] Beckmann, K. H. and Harrick, N. J., "Hydrides and hydroxyls in thin silicon dioxide films," *Journal of The Electrochemical Society* **118**, 614 (1971).

[100] Nagasawa, Y., Yoshii, I., Naruke, K., Yamamoto, K., Ishida, H., and A.Ishitani, "The study of the thermal oxide films on silicon wafers by Fourier transform infrared attenuated total reflection spectroscopy," *Journal of Applied Physics* **68**, 1429 (1990).

[101] Rokhsari, H., Spillane, S. M., and Vahala, K. J., "Loss characterization in microcavities using the thermal bistability effect," *Applied Physics Letters* **85**, 3029 (2004).

[102] Vernooy, D. W., Ilchenko, V. S., Mabuchi, H., Streed, E. W., and Kimble, H. J., "High-Q measurements of fused-silica microspheres in the near infrared," *Optics Letters* **23**, 247 (1998).

[103] Miura, K., Tanaka, K., and Hirao, K., "Laser oscillation of a Nd^{3+}doped fluoride glass microsphere," *Journal of Materials Science Letters* **15**, 1854 (1996).

[104] Park, Y.-S.and Cook, A. and Wang, H., "Cavity QED with diamond nanocrystals and silica microspheres," *Nano Letters* **6**, 2075 (2006).

[105] Dubreuil, N., Knight, J. C., Leventhal, D. K., Sandoghdar, V., Hare, J., and Lefèvre, V., "Eroded monomode optical fiber for whispering-gallery mode excitation in fused-silica microspheres," *Optics Letters* **20**, 813 (1995).

[106] Little, B. E., Laine, J.-P., and Haus, H. A., "Analytic theory of coupling from tapered fibers and half-blocks into microsphere resonators," *J. Lightwave Technol.* **17**, 704 (1999).

[107] Knight, J. C., Cheung, G., Jacques, F., and Birks, T. A., "Phase-matched excitation of whispering-gallery-mode resonances by a fiber taper," *Optics Letters* **22**, 1129 (1997).

[108] Schiller, S., "Asymptotic expansion of morphological resonance frequencies in Mie scattering," *Applied Optics* **32**, 2181 (1993).

[109] M., C., Painter, O., and Vahala, K. J., "Observation of critical coupling in a fiber taper to a silica-microsphere whispering-gallery mode system," *Physical Review Letters* **85**, 74 (2000).

[110] Spillane, S. M., Kippenberg, T. J., Painter, O. J., and Vahala, K. J., "Ideality in a fiber-taper-coupled microresonator system for application to cavity quantum electrodynamics," *Physical Review Letters* **91**, 043902 (2003).

[111] Ma, R., Schliesser, A., Del'Haye, P., Dabirian, A., Anetsberger, G., and Kippenberg, T. J., "Radiation-pressure-driven vibrational modes in ultrahigh-Q silica microspheres," *Optics Letters* **32**(15), 2200 (2007).

[112] Landau, L. D. and Lifshitz, E. M., [*Theory of elasticity*], Pergamon Books Ltd. (1986).

[113] Nishiguchi, N. and Sakuma, T., "Vibrational spectrum and specific heat of fine particles," *Solid State Communications* **38**, 1073 (1981).

[114] Lifshitz, R. and Roukes, M. L., "Thermoelastic damping in micro- and nanomechanical systems," *Physical Review B* **61**, 5600 (2000).

[115] Ekinci, K. L. and Roukes, M. L., "Nanoelectromechanical systems," *Review of Scientific Instruments* **76**, 061101 (2005).

[116] Anetsberger, G., Rivière, R., Schliesser, A., Arcizet, O., and Kippenberg, T. J., "Ultralow-dissipation optomechanical resonators on a chip," *Nature Photonics* **2**, 627 (2008).

[117] Schliesser, A., Rivière, R., Anetsberger, G., Arcizet, O., and Kippenberg, T. J., "Resolved-sideband cooling of a micromechanical oscillator," *Nature Physics* **4**, 415 (2008).

[118] Arcizet, O., Rivière, R., Schliesser, A., Anetsberger, G., and Kippenberg, T. J., "Cryogenic properties of optomechanical silica microcavities," *Physical Review A* **80**(2), 021803 (2009).

[119] Zhou, X. *In preparation* (2011).

[120] Weis, S., Rivière, R., Deléglise, S., Gavartin, E., Arcizet, O., Schliesser, A., and Kippenberg, T. J., "Optomechanically induced transparency," *Science* **330**, 1520 (2010).

[121] Binnig, G., Quate, C. F., and Gerber, C., "Atomic force microscope," *Physical Review Letters* **56**, 930 (1986).

[122] Rugar, D., Budakian, R., Mamin, H. J., and Chui, B. W., "Single spin detection by magnetic resonance force microscopy," *Nature* **430**, 329 (2004).

[123] Jensen, K., Kim, K., and Zettl, A., "An atomic-resolution nanomechanical mass sensor," *Nature Nanotechnology* **3**, 533 (2008).

[124] Naik, A. K., Hannay, M. S., Hiebert, W. K., Feng, X. L., and Roukes, M. L., "Towards single-molecule nanomechanical mass spectrometry," *Nature Nanotechnology* **4**, 445 (2009).

[125] Blom, F. R., Bouwstra, S., Elwenspoek, M., and Fluitman, J. H. J., "Dependence of the quality factor of macromachined silicon beam resonators on pressure and geometry," *Journal of Vacuum Science and Technology B* **10**, 19 (1992).

[126] Hosaka, H., Itao, K., and Kuroda, S., "Damping characteristics of beam-shaped micro-oscillators," *Sensors and Actuators A: Physical* **49**, 87 (1995).

[127] Braginsky, V. B., Mitrofanov, V. P., and Tokmakov, K. V., "Energy dissipation in the pendulum mode of the test mass suspension of a gravitational wave antenna," *Physics Letters A* **218**, 164 (1996).

[128] Liu, X., Morse, S. F., Vignola, J. F., Photiadis, D. M., Sarkissian, A., Marcus, M. H., and Houston, B. H., "On the modes and loss mechanisms of a high Q mechanical oscillator," *Applied Physics Letter* **78**, 1346 (2001).

[129] Verbridge, S. S., Shapiro, D. F., Craighead, H. G., and Parpia, J. M., "Macroscopic tuning of nanomechanics: Substrate bending for reversible control of frequency and quality factor of nanostring resonators," *Nano Letters* **7**, 1728 (2007).

[130] Wilson-Rae, I., "Intrinsic dissipation in nanomechanical resonators due to phonon tunneling," *Physical Review B* **77**, 245418 (2008).

[131] Wilson-Rae, I., Barton, R. A., Verbridge, S. S., Southworth, D. R., Ilic, B., Craighead, H. G., and Parpia, J. M., "High-Q nanomechanics via destructive interference of elastic waves," *Physical Review Letters* **106**, 047205 (2011).

[132] Cole, G., I.Wilson-Rae, Werbach, K., Vanner, M. R., and Aspelmeyer, M., "Phonon-tunnelling dissipation in mechanical resonators," *Nature Communications* **2**, 231 (2011).

[133] Rat, E., Foret, M., Massiera, G., Vialla, R., Arai, M., Vacher, R., and Courtens, E., "Anharmonic versus relaxational sound damping in glasses. I. Brillouin scattering from densified silica," *Physical Review B* **72**, 214204 (2005).

[134] Vacher, R., Courtens, E., and Foret, M., "Anharmonic versus relaxational sound damping in glasses. II. Vitreous silica," *Physical Review B* **72**, 214205 (2005).

[135] Hund, F., "Zur Deutung der Molekelspektren," *Zeitschrift für Physik* **43**, 805–826 (1927). 10.1007/BF01397249.

[136] Pauling, L., "The rotational motion of molecules in crystals," *Physical Review* **36**, 430 (1930).

[137] Phillips, W. A., "Tunneling states in amorphous solids," *Journal of Low Temperature Physics* **3**, 351 (1972).

[138] Anderson, P. W., Halperin, B. I., and Varma, C. M., "Anomalous low-temperature thermal properties of glasses and spin glasses," *The Philosophical Magazine* **25**, 1 (1972).

[139] Enss, C. and Hunklinger, S., [*Low Temperature Physics*], Springer (2005).

[140] Jäckle, J., Piché, L., Arnold, W., and Hunklinger, S., "Elastic effects of structural relaxation in glasses at low temperatures," *Journal of Non-Crystalline Solids* **20**, 365 (1976).

[141] Tielbürger, D., Merz, R., Erhenfels, R., and Hunklinger, S., "Thermally activated relaxation processes in vitreous silica: An investigation by brillouin scattering at high pressures," *Physical Review B* **45**, 2750 (1992).

[142] Bartell, U. and Hunklinger, S., "Pressure-dependence of the low temperature acoustics anomalies in vitreous silica," *Journal de Physique* **43**(NC-9), 489 (1982).

[143] Jäckle, J., "On the ultrasonic attenuation in glasses at low temperatures," *Zeitschrift für Physik* **257**, 212 (1972).

[144] Pohl, R. O., Liu, X., and Thompson, E., "Low-temperature thermal conductivity and acoustic attenuation in amorphous solids," *Review of Mordern Physics* **14**, 991 (2002).

[145] Arcizet, O. Unpublished.

[146] Hunklinger, S., Arnold, W., Stein, S., Nava, R., and Dransfeld, K., "Saturation of the ultrasonic absorption in vitreous silica at low temperatures," *Physics Letters A* **42**, 253 (1972).

[147] Graebner, J. E. and Golding, B., "Phonon echo in a glass at low temperature," *Physical Review B* **19**, 964 (1979).

[148] Zhang, T.-C., Poizat, J.-P., Grelu, P., Roch, J.-F., Grangier, P., Marin, F., Bramati, A., Jost, V., Levenson, M. D., and Giacobino, E., "Quantum noise of free-running and externally-stabilized laser diodes," *Quantum and Semiclassical Optics: Journal of the European Optical Society Part B* **7**, 601 (1995).

[149] Tsunekane, M., Taguchi, N., and I., H., "High-power, efficient, low-noise, continuous-wave all-solid-state Ti:sapphire laser," *Optics Letters* **21**, 1912 (1996).

[150] Hädrich, S., Jauernik, P., and McCrumb, L., "Construction and characterization of a Titanium:Sapphire CW laser system with kHz linewidth," *Solid State Lasers XV: Technology and Devices* **6100**(1), 61000V–1, SPIE (2006).

[151] Sirah Laser- und Plasmatechnik GmbH, *Matisse User's Guide version 1.9*.

[152] Park, Y.-S. and Wang, H., "Regenerative pulsation in silica microspheres," *Optics Letters* **32**, 3104 (2008).

[153] Srinivasan, K. and Painter, O., "Optical fiber taper coupling and high-resolution wavelength tuning of microdisk resonators at cryogenic temperatures," *Applied Physics Letters* **90**(3), 031114 (2007).

[154] Drever, R. W. P., Hall, J. L., Kowalski, F. V., Hough, J., Ford, G. M., Munley, A. J., and Ward, H., "Laser phase and frequency stabilization using an optical resonator," *Applied Physics B: Lasers and Optics* **31**, 97 (1983).

[155] Black, E. D., "An introduction to Pound-Drever-Hall laser frequency stabilization," *American Journal of Physics* **69**, 70 (2001).

[156] White, G. K., "Thermal expansion of reference materials: copper, silica and silicon," *Journal of Physics D* **6**, 2070 (1973).

[157] White, G. K., "Thermal expansion of vitreous silica at low temperatures," *Physical Review Letters* **34**, 204 (1975).

[158] Zhou, X., "Private communication,".

[159] Tilley, D. R. and Tilley, J., [*Superfluidity and Superconductivity*], Adam Hilger (1990).

[160] Kierstead, H., "Dielectric constant and molar volume of saturated liquid ^{3}He and ^{4}He," *Journal of Low Temperature Physics* **23**, 791 (1976).

[161] Ilchenko, V. S. and Gorodetsky, M. L., "Thermal nonlinear effects in optical whispering gallery microresonator," *Laser Physics* **2**, 1004 (1992).

[162] Esel'son, B. N., Kaganov, M. I., Rudavskii, E. Y., and Serbin, I. A., ""Sounds" in superfluid liquids," *Soviet Physics Uspekhi* **17**, 215 (1975).

[163] Landau, L. D. and Lifshitz, E. M., [*Fluid Mechanics*], Pergamond Press (1959).

[164] Zeller, R. C. and Pohl, R. O., "Thermal conductivity and specific heat of noncrystalline solids," *Physical Review B* **4**, 2029 (1971).

[165] Fulde, P. and Wagner, H., "Low-temperature specific heat and thermal conductivity of noncrystalline solids," *Physical Review Letters* **27**, 1280 (1971).

[166] Hao, H.-Y., Neumann, M., Enss, C., and Fleischmann, A., "Contactless technique for thermal conductivity measurement at very low temperature," **75**, 2718 (2004).

[167] Alnis, J., Matveev, A., Kolachevsky, N., Udem, T., and Hänsch, T. W., "Subhertz linewidth diode lasers by stabilization to vibrationally and thermally compensated ultralow-expansion glass Fabry-Pérot cavities," *Physical Review A* **77**, 053809 (2008).

[168] Atkins, K. R., "Third and fourth sound in liquid helium II," *Physical Review* **113**, 962 (1959).

[169] Everitt, C. W. F., Atkins, K. R., and Denenstein, A., "Third sound in liquid helium films," *Physical Review* **136**, A1494 (1964).

[170] American Vacuum Society, "Graphic symbols in vacuum technology," *Journal of Vacuum Science and Technology* **4**, 139 (1967).

[171] O'Connell, A. D., Hofheinz, M., Ansmann, M., Bialczak, R. C., Lenander, M., Lucero, E., Neeley, M., Sank, D., Wang, H., Weides, M., Wenner, J., Martinis, J. M., and Cleland, A. N., "Quantum ground state and single-phonon control of a mechanical resonator," *Nature* **464**, 697 (2010).

[172] Hadjar, Y., *Etude du couplage optomécanique dans une cavité de grande finesse. Observation du mouvement Brownien d'un miroir*, PhD thesis, Université Paris VI (1998).

[173] Cohadon, P., *Bruit thermique et effets de la pression de radiation dans une cavité optique de grande finesse.*, PhD thesis, univesité Paris VI (2000).

[174] Anetsberger, G., Arcizet, O., Unterreithmeier, Q. P., Rivière, R., Schliesser, A., Weig, E. M., Kotthaus, J. P., and Kippenberg, T. J., "Near-field cavity optomechanics with nanomechanical oscillators," *Nature Physics* **5**, 909 (2009).

[175] Anetsberger, G., Gavartin, E., Arcizet, O., Unterreithmeier, Q. P., Weig, E. M., Gorodetsky, M. L., Kotthaus, J. P., and Kippenberg, T. J., "Measuring nanomechanical motion with an imprecision below the standard quantum limit," *Physical Review A* **82**, 061804 (2010).

[176] Milonni, P. W., [*Fast Light, Slow Light and Left-Handed Light*], Institute of Physics Publishing (2005).

[177] Fleischhauer, M. and Imamoglu, A.and Marangos, J. P., "Electromagnetically induced transparency: Optics in coherent media," *Reviews of Modern Physics* **77**, 633 (2005).

[178] Boller, K.-J., Imamolu, A., and Harris, S. E., "Observation of electromagnetically induced transparency," *Physical Review Letters* **66**, 2593 (1991).

[179] Fabre, C., [*Atomes et lumière: intéraction matière rayonnement*], Ecole Doctorale de Physique de la Région Parisienne (2004).

[180] Zhang, J., Peng, K., and Braunstein, S. L., "Quantum-state transfer from light to macroscopic oscillators," *Physical Review A* **68**, 013808 (2003).

[181] Safavi-Naeini, A. H., Alegre, T. P. M., Chan, J., Eichenfield, M., Winger, M., Lin, Q., Hill, J. T., Chang, D. E., and Painter, O., "Electromagnetically induced transparency and slow light with optomechanics," *Nature* **472**, 69 (2011).

[182] Teufel, J. D., Li, D., Allman, M. S., Cicak, K., Sirois, A. J., Whittaker, J. D., and Simmonds, R. W., "Circuit cavity electromechanics in the strong coupling regime," *Nature* **471**, 204 (2011).

[183] Gröblacher, S., Hammerer, K., Vanner, M. R., and Aspelmeyer, M., "Observation of strong coupling between a micromechanical resonator and an optical cavity field," *Nature* **460**, 724 (2009).

[184] Kimble, H. J., "Strong interactions of single atoms and photons in cavity QED," *Physica Scripta* **T76**, 127 (1998).

[185] Stannigel, K., Rabl, P., Sørensen, A. S., Zoller, P., and Lukin, M. D., "Optomechanical transducers for long-distance quantum communication," *Physical Review Letters* **105**, 220501 (2010).

[186] Spierings, G. A. C. M., "Wet chemical etching of silicate glasses in hydrofluoric acid based solutions," *Journal of Material Science* **28**, 6261 (1993).

[187] Kippenberg, T. J., Spillane, S. M., Armani, D. K., and Vahala, K. J., "Fabrication and coupling to planar high-Q silica disk microcavities," *Applied Physics Letters* **83**, 797 (2003).

[188] Kippenberg, T. J., Kalkman, J., Polman, A., and Vahala, K. J., "Demonstration of an erbium-doped microdisk laser on a silicon chip," *Physical Review A* **74**, 051802 (2006).

[189] Williams, K. R., Gupta, K., and Wasilik, M., "Etch rates for micromachining processing - Part II," *Journal of Microelectromechanical systems* **12**, 761 (2003).

[190] Su, K. and Tabata, O., "Effects of aperture size and pressure on XeF_2 etching of silicon," *Microsystem Technologies* **9**, 11 (2002).

[191] McLachlan, A. D. and Meyer, F. P., "Temperature dependence of the extinction coefficient of fused silica for CO_2 laser wavelengths," *Applied Optics* **26**, 1728 (1987).

[192] Ding, L., Belacel, C., Ducci, S., Leo, G., and Favero, I., "Ultralow loss single-mode silica tapers manufactured by a microheater," *Applied Optics* **49**, 2441 (2010).

Acknowledgements

The doctoral work presented along this thesis has been an exceptional experience whose success could be accomplished only thanks to the intervention of persons that I would like here to warmly acknowledge.

I would like to express my strongest gratitude to Prof. Tobias J. Kippenberg who hosted me for my doctoral thesis, starting almost one year after the establishment of his Independent Junior Research Group *Laboratory of Photonics*, also known as the "K-lab". He constantly succeeded in, like the "laboureur" of the fable, guiding me, motivating me and pushing me to discover the treasure hidden in the work that I performed in cavity optomechanics. He has been also for me a precious source of scientific ideas and technical advice that have considerably enriched my stay in his group.

I wish to express my particular acknowledgements to Prof. Theodor W. Hänsch who accomodated not only our group but also myself in his Laser Spectroscopy division of the Max-Planck-Institut für Quantenoptik, providing thus a high-quality work environment whose atmosphere has been particularly beneficial for the pursue of this work. His interest in the progresses of the projects has also been an immense source of motivation for me during this thesis.

From the beginning, it has been possible to work on silica microtoroids only thanks to the courtesy of Prof. Jörg P. Kotthaus who granted access to his clean room to our group and to me presonally, at the Center for NanoScience at the Ludwig-Maximilians-Universität. I would like to thank him for providing this precious support and also to acknowledge Prof. Jochen Feldmann for letting me do part of the "spoke" fabrication process with his equipments.

I also would like to thank Prof. Wilhelm Zwerger for accepting to review this thesis.

The laboratory work required for the particularly challenging project I had partly the charge of has been achieved only thanks to the strong and stimulating interactions among the "cooling" members. Albert Schliesser, in addition to introducing me to the lab, has always stimulated me with his abnegated work and the plethora of ideas that he has always been keen on sharing with me about our common projects. Simultaneously, Olivier Arcizet has provided me with his immense technical and scientific experience in the field and his patient guidance as a post-doc has made our work in common particularly fruitful. With the advent of the "^{3}He"-part of the work, Stefan Weis joined and his commitment to the work together with his precise experimental approach made it extremely pleasant to work with for me. As the last to enter the crew, Samuel Deléglise brought novel perspectives to

the project and his eager to obtain always better results made him an immensely valuable colleague.

From the technical side of the cryogenic installation, I wish to thank the precious assistance of Dr. Thomas Becker and Dr. Pierre Thoumany. The exciting discussions about physics I had additionally with Pierre were a great source of inspiration.

For the mechanical studies of the system, Georg Anetsberger has to be acknowledged, our close and pleasant collaboration giving birth to the "spoke" resonators. Pascal Del'Haye literally accompanied me throughout all this time and became, after my move in his office, a valuable officemate with whom I really enjoyed discussing passionately about physics.

I wish to thank particularly the technicians who worked with me on my various projects: Charly Linner, Wolfgang Simon and Helmut Brückner. Without their talented contributions, the various setup constructions would simply not have been possible.

The administrative tasks have been eased by the helpful contributions of Christina Becker, Ingrid Hermann, Gabriele Gschwendtner and Patricia Marti-Rochat. I wish to have also a considerate thought to Rosemarie Lechner who regrettably cannot read these lines.

Precious work collaborations have also taken place with Philip Altpeter, Federico Bürsgens, Peter Fendel, Prof. Marie Foret, Emanuel Gavartin, Achim Marx, Katharina Predehl and Prof. René Vacher and Xiaoqing Zhou. Ali Dabirian, Jens Dobrindt, Tobias Herr, Johannes Hofer, Nino Karpf, Stefanie Krysak, Rui Ma, Nima Nooshi, Bastian Schröter, Ewold Verhagen, Pierre Verlot, Christine Wang and Yang Yang provided very nice work atmosphere in the group.

Other persons also made my doctoral period pleasant: Nico, Fred, le Tripot, the Quantenkick, Andreas, Marie, Stefie and of course Belina.

Finally, my parents Christine and Jean, and my sister Laura are acknowledged for their continuous and cheering support. Despite the distance, their presence has always felt immense to me.